Computational Design of Compositionally Complex 3D and 2D Semiconductors

by

Duo Wang

A Dissertation Presented in Partial Fulfillment
of the Requirements for the Degree
Doctor of Philosophy

Approved October 2020 by the
Graduate Supervisory Committee:

Houlong Zhuang, Chair
Arunima Singh
Yang Jiao

ARIZONA STATE UNIVERSITY

December 2020

ABSTRACT

The structural and electronic properties of compositionally complex semiconductors have long been of both theoretical interest and engineering importance. As a new class of materials with an intrinsic compositional complexity, medium entropy alloys (MEAs) are immensely studied mainly for their excellent mechanical properties. The electronic properties of MEAs, however, are less well investigated. In this thesis, various properties such as electronic, spin, and thermal properties of two three-dimensional (3D) and two two-dimensional (2D) compositionally complex semiconductors are demonstrated to have promising various applications in photovoltaic, thermoelectric, and spin quantum bits (qubits).

3D semiconducting Si-Ge-Sn and C_3BN alloys is firstly introduced. Density functional theory (DFT) calculations and Monte Carlo simulations show that the $Si_{1/3}Ge_{1/3}Sn_{1/3}$ MEA exhibits a large local distortion effect yet no chemical short-range order. Single vacancies in this MEA can be stabilized by bond reformations while the alloy retains semiconducting. DFT and molecular dynamics calculations predict that increasing the compositional disorder in $Si_yGe_ySn_x$ MEAs enhances their electrical conductivity while weakens the thermal conductivity at room temperature, making the $Si_yGe_ySn_x$ MEAs promising functional materials for thermoelectric devices. Furthermore, the nitrogen-vacancy (NV) center analog in C_3BN (NV-C_3BN) is studied to explore its applications in

quantum computers. This analog possesses similar properties to the NV center in diamond such as a highly localized spin density and strong hyperfine interactions, making C_3BN suitable for hosting spin qubits. The analog also displays two zero-phonon-line energies corresponding to wavelengths close to the ideal telecommunication band width, useful for quantum communications.

2D semiconducting transition metal chalcogenides (TMCs) and PtPN are also investigated. The quaternary compositionally complex TMCs show tunable properties such as in-plane lattice constants, band gaps, and band alignment, using a high through-put workflow from DFT calculations in conjunction with the virtual crystal approximation. A novel 2D semiconductor PtPN of direct bandgap is also predicted, based on pentagonal tessellation.

The work in the thesis offers guidance to the experimental realization of these novel semiconductors, which serve as valuable prototypes of other compositionally complex systems from other elements.

This thesis is dedicated to my parents and grandparents.

ACKNOWLEDGEMENT

I would like to express my very great appreciation to my advisor, Dr. Houlong Zhuang, who has offered me this incredible opportunity of the Ph.D. position to continue my research. I am grateful for his patient guidance throughout my whole Ph.D. period. His constant help and insightful suggestions encouraged me to pursuit my career.

I would also like to thank my committee members of Dr. Arunima Singh and Dr. Yang Jiao, who also taught me very useful class. Both of them always offered me great advice to improve my work.

I would like to appreciate my colleagues Lei Liu and Wenjiang Huang, and Chance Price for their help and discussion. I also want to acknowledge Dr. Karl Sieradzki and Yusi Xie, for helpful discussion in experiment and theory as well as discussing the simulation processes.

I want to give my gratitude to Dr. Mohan Chen for the research discussions. I also want to appreciate the collaboration with Neha Basu from BASIS Scottsdale High School and Sreeharsha Lakamsani from Hamilton High School.

Chapters 2 to 7 in the thesis have been peer-reviewed and published. I am grateful for the comments and suggestions from the anonymous reviewers and editors.

I also thank my friends' accompanying all the time. Moreover, I would also like to appreciate my parents and grandparents, for their constant support and unending care.

TABLE OF CONTENTS

Page

CHAPTER Page

CHAPTER Page

LIST OF TABLES

Table Page

Table Page

Table Page

Table Page

LIST OF FIGURES

Figure Page

Figure Page

Figure Page

Figure Page

CHAPTER I

INTRODUCTIONS

1.1 The materials in need

Semiconductors find their wide applications from quantum computing to aerospace engineering. A semiconductor is a material whose electrical conductivity is in between the conductor such as copper, and the insulator such as glass. Because of the partial filled electron states, the conduction and valence band are overlapped in conductors, whereas in semiconductors, the conduction and valence band are separated. Energy is required to excite the electrons to hop across the band gap and become conductive. Since the energy can be controlled and has many forms, such as photon and phonon, the properties of semiconductors can be manipulated for desired purposes. Decades of efforts have been made to develop the semiconductors in order to fulfill different requirements in practices. For example, the light emitting diodes (LED) technique has been developing to function as the upgraded light source of reliability, versatility, and visibility, comparing to the currently popular yet less efficient incandescent bulb [1]. Taking the advantage of thin film processing and nanoscale quantum dot fabricating, the evolution of LED materials lies in the direction of high color purity, high energy-efficiency, and eco-friendly [2-4]. Besides the photoluminescent applications, this chapter will briefly introduce the semiconductors applications in the fields of energy harvesting and quantum computing.

1.1.1 Semiconductors for energy-harvesting

Based on the report from National Center for Atmospheric Research [5], the climate changing has severed resulted in the Arctic warming, temperature increased, and the loss of sea-ice. It is of urgency to decrease the dependency on the fossil fuel in energy generation in order to reduce the emission of greenhouse gases [6]. Renewable sources of energy such as solar, wind, and geothermal draw people's attention for the sustainable, inexhaustive, and clean nature.

Semiconducting materials are widely used as the devices for energy harvesting from renewable sources. By alloying, semiconductors are versatile to fit for different conditions for the tunable and controllable electronic properties such as carrier effective mass and band gap energy [7,8]. On the one hand, in energy harvesting, various semiconducting alloys such as PbS_xSe_{1-x} [9], $Cu(In_{1-x}Ga_x)(S_{1-y}Se_y)_2$ [10], and $Zn_xCd_{1-x}Se$ [11] are purposed as photovoltaic (PV) materials to convert the solar energy to electric power via photon-electron interaction [12]. For example, metal chalcogenides such as PbS and PbSe are proposed as the PV materials for the large open circuit voltage (V_{OC}) of PbS and large short-circuit photocurrent densities (J_{SC}) of PbSe. The compositional tunable PbS_xSe_{1-x} alloys show the high power conversion efficiency comparing to their binary constituents of PbS and PbSe [9].

On the other hand, semiconductors are also applied as thermoelectric materials for thermoelectric generators (TEG), utilized to collect the heat and transfer it to electric power. The thermoelectric performance (zT) depends on various factors such as electrical and

thermal conductivity, as well as the Seebeck coefficient [13,14]. The alloying and doping approach of semiconductors also have been conducted in order to enhance the *zT*. For example, the SnTe shows a *zT* of 0.6 at 700K [15], by alloying that with MnTe, the $Sn_{1-x}Mn_xTe$ can obtain an tuned band structure, as well as the higher *zT* of 1.3 at 900 K, based on a decreased lattice thermal conductivity.

1.1.2 Semiconductors for quantum computing

Quantum computing is proposed with the benefits of solving a series of problems such as many-body molecular modelling, factorizing a large integer to break public-key cryptography, and discovering drugs to treat pandemic diseases [16], which are difficult or even impossible by the traditional computers or supercomputers. The quantum bit (qubit), as the analog of bit in traditional computer, appears as the fundamental unit of quantum computer. Various semiconductors are proposed as the potential materials for spin qubit, which record the distinguished states of $|0\rangle$ and $|1\rangle$ using the spin information (spin up and down). For example, a nitrogen vacancy (NV) center in diamond, consisting of a nitrogen atom substituting the carbon atom and a lattice vacancy at nearest neighbor, stands out as the promising candidate of spin qubit. Advantages of such system involve the long spin coherence time approaching 1s that allows the possibility of creation high entangled states, as well as a long distance entanglement of more than 1.3 km of two NV center diamonds to ensure the high fidelity in quantum-secure communication [17].

1.2 Outline of this thesis

In the following sections, we would like to discuss several semiconductors designed for the purposes in energy-harvesting as well as the quantum computing. The structure of the thesis is outlined as follow.

Chapter 2 and 3 introduce the entropy driven design of disordered 3D alloy from silicon (Si), germanium (Ge) and tin (Se). The electronic properties and vacancy tolerant semiconducting behavior of such alloy are discussed in Chapter 2, opening the possibility in the application of near-infrared optoelectronics. Besides, the concentration tunable electronic and thermal properties of the $Si_xGe_xSn_y$ alloys are discussed in Chapter 3, for the purpose of thermoelectric applications. In the next section of Chapter 4, we introduce the discover of disordered 2D transition metal chalcogenides (TMC) in quaternary systems from the model based on virtual crystal approximation. The selected entropy stabilized quaternary compositional complex TMC shows the potential in applications of electronic and optoelectronic devices. In Chapter 5, we design the NV center analog in C_3BN, which shows the similar electronic and spin properties as NV center in diamond, making it possible for spin qubit candidate for quantum computing. In Chapter 6 and 7, we propose two 2D semiconductors of PtPN and PtN_2 based on pentagonal tessellation. The tunable band gaps of both two materials are achieved via dimensional engineering to obtain PtPN and PtN_2 nanotubes.

CHAPTER II

SEMICONDUCTING SIGESN HIGH-ENTROPY ALLOY: A DENSITY FUNCTIONAL THEORY STUDY

2.1 Abstract

High-entropy alloys (HEAs), which have been intensely studied due to their excellent mechanical properties, generally refer to alloys with multiple equimolar or nearly equimolar elements. According to this definition, Si-Ge-Sn alloys with equal or comparable concentrations of the three Group IV elements belong to the category of HEAs. As a result, the equimolar elements of Si-Ge-Sn alloys likely cause their atomic structures to exhibit the same core effects of metallic HEAs such as lattice distortion. Here we apply density functional theory (DFT) calculations to show that the SiGeSn HEA indeed exhibits a large local distortion effect. Unlike metallic HEAs, our Monte Carlo and DFT calculations show that the SiGeSn HEA exhibits no chemical short-range order due to the similar electronegativity of the constituent elements, thereby increasing the configurational entropy of the SiGeSn HEA. Hybrid density functional calculations show that the SiGeSn HEA remains semiconducting with a band gap of 0.38 eV, promising for economical and compatible mid-infrared optoelectronics applications. We then study the energetics of neutral single Si, Ge, and Sn vacancies and (expectedly) find wide distributions of vacancy formation energies, similar to those found in metallic HEAs. However, we also find anomalously small lower bounds (e.g., 0.04 eV for a Si vacancy) in the energy distributions,

which arise from the bond reformation near the vacancy. Such small vacancy formation energies and their associated bond reformations retain the semiconducting behavior of the SiGeSn HEA, which may be a signature feature of a semiconducting HEA that differentiates from metallic HEAs.

2.2 Introduction

Candies of different colors and flavors displayed in candy stores are often intriguing to many people (see Figure 2.1). Mirroring that scenario, in the early 1980s and 1990s metallurgists started mixing different types of atoms—each symbolizing one flavor of candy—of (nearly) equal concentration to form alloys [18,19] in the hope of obtaining special properties to extract the best elemental features from each of the combined elements. This mixing process leads to optimization of the overall performance of the resulting alloy, called high-entropy alloy (HEA). The emerging field of HEA is a subject of study for materials scientists, who prefer engineering materials to be both stronger and tougher, which are actually two incompatible mechanical properties. This work explores whether knowledge advanced in the HEA field, which we will review in this section, can be used to design semiconducting HEAs with an emphasis on their applications toward optoelectronics applications.

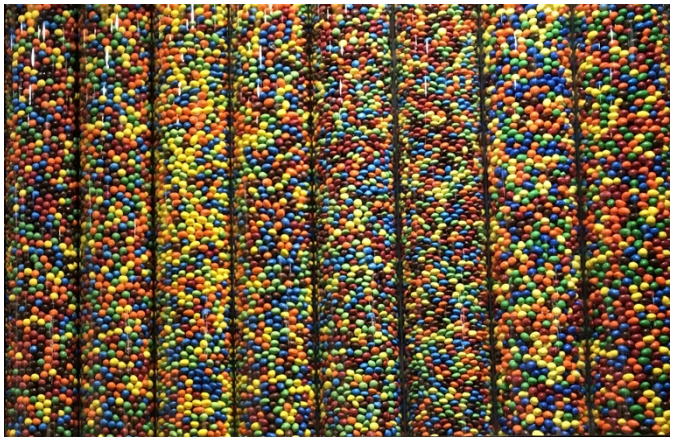

Figure 2.1. Transparent tubes filled with assorted candies, symbolizing high-entropy alloys with multiple principal elements.

Conventional alloy designs often start with selecting one element as the principal constituent and adding other elements to optimize the properties. After centuries of intense efforts on developing these alloys, obtaining targeted properties for traditional alloys is approaching its limit [20]. HEAs represent a new type of alloys that can potentially break the limit due to the presence of a variety of attractive properties currently absent from conventional alloys, making them the center of immense attention [21]. For instance, it is well known that an optimal engineering alloy requires a trade-off between toughness and strength, as these two properties favor and disfavor the movement of dislocations, respectively. Li et al. recently showed that novel FeMnNiCoCr HEAs can overcome this trade-off [22]. Other desirable properties of HEAs include antioxidant capacity [23], high temperature strength [24], high corrosion resistance [25,26], etc.

Two main definitions of HEAs are commonly used in the literature. The first one,

proposed in 2004 by Yeh et al., is based on composition [27], which states that HEAs refer to the alloys containing at least five principal elements, each of which has an atomic concentration between 5% and 35%, rather than unnecessary constraints, i.e., equimolar or near-equimolar concentration. Furthermore, similar to conventional alloys, HEAs may also contain minor elements (i.e., atomic concentration less than 5%) in order to tune the properties of base systems, which further expands the number of possible HEAs [28]. The second definition focuses on the magnitude of the configurational entropy. Because configurational entropy is often dominant in the total entropy of a system in comparison with the other entropies, i.e., vibrational, magnetic, and electronic entropies [29], the total entropy is approximated by the configurational entropy to avoid expensive calculations of the other entropies [30]. According to Boltzmann's entropy formula, the ideal configurational entropy of mixing per mole ΔS_{mix} for an ideal random N-component solid solution can be written as,

$$\Delta S_{\text{mix}} = -R \sum_{i=1}^{N} c_i \ln c_i \tag{2.1}$$

where R (8.31 J/K·mol) is the gas constant, c_i refers to the atomic concentration of the i^{th} element, and N is the total number of elements. If N is fixed, the maximum ΔS_{mix} is achieved when the atomic concentration for all the elements is the same. The second definition therefore implies that HEAs favor equimolar composition. Moreover, this definition further separates HEAs into low ($\Delta S_{\text{mix}} < 0.69\ R$), medium ($0.69\ R < \Delta S_{\text{mix}} <$

1.61 R), and high (ΔS_{mix} > 1.61 R) entropy alloys [31]. Yeh recently suggested that the boundary entropies (0.69 R and 1.61 R) are replaced by more reasonable 1.0 R and 1.5 R, respectively [32].

HEAs generally exhibit four phases: solid solution, intermetallic compound (i.e., a compound with a specific stoichiometry), mixed solid solution and intermetallic compound, and bulk metallic glasses. HEAs with a solid solution phase are often preferred, as most desirable properties are associated with this phase [33]. According to the entropy-based definition of HEAs, the stability of a solid solution phase can be enhanced by increasing the number of elements to maximize the configurational entropy [34,35]. But the probability of at least one pair of elements forming the intermetallic phase is directly proportional to the number of elements, leading to the competition between the solid solution and intermetallic phases [36,37]. It is therefore a daunting task to design new HEAs, i.e., to predetermine the phase given a combination of elements and the concentrations that form a HEA.

HEAs also show four core effects, which are the high configurational entropy effect, the sluggish diffusion effect, the lattice distortion effect, and the “cocktail” effect. These effects describe HEAs from the aspects of thermodynamics, kinetics, structures, and properties, respectively [31,38]. Based on the second law of thermodynamics, the high configurational entropy effect lowers the Gibbs free energy by compensating for the enthalpic change in the system, leading to possible formations of stable phases. Depending

on the competition between enthalpy and entropy, both disordered solid solution phases and ordered intermetallic compounds can form a HEA [39]. The high entropic effect favors a disordered solid solution phase. The sluggish diffusion effect kinetically lowers the rate of atomic diffusion, and thus reduces the overall phase transformation rate in an HEA, in contrast to conventional alloys. Because atoms in HEAs are usually bonded with the atoms of other elements, most of the atoms experience different diffusion paths and have different diffusion barriers [38,40]. Furthermore, forming an HEA by introducing multiple elements with different atomic sizes is associated with the lattice distortion effect. This originates from lattice strain and stress, as different elements have their own atomic radii, bonding energies, and structural preferences. The lattice distortion effect affects properties of an HEA such as hardness, electrical and thermal conductivity [30,31]. The “cocktail” effect of HEAs refers to the enhancement of material properties due to the presence of multiple principal components [32]. This effect emphasizes not only the individual elemental advantage but the synergetic results from the interactions among the atoms of multiple elements.

Significant research efforts have been devoted to studying the mechanical properties of HEAs for a variety of engineering applications. Even though HEAs vary widely from the constituent elements and their compositions, many of them commonly show useful mechanical properties such as high hardness values [41-44], yielding stresses [45-47], fatigue resistance [48-50], and irradiation resistance [51,52].

In contrast to the work on the mechanical properties of HEAs, there are much fewer studies on their functional properties such as magnetic and semiconducting properties [53]. Recently, several studies have started to discover these functional properties in HEAs. For example, by introducing metallic elements including ferromagnetic Fe, Co, and Ni, the resulting HEAs display paramagnetic [54] or even superparamagnetic properties [55]. Generally, introducing non-magnetic elements into HEAs as additional principal components also impacts the magnetism of the original HEAs. The change of magnetism in HEAs depends on the included elements, which cause a structural change and the formation of a solid solution phase. Recent studies also indicate that the saturation magnetization at room temperature and the Curie temperature of HEAs are both tunable by controlling the concentrations of the principal elements [56]. As an example of the semiconducting properties of HEAs, recent studies found that upon successively adding alloying elements Ge, Pb, and Mn to the SnTe binary alloy to form HEAs, the valence bands and the band gaps in the HEAs are modified as a result of the cocktail effect [57]. In particular, the ternary Sn-Ge-Te HEA showed a drastic reduction in the band gap without significantly modifying the original band structure. On the contrary, the Sn-Ge-Pb-Mn-Te HEA not only had a widened band gap, but also more flattened valence bands in the band structure than those in the binary SnTe alloy [57].

In this work, we aim to extend the study of semiconducting properties of HEAs. We choose HEAs consisting of group IV elements (Si, Ge, and Sn) because of the important

roles played by this group of alloys in the optoelectronic devices. According to the definition, it is more accurate to classify the SiGeSn alloy as a medium-entropy alloy (MEA). Nevertheless, MEAs share many common properties with HEAs, so we call the SiGeSn HEA throughout the current work. Separate from the context of HEAs, this group of (binary or ternary) alloys have continuously attracted massive attention over the past several decades. For example, $Ge_{1-x}Sn_x$ alloys display tunable band gaps if the concentration of Ge or Sn is controlled. It is reported that an Sn content up to 8% not only lowers the band gap, but also changes the indirect-band-gap Ge to a direct-band-gap semiconducting alloy [58]. A similar effect is observed in Si-Sn alloys [59]. Inspired by these binary alloys, research on the $Si_xGe_{1-x-y}Sn_y$ ternary alloys also reveals the Sn-content-dependent band gaps as well as the transition between direct and indirect band gaps [60].

Experimentally, it has been challenging to obtain Si-Ge-Sn alloys especially with high Sn content. The difficulty of alloying Si-Ge alloys with Sn can be understood from the three binary (Si-Ge, Si-Sn, and Ge-Sn) phase diagrams. First, the Si-Ge phase diagram shows that any composition of Ge is completely soluble in Si, forming Si-Ge solid solution alloys [61]. Due to this solubility, a number of Si-Ge alloys have been experimentally developed, resulting in a wide range of applications such as in near-infrared devices [62]. By contrast, as shown in the Si-Sn and Ge-Sn phase diagrams [63,64], the solution limit at room temperature is below 1%. The striking differences in the solubility of Ge and Sn in Si can be understood from the Hume-Rothery rules [65], which are commonly used to

predict whether a binary alloy prefers to exhibit a solid solution phase or an intermetallic compound. Because of the limited number of the experimental data, how Hume-Rothery rules can be applied to ternary alloys remains unclear. Nevertheless, we can apply the Hume-Rothery rules to gain an intuitive understanding of Si-Ge-Sn ternary alloys. According to Hume-Rothery, four conditions need to be satisfied to form binary alloys with a solid solution phase: (i) mismatch in atomic radii should not exceed 15%, i.e., size effect; (ii) there must be a similarity between the crystal structures of solute and solvent; (iii) if the solute and solvent have the same valency, complete solubility occurs, i.e., valency effect; (iv) the electronegativity of solute and solvent should be similar. Si and Ge satisfy all four of these conditions: possessing the same cubic diamond structure, similar atomic radii (1.153 Å for Si and 1.24 Å for Ge [66]), same valency (+4), and similar electronegativity (1.90 for Si and 2.01 for Ge at the Pauling scale [66]). Thus, complete solubility exists in Si-Ge binary alloys. For Si-Sn, condition (i) is not satisfied, due to the atomic radius of Sn (1.62 Å [66]) being too large. Condition (ii) is satisfied only at low temperatures, where Sn crystalizes as the same crystal structure called the α-Sn phase, while at higher temperatures a phase transitions occurs and the structure is transformed to a tetragonal structure, i.e., the α-Sn phase. Conditions (iii) and (iv) are both met; the electronegativity of Sn is 1.96 at the Pauling scale [66]. The net effect of these four conditions for Si-Sn is that Si and Sn do not form a solid solution phase. The same net effect applies to the Ge-Sn binary system.

Intensive experimental developments have shown how a higher content of Sn can now

be included in Si-Ge-Sn alloys [67]. Several innovative methods have been developed to fabricate high-Sn content Si-Ge-Sn alloys, including molecular beam epitaxial (MBE) [68] and chemical vapor deposition method (CVD) [69]. However, the limit of Sn content in these Si-Ge-Sn alloys is unknown. And if such a limit exists, what is the electronic structure of the Si-Ge-Sn alloy? In addition, there is no answer to whether the phase transition to the (metallic) α-Sn phase occurs in high-Sn content Si-Ge-Sn alloys.

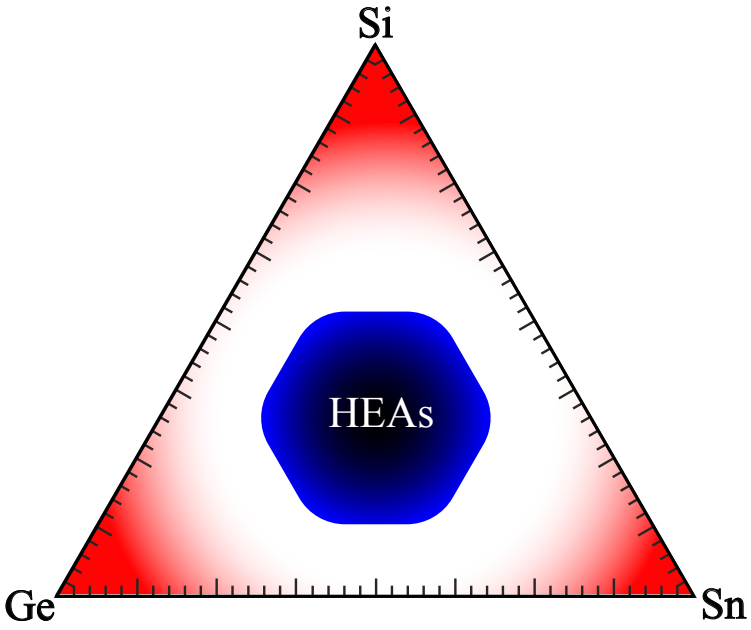

Figure 2.2. Schematic of a Si-Ge-Sn ternary phase diagram. Red shaded areas correspond to the composition spaces of conventional Si-Ge-Sn alloys; blue shaded areas correspond to the Si-Ge-Sn high-entropy alloys (HEAs).

The previous studies on Si-Ge-Sn alloys are constrained to a small area of the composition space. In other words, only three corner regions of the Si-Ge-Sn composition space have been exploited (see Figure 2.2). In these corner regions, Si-Ge-Sn alloys are

referred to as conventional alloys with a dominant element such as Ge, which has a content higher than 70%, and the other two elements in the conventional alloy regarded as doping elements to tune the alloys' properties. Indeed, a significant amount of research has been performed that focuses on the mechanical [70,71], optical [72], and electrical properties [71,73,74] of the alloys at the corners of the Si-Ge-Sn ternary phase diagram, with the Si content between 10% to 20% and the Sn content no more than 10%. On the contrary, little research has been carried out for the Si-Ge-Sn alloys in the middle region of the ternary phase diagram. According to the definition of HEAs mentioned above, the Si-Ge-Sn alloys in the middle region of the composition space should be HEAs. Interestingly, this terminology has never been used for Si-Ge-Sn alloys in the literature.

Similar to studying metal alloys in the center region of the composition space, there are enormous opportunities and challenges to study Si-Ge-Sn alloys in this region from both experiment and theory points of view. On the experimental side, it is worthwhile to fabricate the Si-Ge-Sn HEAs, measure their electronic structures, and to see if they are different from the conventional Si-Ge-Sn alloys. However, the setup of the CVD method may need to be redesigned to accompany the near-equimolar or equimolar content of the three elements. Theoretically, it is a great example of using ab initio density functional theory (DFT) [75,76] calculations to predict properties before an Si-Ge-Sn HEA is successfully fabricated. From the structural perspective, Si-Ge-Sn HEAs are intrinsically associated with the four core effect, which affect the electronic structures, potentially

leading to development of structures offering electromagnetic spectrum dominance. Meanwhile, because of the solid solution phase assumed in the HEAs, we need to employ reasonable supercell models to simulate them.

In this work, we first compute the electronic structure of the SiGeSn HEA to determine whether it is metallic or semiconducting. We then examine if the HEA exhibits a chemical short-range order (CSRO) which is a tendency for atomic clustering (e.g., one Si atom prefers Si/Ge neighbors over Sn atoms). CSRO has been reported in numerous HEAs and dominates several of their properties [77,78]. Furthermore, because point defects are unavoidable in any material due to thermal vibrations, we study the most basic point defect in the SiGeSn HEA, i.e., single vacancies. Studying single vacancies allows an understanding at an atomic level which can provide guidance to future studies of doping the SiGeSn HEAs.

2.3 Simulation Methods

We use the Vienna ab-initio simulation package (VASP; version 5.4.4) for all the DFT calculations and the Perdew-Burke-Ernzerhof (PBE) functional to describe the exchange-correlation interactions [79]. We also use the standard Si, Ge, and Sn potential datasets based on the PBE functional and the projector-augmented wave (PAW) method [80,81] to describe the electron-nuclei interactions. Among the potentials, the $3s^2$ and $3p^2$ electrons of Si atoms, the $4s^2$ and $4p^2$ electrons of Ge atoms, and the $5s^2$ and $5p^2$ electrons of Sn atoms are regarded as valence states. We optimize the supercells using a 2 × 2 × 2

Monkhorst-Pack [82] *k*-point grid and a cut-off energy of 400 eV for the plane wave basis sets. The force convergence criterion is set to 0.01 eV/Å.

We use a special quasi random structure (SQS) as a starting point to simulate the crystal structure of the SiGeSn HEA. The SQS method was developed nearly three decades ago and has been used in many applications for modeling conventional semiconducting alloys (e.g., $Al_{1-x}Ga_xAs$) with small supercells that can be dealt with using standard DFT programs [83]. The goal of this method is to minimize the difference between the correlation functions in a small supercell and those in an alloy with a truly random structure. Recently, the SQS method has been widely used to simulate the structures of metallic HEAs with a solid solution phase [44]. In addition, an SQS structure also serves as an initial structure followed by a combination of MC and DFT simulations to examine the occurrence of CSRO, which has been reported to occur in typical metallic HEAs such as Cr-Co-Ni [77,78] and affect mechanical properties such as stacking fault and point-defect energies. We focus on the SiGeSn HEA with the highest Sn content (i.e., where the ratio of the three elements is 1:1:1).

Based on an MC procedure, we use the mcsqs module [84] implemented in the Alloy Theoretical Automated Toolkit (ATAT) package [85] to generate an SQS structure for the SiGeSn HEA with 216 atoms (corresponding to a 3 × 3 × 3 supercell of the 8-atom unit cell of Si, Ge, or α-Sn). The cutoff distance for computing the correlation functions is set to within the second nearest-neighbor (NN) bond length, as a larger cutoff distance leads

to an unconverged calculation. The SQS structure is then fully relaxed and the shape of the supercell is slightly off perfectly cubic. Figure 2.3 shows a zoomed-in view of the optimized SQS structure. As clearly shown, the four NN atoms of each atom often belong to different elements, confirming the randomness of the atomic positions in the SQS structure. These results represent the SiGeSn HEA with a random solid solution phase.

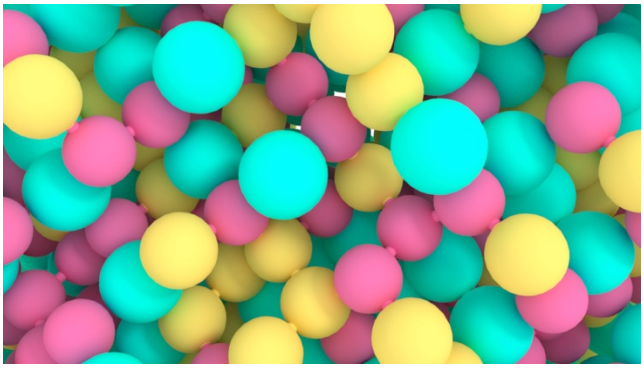

Figure 2.3. Zoomed-in view of the SQS structure of a SiGeSn high-entropy alloy. Si, Ge, and Sn atoms are represented by pink, yellow, and cyan spheres, respectively.

2.4 Results and Discussion

2.4.1 Structural and Electronic Properties of SQS SiGeSn

We first benchmark the above settings by calculating the optimized lattice constants of diamond cubic Si, Ge, and α-Sn as 5.47, 5.78, and 6.65 Å, respectively, which are slightly higher than the corresponding experimental lattice constants of 5.43, 5.66, 6.49 Å respectively [86]. The difference is expected from using the PBE functional that generally overestimates the lattice constants [87]. We also calculate the cohesive energies of isolated

Si, Ge, and Sn atoms place in a vacuum box with unequal side lengths of 22.0, 23.0, and 24.0 Å (to break the symmetry, spin-polarized calculations are invoked). For all the isolated atoms, we obtain a spin magnetic moment of $2\mu_B$, which match the experimental atomic spectra label $_3P_0$. The cohesive energy, i.e., the energy required to break the Si-Si, Ge-Ge, and Sn-Sn bond into isolated atoms is calculated as 4.60, 3.73, and 3.18 eV, respectively, which agrees with the literature values of 4.63, 3.85, and 3.14 eV, respectively [69]. The cohesive energies show that the bond strengths follow the order: Si-Si > Ge-Ge > Sn-Sn bond. Furthermore, we calculate the PBE band gap of diamond cubic structure Si as 0.61 eV (consistent with previously reported 0.75 eV [88]), whereas Ge and α-Sn are predicted to be metal and a semimetal with no gap at the PBE level of theory, consistent again with previous DFT calculations [88,89]. These benchmark calculations validate our DFT simulation parameters to be used throughout the current work.

To further show that the SQS structure is a reasonable model to simulate the SiGeSn HEA, we begin with the fully optimized SQS structure and perform a combination of DFT and MC calculations. For the DFT calculations, we calculate static energies -- similar to those reported in Refs. [77,78] -- to examine whether swapping two atoms of different elements lowers the energy of the SQS structure. This enables us to simultaneously examine whether the SCO occurs in Si-Ge-Sn HEA. We consider three cases of exchanging the atoms: (i) Case 1, by swapping Si with Ge and Sn atoms with an equal probability, (ii) Case 2, by swapping Si with Ge atoms, and (iii) Case 3, by swapping Si with Sn atoms. In

the MC simulations, if the exchange of two atoms leads to a lower energy, the atomic exchange is accepted. If not, it is accepted with the probability calculated by comparing the Boltzmann factor ($e^{-\Delta E/k_B T}$; ΔE: energy change; k_B: Boltzmann constant) at the temperature (T) of 300 K with a random number between 0 and 1.

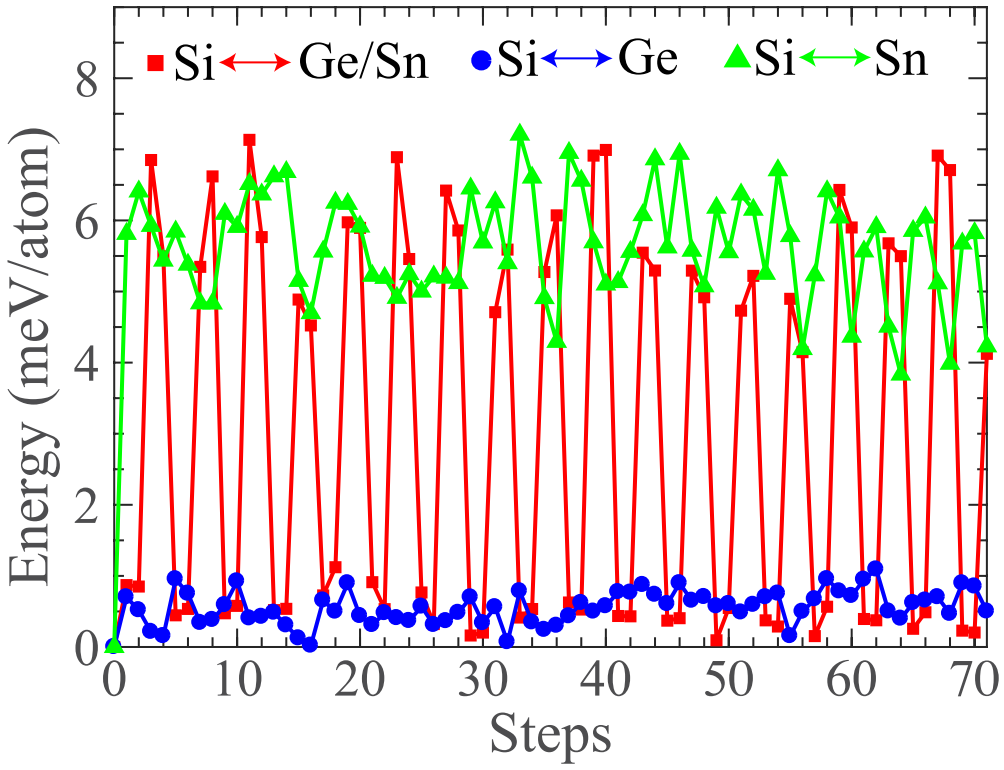

Figure 2.4. Energy change of a special quasi-random structure of the SiGeSn high-entropy alloy as a function of Monte Carlo simulation steps.

Figure 2.4 displays three curves (labeled by Si↔Ge/Sn, Si↔Ge, and Si↔Sn, respectively) showing the energy changes with reference the SQS structure (set to zero) as the MC calculations progress. We observe that all the energy changes are positive, indicating that the initial SQS structure is the most stable structure. Furthermore, the energy

changes by swapping Si and Ge atoms (Case 2) are seen to be much smaller than those by swapping Si and Sn atoms Case 3). The energy changes in Case 2 are close to zero, showing that it is almost energy-free to exchange Si and Ge atoms. This phenomenon is consistent with the complete solubility of Si and Ge resulting from their same valency and relatively small atomic size mismatch. The Si↔Ge/Sn curve (Case 1) shows that every two data points of low energy changes (similar to those in the Si↔Ge curve) are followed by two data points of high energy changes (similar to those in the Si↔Sn curve). This trend of alternating high and low energy changes is due to the fact that in the MC simulation for Case 1, each Si atom is first exchanged with two random Ge atoms, and then exchanged again with two random Sn atoms. As mentioned before, the former exchange results in little difference in the total energy changes, while the latter significantly increases the total energies by approximately 6 meV/atom.

The combined DFT and MC calculations reveal that no CSRO is observed in the SiGeSn HEA, in contrast to the metallic CrCoNi HEA exhibiting CSRO [77,78]. We suggest that the absence of CSRO in the SiGeSn HEA is because of the similarity in the electronegativity of the three elements. As a result, there is no stable (with negative formation energies) binary or ternary intermetallic compound formed from bulk Si, Ge, or α-Sn. By contrast, according to the Materials Project [90], stable binary intermetallic compounds in the CrCoNi HEA such as $CrCo_3$, $CrNi_2$, and Co_3Ni exist with the formation energies of -0.006, -0.021, and -0.022 eV/atom, respectively, which may enhance the

tendency of CSRO in the metallic CrCoNi HEA. It is now well accepted that CSRO significantly reduces the configurational entropy [91,92]. In this regard, the semiconducting SiGeSn HEA should have a higher configurational entropy than the metallic CrCoNi HEA.

Having confirmed the SQS structure as a reasonable one for simulating the SiGeSn HEA, we study the electronic structure of the HEA. Figure 2.5 shows the density of states of the SiGeSn HEA calculated with the PBE and HSE06 [93] hybrid density functionals. As can be seen, the calculations based on the PBE functional predict the SiGeSn HEA to be metallic, whereas the calculations using the more accurate HSE06 functional show that the SiGeSn HEA is actually a semiconductor with a small band gap of 0.38 eV. Many optoelectronic applications such as nigh vision [94], thermal imaging [95], and biomedical sensing [96] requires band gaps in the mid-infrared region (2.5-10 μm [97] i.e., 0.12-0.50 eV). Therefore, the SiGeSn HEA may be useful for these applications and has the advantage of over the commonly used mid-infrared (group III-V and II-VI) materials in costs [97] and in compatibility with the complementary metal-oxide-semiconductor (CMOS) technology [67].

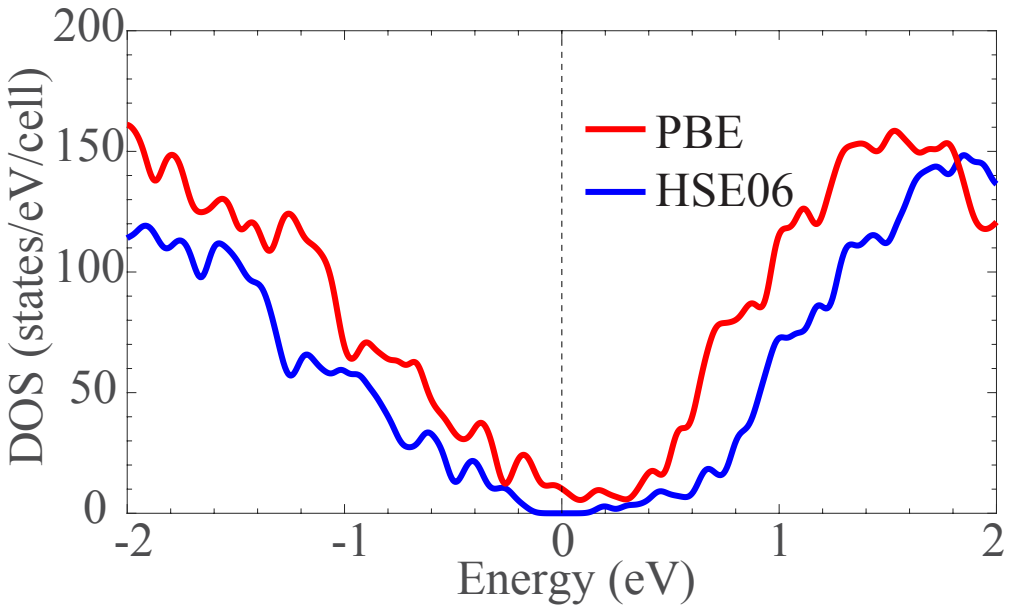

Figure 2.5. Density of states (DOS) of the SiGeSn high-entropy alloy calculated with the PBE and HSE06 functionals.

The lattice distortion effect is ubiquitous in HEAs, so it has become one of the four core effects of HEAs. We here quantify this effect for the SiGeSn HEA. We follow the same method used by Tong et al. for the FeCoNiCr and FeCoNiCrPd HEAs to provide a statistical description of the local distortion effect in SiGeSn [98]. We calculate the distribution of the deviation Δd of the NN bond lengths with reference to the average NN bond length d_{avg} for the optimized SQS structure. Figure 2.6 displays the distribution $\Delta d/d_{avg}$ and its Gaussian fit. The standard deviation of the SiGeSn alloy is determined to be 4.46%, which is larger than those (1.04% and 3.37%, respectively) of the FeCoNiCr and FeCoNiCrPd HEAs. We also apply the hard sphere-model proposed by Zhang et al. to determine the size mismatch δ calculated using the following equation [99],

$$\delta = 100 \times \sqrt{\sum_{i=1}^{N} c_i (1 - r_i / \sum_{j=1}^{N} c_j r_j)} \qquad (2.2)$$

where N is the total number of elements, $c_{i/j}$ are the concentrations of the element in an HEA—$c_{i/j}$ is equal to 1/3 for the SiGeSn HEA, and $r_{i/j}$ represent the atomic radii of Si, Ge, and Sn atoms. δ in Eq. (2.2) is structure independent, i.e. regardless of the atomic arrangement in an alloy being ordered or not. The resulting δ based on Eq. (2.2) is 15.16%, consistent with the large standard deviation of the $\Delta d/d_{\text{avg}}$ data; both metrics ($\Delta d/d_{\text{avg}}$ and δ) reflect the severe local lattice distortion effect.

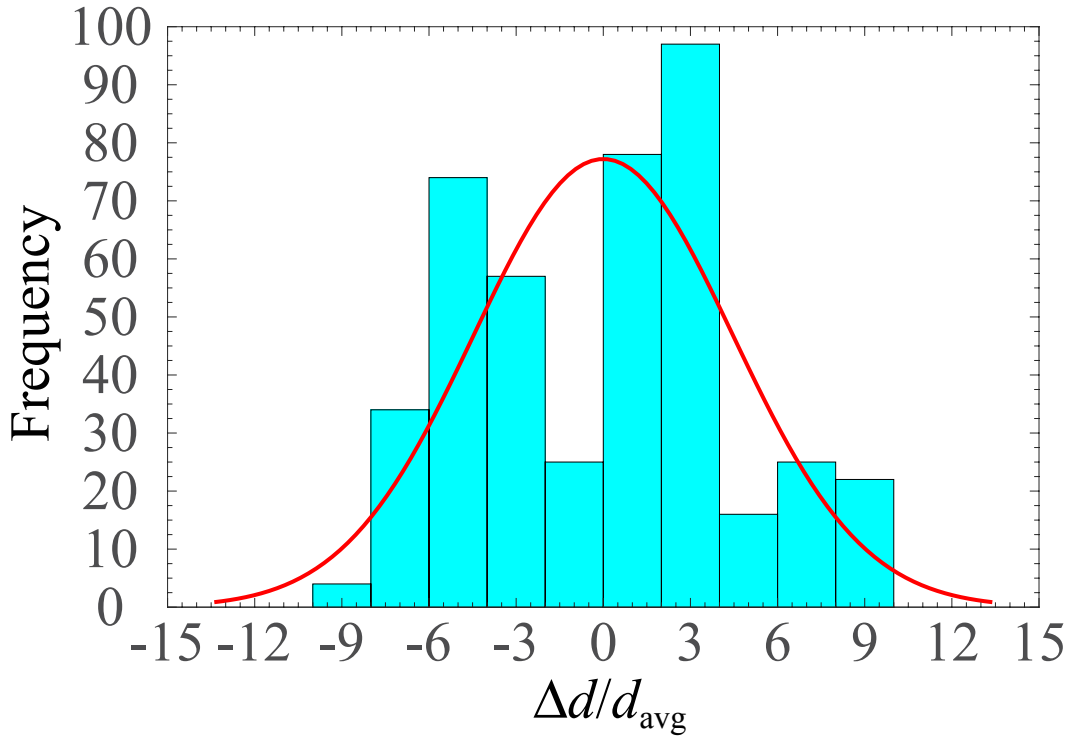

Figure 2.6. Frequencies in the deviation Δd of nearest-neighbor (NN) bond lengths from the average NN bond length in the optimized structure of a SiGeSn HEA.

2.4.2 Vacancy stability of SQS SiGeSn

With the optimized SQS structure, we study the vacancy formation energy of a single vacancy and its dependence on the elements and locations of the vacancy. Unlike in metals, vacancies in semiconductors (e.g., the SiGeSn HEA according to our HSE06 calculations) can exhibit various charge states [100]. Additional terms including the valence band maximum and band gap of a supercell without a defect, and potential alignment between the charged defect and systems should be included as a correction for the energy difference between a supercell with charged defect and a supercell without the defect [101]. While the valence band maximum and band gap can be obtained from HSE06 calculations, the band alignment term depends on the dielectric constant of the SiGeSn HEA structure. Using the PBE functional to calculate this parameter is problematic, as the SiGeSn HEA is metallic, exhibiting an infinite dielectric constant. On the other hand, although the HSE06 functional leads to the conclusion that the SiGeSn HEA is semiconducting (and therefore a finite value of dielectric constant), obtaining a converged dielectric constant requires a very dense grid of k points and advanced theories like density functional perturbation theory [102]. Due to these technical issues associated with time-intensive calculations, we therefore consider only the vacancies without charges in this work. We defer the study of charged vacancy defects, which an important issue, to the future work.

Focusing on the neutral vacancy, the single vacancy formation energy ΔE, describing the energy change caused by removing one atom from the bulk and placing it in a reservoir,

is defined as [103],

$$\Delta E = E_{vac} + \mu - E_{bulk} \tag{2.2}$$

where E_{vac} is the energy of the supercell with a single vacancy, μ is the chemical potential of an atom in the reservoir, and E_{bulk} is the energy of the supercell without a vacancy. Because there are no known intermetallic compounds formed among Si, Ge, and α-Sn, we assume the reservoir to be bulk Si, Ge, and α-Sn for the corresponding vacancies. By the definition shown in Eq. (2.2), we can compare the vacancy formation energies in the SiGeSn HEA and in bulk Si, Ge, or α-Sn on the same footing. Since the chemical potential is the same as the atomic energy in pure bulk, ΔE for bulk Si, Ge, or α-Sn in Eq. 2.2 is reduced to

$$\Delta E = E_{vac} - \frac{n}{n-1} E_{bulk} \tag{2.3}$$

Here, $n = 216$ is the number of atoms in a supercell that is sufficiently large to compute the formation energy of an isolated, neutral vacancy. For all the supercells with a single vacancy, we completely optimize the lattice constants and atomic coordinates with the PBE functional. Table 2.1 shows the calculated single vacancy formation energies of bulk Si, Ge, and α-Sn, which are consistent with the literature. The order of the three vacancy formation energies also agrees well with the order of the cohesive energies, i.e., higher cohesive energy indicates higher vacancy formation energy.

Because the bonding environment of each atom in the SiGeSn HEA is different, the corresponding vacancy formation energy is likely to be distinct. To simulate the three types

(Si, Ge, and Sn) of vacancies in the SiGeSn HEA, we create a single vacancy by consecutively removing one of the 216 atoms and fully optimize the resulting defected 215-atom supercell structure, followed by computing the corresponding ΔE. Figure 2.7 shows the three ranges of ΔE in the SiGeSn HEA and the ranges are summarized in Table 2.1. We can see from Figure 2.7 that the distribution of formation energies for each type of vacancy is nearly continuous. Such wide ranges of vacancy formation energies are expected to some extent and have also been observed in other HEAs. For example, Chen et al. find that the range of the vacancy formation energies of Fe in FeCoCrNi HEAs is from 0.72 to 2.89 eV [104].

Table 2.1. Vacancy formation energies (in eV) of Si, Ge, and Sn in their own bulk crystals and the SiGeSn HEA calculated in this work. For comparison, the experimental and theoretical data of the vacancy formation energies of Si, Ge, and α-Sn in the literature are also shown. For the vacancy formation energies of Si, Ge, or Sn in the SiGeSn HEA, we report a range instead of a single value due to the fact that the energy cost of removing an atom from the HEA depends on the location of the atom.

V_{Si}^{Si}	V_{Ge}^{Ge}	V_{Sn}^{Sn}	V_{Si}^{HEA}	V_{Ge}^{HEA}	V_{Sn}^{HEA}
3.83	2.08	1.33	0.04-2.58	0.20-2.37	0.39-2.55
4.0[a]	2.04-2.62[b], 2.35[c]				

[a]Ref. [105]. Experimental work
[b]Ref. [106]. Theoretical work using different supercells
[c]Ref. [107]. Theoretical work

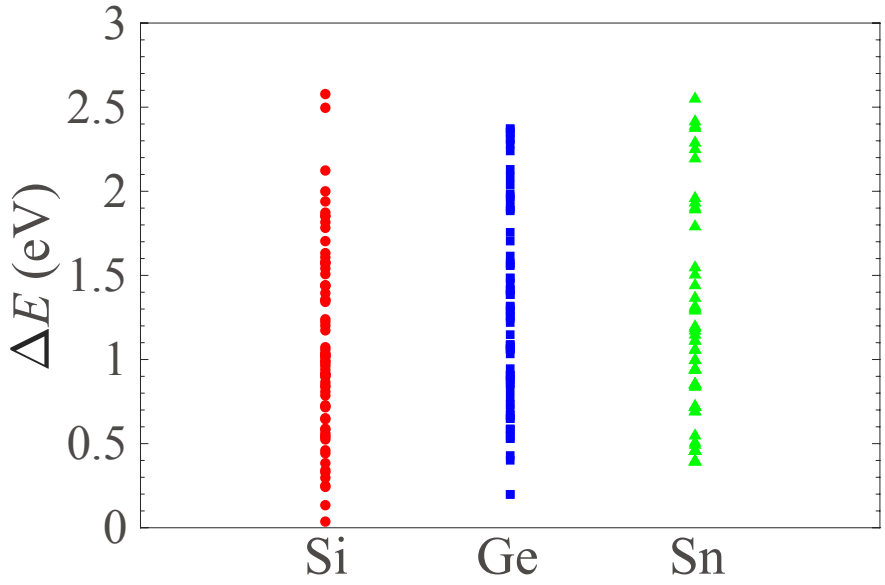

Figure 2.7. Formation energies ΔE of single Si, Ge, or Sn vacancies in the SiGeSn high-entropy alloy.

Figure 2.8(a) displays the dependence of vacancy formation energies on the number of nearest-neighbor Si and Ge atoms of a vacancy; the number of nearest Sn atoms equals four minus the former number, so it is not used as abscissa or ordinate in the plot. As can be seen from Figure 2.8(a), despite a vacancy has the same number of nearest-neighbor Si and Ge atoms (i.e., same abscissa and ordinate) the resulting formation energies can be quite different. For instance, 17 different energies are found if both abscissa and ordinate equal two. This large degeneracy in the number of nearest-neighbor Si atoms and Ge atoms implies that removing an atom to create a vacancy impacts more atoms than the nearest neighbors. Furthermore, bond reformation (see below) is not considered in this simple model. Figure 2.8(b)-(d) show the same dependence for Si, Ge, and Sn vacancies, respectively. For the Si case (Figure 2.8(b)), we observe that the highest vacancy formation

energy occurs when the removed atom is surrounded by four Si atoms, which is consistent with what we shall see below that breaking a Si-Si bond requires the most energy in comparison with breaking a Si-Ge or a Si-Sn bond. We also observe that many low vacancy formation energies fall in the regions where the number of nearest-neighbor Si atoms is below two. For example, the lowest-vacancy-formation-energy structure corresponds to the one with a vacancy that has one nearest-neighbor Si atom, two Ge nearest-neighbor atoms, and one Sn nearest-neighbor atom, respectively. For the Ge case (Figure 2.8(c)), higher vacancy formation energies also tend to occur when the number of nearest-neighbor Si atoms is above or equal to two, while the lowest formation energy appears anomalously where there are three nearest-neighbor Si atoms in spite of the Si-Ge bond strength being the second strongest among the bonds formed from Si, Ge, and Sn atoms. The location of the highest vacancy formation energy for the Sn case (Figure 2.8(d)) is similar to that in the Ge case. In addition, the vacancies that have lower formation energies prefer to have fewer Si atoms as nearest neighbors, a common feature in all the three cases.

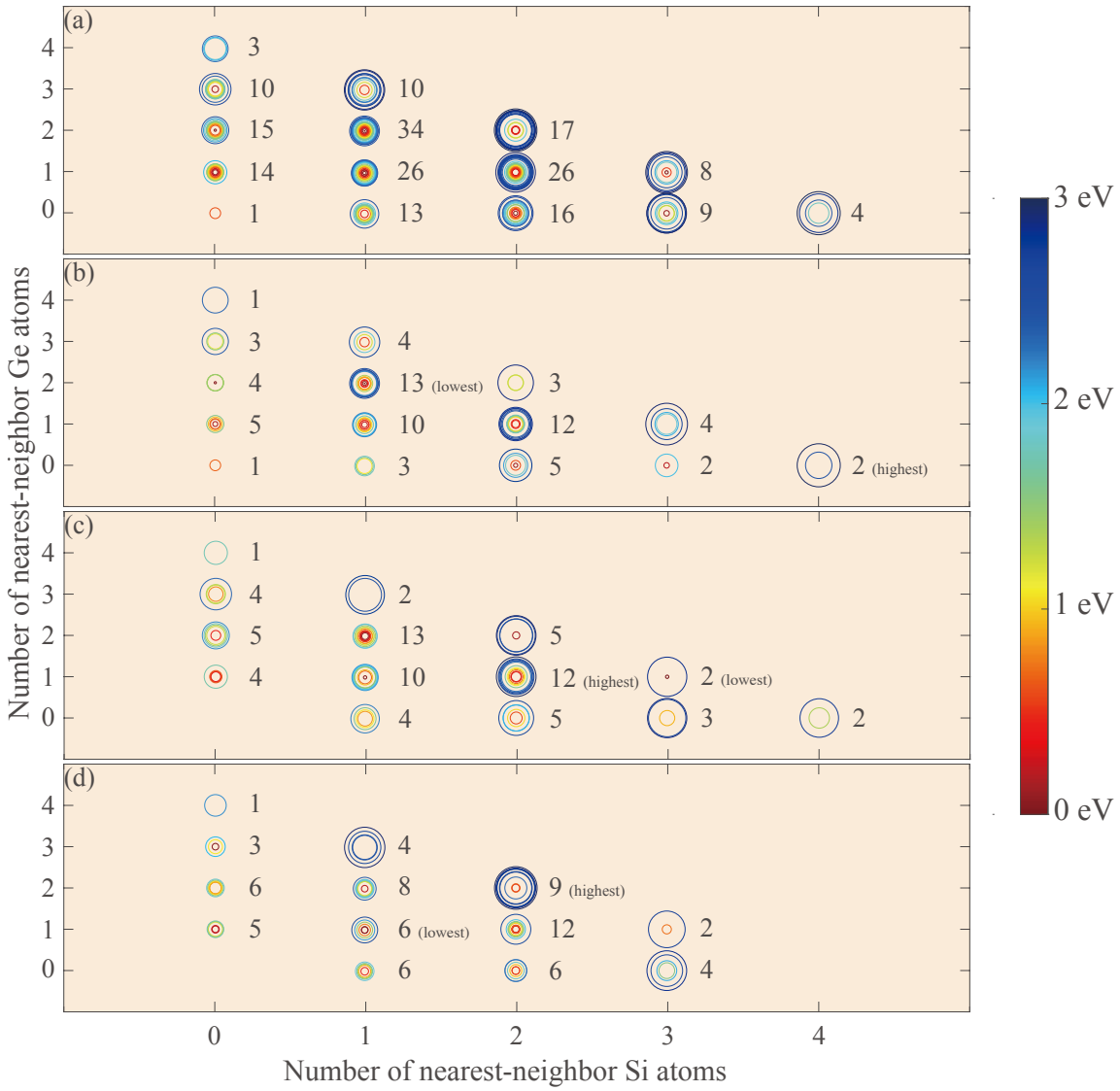

Figure 2.8. Relation between vacancy formation energies and the number of nearest-neighbor Si and Ge atoms near each single vacancy in the SiGeSn high-entropy alloy. (a) is for the entire data set and its division into the (b) Si (c) Ge, and (d) Sn subsets. The radius and color intensity of each circle represent the magnitude of the corresponding vacancy formation energy. The numbers near the circles denote the number of circles that share the same abscissa or ordinate. The texts "highest" and "lowest" label the highest and lowest vacancy formation energies, respectively.

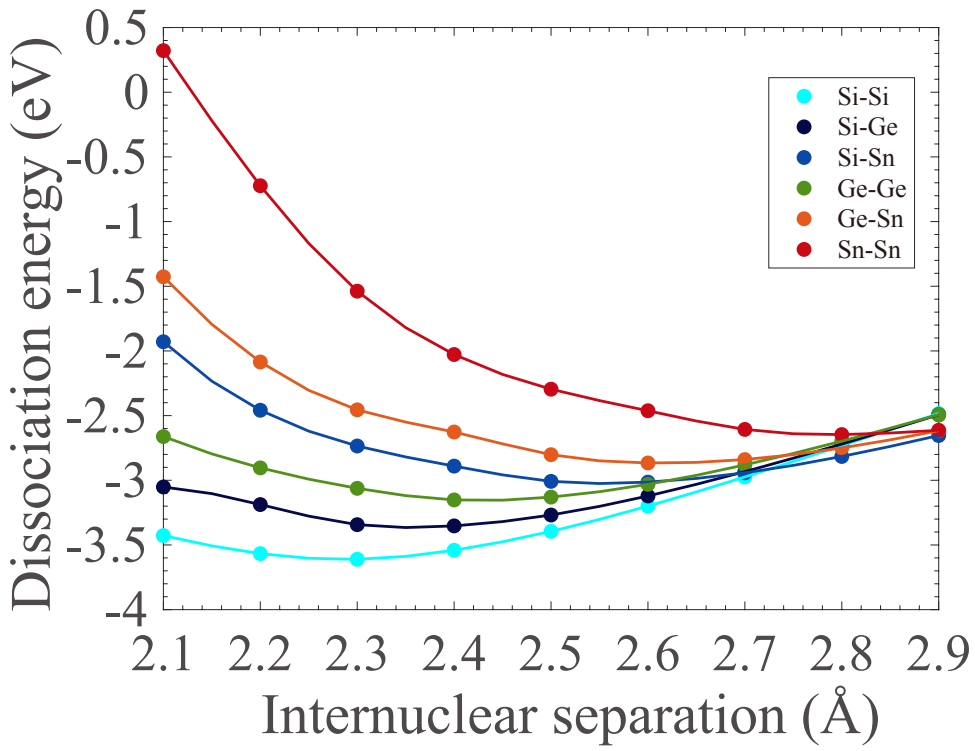

Figure 2.9. Dissociation energies of Si-Si, Si-Ge, Si-Sn, Ge-Ge, Ge-Sn, and Sn-Sn diatomics as a function of internuclear separation.

We also expect that the lower bounds of the three ranges of vacancy formation energies to be higher than the vacancy formation energy in bulk α-Sn, i.e., 1.33 eV. This assumption is made again based on the fact that creating a vacancy is equivalent of breaking chemical bonds. The broken bonds in the SiGeSn HEAs are diversified, such as Si-Ge, Si-Sn, etc. The energies to break these mixed bonds are supposed to lie between the Si-Si and Sn-Sn bonds. To support our assumption, Figure 2.9 depicts the variation of dissociation energy with interatomic distance for Si-Si, Si-Si, Si-Ge, Si-Sn, Ge-Ge, Ge-Sn, and Sn-Sn diatomics. The dissociation energy is calculated as the energy difference of the total energy

of a diatomic molecule (placed in the same vacuum box as used for computing the energies of isolated atoms) from the total energies of the isolated constituent atoms. The dissociation energies for Si-Si, Si-Ge, Si-Sn, Ge-Ge, Ge-Sn, and Sn-Sn are 3.61, 3.35, 3.01, 3.15, 2.87, and 2.65 eV, respectively, which are reasonably consistent with the experimental data of 3.31, 3.08, 2.42, 2.82, 2.38 and 1.99 eV [108-111], respectively; both theoretical and experimental data show that the Si-Si bond strength is the strongest while the Sn-Sn bond is the weakest. All the other bond strengths lie between these upper and lower bounds. The order of the dissociation energies is the same as that of the cohesive energies of bulk Si, Ge, and α-Sn.

Surprisingly, there are 2/3 (144 out of 216) of the vacancy formation energies in the whole data set that are smaller than the vacancy formation energy of bulk α-Sn (1.33 eV). To understand this, Figure 2.10 shows the local atomic structures (before and after geometry optimizations) near the vacancies with the highest and lowest vacancy formation energies for Si, Ge, and Sn. We observe a common phenomenon: for the structures with the highest formation energies, the number of dangling bonds (4) remains unchanged after geometry relaxations, similar to the situation where an atom is removed in bulk Si, Ge, and α-Sn. As a result, the energies of the structures as well as the vacancy formation energies are high. By contrast, in the structures with the lowest formation energies, the atoms with dangling bonds due to removing an atom form new bonds to minimize the number of dangling bonds, thereby reducing the system's energy. For example, Figure 2.10(a)

illustrates that a Ge atom relocates to the location of the Si vacancy reforming four-fold coordinated bonds with nearest-neighboring two Sn atoms, one Ge atom, and one Si atom. This bond reformation makes the corresponding vacancy formation energy negligibly small (0.04 eV). Similar bond reformations are also found near the Ge and Sn vacancies (see Figure 2.10(a) and (b)), leading to the corresponding lowest vacancy formation energies. We speculate that similar bond reformation also exists in a vacancy of metallic HEAs. For example, the formation energy of a single Fe vacancy in bulk Fe is 1.58 eV (this energy is also the lower bound of the vacancy formation energies of bulk Fe, Cr, Co and Ni that form the FeCrCoNi HEA), while the lowest formation energy of a single Fe vacancy in the FeCrCoNi HEA is 0.72 eV. The ratio of these two energies ($1.58/0.72 \simeq 2.19$) is much larger than the corresponding ratio ($1.33/0.04 \simeq 33.25$) in the SiGeSn HEA, manifesting the unique structure and energetics of the vacancies in semiconducting HEAs.

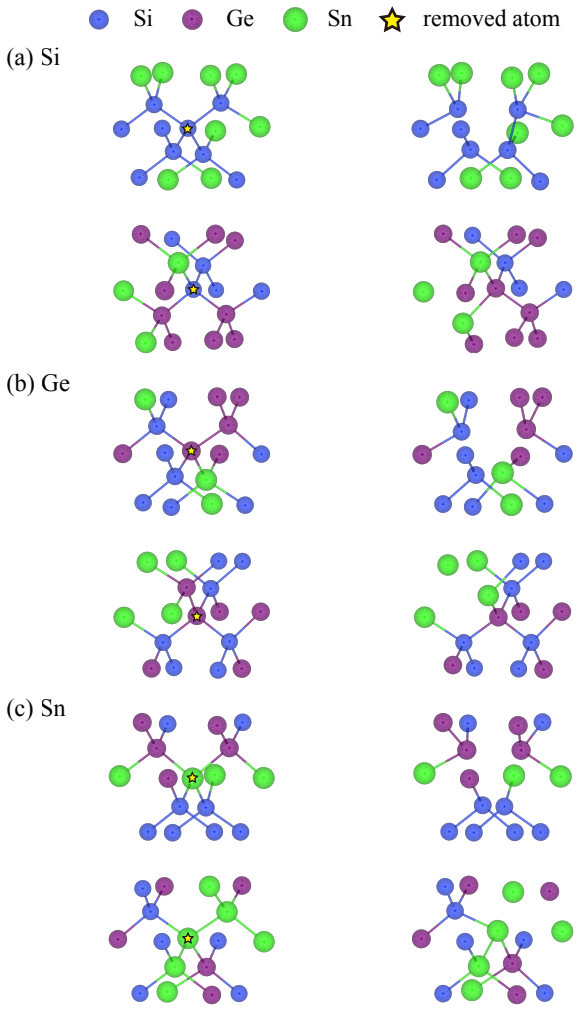

Figure 2.10. Local atomic structures near (a) Si, (b) Ge, and (c) Sn vacancies (denoted by yellow stars). The figures in the left and right columns of each panel show the atomic structures before and after geometry optimizations, respectively.

We now study the effects on the electronic structure of the SiGeSn HEA due to the presence of single vacancies. As shown above, it is necessary to use the HSE06 functional to obtain the more accurate electronic structures of the SiGeSn HEA. Because performing the calculations at the HSE06 level of theory for all the defected supercells—each has 215 atoms—is extremely time consuming, we compute the HSE06 electronic structures only

for the six supercells with the lowest and highest vacancy formation energies for the three types (Si, Ge, and Sn) of vacancies, using their corresponding optimized configurations based on the PBE functional.

Figure 2.11 displays the density of states calculated for the vacancies with the highest and lowest formation energies computed with the HSE06 functional. A vacancy in a semiconductor usually leads to defect states in the band gap. For example, defect states resulted from a neutral oxygen vacancy are seen in the band gap of semiconducting $SrTiO_3$ [112]. We find no such defect states in the band gap of the SiGeSn HEA. Instead, we observe that all the lowest-formation-energy structures with single vacancies are semiconducting with band gaps of 0.31, 0.35, and 0.32 eV for the Si, Ge, and Sn vacancies, respectively, and that all the highest-formation-energy configurations are metallic. These band gaps are nearly identical to that (0.38 eV) of the SiGeSn HEA without a vacancy, implying trivial impacts of the vacancies on the band gap. The absence of the defect states in the lowest-formation-energy structures is because of the bond reformation as shown in Figure 2.10, which provides the otherwise missing orbitals to overlap with the orbitals from the atoms surrounding a vacancy site. Figure 2.10 shows that the vacancy sites in the lowest-formation-energy structures are replaced by another atom either of the different element (i.e., Si by Ge) or the same element (i.e., Ge by Ge and Sn by Sn), thereby the band gap size is almost not affected by these atomic replacements. In the highest-formation-energy vacancy supercells, because unreconstructed dangling bonds exist, and

their energies are large enough to excite the electrons to the energies above the valence band maximum. The excited electrons then form continuous bands bridging the band gap and resulting in overall metallic systems. These vacancies therefore render the SiGeSn HEA unsuitable for optoelectronic applications. Fortunately, we expect a low probability of having these vacancies as their formation energies are very high. In other words, the SiGeSn HEA will be dominated by those low-energy vacancies that retain the semiconducting properties required for doping purposes.

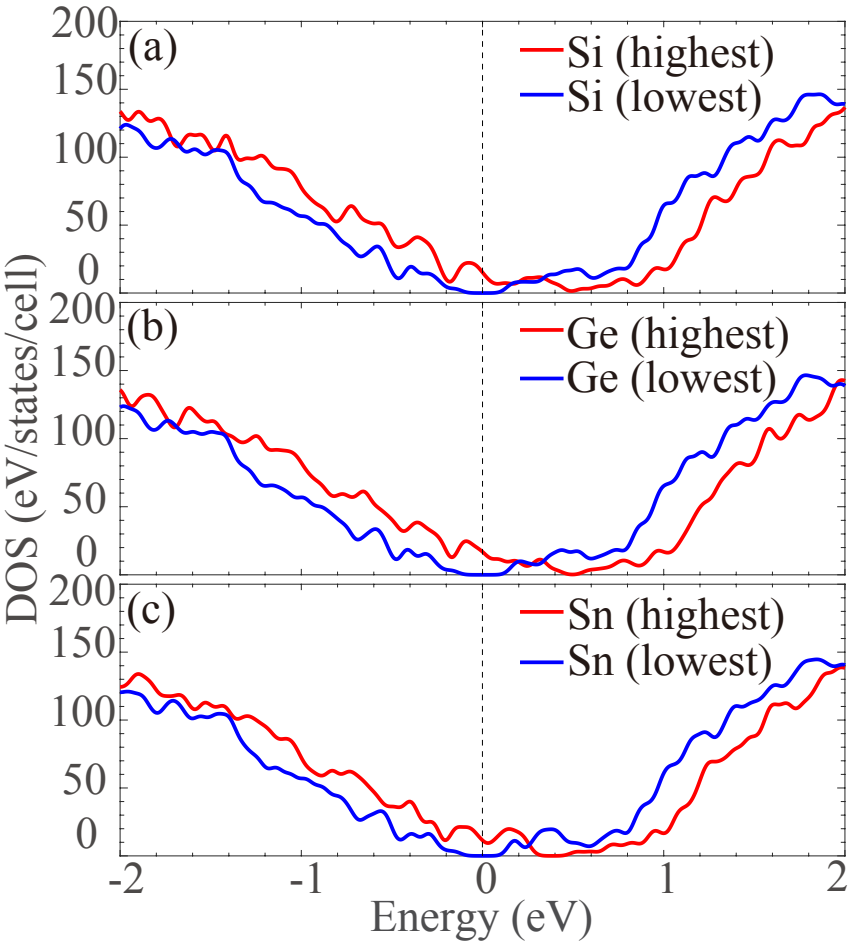

Figure 2.11. Density of states of (a) Si, (b) Ge, and (c) Sn of the SiGeSn high-

entropy alloy with single vacancies of the highest and lowest formation energies.

2.5 Summary

We have studied a Si-Ge-Sn alloy in the context of HEA using DFT calculations. We showed that the SiGeSn HEA is a semiconductor with the band gap in the mid-infrared region. Comparing to metallic HEAs, the SiGeSn HEA exhibits the same, large lattice distortion effect and wide ranges of vacancy formation energies. Nevertheless, we also found two features that distinguish the SiGeSn HEA from metallic HEAs. First, the SiGeSn HEA has no CSRO due to the similar electronegativity of Si, Ge, and Sn, which consequently increases the configurational entropy. Second, single vacancy formation energies of the SiGeSn HEA can be very low owing to the bond reformations near the vacancies. As a result, the band gap of the SiGeSn HEA is almost unaffected by the vacancies that have low formation energies. Overall, investigating Si-Ge-Sn alloys from the perspectives of HEAs will produce fundamental insight on the structure–property interplay of group IV alloys, and our integrated computational methods will assist the design of other groups of semiconducting HEAs exhibit critical electromagnetic properties and applications.

CHAPTER IV

ELECTRICAL AND THERMAL TRANSPORT PROPERTIES OF MEDIUM-ENTROPY $SI_yGE_ySN_x$ ALLOYS

3.1 Abstract

Electrical and thermal transport properties of disordered materials have long been of both theoretical interest and engineering importance. As a new class of materials with an intrinsic compositional disorder, high/medium-entropy alloys (HEAs/MEAs) are being immensely studied mainly for their excellent mechanical properties. By contrast, electrical and thermal transport properties of HEAs/MEAs are less well studied. Here we investigate these two properties of silicon (Si)-germanium (Ge)-tin (Sn) MEAs, where we keep the same content of Si and Ge while increasing the content of Sn from 0 to 1/3 to tune the configurational entropy and thus the degree of compositional disorder. We predict all $Si_yGe_ySn_x$ MEAs to be semiconductors with a wide range of bandgaps from near-infrared (0.28 eV) to visible (1.11 eV) in the light spectrum. We find that the bandgaps and effective carrier masses decrease with increasing Sn content. As a result, increasing the compositional disorder in $Si_yGe_ySn_x$ MEAs enhances their electrical conductivity. For the thermal transport properties of $Si_yGe_ySn_x$ MEAs, our molecular dynamics simulations show an opposite trend in the thermal conductivity of these MEAs at room temperature, which decreases with increasing compositional disorder, owing to enhanced Anderson localization and strong phonon-phonon anharmonic interactions. The enhanced electrical

conductivity and weakened thermal conductivity make $Si_yGe_ySn_x$ MEAs with high Sn content promising functional materials for thermoelectric applications. Our work demonstrates that HEAs/MEAs not only represent a new class of structural alloys but also a novel category of functional alloys with unique electrical and thermal transport properties.

3.2 Introduction

The Seebeck effect refers to the presence of electronic potential between two junctions in a material at different temperatures. The Peltier effect, on the other hand, illustrates the heat generation or loss at an electrified junction of two materials under voltage. These two facts provide the basis of the thermoelectric (TE) effect for the energy conversion between electrical and thermal resources. While the TE effect is universal in all materials, in most of them the effect is too trivial to be utilized [113]. A TE material needs to satisfy multiple criteria to achieve the energy conversion between heat and electricity. The maximum efficiency of the conversion is measured by the TE figure of merit depending on four parameters, i.e., $zT = \frac{S^2\sigma}{\kappa}T$, where S is the Seebeck coefficient, σ stands for the electrical conductivity, κ is the thermal conductivity, and T denotes the absolute temperature of the operating environment [13,14]. According to the definition of zT, an outstanding TE material at a specified temperature requires to possess a high Seebeck coefficient, a high electrical conductivity and a low thermal conductivity. Because of the interdependency of the four parameters, it is not always feasible to increase zT by tuning one of the parameters without affecting the others. For example, the Seebeck coefficient

decreases with increasing carrier density that increases the electrical conductivity [114,115].

Efforts have been made to search for suitable TE materials with high zT. Metals generally have high electrical conductivities, but they also display high thermal conductivities, which balance out the zT and cannot function as suitable TE materials. By contrast, semiconductors, whose zT are generally much higher than metals, have found their great potential in TE applications by virtue of tunable TE properties via alloying. For example, alloying cobalt triantimonide ($CoSb_3$), with iridium (Ir) of similar electronegativity to Co, $CoSb_{3-x}Ir_x$ tends to show covalent bonding and high carrier mobility, which keeps the electrical conductivity unaffected while reducing the thermal conductivity. As a result, an optimized zT of 0.8 is obtained at 600 K [115]. Lead chalcogenides alloys, $(PbTe)_{1-2x}(PbSe)_x(PbS)_x$, serve as another example of increasing the TE performance by coalloying the elements from the same group in the periodic table. The addition of PbTe and PbSe to PbS maintains the stable and homogeneous rock-salt structure and decreases the thermal conductivity of PbS by increasing the scattering strength of phonon resulted from the compositional disorder [116]. As a result of this alloying strategy, the TE performance of $(PbTe)_{1-2x}(PbSe)_x(PbS)_x$ is superior to that of individual binary PbX (X = S, Se, or Te) alloys.

Although many materials have been reported to show outstanding zT at high temperatures such as PbTe with zT of 0.8 at 580 K [117], its zT drop drastically to 0.001 at room temperature, making it unsuitable for room-temperature TE applications. At the

same time, TE materials that are able to operate near room temperature are important for energy-conversion applications in different fields. For instance, the industrial waste heat common from the recycling water is always discarded into environment via the form of exhaust gas or air flow. A major portion of the heat from the low-temperature recycling water/steam is commonly wasted because of lack of commercial conversion devices [118]. As another heat resource, hot springs, one clean, cost-effective, and sustainable geothermal resource, have a temperature of 347 K [119] can be employed. Both of these examples require TE materials that can be efficient in power conversion near room temperature. Only a handful of materials are found to still display considerable zT for TE applications at room temperature. For example, $CsBi_4Te_6$ consists of a Cs^+ layer that separates $[Bi_4Te_6]^-$ bilayers. Owing to this complex structure, the phonons in $CsBi_4Te_6$ exhibit long and convoluted phonon mean free paths that significantly reduce the thermal conductivity [120,121]. As a result, $CsBi_4Te_6$ can reach a high zT of 0.8 and a low thermal conductivity of 1.25 W/(m·K) at room temperature [121]. Among the limited number of TE candidates at room temperature, challenges in manufacturing persist, hindering their wide industrial applications in TE devices. Specifically, fabricating the room-temperature TE materials such as $CsBi_4Te_6$ requires an intensive control of the synthesis process. Therefore, it is important to identify room-temperature TE materials that are amenable to modern manufacturing technologies.

High/medium-entropy alloys (HEAs/MEAs; Following the convention [122,123], if

the number of elements is greater than or equal to five, HEAs is used; otherwise, MEAs is a more accurate terminology.) recently emerge as alternative candidates for TE applications. Different from conventional alloys that have one principal element and the other elements are added to tune the properties [73,124], HEAs/MEAs represent a novel category of alloys with multiple principal components, where all the constituent elements have equal or comparative concentrations [125]. HEAs/MEAs generally exhibit three different phases: solid solution, intermetallic compound, or the mix of these two phases [126,127]. In comparison with conventional alloys, the disorder atomic arrangement in HEAs/MEAs is associated with larger configurational entropy. Including the entropic contribution to the energy, HEAs/MEAs could form stable solid solutions at higher temperatures [128,129]. Many HEAs/MEAs exhibit excellent mechanical properties such as elevated-temperature strength [41,130] and high elastic modulus [131-133]. In addition to mechanical properties, HEAs/MEAs display outstanding functional properties in the applications from superconductors [134-136] to semiconductors with adjustable bandgaps [125]. HEAs/MEAs can be suitable TE materials mainly for two reasons. First, single-phase HEAs/MEAs can maintain a stable solid solution phase with high crystalline symmetry, across which electrons move freely. In line with the concept of 'phonon-glass electron-single-crystal' [137,138], single-phase HEAs/MEAs are expected to show difficulty in conducting phonons but easiness in transporting electrons. Second, the thermal conductivity of HEAs/MEAs can be suppressed by several phonon scattering mechanisms

that involve point defects, lattice distortions, and compositional disorder, which are commonly seen in HEAs/MEAs [139,140]. Indeed, HEAs/MEAs such as $Al_xCoCrFeNi$ [138], PbSnTeSe [141], and $BiSbTe_{1.5}Se_{1.5}$ [139] have been synthesized and employed as TE materials suitable for high (>1000 K), medium (500-900 K), and low working temperatures (300-500 K), respectively.

Manufacturing techniques of Group IV alloys consisting of silicon (Si), germanium (Ge), tin (Sn) are supported by the sophisticated semiconductor industry, it is therefore worthwhile exploring Si-Ge-Sn alloys for TE applications. Binary Si-Ge alloys have long been used as TE materials in waste heat generation and conversion for automotive applications [142-144]. In particular, binary Si-Ge alloys exhibit excellent TE performance at high temperature (> 1000 K) [145-147]. Experiments have also shown that adding Sn to Si-Ge alloys further lowers the thermal conductivity without significantly affecting the electrical conductivity [148]. Consistent with experiment, theoretical studies have found that the thermal conductivity of Si-Ge-Sn alloys can be reduced through controlling the Sn content and decreasing the bulk to thin films [149]. Comparing to Si or Ge atoms, a Sn atom is heavier and has a much larger radius. Heavier and larger Sn atoms in Si-Ge alloys increases the compositional disorder and causes a lattice distortion (see below), leading to strong anharmonic phonon-phonon scattering and thereby decreasing the thermal conductivity [150]. Si-Ge-Sn alloys exhibit a wide range of band gaps up to 1.4 eV that vary with composition and the bandgap types switch between direct and indirect [148,151-

153]. According to the empirical "$10k_BT$" (k_B : the Boltzmann constant) rule proposed by Mahan [154,155], a TE material operating at temperature T should have a band gap of around $10k_BT$ to maximize the zT. Composition-dependent bandgaps in Si-Ge-Sn alloys therefore enable them to achieve optimal TE performance at various operating temperatures [149,156].

In this work, instead of exploring the regions in the composition space representing conventional Si-Ge-Sn alloys that have been the subject of a number of theoretical and experimental studies [67,73,149,157], we focus on a special region of the composition space (see Figure 3.1(a)), where we keep the concentration of Si and Ge equal while varying the concentration of Sn from 0 to 1/3. The chemical formula of these special Si-Ge-Sn alloys can therefore be written as $Si_yGe_ySn_x$, where $2y + x = 1$ and $x \leq 1/3$. In choosing these concentrations, we are able to obtain the trends on how the electrical and thermal conductivities and the TE figure of merit are modified via systematically increasing the configuration entropy and therefore the extent of compositional disorder. Figure 3.1(b) shows that the configurational entropies of $Si_yGe_ySn_x$ MEAs calculated from the Boltzmann entropy formula increase from 0.71 k_B at $x = 0$ to 1.10 k_B at $x = 1/3$. We have recently studied the $Si_{1/3}Ge_{1/3}Sn_{1/3}$ MEA, which exhibits a single phase without a short-range chemical order, a near-infrared bandgap and a wide range of vacancy formation energies [125]. Although no experiments have yet been performed to fabricate this special series of $Si_yGe_ySn_x$ MEAs and it is also challenging to fabricate the Si-Ge-Sn alloys with

high Sn content because of large lattice mismatch [59,125,149,158,159], recent experimental techniques developed by Kouvetakis and coworkers to fabricate conventional Si-Ge-Sn alloys with high Sn content may be adjusted to synthesize these MEAs [159]. Before the experiment becomes available, we here predict the structural, electrical, and thermal transport properties of $Si_yGe_ySn_x$ MEAs and explore their TE applications.

3.3 Simulation Methods

To create simulation cells for the density functional theory (DFT) [75,76] calculations of $Si_yGe_ySn_x$ MEAs, we first generate a 3 × 3 × 3 supercell from an 8-atom unit cell of cubic Si with the diamond structure. The supercell thus consists of 216 Si atoms and we randomly permutate the locations of these atoms and substitute a portion of the atoms with Ge and Sn atoms, depending on the Sn content x. Given the fixed total number of atoms in the supercell, we obtain 11 structures of $Si_yGe_ySn_x$ MEAs with different concentrations of Sn, namely, x = 0, 1/108, 1/54, 1/36, 1/27, 1/18, 1/12, 1/9, 1/6, 1/4, and 1/3. Figure 3.1(a) illustrates the structure of a $Si_yGe_ySn_x$ MEA with the highest configurational entropy (i.e., x = 1/3).

We use the Vienna Ab initio Simulation Package (VASP; version 5.4.4) for all the DFT calculations and the Perdew-Burke-Ernzerhof (PBE) [79] functional to describe the exchange-correlation interactions in geometry optimizations and energy calculations. To remedy the problem of bandgap underestimation due to the PBE functional [160], we apply the modified Becke-Johnson (mBJ) exchange potential, which has been shown to

significantly improve the bandgaps of many semiconductors such as aluminum phosphide (AlP), silicon carbide (SiC), and gallium arsenide (GaAs) [89]. We compute the electronic structures of $Si_yGe_ySn_x$ using this potential based on the fully optimized structures with the PBE functional. The mixing parameter c in the potential is determined self-consistently. To describe the electron-nuclei interactions, we use the standard PBE version of Si, Ge, and Sn potential datasets generated via the projector augmented-wave (PAW) method [80,81] In these PAW potentials, the $3s^2$ and $3p^2$ electrons of Si atoms, the $4s^2$ and $4p^2$ electrons of Ge atoms, and the $5s^2$ and $5p^2$ electrons of Sn atoms are adopted as valence electrons. The plane wave cutoff energy is 400 eV. We fully optimize the 216-atom supercells using a 2 × 2 × 2 Monkhorst-Pack *k*-point grid [82] and the force convergence criterion during the geometry optimization calculations is set to 0.01 eV/Å.

To calculate the Seebeck coefficient and electrical conductivity of $Si_yGe_ySn_x$ MEAs, we use the BoltzTraP2 package [161], which solves the linearized electron Boltzmann transport equation according to rigid-band approximation (rather than the constant relaxation time approximation as implemented in the BoltzTraP package [162]) assuming that the band structure is not affected by temperature and doping. The doping and temperature effects are taken into account in the Fermi-Dirac distribution function $f(\varepsilon, \mu, T)$. The inputs for our BoltzTraP2 calculations are the band energies ε obtained from the mBJ exchange potential and the key outputs are the Seebeck coefficient and electrical conductivity tensors that depend on the electron chemical potential μ from the

following equations [161]:

$$S = \frac{1}{qT}\frac{\int \sigma(\mu,T)(\varepsilon-\mu)\left(-\frac{\partial f(\varepsilon,\mu,T)}{\partial \varepsilon}\right)d\varepsilon}{\int \sigma(\mu,T)\left(-\frac{\partial f(\varepsilon,\mu,T)}{\partial \varepsilon}\right)d\varepsilon} \tag{3.1}$$

and

$$\sigma = \int \sigma(\mu,T)\left(-\frac{\partial f(\varepsilon,\mu,T)}{\partial \varepsilon}\right)d\varepsilon \tag{3.2}$$

where q is the carrier charge and $\sigma(\mu,T)$ is called the transport distribution function according to the linearized electron Boltzmann transport equation. $\sigma(\mu,T)$ describes the carrier transport property that depends on the group velocity, concentration, and lifetime of the carriers. We are not considering the anisotropy in this work, so we report the average Seebeck coefficient and electrical conductivity in the three dimensions. To compute the electrical conductivity, we use a constant relaxation time of 10 femtoseconds, which has been widely used in computing the electrical conductivities of many intrinsic or lightly doped semiconductors [162-165].

To obtain the thermal conductivity of $Si_yGe_ySn_x$ MEAs, we perform classical equilibrium molecular dynamics (EMD) simulations using the Large-scale Atomic/Molecular Massively Parallel Simulator (LAMMPS) [166]. The many-body interatomic interactions are described using a modified Stillinger-Weber potential [167] that was fitted from DFT to reproduce properties such as the phase stability and elastic constants [168,169], and applied to study the thermal conductivity of Si-Ge-Sn alloys [150,170]. The simulation cells used in MD simulations are much larger than those used in

the DFT calculations, and the way we create simulation cells is similar. That is, the MD supercells are based on a 9 × 9 × 9 supercell of the Si unit cell and each supercell consists of 5832 atoms. Because of thermal fluctuations, we create three sets (using three different random seeds) of 5832-atom supercells for each $Si_yGe_ySn_x$ MEA and report the average thermal conductivity. The thermal conductivity of $Si_yGe_ySn_x$ MEAs at room temperature is calculated through EMD simulations based on the Green-Kubo method [171-173]. The time step for the MD simulations is 1.0 fs. In the MD simulations, we first equilibrate the system for 106 steps using the NVT canonical ensemble and the Nosé-Hoover thermostat [166,174] and then runs another 4×10^6 steps for collecting the heat flux data every 1.25×10^4 steps in the NVE micro-canonical ensemble. The thermal conductivity κ_α in the α direction is calculated with the following equation [149]:

$$\kappa_\alpha = \frac{V}{k_B T^2} \int_0^\infty \langle J_\alpha(0) J_\alpha(t) \rangle dt \tag{3.3}$$

where $J_\alpha(t)$ is the heat current at time t; V and T denote volume and temperature, respectively.

We also study the thermal conductivities of $Si_yGe_ySn_x$ MEAs at the DFT level using the Phonopy and Phono3py programs [175,176]. Phonopy and Phono3py programs, post-process the second-order and third-order force constants, respectively, to yield the phonon frequencies, the thermal conductivity and the phonon linewidth by solving the linearized phonon Boltzmann transport equation. To obtain the harmonic phonon frequencies and anharmonic phonon-phonon interactions, we calculate the second-order and the third-order

force constants using the finite-displacement method with a displacement of 0.03 Å. The second-order and third-order force constants are calculated using 4 × 4 × 4 and 2 × 2 × 2 supercells, respectively. The energies and forces of these geometries are evaluated via DFT calculations. It is nevertheless challenging to calculate the third-order force constant for a disordered alloy with a low symmetry, so we create the models of two artificial MEAs, $Si_{3/8}Ge_{3/8}Sn_{1/4}$ and $Si_{1/2}Ge_{3/8}Sn_{1/8}$, which, respectively, have three/four Si atoms, three/three Ge atoms, and two/one Sn atoms in their unit cells. The Sn content of the artificial $Si_{3/8}Ge_{3/8}Sn_{1/4}$ MEA is the same as one of the 11 selected $Si_yGe_ySn_x$ MEAs that has x of 1/4. The total number of supercells to obtain the second-order and third-order force constants via DFT calculations is 18 and 4746, respectively. Although $Si_{1/2}Ge_{3/8}Sn_{1/8}$ is not one of the 11 $Si_yGe_ySn_x$ MEAs, its composition can be reflected by the same small unit cell with the Sn content smaller than 1/3. Correspondingly, the total number of supercells to obtain the second-order and third-order force constants via DFT calculations is 5 and 833, respectively.

3.4 Results and Discussion

3.4.1 Structural Properties

We first investigate the structural properties of the 11 $Si_yGe_ySn_x$ MEAs. Because the shapes of all the supercells slightly deviate from cubic after geometry optimizations, we report the average length of the three lattice vectors. Figure 3.1(d) displays the variation of the average lattice constant a_{avg} of $Si_yGe_ySn_x$ with the Sn content. We can fit the a_{avg} data

to a linear equation (a_{avg} = 5.61 + 1.04x) without introducing the bowing factor. Namely, the average lattice constant follows the Vegard law. This trend is in contrast to group IV binary alloys, which have been shown to exhibit sizable bowing factors [177,178].

We next compute the formation energy E_f of $Si_yGe_ySn_x$ HEAs, defined as the energy change of the following reaction:

$$y\mathrm{Si} + y\mathrm{Ge} + x\mathrm{Sn} \rightarrow \mathrm{Si}_y\mathrm{Ge}_y\mathrm{Sn}_x \quad (3.4)$$

For a better comparison, we calculate the energies of the 216-atom supercells of Si, Ge, and α-Sn with the diamond structure using the same number of atoms. Positive E_f from the ground-state calculations indicates that the product (a $Si_yGe_ySn_x$ MEA) is less stable than the reactants (Si, Ge, and α-Sn). Figure 3.1(e) shows that the energy changes of all the reactions are endothermic and that Ef increases with the Sn concentration although the magnitude of increase is smaller at high Sn content.

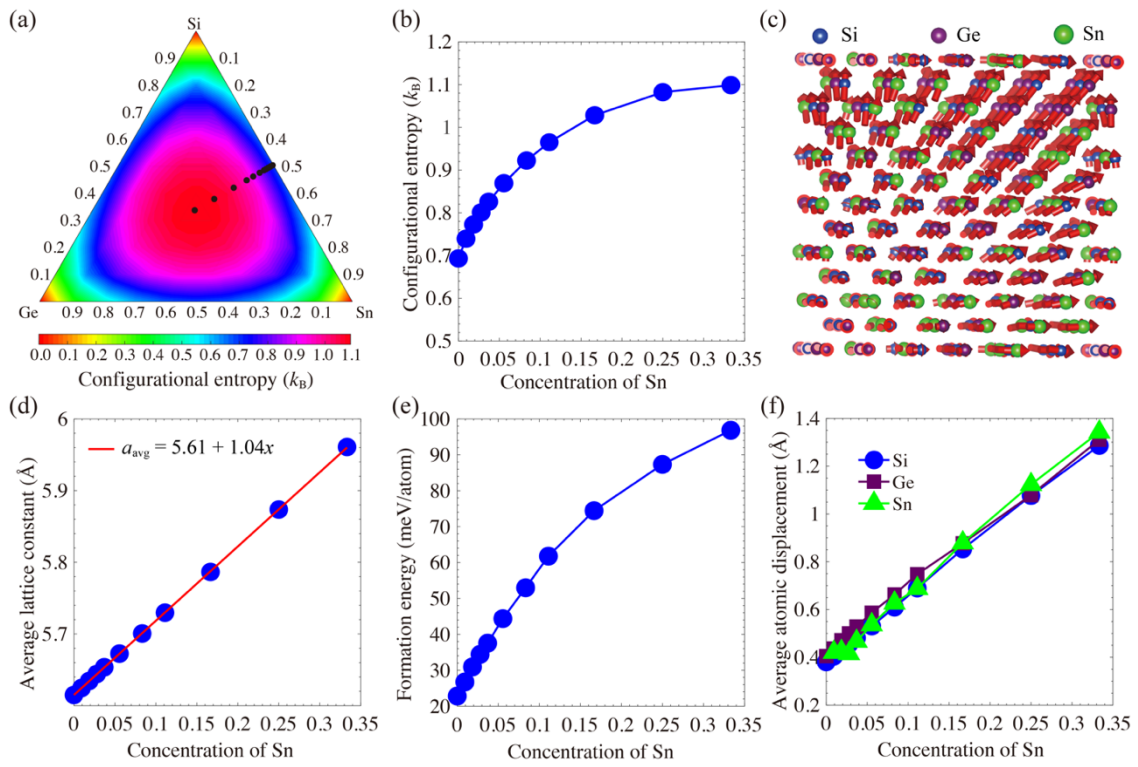

Figure 3.1. (a) Composition space of Si-Ge-Sn alloys color-coded by the configurational entropy. The black dots denote the compositions of the 11 alloys studied in this work. (b) Configuration entropy of $Si_yGe_ySn_x$ MEAs a function of the Sn content x. (c) Atomic structure of $Si_yGe_ySn_x$ (x = 1/3) MEA and displacement field showing a large lattice distortion effect. (d) Average lattice constant and its fit to a linear equation of x, (e) formation energy, and (f) average atomic displacement of $Si_yGe_ySn_x$ MEAs as a function of x.

We note that the configurational entropy is absent in the formation energy calculations. We estimate the entropy contribution, for example, at 500 K that is an estimated temperature at which conventional Si-Ge-Sn alloys are grown using the CVD method [148]. The configurational entropy contribution $-TS_{conf}$ to the Gibbs free energy at this temperature is about -53.3 meV/atom for the equimolar $Si_{1/3}Ge_{1/3}Sn_{1/3}$ MEA with the E_f of 96.8 meV/atom. However, the Gibbs free energy remains positive (43.5 meV/atom) even

considering this part of energy contribution, implying that $Si_yGe_ySn_x$ MEAs are out of thermodynamic equilibrium. As a result, fabricating $Si_yGe_ySn_x$ MEAs is likely to require the same non-equilibrium growth processes used for obtaining the conventional high-Sn content Si-Ge-Sn alloys [73,179].

HEAs/MEAs generally exhibit a notable lattice distortion effect. To illustrate this effect, we compute the atomic displacement field for the atoms in the simulation supercell using the $Si_{1/3}Ge_{1/3}Sn_{1/3}$ MEA as an example. Figure 3.1(c) depicts the atomic displacement field of this MEA with the atomic positions in lattice sites of bulk Si being the reference. Each arrow represents the direction of a displacement and the length of an arrow represents the magnitude of the atomic displacement. Although the atomic displacements occur in different directions, we observe a dominant direction parallel to the (110) plane, where the atoms prefer to relocate. This direction preference causes a large lattice strain along that direction. We calculate the average atomic displacements for each element in the $Si_{1/3}Ge_{1/3}Sn_{1/3}$ MEA. As shown in Figure 3.1(f), the average atomic displacements for all the species increase when the Sn content is increased. This trend is caused by the fact that increasing the Sn content simultaneously creates space for Si and Ge atoms to adjust their locations. We also observe from Figure 3.1(f) that the average atomic displacement for the three elements is nearly the same, regardless of their different atomic radii.

3.4.2 Electronic and Thermal transport Properties

Having studied the structural properties of $Si_yGe_ySn_x$ MEAs, we set out to understand

their electronic structures and associated electrical transport properties. Figure 3.2 displays the band structures of the four $Si_yGe_ySn_x$ (x = 0, 1/12, 1/6, and 1/3) MEAs calculated using the mBJ exchange potential. Due to the presence of heavy Sn atoms, we account for the spin-orbit coupling in computing the band structures. The modified Becke-Johnson exchange potential that yields accurate band gaps comparable to our recent calculation using the HSE06 hybrid density functional [93]. For example, the mBJ band gap of $Si_{1/3}Ge_{1/3}Sn_{1/3}$ is 0.28 eV, close to the HSE06 band gap of 0.38 eV [125]. As can be seen from Figure 3.2, the bandgap type becomes direct as the Sn content is increased to near 1/3. Figure 3.3(a) shows the variation of the bandgaps with the concentration of Sn, revealing that the bandgaps decrease with increasing Sn content and the range of the bandgaps, 0.28-1.11 eV, spans from visible to near-infrared in the light spectrum. Such a wide range of band gaps endow $Si_yGe_ySn_x$ MEAs with potential for applications not only in TE but also in optoelectronics devices.

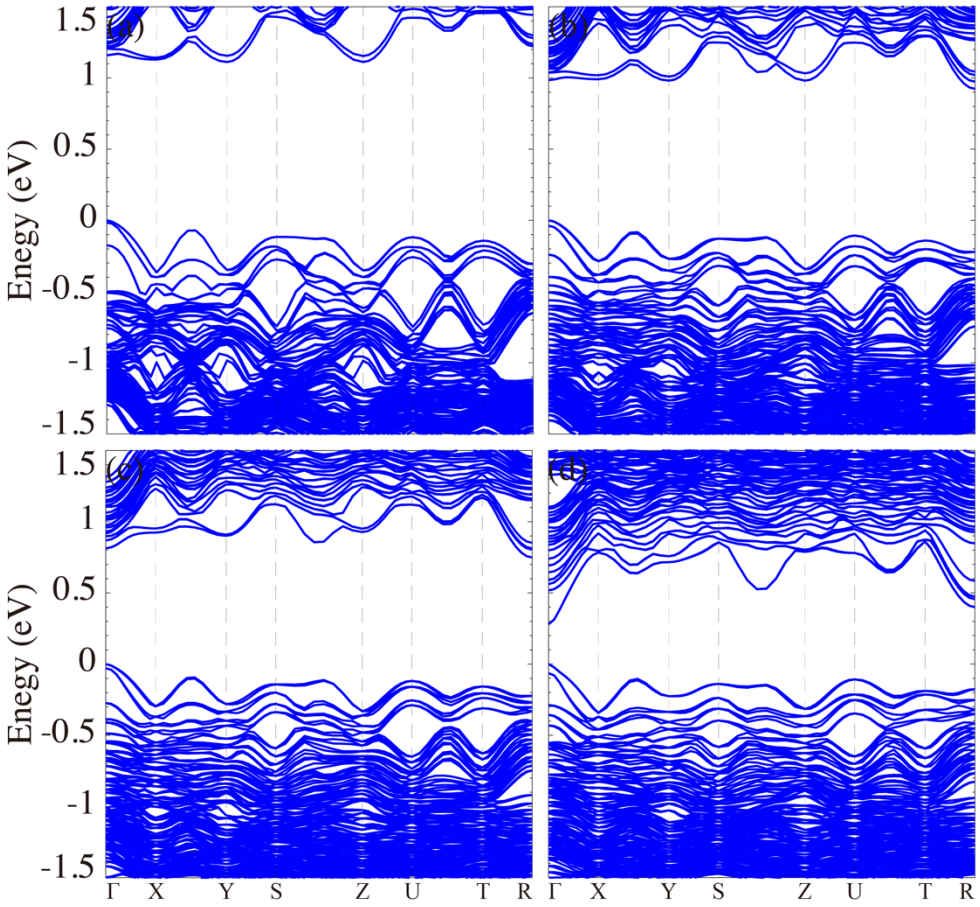

Figure 3.2. Band structures of $Si_yGe_ySn_x$ MEAs with (a) $x = 0$, (b) $x = 1/12$, (c) $x = 1/6$, and (d) $x = 1/3$. The band structures are obtained from the modified Becke-Johnson exchange potential using the optimized structures from DFT calculations with the PBE functional. Spin-orbit coupling is taken into account and the valence band maxima are set to zero. The coordinates of X, Y, S, Z, U, T, and R are (1/2,0,0), (0,1/2,0), (1/2,1/2,0), (0,0,1/2), (1/2,0,1/2), (1/2,1/2,0), and (1/2,1/2,1/2) respectively.

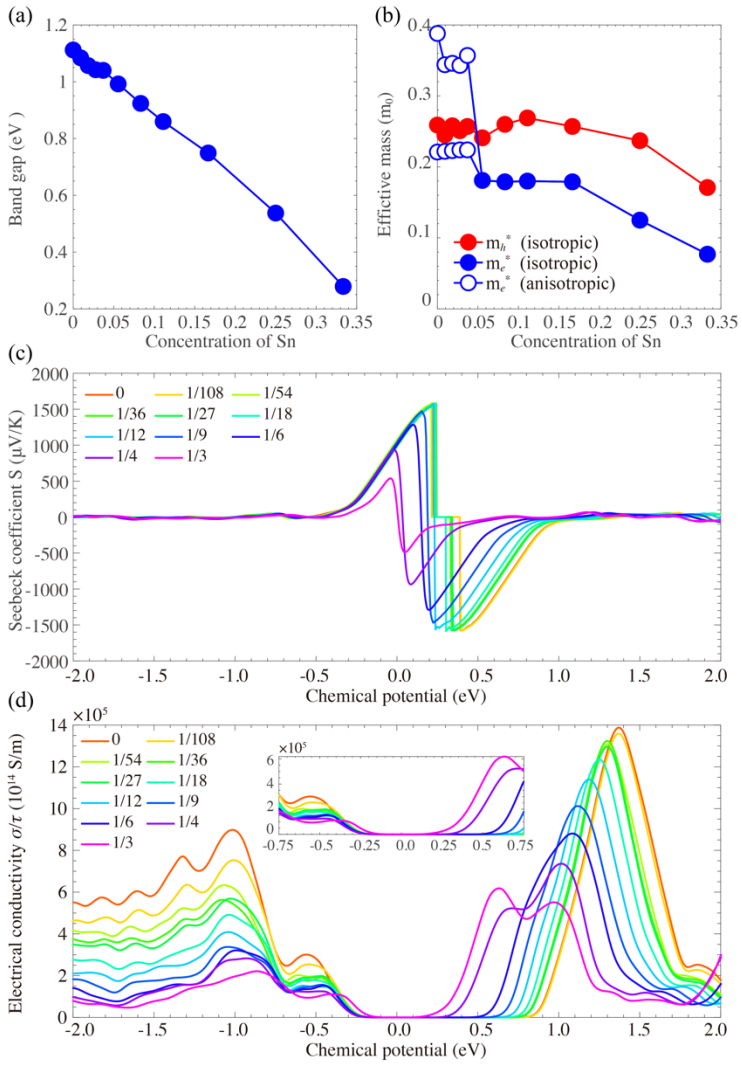

Figure 3.3. Variation of (a) bandgaps and (b) electron and hole effective masses of $Si_yGe_ySn_x$ MEAs with Sn content. (c) Seebeck coefficient and (d) electrical conductivity of $Si_yGe_ySn_x$ MEAs at different electron chemical potentials.

Figure 3.3(b) shows the computed electron and hole effective masses of $Si_yGe_ySn_x$ MEAs. The hole effective mass m_h^* in the whole range of Sn content of $Si_yGe_ySn_x$ MEAs is isotropic, so only one set of data are shown. By contrast, the effective electron mass m_e^* is anisotropic at low Sn content. Increasing the Sn content removes the anisotropy of m_e^*.

Overall, $Si_yGe_ySn_x$ MEAs with high-content Sn has small effective carrier masses. In particular, $Si_{1/3}Ge_{1/3}Sn_{1/3}$ exhibits the lowest m_h^* (0.171 m_0) and m_e^* (0.077 m_0) among the 11 $Si_yGe_ySn_x$ MEAs. The low m_h^* and m_e^* of $Si_yGe_ySn_x$ MEAs with high-content Sn are comparable or even smaller than the corresponding m_h^* and m_e^* of Si, Ge, and GaAs [180], implying high carrier mobility in these MEAs given the same relaxation time and applied electric field.

To evaluate the room-temperature TE figure of merit of the 11 $Si_yGe_ySn_x$ MEAs, we first calculate their Seebeck coefficients and electrical conductivities at 300 K. According to Eq.(3.1) and (3.2), both parameters vary with the chemical potential that can be tuned by *p*/*n*-type doping for a semiconductor. Figure 3.3(c) depicts the calculated Seebeck coefficients of the MEAs as a function of the chemical potential. We observe two typical peaks in the plots of Seebeck coefficients for each MEA, corresponding to the maximum Seebeck coefficients of the cases of *p*-type and *n*-type doping, respectively. Because of the Fermi distribution, the Seebeck coefficients decay rapidly to zero when the chemical potential significantly deviates from the band energies. For all the 11 $Si_yGe_ySn_x$ MEAs, we obtain their maximum Seebeck coefficients that range from 537 to 1583 μV/K. The maximum Seebeck coefficients of $Si_yGe_ySn_x$ MEAs with the Sn content below 1/9 have higher values (> 1500 μV/K). Although the maximum Seebeck coefficient of $Si_{1/3}Ge_{1/3}Sn_{1/3}$ is not the largest among all the MEAs, the value of 537 μV/K appears higher than many other TE materials such as $CuGaTe_2$ and MgAgSb with the maximum Seebeck coefficients

of 277 μV/K [181] and 400 μV/K [182] respectively, calculated with the PBE functional and at the same temperature.

Figure 3.3(d) shows the electrical conductivities (divided by the constant relaxation time $\tau = 10^{-14}$ s) of the $Si_yGe_ySn_x$ MEAs as a function of the chemical potential. We can see the ranges of chemical potentials, which match the band gaps of the 11 MEAs as shown in Figure 3.3(a), correspond to an electrical conductivity of zero. Outside these ranges, the electrical conductivity increases significantly. In a small potential range from -0.3 to 0.75 eV, the electrical conductivity of $Si_{1/3}Ge_{1/3}Sn_{1/3}$ is the highest among all the MEAs, where it peaks at 0.63 eV with an electrical conductivity of 6.2 × 105 S/m. For reference, the electrical conductivity is higher than many other proposed TE materials such as $CuGaTe_2$ (1.3 × 104 S/m) [181] and Mg_2Si (7.1 × 104 S/m) [183] at room temperature.

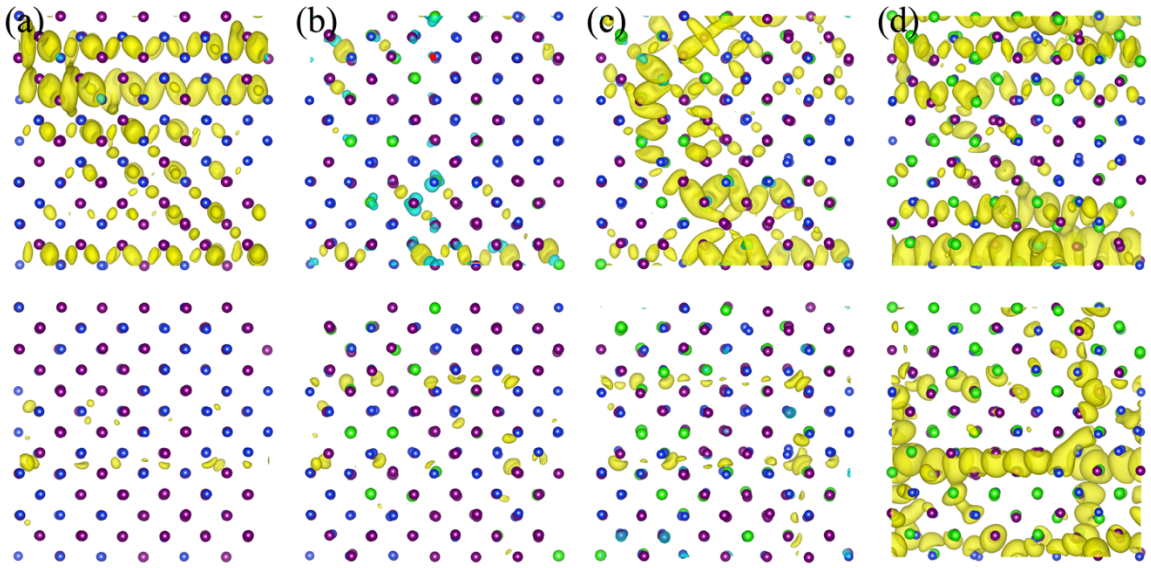

Figure 3.4. Charge density of the valence (top) and conduction (bottom) bands of

$Si_yGe_ySn_x$ MEAs with (a) x = 0, (b) x = 1/12, (c) x = 1/6, and (d) x = 1/3. The isosurface value of $Si_yGe_ySn_x$ MEAs is 1.0 × 10-4 e/Bohr^3.

The high electrical conductivity of $Si_yGe_ySn_x$ MEAs especially the ones with high Sn content is somewhat surprising. According to Anderson [184], one expects electron localization to occur and diminish the electrical conductivity in disordered systems like $Si_yGe_ySn_x$ MEAs. On the contrary, the charge densities of the top valence and bottom conductions bands of four $Si_yGe_ySn_x$ MEAs (x = 0, 1/12, 1/6, and 1/3) shown in Figure 3.4 reveal that, although there is carrier localization to some extent, both electrons and holes become more delocalized as the Sn content is closer to 1/3. The absence of electron/hole Anderson localization is possibly because Si, Ge, and Sn belong to the same group and have nearly the same electronegativity. As a result, the scattering between an electron and any of the three types of nuclei is expected to be similar.

We now compute the thermal conductivity of $Si_yGe_ySn_x$ MEAs and examine the effects of compositional disorder. Figure 3.5(a) shows the calculated thermal conductivity of the 11 $Si_yGe_ySn_x$ MEAs from the EMD simulations. The thermal conductivities of several of these MEAs have been reported in the literature using a variety of methods such as the non-equilibrium MD (NEMD) method with fixed thermostat at the end points, the reversed NEMD Müller-Plathe method, and the EMD Green-Kubo method [171,172,185,186]. Our calculated thermal conductivities are consistent with the literature. For example, the thermal conductivity of $Si_{0.5}Ge_{0.5}$ in the present work is 1.62 W/(m·K),

comparable to 1.06 ± 0.16 W/(m·K) using the NEMD method with the same interatomic potential [187,188]. Because the thermal conductivity at the MD level of theory depends on simulation methods such as the Green-Kubo method, the simulation cell size, and most importantly, the transferability of the Si-Ge-Sn interatomic potential, we emphasize that the absolute values of thermal conductivities of $Si_yGe_ySn_x$ MEAs are not as important as the trend shown in Figure 3.5(a) that the thermal conductivity decreases with the increasing Sn content. As a matter of fact, we benchmark the thermal conductivity of Si using the same set of simulation parameters and obtain the thermal conductivity of 56.1 W/(m·K), which is only about half of the experimental value of 125.5 W/(m·K) [189]. Therefore, although our calculated thermal conductivities await experimental confirmation, they tend to be underestimated in comparison with the future experimental data.

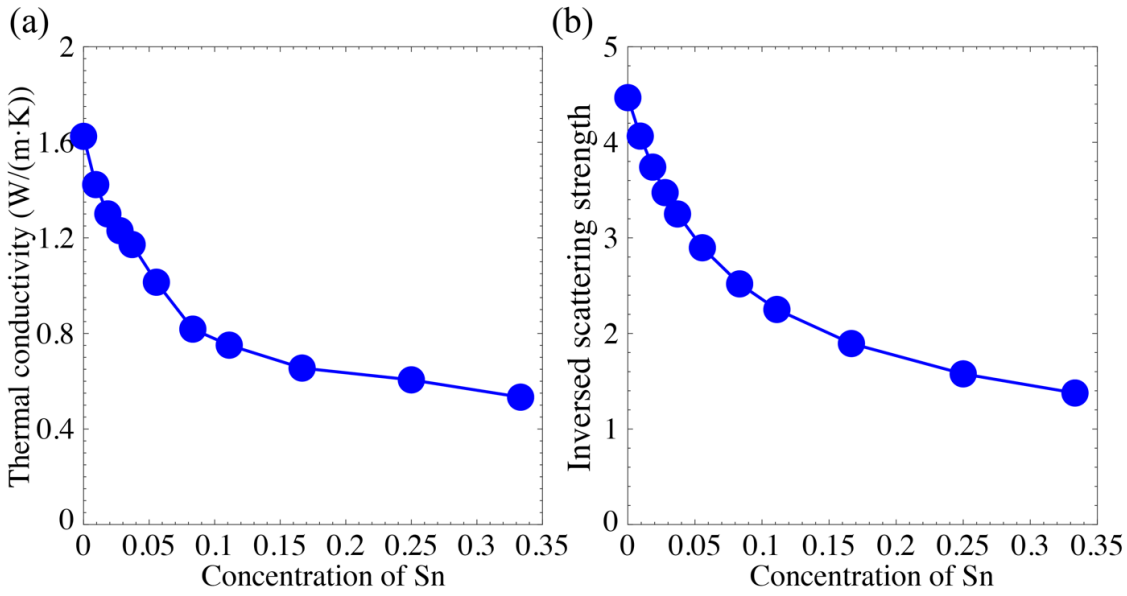

Figure 3.5. (a) Thermal conductivity of $Si_yGe_ySn_x$ MEAs obtained from classical molecular dynamics simulations and (b) the corresponding inversed scattering strengths calculated from Eq. 3.6.

Because $Si_yGe_ySn_x$ MEAs are semiconductors with sizable bandgaps, we do not consider the electron contribution to the thermal conductivity and therefore focus on the phonon contributions to the thermal conductivities of $Si_yGe_ySn_x$ MEAs. To understand the above trend of the decreased thermal conductivity of $Si_yGe_ySn_x$ MEAs with the increasing compositional disorder, we adopt three different perspectives related to phonon behavior: the phonon version of Anderson localization, phenomenal model of phonon scattering, and DFT calculations of phonon scattering. We start with computing the phonon vibrational frequencies and their corresponding normal modes (eigenvectors). We compute the participation ratio (*PR*) for each vibrational mode n using the following equation [150,190]:

$$PR = \frac{(\sum_i e_{i,n}^2)^2}{N \sum_i e_{i,n}^4} \tag{3.5}$$

where $e_{i,n}$ is the phonon eigenvector of mode n and N is the total number of atoms. Figure 3.6 shows the phonon density of states (PDOS) of four $Si_yGe_ySn_x$ (x = 0, 1/12, 1/6, and 1/3) MEAs and their corresponding *PR* plots. We can see that the PDOS of the four MEAs appear similar except that an additional peak occurs in the $Si_{1/3}Ge_{1/3}Sn_{1/3}$ MEA near the frequency of 170 cm^{-1}. Another phenomenon in common is that the *PR* values for all the phonon modes of each MEA are separated into two groups, one with low *PR*, implying large eigenvectors; the other with high *PR*, suggesting small eigenvectors. The boundary between the two groups of *PR*s is called the mobility edge. According to Allen et al. [191], the phonon modes below the mobility edge are classified as locons caused by the phonon version of Anderson localization. The mobility edge separates locons from the so-called propagons and diffusons that positively contribute to the thermal conductivity. We observe that the mobility edges of the four $Si_yGe_ySn_x$ MEAs are located at 243, 213, 179, and 122 cm^{-1}, respectively. Furthermore, as the Sn content increases, the *PR* values of the locons decrease, suggesting increasingly enhanced phonon localizations, which are also manifested by the increasingly localized eigenvectors of the phonon modes with small *PR*s as displayed in Figure 3.7. The more and more localized phonons with the Sn content therefore explains the observed trend in the thermal conductivities (see Figure 3.5(a)) of $Si_yGe_ySn_x$ MEAs.

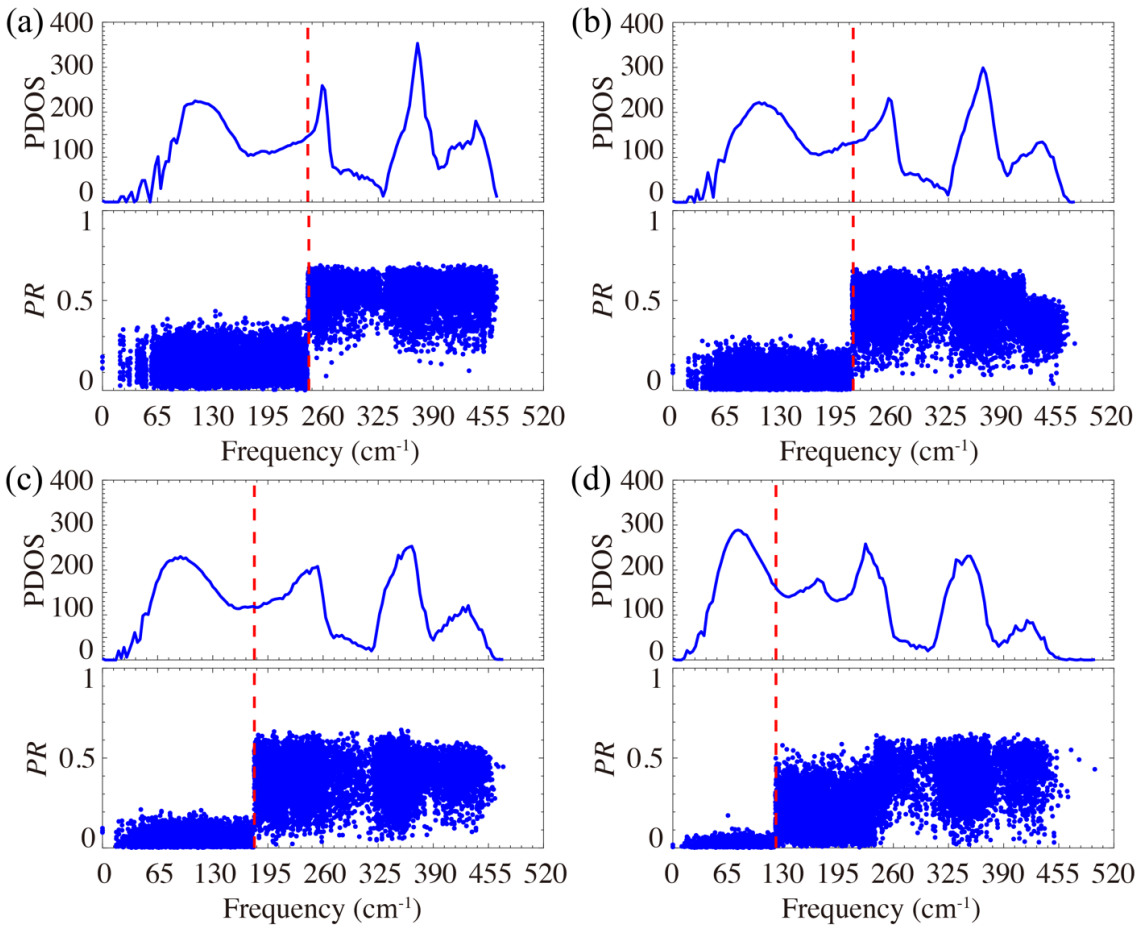

Figure 3.6. Phonon density of states (PDOS) and partition ratio (*PR*) of $Si_yGe_ySn_x$ MEAs with (a) $x = 0$, (b) $x = 1/12$, (c) $x = 1/6$, and (d) $x = 1/3$.

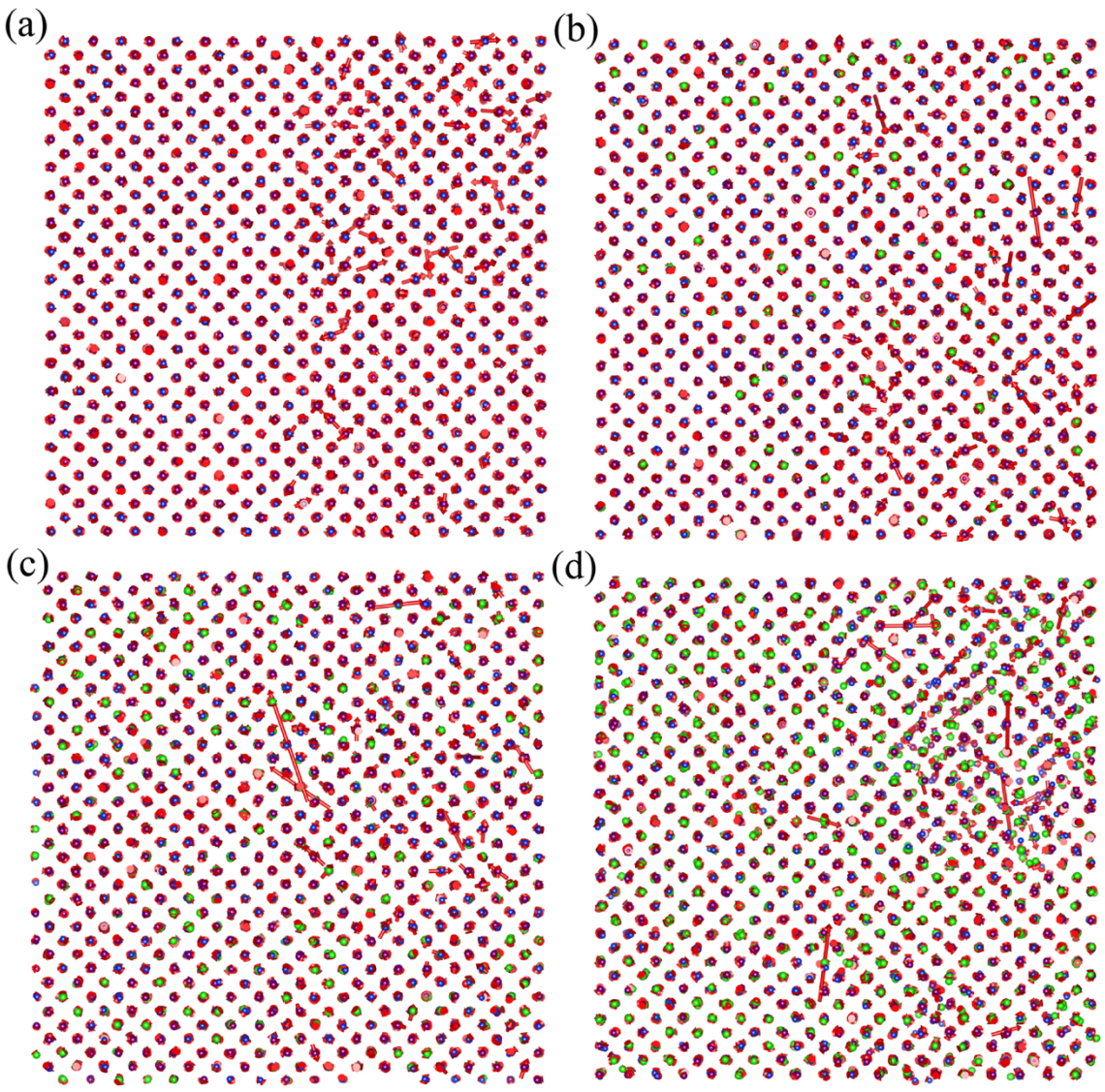

Figure 3.7. Phonon eigenvectors that correspond to the same low partition ratio, 0.022, of $Si_yGe_ySn_x$ MEAs with (a) $x = 0$, (b) $x = 1/12$, (c) $x = 1/6$, and (d) $x = 1/3$. To aid the visualization of the normal modes, we scale the computed eigenvectors by a factor of 20.

In the phenomenal model for understanding the trend in the thermal conductivity of $Si_yGe_ySn_x$ MEAs, we consider phonon scattering by accounting for two effects. The first one is compositional disorder and the second is lattice distortion that has been shown above.

Taking these two factors into account, we can approximate the phonon scattering strength from alloy (caused by the compositional disorder) and strain effects (originated from the lattice distortion) as [149,192],

$$\Gamma = c_i[\left(1 - \frac{M_i}{\overline{M}}\right)^2 + \gamma\left(1 - \frac{a_i}{a_{\mathrm{avg}}}\right)^2] \quad (3.6)$$

where M_i is the atomic mass of the ith element and $\overline{M}$ is the averaged atomic mass dependent on the concentrations c_i of individual elements. Similarly, a_i, are the optimized lattice constants of Si, Ge, and α-Sn using the empirical Si-Ge-Sn interatomic potential. a_{avg} is the average lattice constant of a $Si_yGe_ySn_x$ MEA. γ is an adjusting parameter taken as 39 based on the previous work on conventional Si-Ge-Sn alloys [192]. The inversed phonon scattering strength Γ^{-1} determines the phonon lifetime τ from phonon scattering. τ is proportional to Γ^{-1} with the proportional factor dependent on phonon group velocities and frequencies and lattice constants of a system. Figure 3.5(b) shows the variation of Γ^{-1} with x in $Si_yGe_ySn_x$ MEAs. We observe the same trend as in the thermal conductivity versus the Sn content, i.e., Γ^{-1} decreases as the Sn content increases in the MEAs. This consistent trend implies that the phonon scattering grows increasingly stronger as the compositional disorder increases and thus more thermal energy carriers are scattered rather than transported to conduct heat, leading to the decreased thermal conductivities found in our EMD calculations.

Finally, we attempt to understand the trend the thermal conductivity of $Si_yGe_ySn_x$ MEAs from the perspective of DFT calculations. We first use VASP and Phonopy to

compute the second-order force constant and construct a dynamical matrix and obtain the phonon spectra of two artificial Si-Ge-Sn MEAs of $Si_{1/2}Ge_{3/8}Sn_{1/8}$, and $Si_{3/8}Ge_{3/8}Sn_{1/4}$. We see from Figure 3.8(a) and (b) that phonon frequencies shown in the phonon spectra are all real, showing that these two MEA systems are dynamically stable. The right plot of each diagram in Figure 3.8 shows the accumulated thermal conductivity $\sum\kappa$ at 300 K and the derivative of the thermal conductivity $\mathrm{d}\kappa$ as a function of phonon frequency. We can see that $\sum\kappa$ generally increases with phonon frequencies and becomes nearly a constant at high frequencies. Correspondingly, $\mathrm{d}\kappa$ increases and peaks and decays to zero. From the saturated $\sum\kappa$, we determine the thermal conductivities of $Si_{1/2}Ge_{3/8}Sn_{1/8}$ and $Si_{3/8}Ge_{3/8}Sn_{1/4}$ as 41.1 and 19.8 W/(m·K), respectively. We expect these DFT thermal conductivities to be more accurate than those from our EMD simulations. For example, our calculated DFT thermal conductivity of Si (122.9 W/(m·K)) for benchmark is consistent with the experimental value of 125.5 W/(m·K) [189] and with 129.5 W/(m·K) from previous DFT calculations [193]. Both $\sum\kappa$ and $\mathrm{d}\kappa$ show that the thermal conductivities of the four systems originate mainly from the contributions of phonons with relatively low frequencies. For the integration range from 0 to 100 cm^{-1}, the $\sum\kappa$ of $Si_{1/2}Ge_{3/8}Sn_{1/8}$ and $Si_{3/8}Ge_{3/8}Sn_{1/4}$ reaches 83% and 92%, respectively, of their corresponding total thermal conductivities. Increasing the integration range up to 150 cm^{-1}, the $\sum\kappa$ of $Si_{1/2}Ge_{3/8}Sn_{1/8}$ increases to 95%, whereas the $\sum\kappa$ of $Si_{3/8}Ge_{3/8}Sn_{1/4}$ reaches 96%, respectively, of their total thermal conductivities. In other words, comparing to $Si_{1/2}Ge_{3/8}Sn_{1/8}$, $Si_{3/8}Ge_{3/8}Sn_{1/4}$ with higher Sn

content exhibits a smaller thermal conductivity and the $\sum \kappa$ saturates much more rapidly.

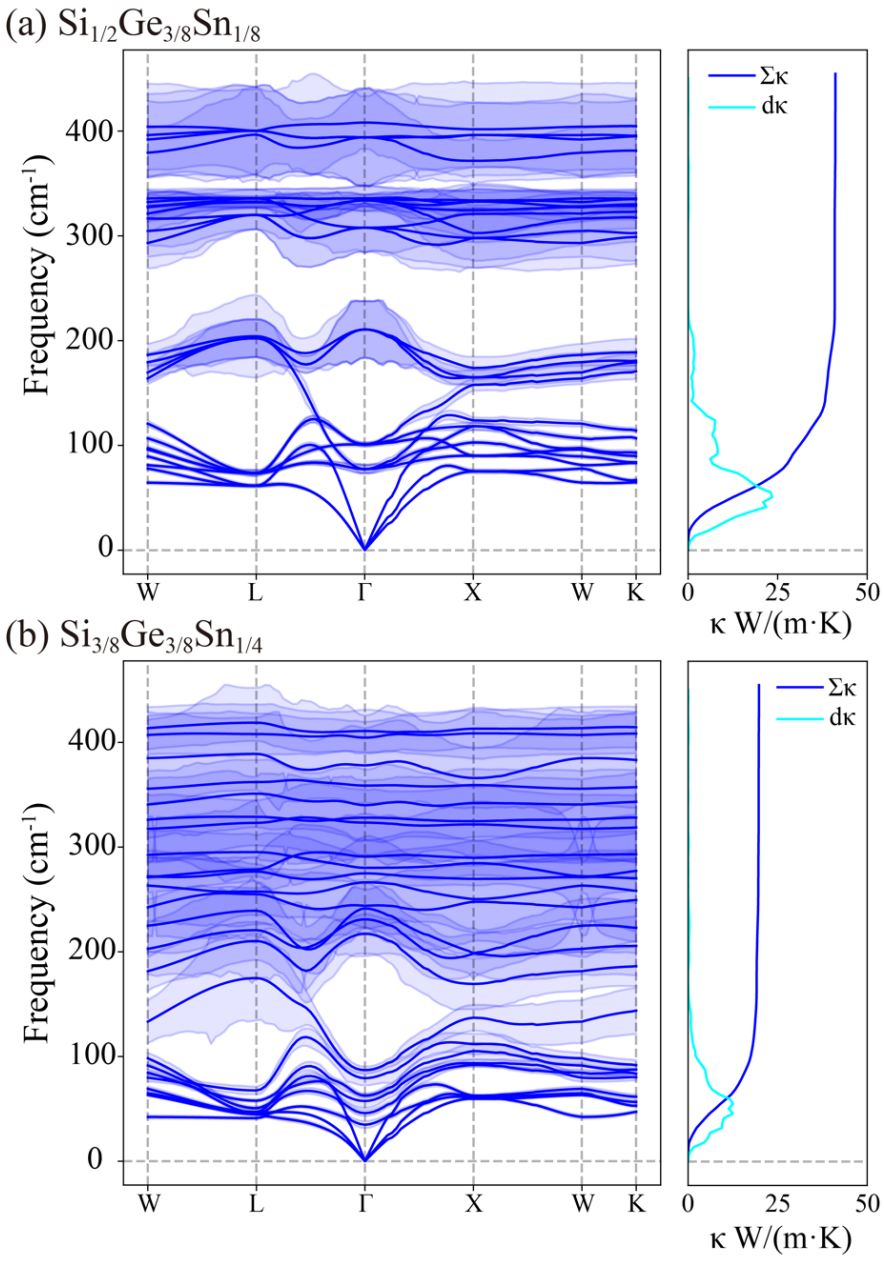

Figure 3.8. Phonon spectrum and linewidth, thermal conductivity derivative $d\kappa$, and cumulated thermal conductivity $\sum \kappa$ of two artificial MEAs (a) $Si_{1/2}Ge_{3/8}Sn_{1/8}$, (b) $Si_{3/8}Ge_{3/8}Sn_{1/4}$. To aid the visualization of phonon linewidth, we scale the computed values by a factor of 50.

The anharmonic phonon-phonon interactions play important roles in decreasing the thermal transport of a material. To interrogate the effects of compositional disorder on the anharmonic phonon-phonon interactions and consequently the thermal conductivities of $Si_{1/2}Ge_{3/8}Sn_{1/8}$ and $Si_{3/8}Ge_{3/8}Sn_{1/4}$, we focus on the phonon linewidths caused by anharmonic phonon-phonon interactions. Unlike the linewidth in the phenomenal model that considers the alloy and strain effects, the linewidth in DFT calculations here account for the alloy and Umklapp scattering effects [149,194]. We can derive the phonon lifetime τ_λ through an inverse relationship with phonon linewidth, $\tau_\lambda = 1/(2\Gamma_\lambda)$. Experimentally, the phonon linewidth $2\Gamma_\lambda$ can be measured via time-resolved Raman spectroscopy, where $2\Gamma_\lambda$ approximately equals to the full width at half maximum of the Raman spectrum peak [195,196]. Theoretically, anharmonic phonon-phonon interactions are described by the frequency (ω)-dependent phonon self-energy $\Delta(\omega) - i\Gamma(\omega)$ [195]. The real part $\Delta(\omega)$ gives the frequency shift due to the phonon-phonon scattering, whereas the imaginary part $\Gamma(\omega)$ is associated with the probability of phonon decay that can be written as,

$$\Gamma_\lambda = \frac{18\pi}{\hbar^2}\sum_{\lambda_1\lambda_2}\left|V_{\lambda\lambda_1\lambda_2}\right|^2 S(\lambda,\omega) \tag{3.7}$$

Here, $V_{\lambda\lambda_1\lambda_2}$ denotes a third-order tensor representing the many-body interactions following the direction for the energy decreasing most rapidly regarding three displacements from the equilibrium positions [197,198]. $S(\lambda,\omega)$ written below

$$S(\lambda,\omega) = \left(1 + n_{\lambda_1} + n_{\lambda_2}\right)\delta\left(\omega_\lambda - \omega_{\lambda_1} - \omega_{\lambda_2}\right) + \left(n_{\lambda_1} - n_{\lambda_2}\right)[\delta\left(\omega_\lambda + \omega_{\lambda_1} - \omega_{\lambda_2}\right) - \delta\left(\omega_\lambda - \omega_{\lambda_1} + \omega_{\lambda_2}\right)] \tag{3.8}$$

results from two types of phonon decay processes: (1) the down-conversion process where the initial phonon is decomposed into two phonons of lower frequencies $\delta(\omega_\lambda - \omega_{\lambda_1} - \omega_{\lambda_2})$, and (2) the up-conversion process where the phonon at non-equilibrium state absorbs another phonon to form a higher-frequency phonon, $\delta(\omega_\lambda + \omega_{\lambda_1} - \omega_{\lambda_2})$ and $\delta(\omega_\lambda - \omega_{\lambda_1} + \omega_{\lambda_2})$ [176,197,199]. n_{λ_i} in Eq. 8 represents the Bose-Einstein distribution function, i.e., $n_{\lambda_i} = [\exp(\hbar\omega_{\lambda_i}/k_B T) - 1]^{-1}$.

Figure 3.8 shows the calculated phonon linewidths of $Si_{1/2}Ge_{3/8}Sn_{1/8}$ and $Si_{3/8}Ge_{3/8}Sn_{1/4}$ overlapped with the corresponding phonon modes. We observe that large phonon linewidth caused by the anharmonic phonon-phonon interactions in the optical branches suppresses the increase of thermal conductivity. We calculate the average phonon linewidth in different ranges of phonon frequencies. For $Si_{1/2}Ge_{3/8}Sn_{1/8}$, the averaged phonon linewidth of all the phonon modes is 0.563 cm^{-1}, whereas the overall averaged phonon linewidth of $Si_{3/8}Ge_{3/8}Sn_{1/4}$ is 0.888 cm^{-1}, 58% higher than $Si_{1/2}Ge_{3/8}Sn_{1/8}$. Because the major contribution of thermal conductivity at 300 K results from the relatively lower-frequency phonon modes, we compute the average phonon linewidth for $Si_{1/2}Ge_{3/8}Sn_{1/8}$ and $Si_{3/8}Ge_{3/8}Sn_{1/4}$ using their phonon modes with the frequencies in the range from 0 to 150 cm^{-1}. This region is also where the thermal conductivity derivative increases rapidly for all the four systems. Once again, the averaged phonon linewidth of $Si_{3/8}Ge_{3/8}Sn_{1/4}$ (0.150 cm^{-1}) is longer than that of $Si_{1/2}Ge_{3/8}Sn_{1/8}$ (0.075 cm^{-1}). We therefore conclude that the anharmonic phonon-phonon interactions cause the increase of phonon linewidth in the low-

frequency region of $Si_{3/8}Ge_{3/8}Sn_{1/4}$, shortening the phonon lifetime and suppressing the increase of thermal conductivity in the high-frequency region.

With the calculated Seebeck coefficients, electrical conductivities, and thermal conductivities, we compute the figure of merit at room temperature for the 11 $Si_yGe_ySn_x$ MEAs. Because the underestimated EMD thermal conductivities lead to overestimated figure of merit, we scale the computed figure of merit by a factor of 1/2.19 (The denominator comes from the ratio between the DFT and EMD thermal conductivities of Si). Figure 3.9 shows that, at different chemical potentials, $Si_yGe_ySn_x$ MEAs can achieve figure of merit that is comparable to that of other room-temperature TE materials.

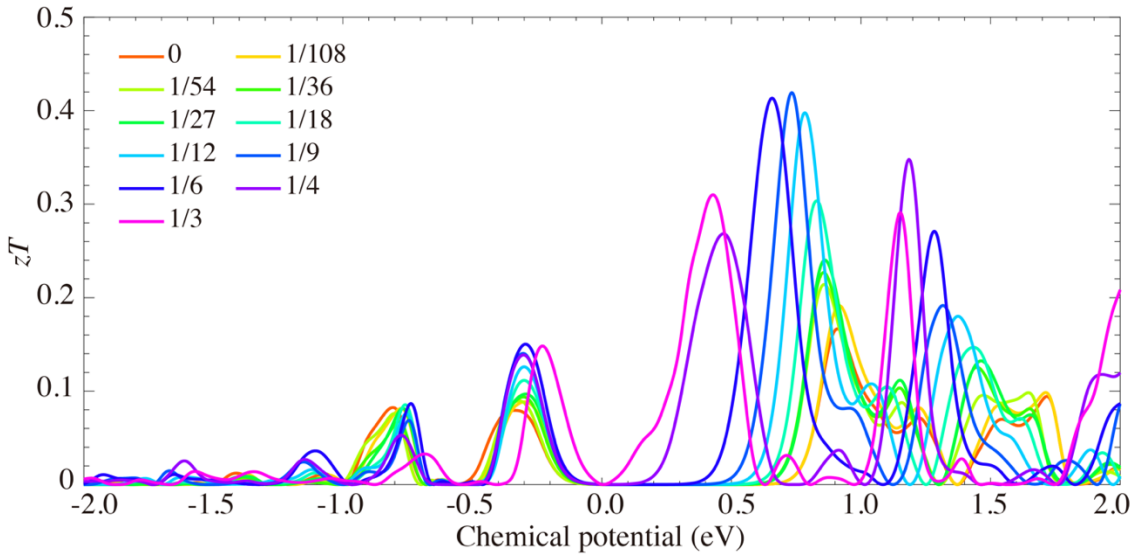

Figure 3.9. Scaling figure of merit of $Si_yGe_ySn_x$ MEAs at different electron chemical potentials. The scaling factor is 1/2.19 due to the underestimated thermal conductivity in the molecular dynamics simulations.

3.5 Summary

We have performed DFT and classical MD calculations to investigate the electrical and thermal transport properties of $Si_yGe_ySn_x$ MEAs. We found that $Si_yGe_ySn_x$ MEAs exhibit a wide range of bandgaps that span from visible to near-infrared in the light spectrum and that $Si_yGe_ySn_x$ MEAs with high Sn content have small electron and hole effective masses. Furthermore, we showed that the electron Anderson localization is not as distinct as phonon Anderson localization. The excellent electrical properties of $Si_yGe_ySn_x$ MEAs make them promising for applications in a variety of electronic devices. Meanwhile, we found $Si_yGe_ySn_x$ MEAs show low thermal conductivities, owing to the phonon Anderson localization and strong anharmonic phonon-phonon interactions caused by the lattice distortion and compositional disorder. The high electrical conductivities and low thermal conductivities endow $Si_yGe_ySn_x$ MEAs with great potential for high TE performance at room temperature. Our prediction calls for future experimental verification and also for simulation models to obtain more accurate thermal transport properties for these MEAs.

CHAPTER V

HIGH-THROUGHPUT COMPUTATIONAL CHARACTERIZATION OF TWO-DIMENSIONAL COMPOSITIONALLY COMPLEX TRANSITION-METAL CHALCOGENIDE ALLOYS

4.1 Abstract

Many two-dimensional (2D) binary transition-metal chalcogenides (TMCs) such as molybdenum disulfide have been synthesized, exhibiting a wide range of structural and electrical properties promising for energy conversion applications such as photovoltaics, photocatalysts, and optoelectronics. Alloying these binary TMCs has the potential to form multinary TMCs also known as 2D compositionally complex TMC alloys (CCTMCAs) that are expected to possess a combination of remarkable properties from the constituent binary TMCs. While the experimental exploration of 2D CCTMCAs just begins to emerge, it is imperative to design a computational strategy to efficiently discover novel 2D CCTMCAs for various applications. However, exploring the compositional space of 2D CCTMCAs via density functional theory (DFT) calculations based on the supercell method is computationally challenging, given that there is an enormous amount of possible combinations of binary TMCs. Here we adopt a high-throughput workflow that performs DFT calculations based on models from the virtual crystal approximation (VCA) method (VCA-DFT). To test our high-throughput workflow, we use the Mo-W-S-Se, Mo-W-S-Te, and Mo-W-Se-Te 2D CCTMCAs as examples. We demonstrate the capability of this

workflow in predicting five key properties of 2D CCTMCAs including in-plane lattice constants, band gaps, effective hole and electron masses, spin-orbit coupling (SOC), and band alignments from 2D CCTMCAs with different compositions. We also validate the VCA-DFT results by computing the same properties using the unit cell model for Janus structures and the supercell model based on special quasi-random structures (SQS) for ternary and quaternary structures. We find that the VCA-DFT method generally can predict the abovementioned five properties at an accuracy comparable to that of DFT calculations using unit cells or SQS models, with some exceptions including the inaccurate prediction of the locations of conduction band minima of MoSTe and WSTe and thus inaccurate effective hole masses and band gaps. We also show that both ternary and quaternary 2D CCTMCAs can form type II heterostructures, important for carrier separation and transportation as in photovoltaics and photocatalysts. Finally, we focus on three quaternary 2D CCTMCAs, $Mo_{0.5}W_{0.5}SSe$, $Mo_{0.5}W_{0.5}STe$, and $Mo_{0.5}W_{0.5}SeTe$, with the maximum configurational entropy as examples. We study the thermodynamic stability of these quaternary alloys and find that they have lower Gibbs free energies than ternary 2D CCTMCAs. These three quaternary 2D CCTMCAs are excellent examples of room temperature entropy-stabilized alloys. They also show high electrical conductivity at room temperature, making them possible for the applications of light adsorption devices. Our work shows that the high-throughput workflow based on VCA-DFT calculations provides a tradeoff between efficiency and accuracy, opening up ample opportunities in the

computational design of many other 2D CCTMCAs for a variety of applications.

4.2 Introduction

Binary two dimensional (2D) transition metal chalcogenides (TMCs) exhibit strong in-plane chemical bonds and weak out-of-plane interactions, allowing for stable monolayers [200,201]. The properties of 2D TMCs such as MX_2 have been investigated from both computational simulation and the experimental works [202-206]. Strain engineering on MX_2 gives rise to tunable properties such as band gaps and effective masses. Moreover, monolayer MX_2 have direct band gaps ranging from 1.0 to 2.0 eV [202]. They also display thickness-dependent electronic properties of band gap [207], which transitions from indirect in multiple layers and bulk MX_2 to direct in monolayer MX_2. Owing to these excellent properties, binary 2D TMCs have recently grown in prominence with their promising applications such as photovoltaics, photodetectors, and field-effect transistors [7,8,203,206].

However, a general problem of binary 2D TMCs, is their fixed properties such as band gaps, which limit their applications in fields such as optoelectronics and photovoltaics where adjustable band gaps are needed to accommodate different wavelength ranges [208-211]. To maximize the efficiency in light-electricity energy conversion, different modification processes such as alloying [7,8], mechanical straining [212], and forming heterostructures [213] have been applied for achieving tunable electronic properties such as band gaps. One of these methods is to obtain van der Waals (vdW) heterostructures by

stacking together two different binary monolayers [214]. Different vdW heterostructures have many applications such as field-effect tunneling transistors [215], photovoltaics [216], and other optoelectronic devices [217]. 2D TMCs based vdW heterostructures have been used in heterojunction photovoltaics. For example, the WS_2/WSe_2 vdW heterostructure, has been investigated via DFT calculations and experiment and shown to be a promising candidate for photovoltaics because of the high light adsorption efficiency and high carrier mobility [218,219]. In addition to vertical vdW heterostructures, lateral heterostructures from two or more TMCs have recently also been predicted by theoretical calculations [220-222] and demonstrated in experiments [219,223].

Apart from forming heterostructures, alloying multiple materials of different elements together to form bulk compositionally complex alloys (CCAs) such as CoCrFeMnNi and Al_xCoCrFeNi [224-227] has been shown to allow for a high tunability in band structures. In contrast to conventional alloys that are comprised of one or two principal elements and of much lower percentages of other elements [37,228], CCAs encompass not only conventional alloys but also high-entropy alloys that have more than five principal elements of equal or near-equal molar ratios [130,229,230]. In CCAs, the composition consisting of multiple elements has fundamental effects on configurational entropy, free energy, phase selection, and stability [229,231]. For example, the increasing of temperature will cause the decrease of Gibbs free energy in the system of high configurational entropy, thus increasing the stability of CCAs [232]. Moreover, despite the complexity in local

atomic structures caused by random distribution of elements in a multinary alloy [233], CCAs with a single solid solution phase and the atoms on the sites of a specific Bravais lattice (e.g., face-centered cubic or body-centered cubic) exhibit many attractive functional properties [228,229,234]. For example, the high electrical conductivity and low thermal conductivity in CCAs such as $Al_xCoCrFeNi$ and Pb-Sn-Te-Se, makes them promising for thermoelectric applications [138,139,141,235]. Furthermore, CCAs such as $FeCoNi(AlSi)_x$ are also promising candidates as soft magnetic materials due to their high saturation magnetization, high electrical resistivity, and high malleability [33]. The presence of several different exchange interactions in CCAs causes sluggish magnetic phase transitions and enhances the magnetocaloric effect (MCE) of these materials [236,237]. In addition, due to their multi-component nature, CCAs such as FeCoNiCuMn of certain stoichiometries have been shown to have a tunable Curie temperature TC that reaches room temperature [237], and the combination of tunable TC and enhanced MCE makes these CCAs attractive as magnetic refrigerant materials [236,237].

More recently, research has emerged focusing on using 2D CCAs such as $Mo_{1-x}W_xS_2$ and $(Al_xGa_{1-x})_{0.5}In_{0.5}P$ in energy conversion applications, such as photovoltaics, photocatalysts, and optoelectronic devices [7,8,238]. The entropic effect benefits the design and fabrication of multiple-component 2D CCAs with similar concentrations of the constituent elements. Instead of conventional 2D materials with fixed structural and electronic properties, this multi-component design opens up opportunities for tunable

properties such as lattice constants and band gaps [239,240]. Desired phases and stoichiometries can be achieved through adjusting the contents of each element to enhance materials properties such as catalytic activity and light conversion efficiency [241]. For example, in order to acquire an optimal range of band gaps and thus optimized absorption coefficients, ternary [242,243], quaternary [244-246], and even penternary [247,248] CCAs have been computationally simulated and fabricated for photovoltaic applications. Moreover, the alloying method is able to modify the lattice constant of CCAs based on their constituent elements. For example, lattice strain can occur in van der Waals heterostructures due to lattice mismatch. The 2D CCAs from alloying with the components of similar crystal structures and in-plane lattice constants can bring in heterostructures and multijunction of the materials with small lattice mismatch, which lowers the interface strain in a heterostructure [249-251].

Quaternary 2D TMC alloys present themselves as potential CCAs due to their multi-elemental composition and high configurational entropy induced by alloying from binary TMCs. Because of tunable structural and electronic properties of multinary TMCs, it is important to investigate the thermodynamically favorable 2D compositionally complex transitional metal chalcogenide alloys (CCTMCAs) for high efficiency energy conversion applications such as photovoltaics, photocatalysts, and optoelectronics, as well as the spintronic applications of random-access memory (RAM) [208,209,252-256]. For example, quaternary 2D CCTMCAs such as $Cd_{1-x}Zn_xO_yS_{1-y}$ are found suitable in photovoltaics

applications because of their high carrier mobilities and suitable range of direct band gaps [257-259]. In photovoltaics, the efficiency of a device is linked to effective carrier masses, which relate to the charger extraction and recombination dynamics and control the open-circuit voltage [210,260,261]. The carrier mobility, as one of the key properties of photovoltaics, depends on both the momentum relaxation time and effective mass, where the momentum relaxation time is inversely linked to the effective mass in lattice scattering [262]. It is shown that a large effective mass results in a decreased charge carrier mobility, which therefore lowers the efficiency of light conversion in photovoltaics [263]. Moreover, quaternary 2D CCTMCAs such as $Cu_2Mo(S_ySe_{1-y})_4$ are proposed as potential photocatalysts [264]. In the process of electrochemical water splitting, the band gap of a 2D CCTMCA determines the acceptable photon frequency during light adsorption, whereas the band alignments of conduction band minimum (CBM) and valence band maximum (VBM) are also considered essential in matching potentials of hydrogen/oxygen evolution reactions (H^+/H_2, H_2O/O_2) energy at different pH levels [254,265]. Additionally, 2D CCTMCAs are also found as potential spintronic applications in spin-logic devices such as RAM for their strong SOC. These functions rely on the controlling of the electron/hole spins, which comes from the metal d-orbital states in the heavy metal atoms in 2D CCTMCAs [256,266,267]. To sum up, 2D CCTMCAs play significant roles in the applications of energy conversion and spintronics. In order to understand the dependency of various properties of 2D CCTMCAs and their effects in those applications, it is essential

to characterize the properties of 2D CCTMCAs such as lattice constants, band alignment, effective carrier masses, spin orbit splitting, and so on.

Different methods like Korringa-Kohn-Rostoker coherent-potential-approximation (KKR-CPA) method and density functional theory (DFT) calculation have been used to study various properties such as lattice parameters, band gap, and band alignment in CCAs [7,213,268]. Reports using the KKR-CPA method to study bulk CCAs have confirmed a reduction in electron mean free path and subsequent decrease in electrical and thermal (from electronic contributions) conductivities with increasing principal elements [232]. Similarly, the KKR-CPA method has been used to study the electronic, magnetic, and transport properties of the Fe-intercalated bulk TaS_2 TMC alloys [269]. DFT calculations, on the other hand, have been widely used in studying the properties of 2D CCTMCAs such as band gaps and phase stability. During DFT calculation, models of random alloy and special quasi-random structure (SQS) are proposed in order to simulate the disorder CCAs. For example, the DFT calculations using a random alloy model have shown tunable band gaps of quaternary $Mo_{1-x}W_xS2_ySe_{2(1-y)}$ 2D CCTMCAs dependent on the composition, which are consistent with the experiment [7]. DFT calculations on the same 2D CCTMCAs have also demonstrated a spinodal decomposition from miscibility gap and the formation of lateral heterostructures at certain compositions of the alloy. This decomposition is also confirmed from experimentally observed phase segregation due to the miscibility gap [213]. Moreover, the combination of DFT using SQS models to study the formation enthalpies of

ternary TMC alloys has shown that $MoSe_{2(1-x)}Te_{2x}$, $WSe_{2(1-x)}Te2x$, $MoS_{2(1-x)}Te_{2x}$, and $WS_{2(1-x)}Te_{2x}$ alloy systems are unstable at 0 K [268].The SQS approach has also been used to form disordered alloy models for ternary 2D CCTMCAs alloys, where using the SQS approach to calculate bowing parameters has shown that the in-plane lattice constant varies almost linearly with changes in the composition of ternary TMC alloys [268]. Comparing to the KKR-CPA method, DFT calculations can predict more accurate structural and electronic properties such as lattice constants, electronic density of states, and band gaps [270-272]. However, when dealing with quaternary 2D CCTMCAs with different compositions, supercells with a number of atoms are required, which makes the DFT calculations very time-consuming. Therefore, alternative methods are desired in efficiently characterizing structural and electronic properties.

Virtual crystal approximation (VCA), as an alternative method to investigate the CCAs of different compositions, has been applied to reduce computational cost while achieving a comparative accuracy to supercell-DFT calculations using an averaged potential from mixing elemental potentials [273]. Specifically, the VCA method provides a convenient and efficient way to model CCAs by generalizing their multi-elemental composition into the weighted average of the individual alloying elements [274]. In comparing to regular DFT calculations of large supercells in investigating multinary CCAs, DFT calculation using VCA method (VCA-DFT) are performed significantly smaller unit cells, offering much greater simplicity and lower computational cost. Namely, calculations

using the VCA model is much faster than the using the SQS model. For example, optimizing the MoWSSe (see below) with the former model and 64 computer cores costs about 35 seconds whereas with the latter costs about 5600 seconds. Note that, as a result of this simplification, VCA neglects any short-range order and local distortions and therefore cannot replicate the fine details of an alloy. The VCA-DFT method as implemented in the Vienna Ab initio Simulation Package (VASP) has found successful applications in studying TMC systems such as $WSe_{2(1-x)}Te_{2x}$ [275]. The VCA-DFT method has also been used to obtain structural properties [276,277], phase determination [278], and electronic properties such as band gaps and effective masses of carriers [279,280], the results of which are all comparable to experiments [281,282]. Therefore, utilizing the VCA-DFT method is helpful in characterizing the CCAs of different compositions, facilitating materials screening and selection for different applications.

In this work, we propose a high-throughput workflow to investigate the properties of 2D CCTMCAs as candidates for various energy and information technology applications such as light conversion and computer logic systems. We use the Mo-W-S-Se, Mo-W-S-Te, and Mo-W-Se-Te 2D CCTMCAs as examples to illustrate the search and selection of 2D CCTMCAs with different structural and electrical properties via VCA-DFT calculations. Meanwhile, we adopt the unit cell and SQS models to benchmark the accuracy of the results from using the VCA-DFT method. We show that the structural and electronic properties of 2D CCTMCAs including in-plane lattice constants, band gaps, effective

carrier masses, spin-orbital splitting, and band alignment are in good agreement with the DFT calculations based on the unit-cell (unit-cell-DFT) and SQS (SQS-DFT) models. We then select nine ternary and three quaternary 2D CCTMCAs to investigate the stability using the metrics of formation energy and Gibbs free energy. We then focus on the three quaternary 2D CCTMCAs, $Mo_{0.5}W_{0.5}SSe$, $Mo_{0.5}W_{0.5}STe$, and $Mo_{0.5}W_{0.5}SeTe$, which are found to be able to form type II band alignments with other quaternary 2D CCTMCAs, owing to their high configuration entropy. These three quaternary 2D CCTMCAs have negative Gibbs free energies at 300 K, serving as good examples as entropy-stabilized multinary 2D alloys. Additionally, $Mo_{0.5}W_{0.5}SSe$, $Mo_{0.5}W_{0.5}STe$, and $Mo_{0.5}W_{0.5}SeTe$ show high electrical conductivity at room temperature (300 K), making them possible to be utilized in energy conversion applications. Given that many multinary 2D materials are being successfully synthesized, our work serves as an example of placing these 2D materials in the context of 2D high-entropy alloys (HEAs). In doing so, one gains not only novel perspectives but also an extra degree to freedom (entropy) to control the stability. Furthermore, we show in this work that the VCA model is suitable for modeling multinary 2D alloys with a balanced tradeoff between accuracy and efficiency, opening up a wide range of opportunities for studying other multinary 2D alloys.

4.3 Simulation Methods

We apply the VCA-DFT method in the Vienna Ab Initio Package (VASP) [283] to study the Mo-W-S-Se, Mo-W-S-Te, and Mo-W-Se-Te 2D CCTMCAs, $Mo_yW_{1-y}S_{2x}Se_{2(1-x)}$,

$Mo_yW_{1-y}S_{2x}Te_{2(1-x)}$, and $Mo_yW_{1-y}Se_{2x}Te_{2(1-x)}$, with x and y ranging from 0 to 1 at an incremental step of 0.05. The range of x and y results in three sets of 441 quaternary 2D CCTMCAs. Figure 4.1(a) illustrates the structure model from the VCA method, and Figure 4.1(b) and (c) display a 4 × 4 × 1 SQS supercell obtained from the ATAT package [284]. We perform all the calculations using VASP, and the plane waves of kinetic energies smaller than 500 eV are included in the basis sets. We use the standard projector augmented wave (PAW) potential files [80,81] for Mo, W, S, Se, and Te. The Perdew-Burke-Ernzerhof (PBE) functional [79] in DFT is well known to underestimate band gaps [285,286]. If more advanced theories accounting for many-body effects that are missing in the PBE functional are used, the theoretical band gaps will generally be higher. The PBE calculated optical band gaps of WSSe and MoSSe agree well with the experimental band gaps [287]. We use a Monkhorst-Pack [82] 15 × 15 × 1 *k*-point grid. The in-plane lattice constants and atomic coordinates of all systems are fully optimized using a quasi-Newton algorithm with the force convergence criterion of 0.01 eV/Å. We calculate the band structures along the Γ→M→K→Γ special *k*-point path (each line segment has 40 *k* points), where we extract the band gaps and effective carrier masses. We also calculate effective electron and hole masses using the Sumo package [288] and report the averaged effective masses in the K-M and K-Γ directions. To calculate the spin-orbit splitting magnitude, we include SOC in the calculations. We calculate the electrical conductivities of three quaternary 2D CCTMCAs using the BoltzTraP module as implemented in the Pymatgen library [162,289].

Calculations using the VCA model is much faster than the using the SQS model. For example, optimizing the MoWSSe with the former model and 64 computer cores costs about 35 seconds whereas with the latter costs about 5600 seconds.

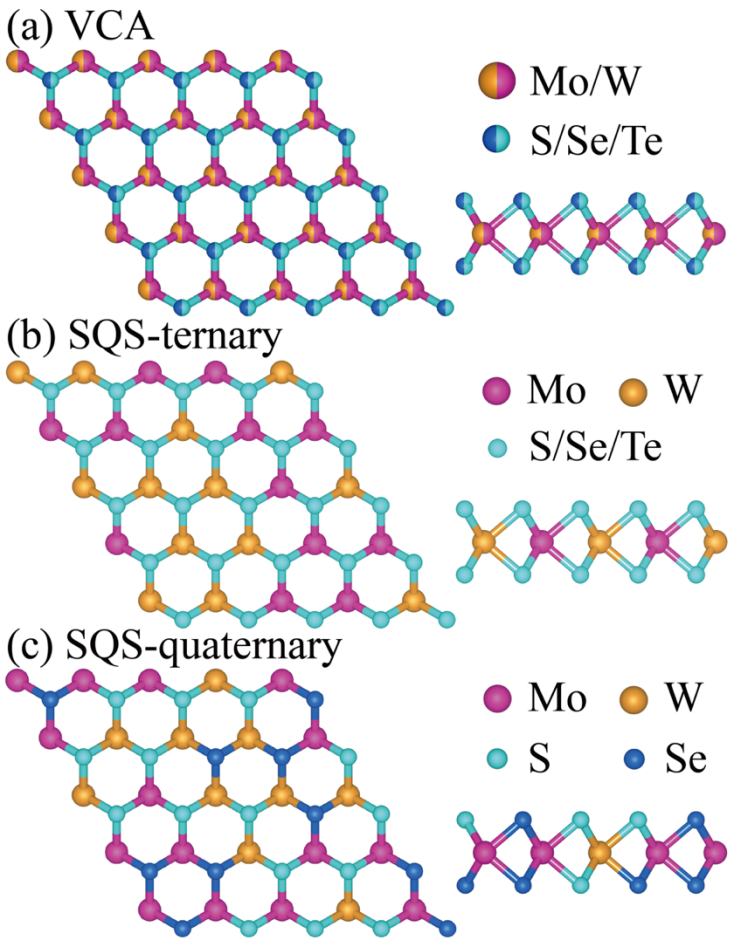

Figure 4.1. Top and side views of the atomic structure of 2D CCTMCAs based on (a) the VCA method, and (b) and (c) the SQS method for ternary and quaternary 2D CCTMCAs, respectively.

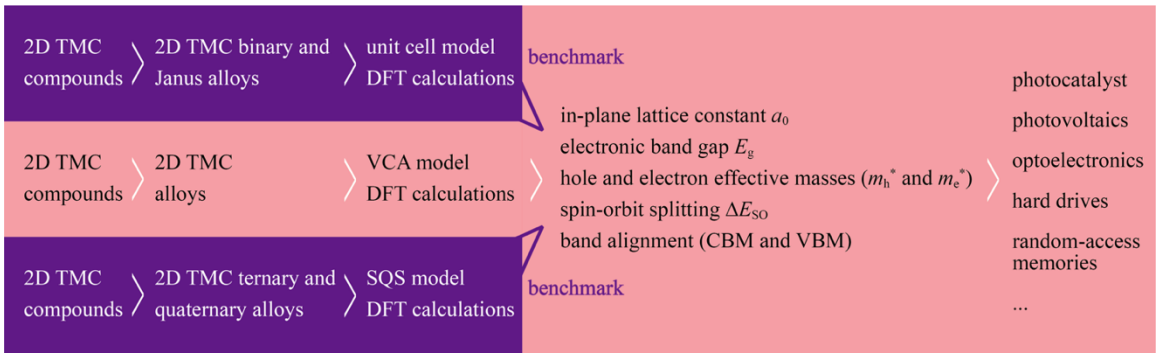

Figure 4.2. High-throughput workflow for designing 2D CCTMCAs.

Many previous computational studies have shown that 2D TMCs have potential in energy conversion and spintronic applications due to their excellent structural and electronic properties [208,209,252-256]. However, a systematic workflow that can be applied to search for materials for various applications in an efficient manner is lacking. In order to efficiently discover those materials from 2D TMCs, we propose a workflow (see Figure 4.2) that utilizes VCA-DFT to obtain essential structural and electronic properties. The workflow consists of firstly proposing several simple binary TMC compounds. Different alloying 2D CCTMCAs can thus be generated by the combination of the binary compounds. Then the workflow applies DFT calculations using the averaged pseudopotential of corresponding elements to characterize the VCA model. We compute five essential properties for selecting materials in various applications, which are in-plane lattice constant, band gap, hole and electron effective masses, spin-orbital splitting, and band alignment of CBM and VBM. Due to lack of Bloch bands, the effective masses reported here are meant to be comparable to the effective masses originated from the effect

band structure that can be obtained from calculations using periodic supercells. Therefore, at the same time, the reliability and accuracy of the calculation process is cross examined by benchmarking DFT calculations using unit-cell and SQS models. We use three-atom unit cells to model the binary MX_2 and Janus MXY ($X \neq Y$ = S, Se, or Te) structures of TMCs, whereas for the complex ternary and quaternary 2D CCTMCAs, we create SQS supercells to simulate the disordered structures. Specifically, we validate our VCA-DFT calculations using six binary TMC unit cells and six Janus unit cells, as well as three ternary SQS supercells and three quaternary SQS supercells with special stoichiometries that are $Mo_{0.5}W_{0.5}S_2$, $Mo_{0.5}W_{0.5}Se_2$, $Mo_{0.5}W_{0.5}Te_2$, $Mo_{0.5}W_{0.5}SSe$, $Mo_{0.5}W_{0.5}STe$, and $Mo_{0.5}W_{0.5}SeTe$.

4.4 Results and Discussion

4.4.1 Benchmark calculations of the VCA-DFT model

We perform VCA-DFT calculations to obtain five essential structural and electronic properties including the in-plane lattice constant, band gap, hole and electron effective masses, spin-orbit splitting, and band alignment, in order to search for suitable 2D CCTMCAs in potential applications of energy conversion and spin-logic devices. First of all, the in-plane lattice constant of a 2D material is a fundamental parameter in describing the monolayer geometry. Besides, the lattice constants of 2D CCTMCAs are helpful to understand the composition-dependent lattice change, which is important in considering the lattice matching of two different 2D CCTMCAs during designing the 2D stacked

heterostructure, in order to avoid the misfit and change of the crystal structure. Secondly, it is essential to tune band gaps to fit in the range of photonic frequency of different light sources in light adsorption devices in photovoltaics and photocatalysts. An appropriate band gap range matching photonic frequency increases the efficiency of harvesting light energy. Thirdly, effective masses of electrons and holes are critical in predicting carrier optical response and transport property of semiconductors [290,291]. The effective masses also determines the effective density of states, which further impacts the open circuit voltage [263]. Fourthly, 2D Group-VI TMCs, such as MoS_2, $MoSe_2$, WS_2, and WSe_2, have been heavily investigated as potential materials in the field of spintronics and valleytronics due to their broken inversion symmetry [292-295]. These 2D materials contain two inequivalent valleys that occur at the +K and –K points at the edges of the first Brillouin zone, and time reversal symmetry in TMCs causes spin splitting with opposite spin signs at the +K and –K valleys, resulting from strong SOC in TMCs [292]. Due the broken inversion symmetry in TMCs, this coupling between spin and valley pseudospin causes the splitting of valence bands [292], and in MoS_2 specifically, SOC interactions have been shown to split the valence bands by around 0.16 eV [293,294]. The strong SOC in TMCs has been shown to allow for higher spin and valley polarization lifetime along with the manipulation of spin through valley properties [292]. Finally, band alignment describes an electronic property about a material's light conversion efficiency. In the design of thin film photovoltaics, the adjustment of conduction band alignment to a desired range is regarded

as one of the most important factors to reach a high conversion efficiency [296,297]. Specifically, in combining two materials for photovoltaics, a heterojunction between p-type and n-type semiconductors needs to be utilized to provide a type II band alignment to provide pathways for exciton diffusion, separation, and dissociation, and carrier transportation [298-301].

Following the above high-throughput procedure, we begin with computing the five properties of MX_2 (M = Mo, W; X = S, Se, or Te) using unit-cell-DFT calculation as a benchmark to the corresponding VCA-DFT results. All 2D MX_2 in this work are assumed to adopt the 2*H* phase. Table 4.1 lists these calculated properties for the six MX_2. We can see that the VCA-DFT method leads to identical results compared to the DFT results using a 3-atom unit cell. We also include the results from the literature for comparison. The VCA-DFT values for the five properties also agree well with previous studies. For example, the in-plane lattice constants and band gaps of MoS_2 (WSe_2) 3.18 Å (3.32 Å) and 1.67 eV (1.55 eV) from our VCA-DFT calculations, are nearly identical to 3.18 Å (3.32 Å) and 1.68 eV (1.53 eV) in the Refs. [302,303]. We also notice that the in-plane lattice constants of the six binary TMCs share three values, 3.18, 3.32, and 3.55 Å, where the binary TMCs of same chalcogen element have the same lattice constants. This is understood by the large difference in the anion radii of S^{2-} (1.70 Å), Se^{2-} (1.84 Å), and Te^{2-} (2.07 Å), whereas the cations of Mo^{4+} and W^{4+} possess similar ionic radii of 0.79 and 0.80 Å, respectively [304]. Moreover, the discrepancy in the covalent radii between Mo (1.54 Å) and W (1.62 Å) is

also smaller than that among S (1.05 Å), Se (1.20 Å), and Te (1.38 Å) [305]. For the CBM and VBM, the VCA-DFT results match well with other DFT calculation results at the PBE level. Additionally, the CBM values of $MoTe_2$, WS_2, and WSe_2 are closer to the DFT calculation results in Ref. [306] using the PBE functional including SOC.

Table 4.1. In-plane lattice constant a_0, band gap E_g, hole and electron effective masses m_h^* and m_e^*, spin-orbit splitting ΔE_{SO}, conduction band minimum (CBM) and valencene band maximum (VBM) with reference to the vacuum level of MX_2 with the 2*H* structure. The first row of each property is obtained from using the VCA-DFT method, whereas the second row is from the literature.

	MoS_2	$MoSe_2$	$MoTe_2$	WS_2	WSe_2	WTe_2
a_0 (Å)	3.18	3.32	3.55	3.18	3.32	3.55
	3.18[a]	3.32[b]	3.55[c]	3.18[b]	3.32[b]	3.55[d]
E_g (eV)	1.67	1.44	1.08	1.81	1.54	1.07
	1.68 [b]	1.43[b]	1.06[b]	1.81[b]	1.53[b]	1.08[e]
m_h^* (m_0)	0.59	0.66	0.71	0.43	0.46	0.44
	0.58[f]	0.67[f]	0.70[f]	0.42[g]	0.51[g]	0.42[h]
m_e^* (m_0)	0.49	0.56	0.58	0.32	0.35	0.33
	0.49[f]	0.56[f]	0.57[f]	0.31[g]	0.39[g]	0.33[h]
ΔE_{SO}	0.15	0.19	0.22	0.43	0.47	0.48
	0.15[i]	0.19[i]	0.22[i]	0.43[i]	0.47[i]	0.49[i]

CBM	-4.27	-3.89	-3.80	-3.89	-.3.56	-3.63
	-4.29[j]	-3.89[j]	-3.74[j]	-4.09[j]	-3.69[j]	-3.61[j]
VBM	-5.94	-5.33	-4.89	-5.70	-5.11	-4.70
	-5.98[j]	-5.31[j]	-4.84[j]	-5.87[j]	-5.20[j]	-4.72[j]

[a]Ref. [302]; [b]Ref. [303]; [c]Ref. [307]; [d]Ref. [245]; [e]Ref. [308]; [f]Ref. [309]; [g]Ref. [310]; [h]Ref. [311]; [i]Ref. [312]; [j]Ref. [313]

Table 4.2. In-plane lattice constant a_0, band gap E_g, hole and electron effective masses m_h^* and m_e^*, spin-orbit splitting ΔE_{SO}, conduction band minimum (CBM) and valencene band maximum (VBM) with reference to the vacuum level of Janus *MXY* with the 2*H* structure. The first row of each property is obtained from using the VCA-DFT method, whereas the second row is from using three-atom unit cells to simulate monolayer Janus structures.

	MoSSe	WSSe	MoSTe	WSTe	MoSeTe	WSeTe
a_0 (Å)	3.26	3.26	3.40	3.39	3.45	3.47
	3.25	3.25	3.36	3.36	3.43	3.43
E_g (eV)	1.54	1.66	1.31	1.40	1.23	1.29
	1.56	1.69	1.03	1.24	1.27	1.35
m_h^* (m_0)	0.64	0.45	0.73	0.49	0.73	0.49
	0.68	0.48	5.51	3.67	0.84	0.55
m_e^* (m_0)	0.54	0.35	0.62	0.38	0.61	0.37
	0.54	0.36	0.71	0.47	0.64	0.39

ΔE_{SO}	0.17	0.45	0.21	0.49	0.21	0.49
	0.17	0.44	0.19	0.42	0.20	0.46
CBM	-3.94	-3.59	-3.79	-3.49	-3.86	-3.59
	-4.07	-3.70	-4.04	-3.70	-3.84	-3.57
VBM	-5.48	-5.25	-5.10	-4.88	-5.09	-4.88
	-5.63	-5.40	-5.07	-4.94	-5.11	-4.91

Many previous studies suggested that the VCA-DFT calculation is applicable to disordered semiconductor alloys [314,315], but this method does not consider the effects of lattice relaxation and assumes that the atoms are fixed at the ideal lattice sites [316]. We further benchmark VCA-DFT calculation by using the DFT calculation from unit cell models for Janus structure and SQS supercells for ternary structures (see Table 4.2 and Table 4.3) and quaternary systems (see Table 4.4) to ensure that the VCA-DFT results are consistent. Based on our results of VCA-DFT versus unit-cell-DFT and SQS-DFT calculations, the VCA-DFT method leads to comparable results such as lattice constants, band gaps, spin-orbital splitting, and band alignments with the unit-cell-DFT and SQS-DFT results. The results from VCA-DFT calculations of binary and ternary CCTMCAs are also comparable to those recorded in the Computational 2D Materials Database (C2DB) [317]. Some exceptions happen during validating the band gap and effective hole mass in

the Janus MoSTe and WSTe structures, where the VCA-DFT calculations lead to the inconsistent conduction band as CBM, effective hole mass, and band gap compared to the DFT calculation using the unit cell models. Because its use of the averaged potential, the VCA-DFT is not always capable of predicting the local atomic environment [278,318,319], where a large difference in ionicity could result in low accuracy in predicting the electronic properties such as band alignment and band gap [319]. Moreover, when using the VCA-DFT in ground state calculation, the prediction of formation energy of 2D CCTMCAs shows the discrepancy from the SQS-DFT calculated result. Therefore, it is essential to use the unit-cell and SQS models to benchmark the VCA-DFT results. This not only validates the accuracy of VCA-DFT calculations on 2D CCTMCAs but also provides an indication when there is deviation in VCA-DFT results.

Table 4.3. In-plane lattice constant a_0, band gap E_g, hole and electron effective masses m_h^* and m_e^*, spin-orbit splitting ΔE_{SO}, conduction band minimum (CBM) and valencene band maximum (VBM) with reference to the vacuum level of ternary 2D CCTMCAs with the 2*H* structure. The first row of each property is obtained from using the VCA-DFT method, whereas the second row is from using 48-atom SQS supercells of monolayer ternary structures.

	$Mo_{0.5}W_{0.5}S_2$	$Mo_{0.5}W_{0.5}Se_2$	$Mo_{0.5}W_{0.5}Te_2$
a_0 (Å)	3.18	3.32	3.55
	3.18	3.32	3.55
E_g (eV)	1.74	1.50	1.09

	1.71	1.46	1.06
m_h^* (m_0)	0.51	0.56	0.57
	0.49	0.51	0.55
m_e^* (m_0)	0.40	0.46	0.44
	0.33	0.38	0.44
ΔE_{SO}	0.29	0.33	0.35
	0.29	0.30	0.24
CBM	-4.11	-3.73	-3.72
	-4.12	-3.76	-3.73
VBM	-5.84	-5.23	-4.81
	-5.83	-5.22	-4.79

Table 4.4. In-plane lattice constant a_0, band gap E_g, hole and electron effective masses m_h^* and m_e^*, spin-orbit splitting ΔE_{SO}, conduction band minimum (CBM) and valencene band maximum (VBM) with reference to the vacuum level of quaternary 2D CCTMCAs with the 2*H* structure. The first row of each property is obtained from using the VCA-DFT method, whereas the second row is from using 48-atom SQS supercells of monolayer quaternary structures.

	$Mo_{0.5}W_{0.5}SSe$	$Mo_{0.5}W_{0.5}STe$	$Mo_{0.5}W_{0.5}SeTe$
a_0 (Å)	3.26	3.40	3.45
	3.25	3.35	3.43
E_g (eV)	1.60	1.35	1.26
	1.57	1.29	1.23
m_h^* (m_0)	0.54	0.61	0.61
	0.52	0.53	0.55
m_e^* (m_0)	0.44	0.49	0.48
	0.49	0.59	0.37
ΔE_{SO}	0.31	0.35	0.36
	0.29	0.20	0.25
CBM (eV)	-5.37	-5.00	-4.99
	-5.48	-5.04	-4.93
VBM (eV)	-3.76	-3.64	-3.72
	-3.90	-3.75	-3.69

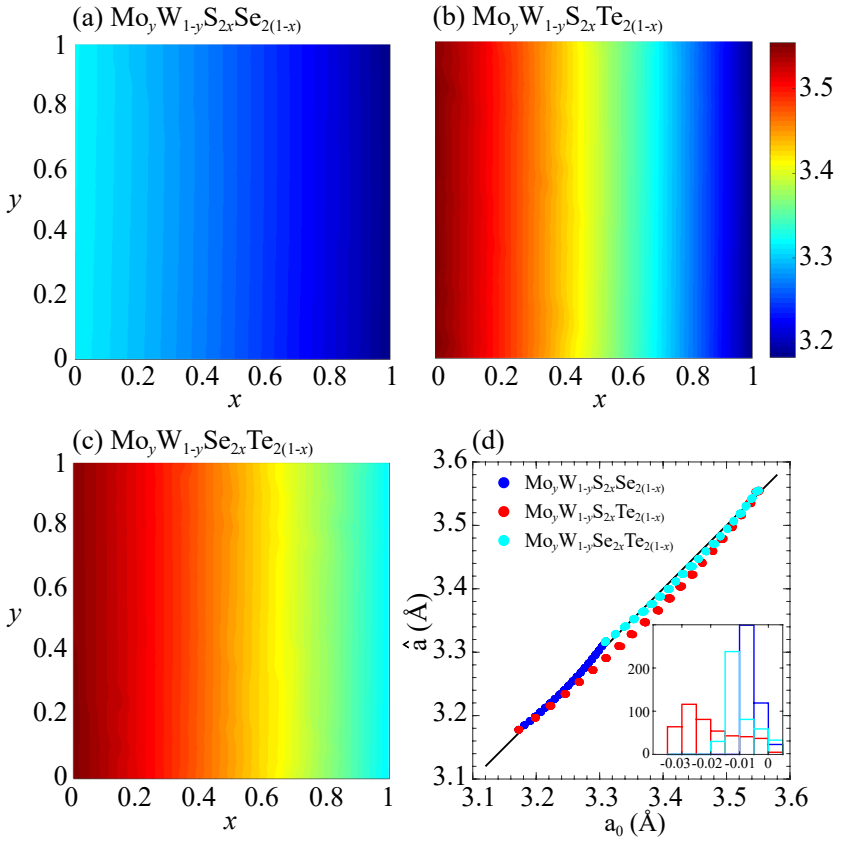

Figure 4.3. In-plane lattice constants of (a) $Mo_yW_{1-y}S_{2x}Se_{2(1-x)}$, (b) $Mo_yW_{1-y}S_{2x}Se_{2(1-x)}$, and (c) $Mo_yW_{1-y}Se_{2x}Te_{2(1-x)}$ 2D CCTMCAs calculated with the PBE functional. (d) Comparison between the in-plane lattice constants from the VCA-DFT method and from the estimation in Eq.4.2.

4.4.2 Structural and electrical properties of general CCTCMAs

Figure 4.3(a)-(c) displays the in-plane lattice constants of 2D CCTMCAs $Mo_yW_{1-y}S_{2x}Se_{2(1-x)}$, $Mo_yW_{1-y}S_{2x}Te_{2(1-x)}$, and $Mo_yW_{1-y}Se_{2x}Te_{2(1-x)}$, and the range of in-plane lattice constants for each set of 2D CCTMCAs is summarized in Table 4.5. Consistent with the trend shown in Table 4.5, the in-plane lattice constants strongly depend on the content (x) of chalcogen, while the change in the content of transitional metal (y) almost has no effect.

To further investigate the relationship between the composition and the lattice constant, we hypothesize the following chemical reaction:

$$\mathrm{Mo}_y\mathrm{W}_{1-y}\mathrm{S}_{2x}\mathrm{Se}_{2(1-x)} \rightarrow xy\mathrm{MoS}_2 + (1-x)y\mathrm{MoSe}_2 + x(1-y)\mathrm{WS}_2 + (1-x)(1-y)\mathrm{WSe}_2 \quad (4.1)$$

We the adopt Vegard's law [320] to link the 2D CCTMCAs with binary TMCs in Eq.4.1 and summarize the relationship between lattice constants $\hat{a}$ of quaternary 2D CCTMCAs (e.g., $Mo_yW_{1-y}S_{2x}Se_{2(1-x)}$) and binary TMCs (e.g., MoS_2, $MoSe_2$, WS_2, or WSe_2). As an example, the lattice constant of a quaternary compound $Mo_yW_{1-y}S_{2x}Se_{2(1-x)}$ can be written as

$$\hat{a} = xya_{\mathrm{MoS}_2} + (1-x)ya_{\mathrm{MoSe}_2} + x(1-y)a_{\mathrm{WS}_2} + (1-x)(1-y)a_{\mathrm{WSe}_2} \quad (4.2)$$

That is, the lattice constants of quaternary 2D CCTMCAs can be approximated as the combination of compositionally dependent lattice constants of the binary TMCs. Figure 4.3(d) compares a_0 from VCA-DFT calculations and $\hat{a}$ from Eq. 4.2. In the inset, we show the distribution of the deviation between two sets of data. The results from these two methods agree well with each other, with average deviations of 0.006, 0.020, and 0.010 Å for these three 2D CCTMCAs, respectively.

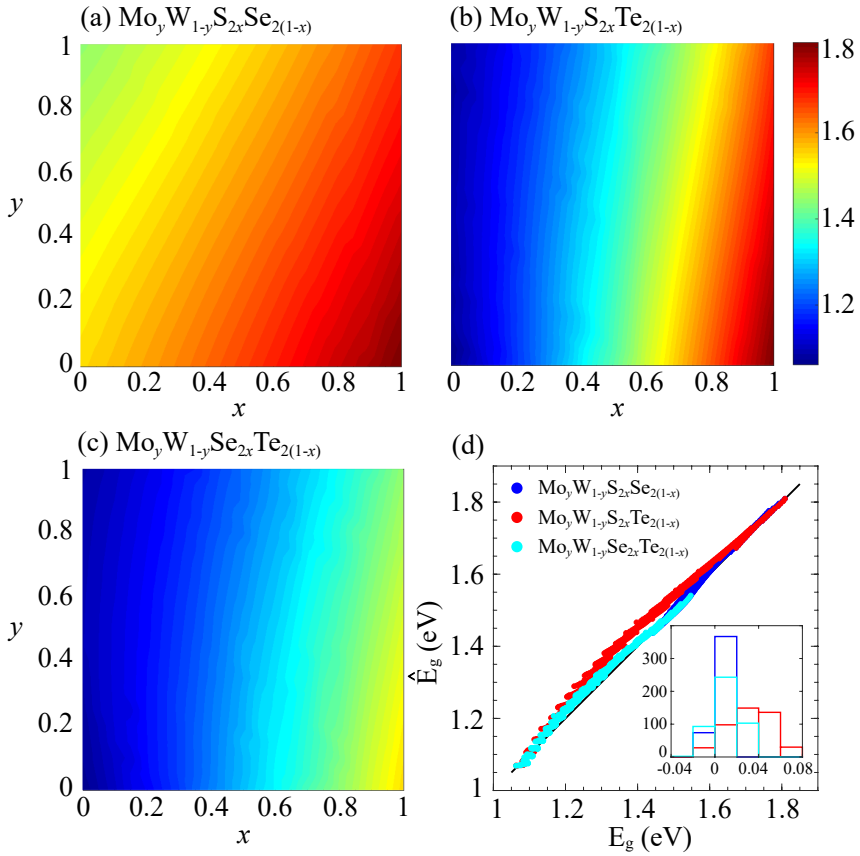

Figure 4.4. Band gaps of (a) $Mo_yW_{1-y}S_{2x}Se_{2(1-x)}$, (b) $Mo_yW_{1-y}S_{2x}Se_{2(1-x)}$, $Mo_yW_{1-y}S_{2x}Te_{2(1-x)}$, and (c) $Mo_yW_{1-y}Se_{2x}Te_{2(1-x)}$ 2D CCTMCAs calculated with the PBE functional. (d) Comparison between the band gaps from the VCA-DFT method and from the estimation in Eq. 4.3.

Figure 4.4(a)-(c) display the band gaps of 2D CCTMCAs Mo-W-S-Se, Mo-W-S-Te, and Mo-W-Se-Te, which show that the band gaps range from 1.44 ~ 1.81 eV, 1.06 ~ 1.81 eV, and 1.06 ~ 1.55 eV, for the Mo-W-S-Se, Mo-W-S-Te, and Mo-W-Se-Te 2D CCTMCAs, respectively. We again apply Vegard's law [320] to estimate the band gaps of 2D CCTMCAs by using the band gaps of binary TMCs (see Table 4.1). Similar to Eq. 4.2, we can write the formula for the band gap using the binary TMCs. For example, for the Mo-

W-S-Se 2D CCTMCAs, their band gaps can be written as,

$$E_{\mathrm{g}} = xyE_{\mathrm{g,MoS_2}} + (1-x)yE_{\mathrm{g,MoSe_2}} + x(1-y)E_{\mathrm{g,WS_2}} + (1-x)(1-y)E_{\mathrm{g,WSe_2}} \quad (4.3)$$

and the other two 2D CCTMCA systems have the similar formulas. Figure 4.4(d) compares the band gaps resulted from VCA-DFT calculations and from Eq.4.3. As can be seen, the calculated band gaps of the Mo-W-S-Se, Mo-W-S-Te, and Mo-W-Se-Te 2D CCTMCAs from the two methods are nearly identical, with the average deviations of merely 0.007, 0.039, and 0.011 eV respectively. This consistency indicates that using VCA-DFT can lead to reliable lattice constants and band gaps of 2D CCTMCAs in an efficient way.

The diverse lattice constants and band gaps of 2D CCTMCAs are essential for various applications such as in the design of heterostructures for light harvesting [242,321]. For example, the growth of heterostructures requires a lattice match between a 2D CCTMCA as the substrate layer and another 2D CCTMCA grown on the substrate. The matching in lattice constants of two monolayers of 2D CCTMCAs is beneficial for reducing the bilayer strain, whereas the wide band gap ranges of 2D CCMTCAs could also be helpful in maximizing the light conversion efficiency for many applications [268,322]. Figure 4.5 depicts the relationship between lattice constants and band gaps of the three 2D CCTMCAs. We know from the plot that there are majorly two regions based on heterostructure lattice matching, bounded by three edges of MoS_2/WS_2, $MoSe_2/WSe_2$, and $MoTe_2/WTe_2$ to the

left, middle, and right edges. The two regions correspond to $Mo_yW_{1-y}S_{2x}Se_{2(1-x)}/Mo_yW_{1-y}S_{2x}Te_{2(1-x)}$, and $Mo_yW_{1-y}Se_{2x}Te_{2(1-x)}/Mo_yW_{1-y}S_{2x}Te_{2(1-x)}$ heterostructures, respectively. The lattice constant and band gap distributions of three 2D CCTMCAs in Figure 4.5 therefore provides guidance in designing heterostructures (see below) from a pair of 2D CCTMCA monolayers in order to minimize the lattice mismatch as well as to maintain the desired band offset value.

Table 4.5. Ranges of in-plane lattice constant a_0, band gap E_g, hole and electron effective masses m_h^* and m_e^*, spin-orbit splitting ΔE_{SO}, conduction band minimum (CBM) and valencene band maximum (VBM) with reference to the vacuum level of quaternary 2D CCTMCAs with the 2*H* structure.

	$Mo_yW1\text{-}yS_{2x}Se_{2(1-x)}$	$Mo_yW_{1-y}S_{2x}Te_{2(1-x)}$	$Mo_yW_{1-y}Se_{2x}Te_{2(1-x)}$
a_0 (Å)	3.18 ~ 3.32	3.18 ~ 3.55	3.32 ~ 3.55
Eg (eV)	1.44 ~ 1.81	1.06 ~ 1.81	1.06 ~ 1.55
m_h^* (m_0)	0.43 ~ 0.67	0.43 ~ 0.73	0.44 ~ 0.73
m_e^* (m_0)	0.32 ~ 0.57	0.32 ~ 0.62	0.32 ~ 0.61
ΔE_{SO}	0.15 ~ 0.47	0.15 ~ 0.49	0.19 ~ 0.49
CBM (eV)	-4.27 ~ -3.55	-4.32 ~ -3.46	-3.94 ~ -3.56
VBM (eV)	-5.94 ~ -5.10	-5.94 ~ -4.68	-5.33 ~ -4.70

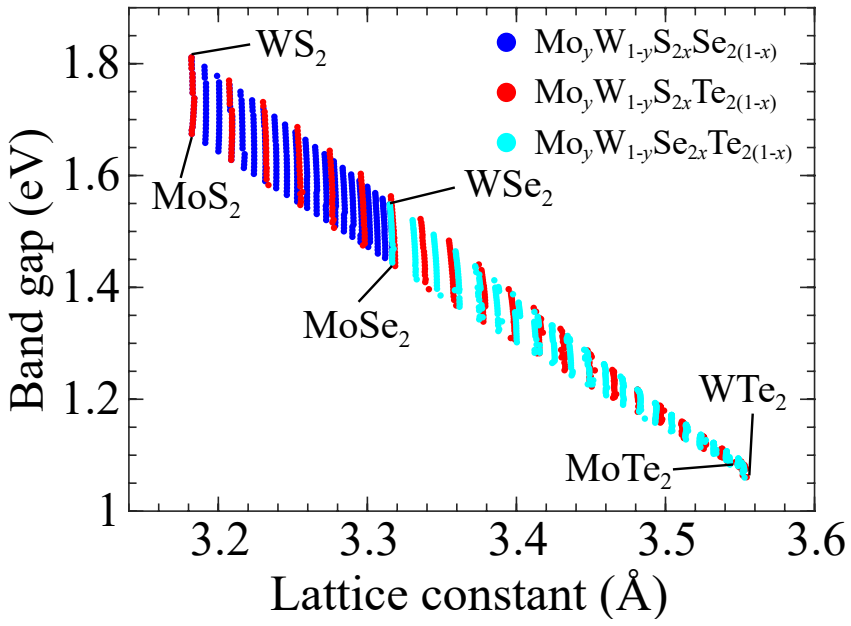

Figure 4.5. Relation between the predicted band gaps and the lattice constants of three sets of 2D CCTMCAs calculated with the PBE functional.

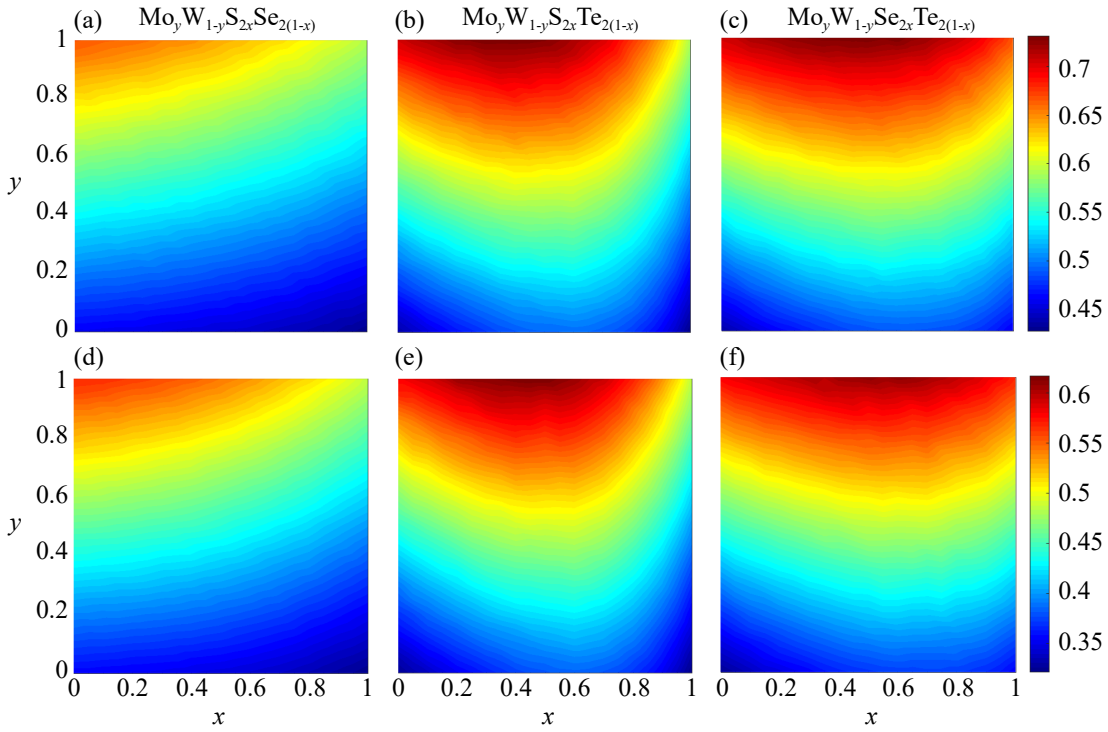

Figure 4.6. Hole effective masses of (a) $Mo_yW_{1-y}S_{2x}Se_{2(1-x)}$, (b) $Mo_yW_{1-y}S_{2x}Se_{2(1-x)}$,

$Mo_yW_{1-y}S_{2x}Te_{2(1-x)}$, and (c) $Mo_yW_{1-y}Se_{2x}Te_{2(1-x)}$ 2D CCTMCAs, calculated with the PBE functional. The corresponding electron effective masses are shown in (d), (e), and (f).

Figure 4.6 displays the hole and electron effective masses of 2D CCTMCAs. The four corners of Figure 4.6(a) stand for the effective carrier masses of MoS_2, $MoSe_2$, WS_2, and WSe_2. We observe that increasing the W content (i.e., decreasing y while x is fixed) generally reduces the effective masses. For the Mo-W-S-Se 2D CCTMCAs, increasing the Se content lowers the effective masses of both electrons and holes. The relationship between the effective masses and two anion contents (x and 1-x value) is complicated in the other two 2D CCTMCAs. The lower effective carrier mass is found at the two regions of x close to 0 and x close to 1, where one of the chalcogens dominates in the 2D CCTMCAs. For example, in the Mo-W-S-Te 2D CCTMCAs, the effective carrier mass first increases as the content of S increases from 0 to 0.6, and then decreases as the content of S further increases up to 1.0. In designing heterostructures, low effective masses are beneficial to enhance the carrier transport and thus improve the collected photocurrent during the light harvesting process [263,323,324]. However, too small effective carrier masses are associated with a large curvature of electronic dispersion and thus sharp band edges, affecting the local density of states. As a result, the overall collected photocurrent will decrease, thus degrading the efficiency of light conversion [325]. Therefore, small effective carrier masses and local carrier concentration are competing with each other to maintain an optimal light conversion of photovoltaics and photocatalysts. The compositional

variation of 2D CCTMCAs results in the tunable effective mass ranges for both electrons and holes. The design using compositionally complex systems offers a promising method in adjusting the effective carrier mass for efficient light adsorption devices.

Figure 4.7 shows the calculated spin-orbit splitting of 2D CCTMCAs. Compared to monolayer MoS_2, which has a ΔE_{SO} of 0.15 eV [312], the 2D CCTMCAs generally can have higher values of ΔE_{SO} and up to more than three times of the value of MoS_2. As a proposed candidate for spintronics devices, graphene shows a ΔE_{SO} of about 0.01 eV [326], which is much lower than those of the 2D CCTMCAs, suggesting that the 2D CCTMCAs has the potential in spintronic applications for spin-logic devices such as RAM [327]. Strong spin-orbit splitting and its insensitivity to anion species in 2D CCTMCAs results from the presence of out-of-plane mirror symmetry and absence of inversion symmetry [328,329]. As a consequence, the resulting electric field is generated in the plane of cations causing electrons to move in the same plane. The SOC interactions split the energy degeneracy of these electrons and the splitting magnitude depends on only the atomic numbers of the cation species (Mo and W, and the latter is much heavier, so is the stronger SOC and ΔE_{SO}). Figure 4.7 also reveals that ΔESO is more dependent on the content of cations than that of anions. By increasing the content of the cations, e.g., reducing y, the ΔE_{SO} increases rapidly from 0.15 eV to nearly 0.50 eV. By contrast, increasing x does not alter ΔE_{SO} as much as change y. The strong spin-orbit splittings of 2D CCTMCAs suggest the possibility of utilizing them for spintronic applications. This is understood from the

source of SOC from the interaction between electron and magnetic field induced by the nucleus spin. Because the magnetic field is directly related to the charge from the nucleus, a larger atomic number will have a stronger SOC [328,330,331].

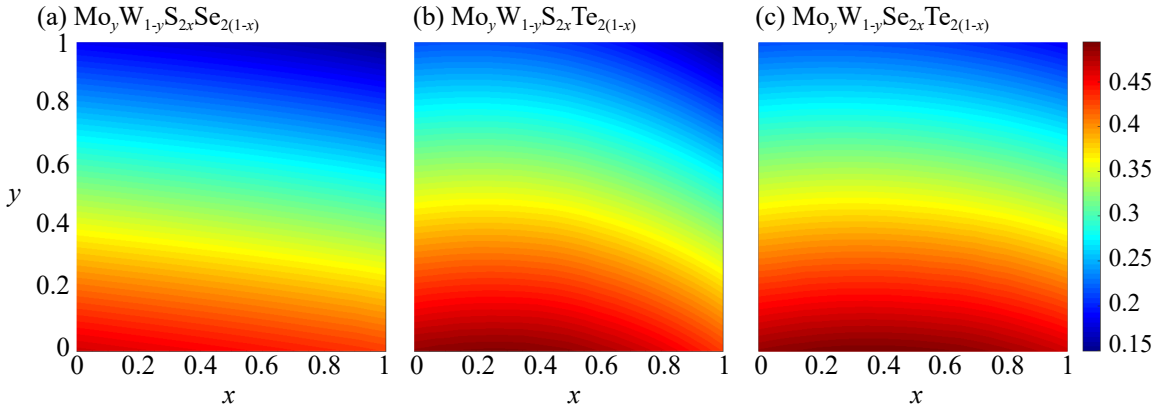

SFigure 4.7. Spin-orbit splitting of (a) $Mo_yW_{1-y}S_{2x}Se_{2(1-x)}$, (b) $Mo_yW_{1-y}S_{2x}Se_{2(1-x)}$, $Mo_yW_{1-y}S_{2x}Te_{2(1-x)}$, and (c) $Mo_yW_{1-y}Se_{2x}Te_{2(1-x)}$ 2D CCTMCAs calculated with the PBE functional.

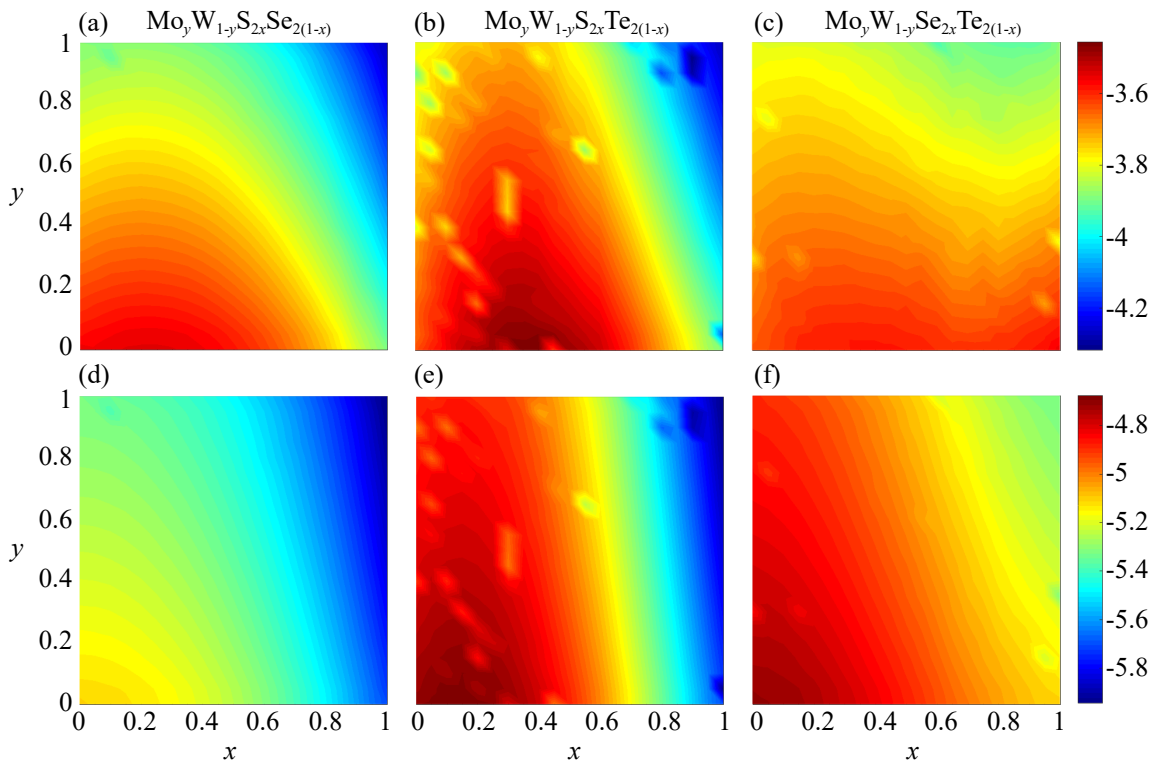

Figure 4.8. Conduction band minima of (a) $Mo_yW_{1-y}S_{2x}Se_{2(1-x)}$, (b) $Mo_yW_{1-y}S_{2x}Se_{2(1-x)}$, $Mo_yW_{1-y}S_{2x}Te_{2(1-x)}$, and (c) $Mo_yW_{1-y}Se_{2x}Te_{2(1-x)}$ 2D CCTMCAs. The corresponding valence band maxima are shown in (d), (e), and (f), calculated with the PBE functional.

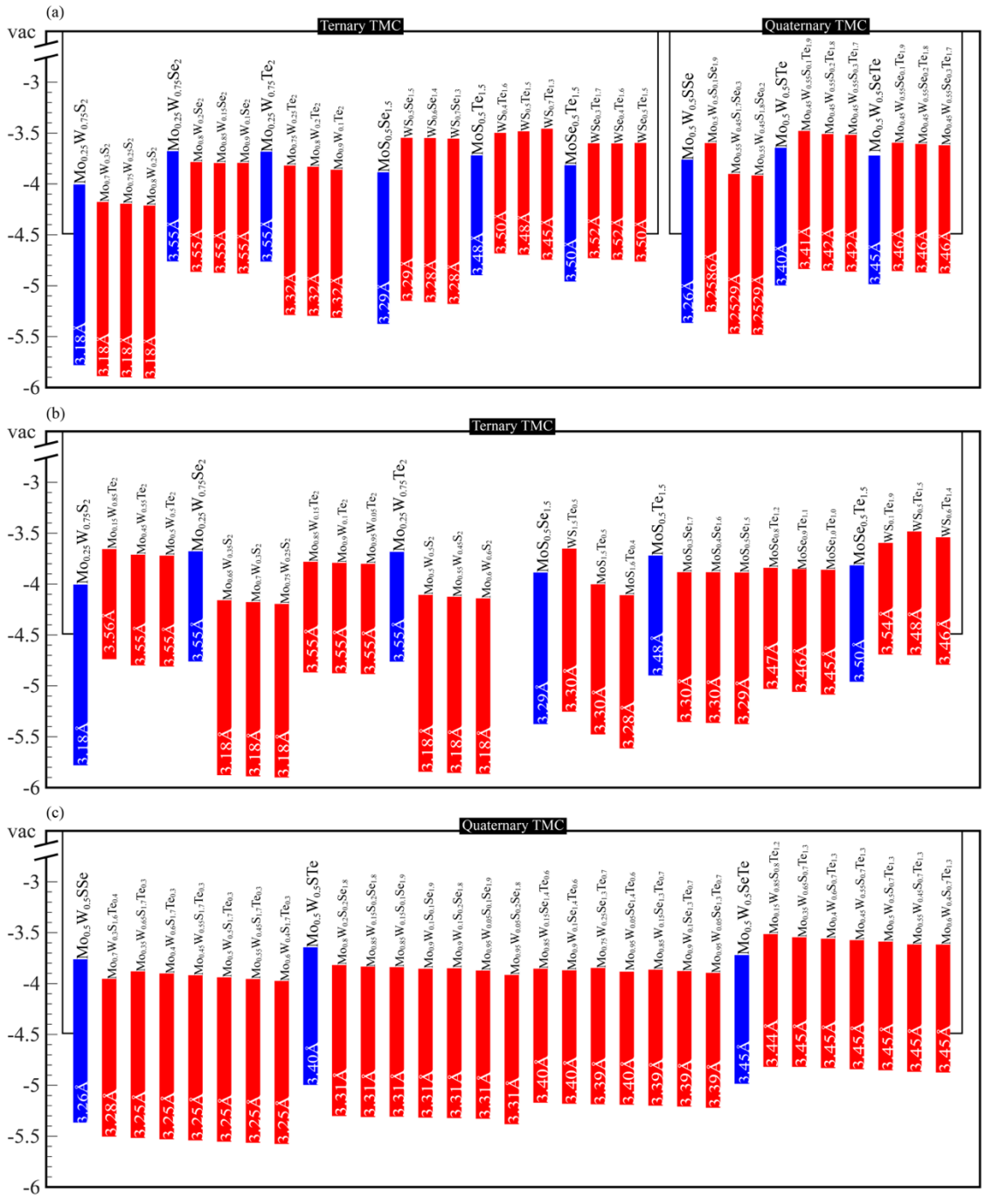

Figure 4.9. Band alignment of ternary and quaternary 2D CCTMCAs. The red bars are selected to compare to the reference blue bars with ((a) or (b)) the same elements and (c) different elements. The stoichiometry of each 2D CCTMCA is shown above the bars and the number at the bottom of each bar denotes the corresponding in-plane lattice constant.

Figure 4.8 shows the CBM and VBM of 2D CCTMCAs with reference to the vacuum level. Because VCA cannot capture the effect of an out-of-plane dipole moment, the difference in the vacuum levels on the two chalcogen sides of a monolayer CCTMCA is not taken into account. The conduction band offset (CBO) and valence band offset (VBO) are calculated, respectively, as the differences in the CBMs and VBMs of two 2D CCTMCAs. From the maximum and minimum values of CBM and VBM in the three sets of 2D CCTMCAs, we determine the ranges for CBO as from 0.049 to 0.861 eV and VBO as from 0.001 to 1.265 eV. Previous studies have shown that the stacking bilayer structure of TMCs can achieve ranges of CBO from 0.76 ± 0.12 eV and VBO from 0.83 ± 0.07 eV [332-335]. Because of the wide range of band offsets, it is possible to obtain different types of heterostructures using one 2D CCTMCA and pairing it with another 2D CCTMCA. Additionally, the band gap ranges between the CBOs and VBOs correspond to the photon frequencies within the near-infrared region of the solar spectrum, endowing the potential of employing 2D CCTMCAs for the applications of high-efficiency photovoltaics [336,337]. Figure 4.9(a) displays 27 selected CBM and VBM of 2D CCTMCAs of ternary or quaternary systems that can form type II heterostructures with the selected reference ternary and quaternary 2D CCTMCAs. For example, the CBO and VBO of the $Mo_{0.5}W_{0.5}STe/Mo_{0.95}W_{0.05}S_{0.2}Se_{1.8}$ heterostructure are 0.27 and of 0.39 eV, respectively.

At the same time, in the design of heterostructure 2D CCTMCAs, because of the composition-dependent wide range of CBO and VBO, versatile heterostructures are

achievable by stacking different composition/type of 2D CCTMCAs together. The search of pairing 2D CCTMCAs to form stacked heterostructures should also account for the relationship between lattice constants and band gaps (see Figure 4.5). Specifically, in designing the heterostructure, to minimize the lattice mismatch, two systems with small difference in lattice constants are preferred. We here investigate two sets of 2D CCTMCAs of Mo-W-S-Se and Mo-W-S-Te, and Mo-W-S-Te and Mo-W-Se-Te, as shown in Figure 4.5, where the range of lattice constants of two 2D CCTMCAs in each set overlaps with each other. Figure 4.9(b) and (c) shows the band alignments between some selected 2D CCTMCAs (in red color) that can match with the reference 2D CCTMCA (in blue color) in ternary and quaternary systems. From the results of both ternary and quaternary 2D CCTMCAs, we find many of them can form type II heterostructures with a small lattice mismatch from the reference material, indicating the potential of 2D CCTMCAs as building blocks for light harvesting heterostructures. Because the Mo-W-S-Se 2D CCTMCAs have a relatively small range of in-plane lattice constants (see Figure 4.3), Figure 4.9(b) shows that there is no ternary Mo/W-Se-Te 2D CCTMCA that satisfy both small lattice mismatch and type II band alignment with the reference of ternary Mo/W-S-Se 2D CCTMCA. The ternary Mo-W-S/Se and Mo-W-S/Te 2D CCTMCAs heterostructure shows that the largest lattice mismatch can reach to 10% between $Mo_yW_{(1-y)}S_2$ and $Mo_yW_{(1-y)}Te_2$ (e.g., the lattice mismatch in the $Mo_{0.25}W_{0.75}S_2/Mo_{0.15}W_{0.85}Te_2$ heterostructure is 11.9%). The ternary Mo/W-S-Te system has a relatively large range of lattice constants,

making it easier to find the 2D CCTMCA monolayers from both Mo/W-S-Se and Mo/W-Se-Te that can show the type II alignment with each other with a negligible lattice mismatch. For example, the lattice mismatch is nearly zero for the $MoS_{0.5}Se_{1.5}/WS_{1.5}Te_{0.5}$ and $MoS_{0.5}Te_{1.5}/MoSe_{0.8}Te_{1.2}$ heterostructures. In quaternary 2D CCTMCAs (see Figure 4.9(d)) , since there is more degree of freedom of 2D CCTMCA monolayers from both anion and cation content variations, the lattice mismatch between Mo-W-S-Se and Mo-W-S-Te 2D CCTMCAs drops to near 0%. There is still no Mo-W-S-Te and Mo-W-Se-Te 2D CCTMCA heterostructure that has a small lattice mismatch and can form a type II band alignment, which is consistent with Figure 4.5. Similar to ternary Mo/W-S-Te 2D CCTMCAs, the quaternary Mo-W-S-Te 2D CCTMCAs with a wide range of lattice constants can form the type II alignment of both Mo-W-S-Se and Mo-W-Se-Te 2D CCTMCA monolayers with almost zero lattice mismatch. The abundant choices in selecting 2D CCTMCA heterostructures with small lattice mismatch and suitable band offset range open up opportunities for a variety of heterostructure.

4.4.3 Energetic stability of high-entropy CCTMCAs

One concern in designing 2D CCTMCAs is their thermodynamic stability. Here we address this concern by focusing on the Gibbs free energy in nine ternary and three quaternary 2D CCTMCAs with equal x and y. The three quaternary 2D CCTMCAs are modelled using the SQS method. We compute the Gibbs free energy, a combination of the ground-state energy of mixing at 0 K and the temperature-dependent energy from

configurational entropy, to evaluate the stability of 2D CCTMCAs at different temperatures. We first compute the energy reference in the 2D CCTMCAs of quaternary 2D CCTMCAs such as $Mo_yW_{1-y}S_{2x}Se_{2(1-x)}$ by assuming the 2D CCTMCAs is made from four parent binary alloys of MoS_2, $MoSe_2$, WS_2, and WSe_2. Therefore, based on Vegard's law [320], the reference formation energy Eref is represented as a function of the ground state energies E_f of the four binary TMCs and the coefficients from the content of each element, which can be written as,

$$E_{\mathrm{ref},1}(x,y) = xyE_{f,\mathrm{MoS_2}} + (1-x)yE_{f,\mathrm{MoSe_2}} + x(1-y)E_{f,\mathrm{WS_2}} + (1-x)(1-y)E_{f,\mathrm{WSe_2}} \quad (4.4)$$

Similarly, we have reference formation energies for the other two systems written as,

$$E_{\mathrm{ref},2}(x,y) = xyE_{f,\mathrm{MoS_2}} + (1-x)yE_{f,\mathrm{MoTe_2}} + x(1-y)E_{f,\mathrm{WS_2}} + (1-x)(1-y)E_{f,\mathrm{WTe_2}} \quad (4.5)$$

and

$$E_{\mathrm{ref},3}(x,y) = xyE_{f,\mathrm{MoSe_2}} + (1-x)yE_{f,\mathrm{MoTe_2}} + x(1-y)E_{f,\mathrm{WS}_{e2}} + (1-x)(1-y)E_{f,\mathrm{WTe_2}} \quad (4.6)$$

We define the enthalpy of mixing (E_{mix}) by subtracting the reference energy from the enthalpy based on the DFT calculation of the quaternary system as,

$$E_{\mathrm{mix}}(x,y) = E_f(x,y) - E_{\mathrm{ref}}(x,y) \quad (4.7)$$

In the calculation of energy of mixing for ternary 2D CCTMCAs such as MoSSe or $MoWS_2$, we use two binary alloys of $MoS_2/MoSe_2$, or MoS_2/WS_2 as the reference.

The configurational entropy of mixing of the system can be written as [338]

$$S_{\mathrm{mix}}(x,y) = -k_{\mathrm{B}}N[x\ln x + (1-x)\ln(1-x) + y\ln y + (1-y)\ln(1-y)] \quad (4.8)$$

Based on Eq.4.8, we know that the nine ternary and three quaternary 2D CCTMCAs with $x = y = 0.5$ have the highest configurational entropy among all the 2D CCTMCAs. The Gibbs free energy of mixing (G^{T}_{mix}) for the 2D CCTMCAs system equals the energy of mixing (E_{mix}) subtracted by the multiplication of temperature (T) and configurational entropy (S_{mix}), i.e.,

$$G^{T}_{\mathrm{mix}}(x,y) = E_{\mathrm{mix}}(x,y) - TS_{\mathrm{mix}}(x,y) \quad (4.9)$$

In order to demonstrate the stability of the ternary 2D CCTMCAs, Table 4.6 lists the energies of mixing and Gibbs free energies of nine 2D CCTMCAs. Based on the relative contents of each element, the configuration entropy for those selected ternary and Janus ternary 2D CCTMCAs is S = k_{B}ln2 [338]. For the nine ternary 2D CCTMCAs, the negative energy of mixing Emix and the Gibbs free energy of $MoWS_2$, $MoWSe_2$, and $MoWTe_2$ indicates these three ternary alloys are stable at 0 K, 300 K and 600 K. For the six Janus structures, on the other hand, the energy of mixing at 0 K and 300 K are all positive, implying the unstable structures at 0 K and 300 K. MoSSe and WSSe become stable and have negative Gibbs free energies at 600 K. The Gibbs free energies of the Mo/W-S-Te and Mo/W-Se-Te based 2D CCTMCAs at 600 K remain positive, suggesting that even at high temperature, these four Janus structures are still unstable and likely to suffer from decomposition.

Table 4.6. The formation energies, Gibbs free energies of mixing of nine ternary monolayer 2D CCTMCAs with the 2*H* structure.

	$MoWS_2$	$MoWSe_2$	$MoWTe_2$
E_{mix} (eV)	-0.005	-0.004	-0.002
$G_{\mathrm{mix}}^{300\mathrm{K}}$ (eV)	-0.023	-0.022	-0.020
$G_{\mathrm{mix}}^{600\mathrm{K}}$ (eV)	-0.041	-0.040	-0.038

	MoSSe	WSSe	MoSTe	WSTe	MoSeTe	WSeTe
E_{mix} (eV)	0.027	0.030	0.199	0.224	0.078	0.088
$G_{\mathrm{mix}}^{300\mathrm{K}}$ (eV)	0.009	0.012	0.181	0.206	0.060	0.070
$G_{\mathrm{mix}}^{600\mathrm{K}}$ (eV)	-0.009	-0.006	0.163	0.188	0.042	0.052

Table 4.7. The formation energies, Gibbs free energies of mixing (at the temperatures of 300 K and 600 K), and nonideality of the four quaternary 2D CCTMCA monolayers with the 2*H* structure.

	Mo0.5W0.5SSe	Mo0.5W0.5STe	Mo0.5W0.5SeTe
E_{mix} (eV)	-0.003	0.052	0.028
$G_{\mathrm{mix}}^{300\mathrm{K}}$ (eV)	-0.111	-0.055	-0.079
$G_{\mathrm{mix}}^{600\mathrm{K}}$ (eV)	-0.218	-0.163	-0.187
$\Delta\mu$ (eV)	0.222	0.474	0.252

Table 4.7 summarizes the energy of mixing and Gibbs free energy of three quaternary 2D CCTMCAs at 0 K, 300 K, and 600 K. We can observe that the calculated formation energy of $Mo_{0.5}W_{0.5}SSe$ is negative, indicating this quaternary 2D CCTMCA is stable at 0 K. Indeed, monolayer $Mo_{0.5}W_{0.5}SSe$ has also been experimentally synthesized [339]. By contrast, for the other two 2D CCTMCAs, $Mo_{0.5}W_{0.5}STe$ and $Mo_{0.5}W_{0.5}SeTe$, the formation energies are positive, which is related to the large lattice difference among the four corresponding binary TMCs of each quaternary 2D CCTMCA system [268,340]. The difference in the atomic radii of S and Te is larger than that between the atomic radii of Se and Te, which also explains the higher formation energy of $Mo_{0.5}W_{0.5}STe$ than $Mo_{0.5}W_{0.5}SeTe$.

However, it is possible to stabilize the quaternary systems by considering the temperature effect in the Gibbs free energy. For each of the three quaternary 2D CCTMCAs we choose, the configurational entropy is 3 $k_B$ln2. Table 4.7 shows that the Gibbs free energies of mixing Gmix for all the three 2D CCTMCAs are negative at room temperature, indicating the stable structures of three quaternary system at the temperature of 300 K and 600 K. We can see that the temperature-dependent entropy term contributes to the lowering of Gibbs free energy in a great deal, and both $Mo_{0.5}W_{0.5}STe$ and $Mo_{0.5}W_{0.5}SeTe$, which show the positive energy of mixing, have negative Gibbs free energies at 300 K. Compared to the Janus structure 2D CCTMCAs of Mo/W-S-Te and Mo/W-Se-Te, whose Gibbs free energies remain positive even at 600 K, we can conclude that the entropy effect is beneficial

for stabilizing quaternary 2D CCTMCAs. Therefore, the method of designing multinary 2D CCTMCA not only result in the tunable properties, but also lead to stable alloying phase by taking the advantage of the entropy effect.

From Table 4.7 and the above discussion, we know that the positive formation energy of both $Mo_{0.5}W_{0.5}STe$ and $Mo_{0.5}W_{0.5}SeTe$ can be stabilized at high temperature. However, these two quaternary 2D CCTMCAs still show the unstable phase at low temperature, which could result in the phase separation. Even though the process of phase separation in quaternary 2D CCTCAs is complicated, we can predict the direction where the quaternary 2D CCTMCAs will undergo a phase separation into a group from two dissimilar binary TMCs. We assume that a quaternary 2D CCTMCA ($Mo_{0.5}W_{0.5}STe$, for example) can be made up from four different binary TMCs with different cation anion pairs (MoS_2, WTe_2, $MoTe_2$, and WS_2), which can further be categorized into two groups ((MoS_2-WTe_2) and ($MoTe_2$-WS_2)). We then calculate the energy difference between these groups to predict the phase separation from quaternary 2D CCTMCA to binary TMCs group. As an example of the $Mo_{0.5}W_{0.5}STe$ phase transformation, by taking two groups of binary TMCs (MoS_2-WTe_2) and ($MoTe_2$-WS_2) as reference, we can predict the stable group when phase separation happens using the nonideality of the solution. The nonideality Δμ is calculated via the chemical potential difference between two groups of binary TMCs, such as MoS_2-WTe_2 and $MoTe_2$-WS_2 [213],

$$\Delta\mu_2 = (\mu_{MoS_2} + \mu_{WTe_2}) - (\mu_{MoTe_2} + \mu_{WS_2}) \quad (4.10)$$

Similarly, we write Δμ for the other two 2D CCTMCAs as

$$\Delta\mu_1 = (\mu_{\mathrm{MoS_2}} + \mu_{\mathrm{WSe_2}}) - (\mu_{\mathrm{MoSe_2}} + \mu_{\mathrm{WS_2}}) \tag{4.11}$$

and

$$\Delta\mu_3 = (\mu_{\mathrm{MoSe_2}} + \mu_{\mathrm{WTe_2}}) - (\mu_{\mathrm{MoTe_2}} + \mu_{\mathrm{WS}_{e2}}) \tag{4.12}$$

The calculated nonideality results for the three 2D CCTMCAs are shown in Table 4.7, where the $\Delta\mu_1$ is in agreement with the previous work [213]. The positive $\Delta\mu_2$ of $Mo_{0.5}W_{0.5}STe$ indicates that the latter binary group of ($MoTe_2$-WS_2) is more stable, into which the quaternary 2D CCTMCA would decompose. We can see from the results that for the three quaternary 2D CCTMCAs systems of Mo-W-S-Se, Mo-W-S-Te, and Mo-W-Se-Te, the most stable binary TMC groups are $MoSe_2$-WS_2, $MoTe_2$-WS_2, and $MoTe_2$-WSe_2, respectively. Previous experimental result has shown one example of the phase separation in Mo-W-S-Se quaternary 2D CCTMCAs in Ref. [213] as the spinodal decomposition of quaternary 2D CCTMCAs Mo-W-S-Se into two ternary 2D CCTMCAs within the miscibility gap.

According to the calculated Gibbs free energies, we find that the three quaternary 2D CCTMCAs from SQS supercell are stable at room temperature. We henceforth focus on these three quaternary 2D CCTMCAs in discussing their electronic properties such as band structure and electrical conductivity, for the purpose of applying them as the potential materials in energy conversion applications. Figure 4.10 displays the band structures of three quaternary 2D CCTMCAs calculated with the PBE functional without and with

considering the spin-orbit coupling (SOC). We can see that the calculations with or without considering SOC show the direct band gap of these three 2D CCTMCAs at *K* point. The SO splitting energies at the *K* point for $Mo_{0.5}W_{0.5}SSe$, $Mo_{0.5}W_{0.5}STe$, and $Mo_{0.5}W_{0.5}SeTe$ are 0.31, 0.35, and 0.36 eV, respectively.

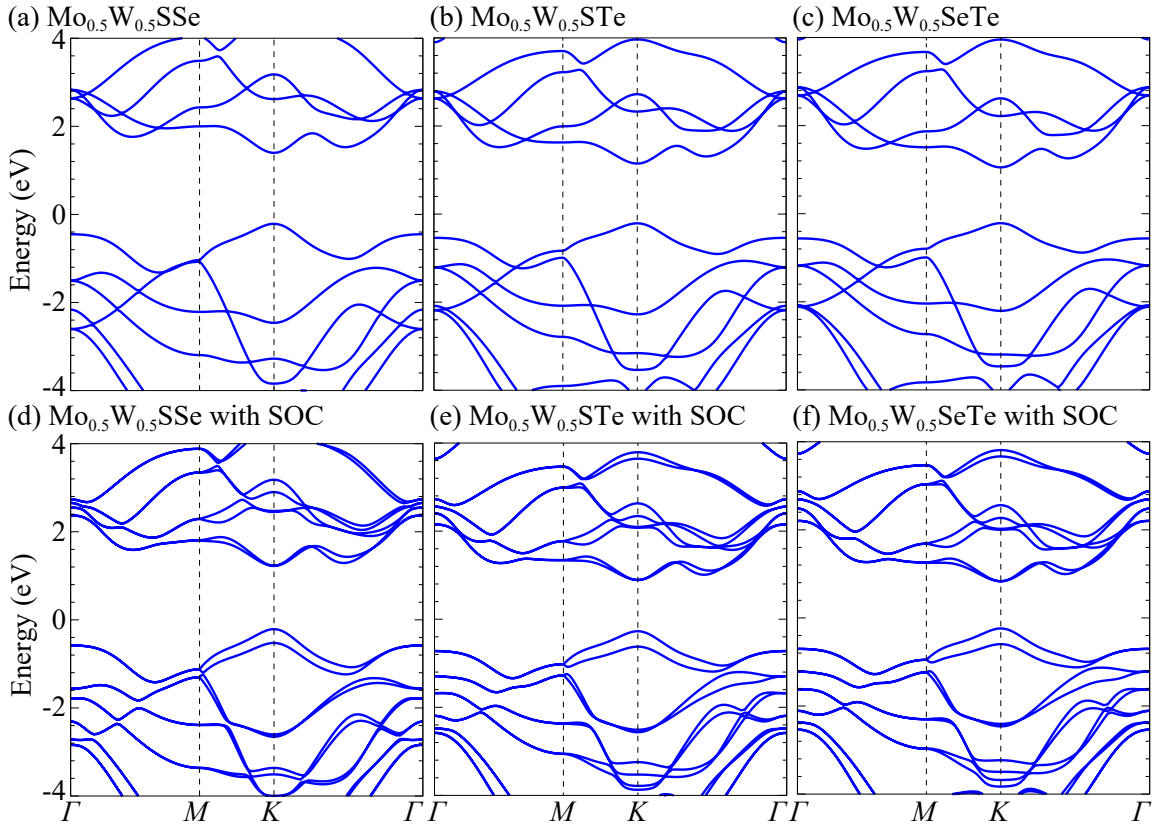

Figure 4.10. Band structures of three quaternary 2D CCTMCAs, $Mo_{0.5}W_{0.5}SSe$, $Mo_{0.5}W_{0.5}STe$, and $Mo_{0.5}W_{0.5}SeTe$. Spin-orbit coupling is not considered in the panels (a), (b), and (c), whereas it is accounted for in panels of (d), (e), and (f).

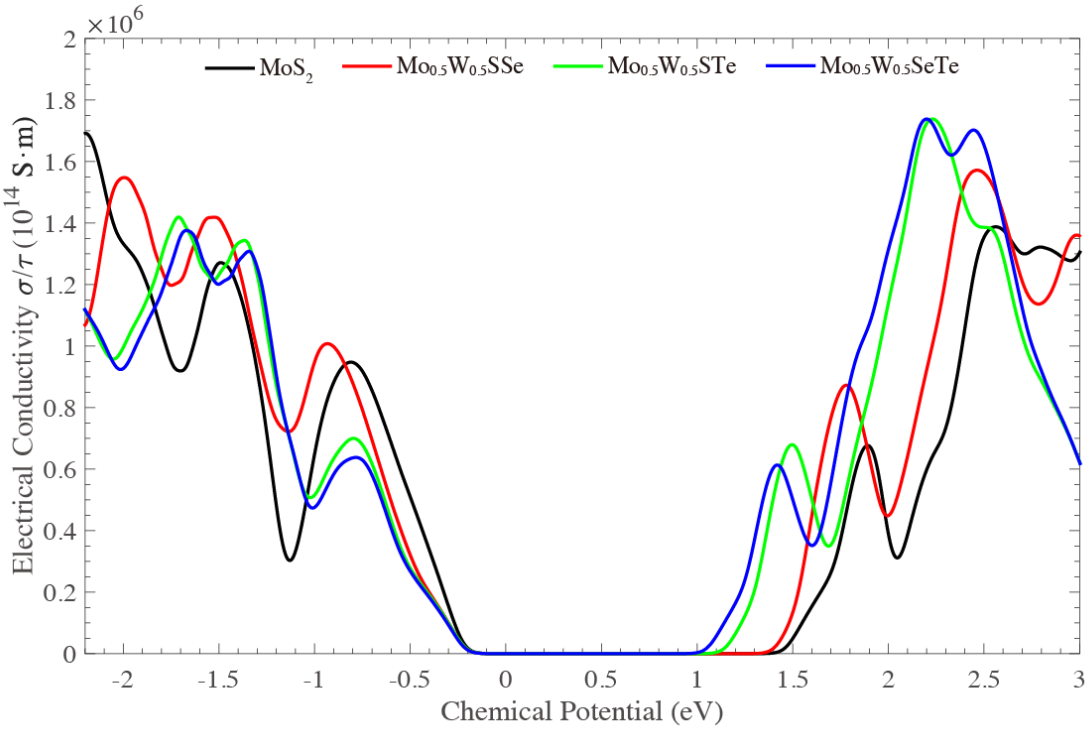

Figure 4.11. Electrical conductivity of $Mo_{0.5}W_{0.5}SSe$, $Mo_{0.5}W_{0.5}STe$, and $Mo_{0.5}W_{0.5}SeTe$ at 300 K as a function of the chemical potential. Electrical conductivity of MoS_2 is also plotted as benchmark.

4.4.4 Electrical conductivity of high-entropy CCTMCAs

Figure 4.11 displays the electrical conductivity of $Mo_{0.5}W_{0.5}SSe$, $Mo_{0.5}W_{0.5}STe$, and $Mo_{0.5}W_{0.5}SeTe$ at 300 K. We also compute the electrical conductivity of monolayer MoS_2 and benchmark the results with the literature [341]. The relaxation time used in these calculations is taken as an approximated constant value of 10.0 fs, which has been used in the calculations of electrical conductivity for other monolayer semiconductors such as SnSe, Sc_2C, and $TiSe_2$ [342-344]. We first observe that the band gaps of these three 2D CCTMCAs, corresponding to the regions where the conductivity equals to zero, are in

agreement with the VCA-DFT results (see Figure 4.5). These band gaps lie from the visible light range to the near-infrared region, which enable the photovoltaic effect in a wider region to enhance the photovoltaic conversion efficiency [345]. In Figure 4.11, the negative (left) side of the chemical potential illustrates the holes conductivity (*p*-type), and the positive (right) side is for the conductivity from electrons (*n*-type). By changing the chemical potential that can be realized by different methods such as doping or applied gate voltage [346], 2D CCTMCAs can reach a high conductivity of 1.7×10^6 S·m, which guarantees the high carrier transport within the single layer. Moreover, the three quaternary 2D CCTMCAs exhibit higher electron conductivity comparing to pristine MoS_2 monolayer. The high conductivity of three examples shows their potential in the energy conversion applications such as photovoltaics.

4.5 Summary

In summary, we propose a workflow using the DFT calculation from VCA models in search of suitable multinary 2D CCTMCAs in different applications in energy conversion and spintronics. We have computationally characterized five critical structural and electrical properties of 2D CCTMCAs and also benchmarked DFT results using unit cell and SQS models to validate the accuracy of calculation from VCA method. We find that VCA-DFT calculations lead to comparable results of lattice constants, band gap, electron and hole effective masses, spin orbit splitting, and band alignment with the unit-cell-DFT and SQS-DFT results, with some exceptions in the CBM, effective hole masses, and band

gaps of MoSTe and WSTe, which are caused by the inaccurate prediction of the location of CBM in VCA-DFT calculations. Our results show that the multinary 2D CCTMCAs exhibit tunable properties such as band gaps, lattice constants, effective masses, and band alignments. These tunable properties are helpful in designing the lattice matching type II heterostructures for the applications of light adsorption and conversion devices. The strong SOC of 2D CCTMCAs also suggests the possibility of utilizing the multinary 2D CCTMCAs in spintronics. In addition to the high-throughput computational characterization of 2D CCTMCAs workflow, we propose three quaternary 2D CCTMCAs, $Mo_{0.5}W_{0.5}SSe$, $Mo_{0.5}W_{0.5}STe$, and $Mo_{0.5}W_{0.5}SeTe$ at room temperature, serving as excellent examples to illustrate the entropy-stabilized alloys from multiple component design of 2D CCTMCAs. In addition, they also show high electrical conductivity as promising materials for energy conversion applications. Although currently most research on quaternary TMC alloys centers on Mo/W-based alloys, 2D nanosheets of $TaSe_2$, $NbSe_2$, and $NiTe_2$ (Ta: Tantalum, Nb: Niobium) have been obtained in experiments, indicating that alloying of these TMCs may be used to develop 2D CCTMCAs [347]. The high-throughput workflow we proposed enables the extension of the research on the 2D CCTMCAs consisting of other transition metal, metal, and chalcogen elements.

CHAPTER VI

SPIN QUBIT BASED ON THE NITROGEN-VACANCY CENTER ANALOG IN A DIAMOND-LIKE COMPOUND C_3BN

5.1 Abstract

The Nitrogen-vacancy (NV) center in diamond plays important roles in emerging quantum technologies. Currently available methods to fabricate the NV center often involve complex processes such as N implantation. By contrast, in a diamond-like compound C_3BN, creating a boron (B) vacancy immediately leads to an NV center analog. We use the strongly constrained and appropriately normed (SCAN) semilocal density functional—this functional leads to nearly the same zero-phonon line (ZPL) energy as the experiment and as obtained from the more time-consuming hybrid density functional calculations—to explore the potential of this NV center analog as a novel spin qubit for applications in quantum information processing. We show that the NV center analog in C_3BN possesses many similar properties to the NV center in diamond including a wide band gap, weak spin-orbit coupling, an energetically stable negatively charged state, a highly localized spin density, a paramagnetic triplet ground state, and strong hyperfine interactions, which are the properties that make the NV center in diamond stand out as a suitable quantum bit (qubit). We also predict that the NV center analog in C_3BN to exhibit two ZPL energies that correspond to longer wavelengths close to the ideal telecommunication band for quantum communications. C_3BN studied here represents only

one example of A_3XY (A: group IV element; X/Y: group III/V elements) compounds. We expect many other compounds of this family to have similar NV center analogs with a wide range of ZPL energies and functional properties, promising to be new hosts of qubits for quantum technology applications. Furthermore, A_3XY compounds often contain group IV elements such as silicon and germanium, so they are compatible with the sophisticated semiconductor processing techniques. Our work opens up ample opportunities towards scalable qubit host materials and novel quantum devices.

5.2 Introduction

Despite in its early infancy, quantum computers hold great potential for solving extremely challenging problems faced by currently available supercomputers, ranging from factorizing a large integer to break public-key cryptography to discovering drugs to treat pandemic diseases [16]. At the heart of the superpowers of quantum computers are the materials that constitute the quantum bits (i.e., qubits) having two energy levels that are analogous to the classical bits represented by 0s and 1s. To realize the full potential of quantum computers in the foreseeable future, advancing the development of building blocks is the key. Among the many proposed candidates for qubit materials such as trapped ions [348] and superconducting circuits [349] that work at near absolute zero, solid-state spin qubits based on defect centers embedded in wide-band-gap semiconductors such as diamond are promising that can lead to novel quantum devices capable of operating at room temperature [350].

The NV center in diamond corresponds to a peculiar defect configuration, where one C atom in a pair of nearest-neighboring (NN) C atoms is removed and the other replaced by a N atom. Although the defect can exhibit different charge states, the NV center commonly refers to the negatively charged state with an extra electron denoted as NV^{-1}. This charged state engages the interplay of six electrons, three of which come from the three C dangling bonds surrounding the C vacancy, two from the N atom (the other three electrons of the N atom are shared with its three NN C atoms), and the rest from the donor in the bulk [351]. The total spin resulting from the energy distribution of the six electrons is one and the ground and excited states of the NV center are triplet states with sublevels of $m_s = 0$, -1, or 1. The ms = ± 1 states are separable by a small microwave field causing the Zeeman spitting. The superposition of the ms = 0 state and one of the ms = ± 1 states behaves as the $|0\rangle$ and $|1\rangle$ levels of a qubit, respectively. The initialization and readout of a qubit based on the NV center are realized via optical pumping and spin-dependent fluorescence, respectively [352]. NV center qubits have been shown to exhibit long room-temperature coherence times (T_2) on the timescale of microseconds [353], owing to weak spin-orbit coupling and hyperfine interactions [354]. Furthermore, the spins in two NV center qubits have been demonstrated to entangle at room temperature [355], an encouraging step towards scalable quantum register consisting of multiple qubits.

Despite the abovementioned potential of the NV center in diamond has shown in quantum technology applications, there are limitations from the perspectives of

manufacturing and zero-phonon line (ZPL) energy. In terms of manufacturing, fabricating these defect centers in a prescribed manner is challenging. Two common methods to create the NV center are (i) chemical vapor deposition (CVD) growing diamond and (ii) high-energy N implantation followed by annealing processes [356]. The locations of the NV center resulted from both methods cannot be accurately manipulated at the atomic scale [352], leading to randomly distributed NV centers and degrading the quality of a quantum register. Furthermore, it is challenging to fabricate devices from diamond [357]. Significant amounts of experimental and theoretical efforts have been spent to identify defect centers in other wide-band-gap semiconductors such as SiC polytypes [358] and GaN [359]. In terms of the ZPL energy, it takes up only 3-4% of the total emission [360]. Because future quantum computers based on the NV center qubits will communicate through optical fiber, enhancing the ZPL wavelengths so that they can match the ideal telecommunication band wavelength is important to minimize the optical loss.

We aim to search for defect centers for hosting spin qubits from a new group of functional semiconductors with a common formula A_3XY, where A is a group IV element, X and Y are groups III and V elements, respectively. We expect A_3XY to be free of the limitations posed by diamond and meanwhile to possess the potential as novel qubit materials for three reasons. First, as illustrated in Figure 5.1(a)-(c), the structure of an A_3XY compound consists of tetrahedral molecular geometry similar to that in diamond, although the former geometry does not have the C_{3v} symmetry as the latter. Each X or Y atom has

three nearest neighboring *A* atoms, so the overall structure can be regarded as embedding *XY* diatomic units in diamond. *X* and *Y* atoms have eight valence electrons, so the average number of valence electrons per atom in A_3XY is the same as in diamond. The special atomic arrangement as well as the isoelectric feature facilitate the formation of an NV center analog. In other words, removing one *X* atom and negatively charge it with an extra electron is akin to creating a charged *Y*-vacancy center in A_4. Second, the mature semiconductor industry is well prepared for new materials that contain group IV elements such as silicon and germanium. A_3XY compounds lie in this category, so the quantum devices made of A_3XY are most likely compatible to the existing semiconductor techniques and scalable to integrate a significant number of qubits. Third, one notable difference of A_3XY from pure bulk $A_4$is that A_3XY have mixed non-polar and polar bonds, which are expected to affect the ZPL wavelengths via the presence of diverse band gaps and functional properties.

Synthesizing A_3XY using conventional CVD method is nevertheless challenging and subject to the possibility of phase separation. Kouvetakis et al. overcame this challenge via molecular beam epitaxy based on a gas source and successfully synthesized a prototype A_3XY compound Si_3AlP. Recent theoretical studies have predicted Si_3AlP to have a direct band gap that is potentially helpful for solar cell applications due to its direct band gap [361]. It was also suggested that the same experimental approaches could be applied to synthesize many other A_3XY compounds [362].

In this work, we focus on one representative example of A_3XY compounds, i.e., C_3BN. We explore the potential of C_3BN as a novel semiconductor to host spin qubits. Experimentally, Langenhorst and Solozhenko synthesized this compound via a shock-compression method at high pressure and temperature [363]. Theoretically, the crystal structure of C_3BN and structural properties such as bulk modulus were first reported in Ref. [364] via density functional theory (DFT) calculations. A more recent DFT study predicts that the hardness of C_3BN is comparable to diamond [365]. As mentioned above, if C_3BN can be successfully synthesized, removing a B atom in C_3BN is equivalent of creating a NV center analog and the whole C_3BN structure has the same number of electrons per atom as diamond. Because the majority atoms in are C and the properties should be similar to those of diamond. Here we apply DFT calculations to compute the properties that are deemed as required ones for a charge defect in a semiconductor to be a qubit candidate. These properties include the electronic structure of bulk C_3BN, the defect formation energy, electronic structure, defect energy levels, and hyperfine tensors of the NV-center analog. We compute the same properties of diamond and the NV center for a throughout comparison. We show that the NV center analog in C_3BN satisfies all the criteria for a defect center to become a candidate of qubit materials, endowing C_3BN with a promising potential for hosting spin qubits.

5.3 Simulation Methods

We use the Vienna Ab initio Simulation Package (VASP) for all the DFT calculations

[366]. The potential datasets for the C: $2s^2 2p^2$, B: $2s^2 2p^1$, and N: $2s^2 2p^3$ valence electrons are from the Projector augmented-wave method [80,81]. In all the VASP calculations, the plane waves cutoff kinetic energy is set to 400 eV. For the exchange-correlation interactions, we use the strongly constrained and appropriately normed (SCAN) semilocal density functional, which is one of the most recently developed meta-GGA functionals developed by Perdew and coworkers [367]. This functional not only includes electron density but also local kinetic energy density in the exchange-correlation approximations. SCAN is known to satisfy all the 17 known exact constraints for a semi-local functional. Although SCAN has been applied to many semiconductors to predict their band gaps [368], it has not yet been applied to study the defect levels of the NV center. This work therefore also serves a first example to test the accuracy of this functional in describing the NV center.

To obtain the ground-state structure of C_3BN, we adopt the optimized structure of Si_3AlP reported in Ref. [361] as the starting structure for geometry optimizations. The simulation cell contains 12 C, 4 B, and 4 N atoms. Symmetry analysis on the optimized structure shows that the crystal structure of C_3BNbelongs to the monoclinic Bravais lattice with the space group of *Cc* (group number: 9). In the geometry optimizations of C_3BN and diamond, all the six lattice parameters and atomic coordinates are fully optimized until the force threshold of 0.01 eV is achieved. The Monkhorst-Pack *k*-point grids [82] for these two systems are 4 × 4 × 7 and 8 × 8 × 8, respectively. The optimized lattice parameters of C3BN are a = 5.669 Å, b = 5.670 Å, c = 3.595 Å, $\alpha = \beta = 90°$, $\gamma = 89.755°$ and the

optimized lattice parameters of diamond are $a = b = c = 3.549$ Å and $\alpha = \beta = \gamma = 90°$. The symmetry of C_3BN is much lower than diamond as can be seen from the tetrahedral molecular geometry illustrated in Figure 5.1(c). We calculate the energies of the 36-atom unit cell of B and the 2-atom cell of a N_2 molecule placed in the center of a vacuum box. These two energies will be used to calculate the defect formation energy (see below). The *k*-point grids of these two calculations are $10 \times 10 \times 4$ and $1 \times 1 \times 1$ (Γ point) , respectively. We compute the dielectric constant tensor also using the 20-atom and 8-atom cells for C_3BN and diamond, respectively. The dielectric constant tensor is calculated based on the density functional perturbation theory (DFPT) [102]. Because the SCAN version of DFPT is not yet implemented in VASP, we switch to the Perdew-Burke-Ernzerhof (PBE) functional [79] with the optimized geometry using the SCAN functional to compute the dielectric-constant tensor, where local field effects are accounted for on the Hartree level. We calculate the band structure of C_3BN and diamond using their primitive cells that have 10 and 2 atoms, respectively. The corresponding Monkhorst-Pack *k*-point grids are $8 \times 8 \times 6$ and $12 \times 12 \times 12$, respectively. We consider the spin-orbit coupling (SOC) [369] in the band structure calculations.

To simulate the NV-center analog in C_3BN, we first create a $2 \times 2 \times 3$ supercell of C_3BN (240 atoms) from the optimized 20-atom cell so that the three lattice vectors have nearly the same length, and then we remove one B atom whose crystalline coordinates are (0.351, 0.451, 0.499) and we add an extra electron to the supercell. For the simulations of

the NV center in diamond, we use a 3 × 3 × 3 supercell (216 atoms) (see Figure 5.1(a) and (b)) and remove one C atom positioned at (0.500, 0.333, 0.500) and substitute one of its NN C atoms by a N atom located at (0.583, 0.417, 0.583). For the geometry optimizations of these two supercells, we use a single *k* point (Γ point) and optimize only the atomic coordinates while keeping the lattice constants fixed. For the calculations of density of states, spin density, and hyperfine structure, we use a 2 × 2 × 3 *k*-point grid.

5.4 Results and Discussion

5.4.1 Structural and electronic properties of C_3BN

We start with computing the band structures of C_3BN and diamond without defects. The band structure of diamond is used for comparison and also for benchmarking the accuracy of the SCAN functional in describing band gaps. Weber et al. summarized nine conditions that a viable semiconductor to host spin qubits [357]. Two of them can be evaluated from the band structure of the candidate, i.e., it must have a wide band gap and weak SOC. The former criterion is required to accommodate deep defect levels; the latter is preferred to avoid disturbing the electron spin and thereby maintaining the long coherence time. Note that strong SOC is not always an unfavorable characteristic for qubits. As a matter of fact, it becomes a desirable property in some other types of qubit host materials such as semiconductor nanowires [370].

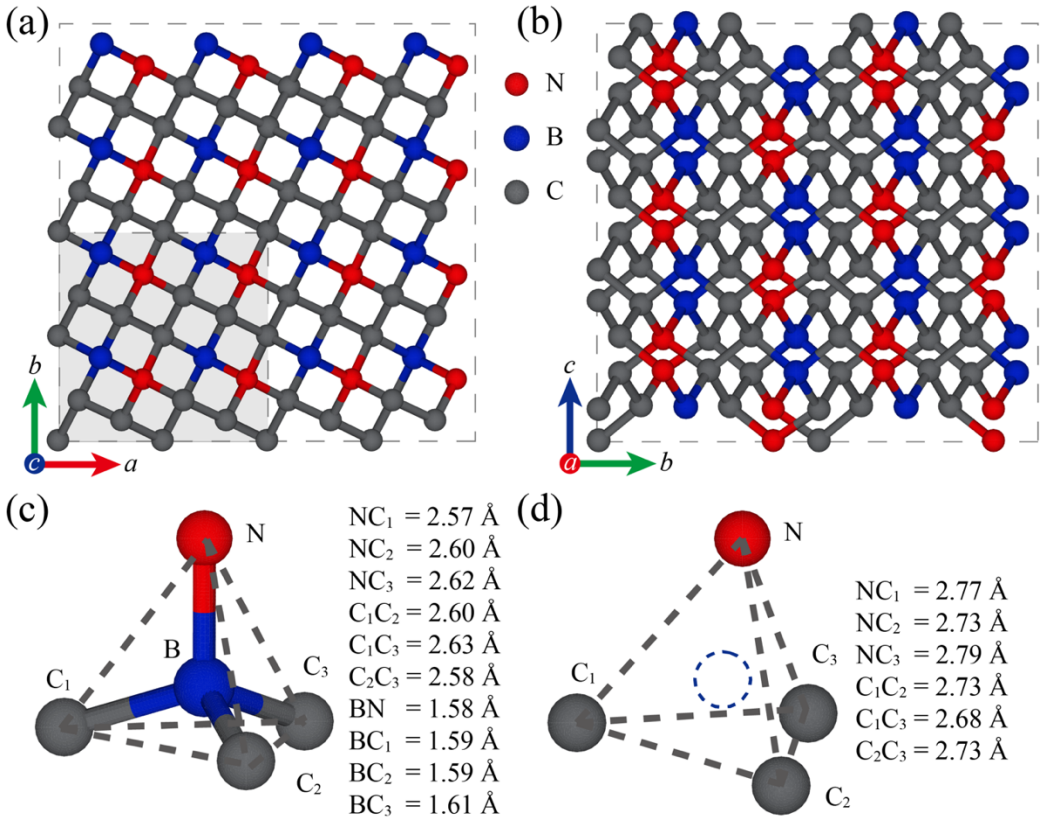

Figure 5.1. (a) Top and (b) side views of the atomic structures of C_3BN as an example of A_3XY compounds. Here, A = C, X = B, and Y = N. A unit cell of C_3BN is enclosed in the shaded area of (a). Optimized tetrahedral geometries of C_3BN (c) without and (d) with the B vacancy (denoted by the dashed circle). The interatomic distances are shown for both tetrahedral geometries.

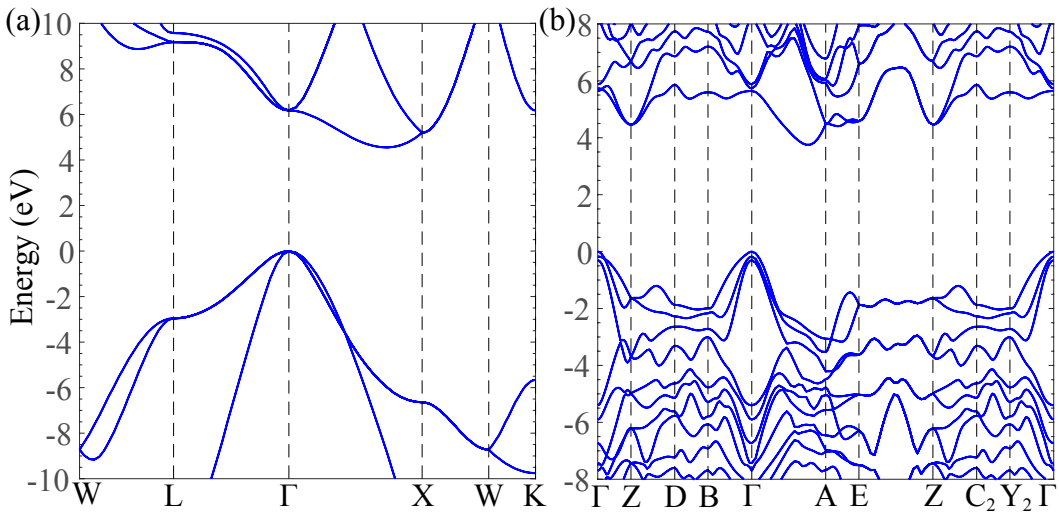

Figure 5.2. Band structures of (a) diamond and (b) C_3BN calculated with the SCAN functional and spin-orbit coupling is taken into account. The notations of special *k* points are adopted from Ref. [371]. The valence band maxima are set to zero.

We evaluate the feasibility of C_3BN as a novel semiconductor for hosting spin qubits using the two criteria. Figure 5.2(a) shows the band structure of diamond with SOC taken into account. We can see that diamond has an indirect band gap of 4.55 eV. Although the SCAN band gap remains underestimating the experimental band gap of 5.50 eV [372], the SCAN functional improves the band gap in comparison to the PBE band gap calculated to be 4.14 eV. The calculated SCAN and PBE band gaps of diamond are both consistent with previous work [368]. Using the SOC splitting at the valence band maximum (VBM) as a metric of SOC strength [351], we find this is negligibly small for diamond. Figure 5.2(b) shows that C_3BN exhibits an indirect band gap of 3.75 eV, which is smaller than that of diamond, with the VBM at the Γ point and the conduction band located between the Γ and A points. Furthermore, the top two valence bands at the Γ point are nearly degenerate,

indicating again a negligible SOC splitting and therefore trivial SOC. Although more advanced theory such as many-body G_0W_0 calculations [373] may correct the band gap of C_3BN to even larger numbers, the SCAN band gap is already wide enough to hold deep defect states. Together with the weak SOC, C_3BN seems promising to be another wide-band-gap semiconductor to host spin qubits.

Figure 5.1(c) shows the tetragonal molecular motif in the optimized structure of C_3BN. Most of the interatomic distances are not equal and greater than the NN C-C bond length of 1.536 Å in diamond, revealing the low symmetry of this motif as well as of the bulk. The structure of the motif belongs to the C_1 point group. As can be seen in Figure 5.1(d), creating the NV-center analog leads to enlarged interatomic distances and the point group remains the same.

5.4.2 Stability of the NV center analog in C_3BN

Although not explicitly listed as one of the nine criteria by Weber et al., the stability of charged defects in a semiconductor is important and needs to be examined. Specifically, as a metric of stability, the defect formation energy provides not only the equilibrium concentration of a charged defect [357] but also the range of Fermi energies (within the limit of the band gap) [374], where a charged state can be more stable than the other possible charged states. We therefore evaluate the stability of charge defects (q = 0, -1, or -2) in C_3BN by computing the defect formation energy $E^{\mathrm{f}}[C_3BN{:}\,NV^q]$ following the commonly used equation [375]:

$$E^{\mathrm{f}}[C_3BN{:}\,NV^q] = E_{tot}[C_3BN{:}\,NV^q] - E_{tot}[C_3BN{:}\,bulk] + \mu_B + q(\varepsilon_F + \varepsilon_{VBM}^{bulk} + \Delta V) \quad (6.1)$$

where $E_{tot}[C_3BN{:}\,NV^q]$ and $E_{tot}[C_3BN{:}\,bulk]$ are the total energies of the C_3BN supercells without and with a charged defect, respectively. μ_B is the chemical potential of bulk B. ε_F is the Fermi energy with reference to the VBM ε_{VBM}^{bulk} of the bulk. ΔV is the energy correction term due to the energy alignment of the VBM [376]. For comparison, we also compute the formation energy of charged defect in diamond $E^{\mathrm{f}}[C{:}\,NV^q]$ written in a similar equation:

$$E^{\mathrm{f}}[C{:}\,NV^q] = E_{tot}[C{:}\,NV^q] - E_{tot}[C{:}\,bulk] - \mu_N + 2\mu_C + q(\varepsilon_F + \varepsilon_{VBM}^{bulk} + \Delta V) \quad (6.2)$$

where $E_{tot}[C{:}\,NV^q]$ and $E_{tot}[C{:}\,bulk]$ are the total energies of the diamond supercells without and with charges, respectively. μ_N is the chemical potential of N taken as half of the energy of a N_2 molecule. A factor of 2 in Eq. (6.2) is because of the two missing C atoms to create the NV center. μ_C is the chemical potential of C in bulk diamond, namely, $E_{tot}[C{:}\,bulk]/216$.

The energy correction term ΔV in Eqs. (6.1) and (6.2) also depends on the dielectric-constant tensors of C_3BN and diamond. We therefore calculate the dielectric constants in C_3BN whose ε_{aa}, ε_{bb}, and ε_{cc} components are 5.51, 5.75, and 5.52, respectively. The other three components are almost zero. For comparison, the computed dielectric constant of diamond, 5.50, is consistent with the experimental dielectric constant 5.68 [377], showing the accuracy of the SCAN functional. We notice that the dielectric constant components of

C_3BN in the *a* and *c* directions are nearly the same as those in diamond, manifesting the high similarity between C_3BN and diamond in these two directions. Figure 5.1(a) shows that along the positive *a* direction, B and N atoms appear to locate in zigzag chains, each of which can be denoted as (BN)(BN)(BN). Because each diatomic (B and N) unit is close in distance, the pattern can also be regarded as (NB)(NB)(NB) along the negative a direction. These two different plausible denotations imply that the polarization due to the BN polar bonds along the positive and negative *a* directions will cancel out, leading to almost the same dielectric constant with diamond in the *a* direction. Similarly, Figure 5.1(b) shows that along the positive or negative *c* direction, B and N atoms always follow the same (BN)(NB)(BN)(NB)(BN)(NB) pattern. As a result, the polarization in the BN bonds plays little role in affecting the dielectric constant in the *c* direction. By contrast, along the positive and negative *b* directions, the distance between the diatomic unit is so large that the pattern can only be regard as (BN)(BN)(BN) or (NB)(NB)(NB). The dielectric constants of C_3BN in the *b* direction is therefore slightly larger than diamond due to the polar nature of B-N bonds.

In computing the defect formation energy, we consider the neutral state, $q = 0$, and two charged states, $q = -1$ and -2. When $q = -1$, the state refers to the NV-center analog in C_3BN or the NV center in diamond. We consider the $q = -2$ state to identify the upper bound of the Fermi energy where the NV-center analog or NV center remains more stable. Figure 5.3 shows the defect formation energy of C_3BN and diamond as a function of the Fermi

energy with reference to the VBM. Our computed defect formation energy for the neutral defect in diamond is 5.92 eV, which is comparable to 6.21 eV using a 511-atom supercell [378] and to ~6.10 eV using a 63-atom supercell [357] with the HSE06 functional [93]. Figure 5.3(a) also shows that the lower bound of the Fermi energy is 1.78 eV, above which the NV center in diamond is more stable than the other two defect states. This lower bound is smaller than ~2.70 and 2.78 eV in Refs. [378] and [357], respectively, possibly due to the different functional used in the current calculations. Our calculations cannot provide an upper bound for the Fermi energy in diamond because of the underestimated band gap by the SCAN functional. However, we consistently show that the NV center is stable in a wide range of Fermi energies. Figure 5.3(b) shows the formation energies of the three charge states of C_3BN. For the neural defect, the formation energy is 6.82 eV in C_3BN, higher than that (5.92 eV) in diamond, implying that it is relatively more energy-consuming to create a B vacancy in C_3BN than to generate two C vacancies, one of which is further replaced by a N atom. More importantly, the NV-center analog is the most stable among the three defect states, if the Fermi energies are within the energy range of 1.52 to 3.26 eV. The lower bound is nearly in the middle of the band gap and comparable to that of diamond, indicating that the defect state is deep enough to trap an extra electron. Although the HSE06 functional may give a more accurate band gap of C_3BN and then more accurate lower and upper bounds of Fermi energies, we expect our conclusion that the NV-center analog as a deep charged state to remain the same, according to our results using the SCAN functional.

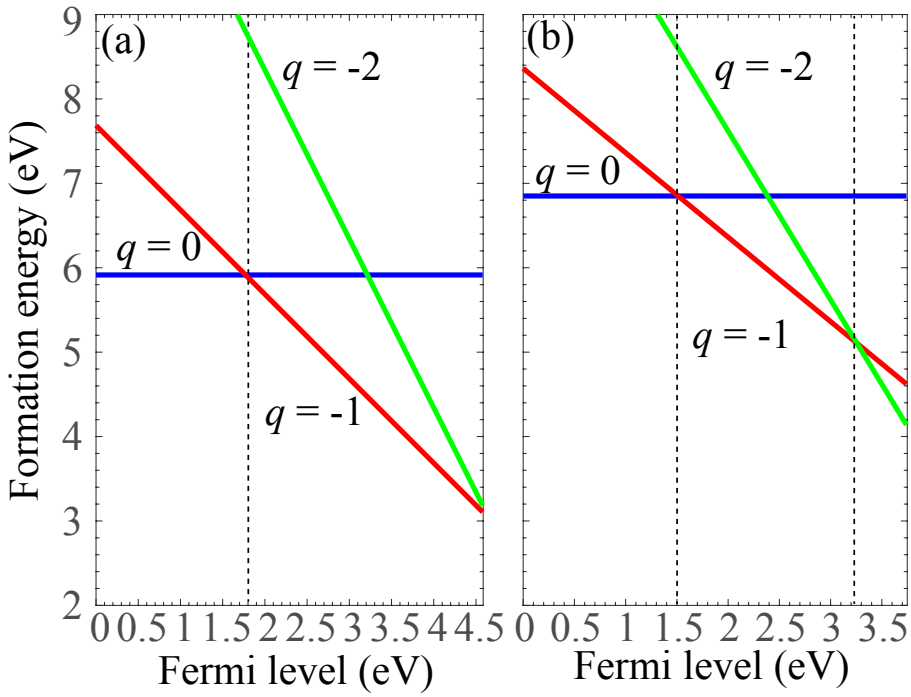

Figure 5.3. Defect formation energy of (a) diamond and (b) C_3BN. Only one dashed line is shown to represent the lower bound in diamond, where the q = -1 state is the most stable due to the underestimated band gap with the SCAN functional. The region where the q = -1 state in C_3BN is the most energetically stable is enclosed by two dashed lines.

5.4.3 Electronic properties of the NV center analog in C_3BN

Having shown the stability of the NV center analog in C_3BN, we now focus on studying the electronic structure of this analog. Figure 5.4 shows the spin density of states (SDOS) and energy levels of the defect states of the NV center and its analog. For the NV center, its electronic structure has been well studied using different levels of theory. Reference [379] provides an excellent overview this topic. Interestingly, we notice that the SCAN functional has not yet been applied to study the NV center. We show here that using the SCAN functional can reproduce all the key features in the electronic structure of the

NV center. First of all, our calculated SDOS agrees well with the SDOS obtained from the PBE functional [380]. The spin-up and spin-down DOS curves are nearly symmetrical except in the band gap where we observe four SDOS peaks. The two spin-up DOS peaks are located at the energies of around -0.273 and -1.443 eV, respectively. By computing the integrated DOS, we find that the higher-energy DOS is occupied by two degenerate electrons often labeled as the e_x and e_y states [351]. Consistent with the smaller area enclosed below the peak, the lower-energy DOS is occupied by only one electron labeled as the $a_1(2)$ state. The two spin-down DOS peaks are located at the energies of about -0.562 and 1.685 eV, respectively. Only the lower-energy DOS is occupied by one electron with the same label, $a_1(2)$. The higher-energy spin-down DOS peak has the same labels as their spin-up counterparts, e_x and e_y. This peak is capable of hosting two degenerate electrons. The remaining two electrons of the NV center are embedded in the valence bands. The net effect of the energy distribution of the six electrons is the paramagnetic state with a total spin moment of one Bohr magneton. As described in the Introduction section, this paramagnetic spin is the key factor that makes the NV center a qubit that can be manipulated by magnetic and optical methods.

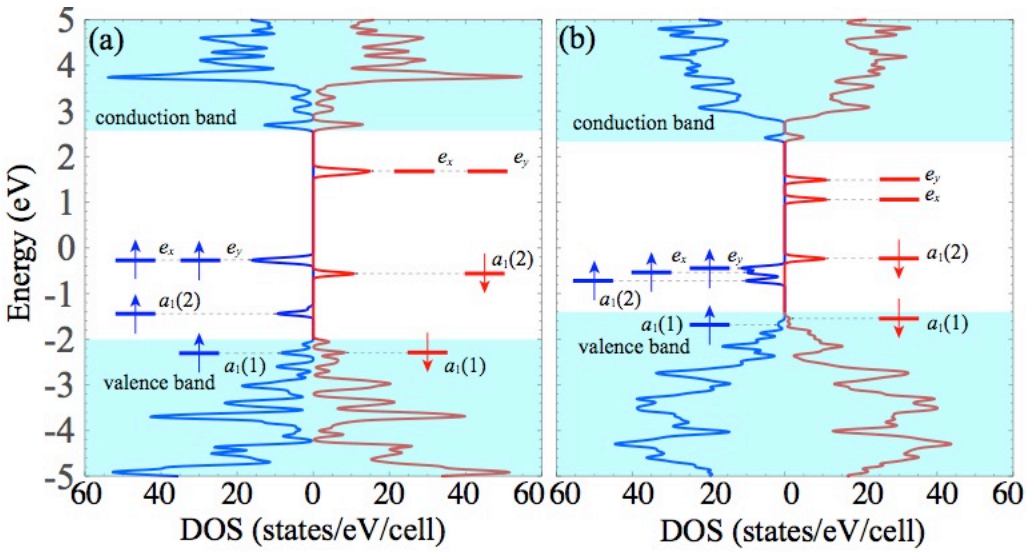

Figure 5.4. Spin density of states of (a) diamond with the NV center and of (b) C_3BN with the NV center analog. Occupied and empty energy levels are represented by line segments with and without overlapped upward (spin-up) and downward (spin-down) arrows, respectively. The upper and lower shaded areas represent the conduction and valence bands, respectively.

Similar to diamond, the SDOS curves shown in Figure 5.4(b) are also almost symmetric except in the band gap, where we can see six instead of four peaks in diamond. The increased number of peaks is a result of the lowered symmetry in comparison to diamond. Furthermore, two of the six electrons are immersed in the valence band, so they are as well of no significant relevance. The other four electrons in the gap are distributed differently from they are in the NV center. In particular, we notice that the e_x and e_y electrons in the spin-up channel are no longer degenerate and the $a_1(2)$ electron (We use the same notations only for the convenience of comparison.) in the same channel now has a closer energy to the other two spin-up electrons. The three electrons interact to some

extent forming a continuous band of width about 0.53 eV. In the spin-down channel, one electron occupies the $a_1(2)$ energy level and the degeneracy of the empty e_x and e_y states is broken separating into two levels with an energy spacing of around 0.43 eV. The total spin moment of the NV center analog is the same as the NV center. This paramagnetic triplet state satisfies another criterion [357] to endow the NV center analog with the potential of hosting a new spin qubit.

Figure 5.5 compares the spin densities of the NV center in diamond and the NV center analog in C_3BN. As can be seen, the spin densities in both the NV center and its analog are highly localized in the C atoms near the vacancy, manifesting another similarity between the C_3BN and diamond. Localized states are often described better by the HSE06 functional than by the PBE functional [101,381]. Our results show that the SCAN functional can also capture this localization very well. The localized spin densities in NV center and its analog form bound states [357], ensuring them to behave as an "artificial atom" that is well protected from the environment and subject to convenient initialization, measurement, and readout.

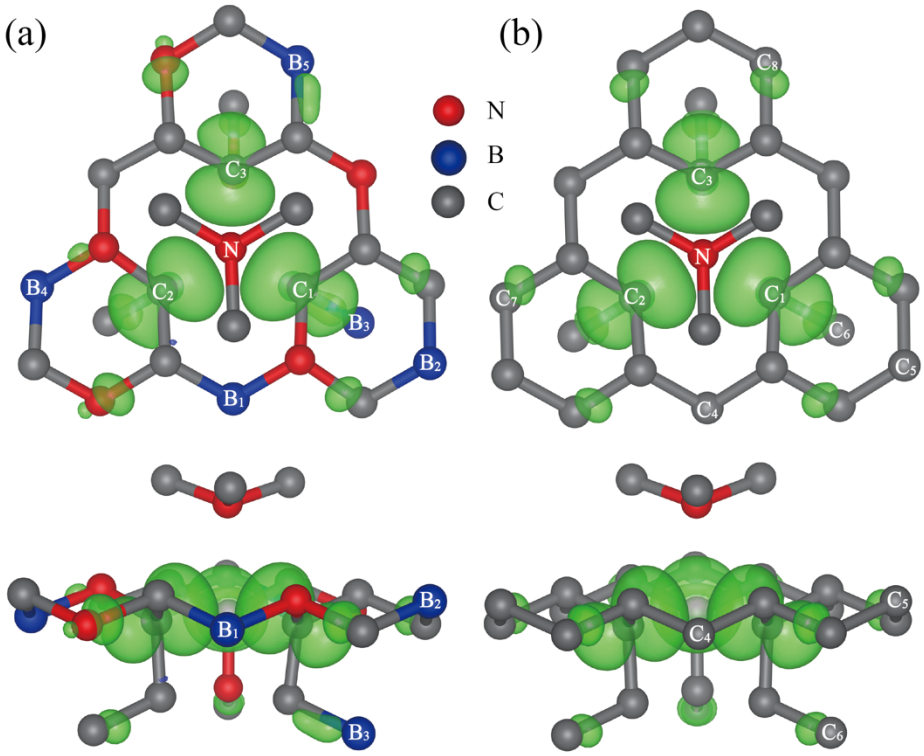

Figure 5.5. Spin density of (a) the NV center in diamond and (b) the NV center analog in C_3BN. The isosurface value is set to 0.005 e/a_0^3, where a_0 is the Bohr radius.

5.4.4 ZPL energy and hyperfine structure of the NV center analog in C_3BN

Because photoluminescence is the main optical approach to manipulate a paramagnetic spin qubit, three of the nine criteria summarized by Weber et al. are related to light-qubit interactions [357]. Over several decades of complimentary experimental and theoretical studies [382,383], a somewhat complete description of light-NV center interactions with fine details such as the non-radiative intersystem crossing is now available for the NV center in diamond. By contrast, the NV center analog in C_3BN has not yet been fabricated, we therefore focus on understanding the spin-conserving radiations

based on the energy diagrams shown in Figure 5.4. In particular, we predict the potential energy as function of configuration coordinate of the NV center analog in C_3BN, following the Frank-Condon approximation [384,385]. From the potential energy curves, we extract the critical information such as the ZPL energy that could be confirmed in future photoluminescence measurements. Owing to the broken degeneracy of the two spin-down excited states e_x and e_y in the NV center analog in C_3BN, there are two possible cases of spin-conserving optical transitions: case 1, transition from the spin-down $a_1(2)$ state to the spin-down e_x state; case 2, transition from the spin-down $a_1(2)$ state to the spin-down e_y state. We thus expect to observe two ZPL peaks for the NV center analog in C_3BN. We predict the ZPL energies and other states using the constrained DFT [386] as implemented in VASP. Figure 5.6 shows the sketches of potential energy curves for the NV center in diamond and for the two cases of the NV center analog in C_3BN. The curves for each system involved four states A, B, C, and D. State A is the ground state of the NV center or its analog; state B is the energy of placing the spin-down $a_1(2)$ electron at the spin-down e_x and e_y state without atomic relaxation; state C is the energy reduction from optimizing the structure of state B and this energy reduction corresponds to the Stokes shift (S). Placing the electron back to the $a_1(2)$ state followed by geometry optimizations leads to state D, whose energy is less than that of state C by an amount of the anti-Stock-shift (AS).

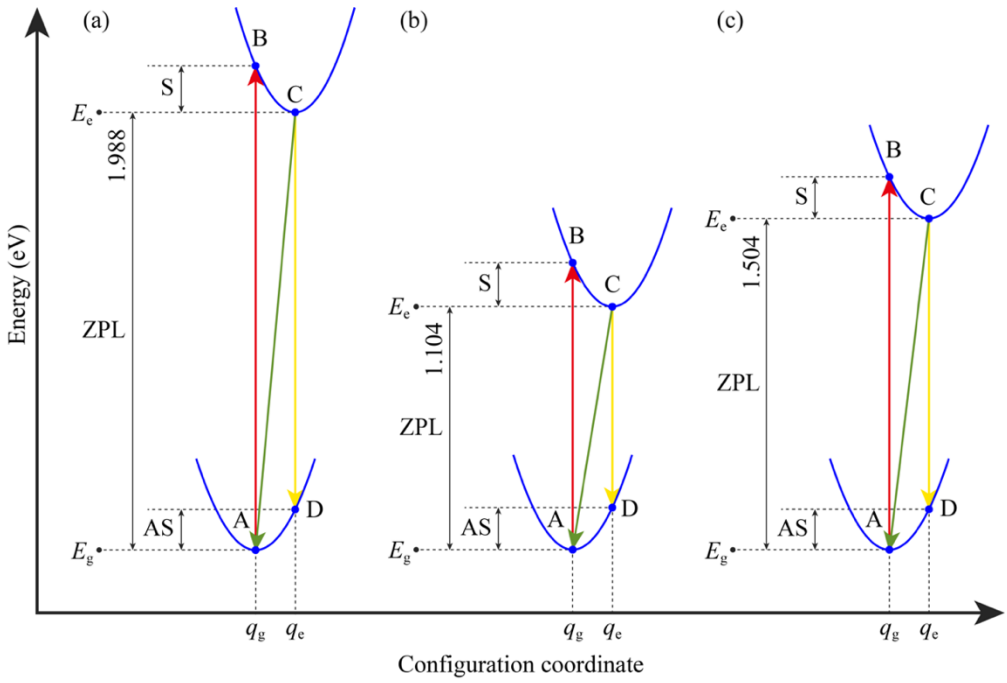

Figure 5.6. (a) Sketched potential energy curves of the NV center in diamond and of the NV center analog with (b) case 1 and (c) case 2 transitions.

Table 5.1 lists the ZPL energies, A→B and C→D transition energies, and the S and AS energies. We notice that these data for the NV center in diamond calculated using the SCAN functional is in excellent agreement with the results obtained from using the more time-consuming HSE06 functional [381] and also with the experimental data [387]. These promising results indicate that it is worthwhile using the SCAN functional to study other emerging candidates of point defects such as divacancy in 4*H*-SiC [388] for hosting spin qubits. Figure 5.6 and Table 5.1 reveal an attractive property of the NV center analog in C_3BN. That is, the ZPL energies in the two cases are much smaller than that of the NV center in diamond. These lower excitation energies, corresponding to the significantly

longer photon wavelengths of 1123 and 824 nm, respectively, which are closer to the ideal telecommunication band between 1310 nm (the "O-band") and 1550 nm (the "C-band") [389]. We therefore expect the NV analog in C_3BN to be advantageous over the NV center in experiencing less optical loss in optical fiber that connects qubits to form a quantum network.

Table 5.1. Zero-phonon line (ZPL) energy, A→B and C→D transition energies, and the Stokes (S) and anti-Stokes-shift (AS) of diamond and C_3BN computed with the SCAN functional. The notations are shown in Figure 5.6. Many data for the NV center in diamond are available. We show here two representative references for comparison: one from using the HSE06 hybrid density functional, the other from experimental data.

	ZPL	A→B	S	C→D	AS
Diamond[1]	1.988	2.199	0.211	1.804	0.184
Diamond[2]	1.955	2.213	0.258	1.738	0.217
Diamond[3]	1.945	2.180	0.235	1.760	0.185
C_3BN[4]	1.104	1.303	0.199	0.912	0.192
C_3BN[5]	1.504	1.693	0.189	1.320	0.184

[1]This work using the SCAN functional
[2]Ref. [381] using the HSE06 functional
[3]Ref. [387]; experimental data
[4]This work, case 1 transition, using the SCAN functional
[5]This work, case 2 transition, using the SCAN functional

Finally, we evaluate the hyperfine structure of the NV center and its analog. The

hyperfine interactions between the nuclear spin and the qubit spin are the main source that lead to the decoherence of spin qubits [390]. The sources of hyperfine interactions in diamond are isotopes ^{13}C and ^{14}N with nuclear spins of 1/2 and 1, respectively. An extra source in C_3BN is isotope ^{11}B with a nuclear spin of 3/2. Due to the high chance of presence of ^{13}C in the NV center [391], the hyperfine interactions have recently been employed for quantum error correction [392] and entanglement distillation [393]. In this context, stronger hyperfine interactions become a preferable property. In experiment, two of the three C atoms are ^{13}C and the third one is ^{12}C with no nuclear spin [394,395]. The two nuclear qubits along with the one spin qubit form a three-qubit register. We here consider an extreme scenario, where all the three C atoms near the vacancy are isotope ^{13}C. We calculate the hyperfine tensors that include the Fermi contact and dipole-dipole coupling terms [396]. The gyromagnetic ratios of these three isotopes (^{13}C, ^{14}N, and ^{11}B) are 10.7084 [397], 3.077 [397], and 13.7 [398], respectively, adopted as inputs for the calculations. Table 5.2 reports the computed hyperfine tensors of the nine atoms near the vacancy site in diamond and C_3BN. We can see that the three ^{13}C atoms exhibit the strongest hyperfine interactions in both systems whereas the ^{14}N atoms shows negligible hyperfine interactions. The hyperfine tensors of the C atoms in C_3BN are comparable and some of them are even higher than their counterparts in diamond, suggesting that a three-qubit register in C_3BN can also be employed for quantum error correction and entanglement distillation. Table 5.2 also shows that the hyperfine tensors for the other C atoms in diamond and the

corresponding B atoms in C_3BN are smaller by an order of magnitude, as these atoms are relatively further apart from the spin densities. We note that the hyperfine interaction because of ^{11}B cannot be removed via isotope engineering (unlike C in diamond which can be isotopically purified to have zero-spin ^{12}C), so we should expect small effects of ^{11}B atoms on the decoherence of the spin qubit in C_3BN.

Table 5.2. Principal values (in MHz) of the total hyperfine tensors of three C, one N, and five C/B atoms near the vacancy in diamond and C_3BN. The notations for these nine atoms are shown in Figure 5.5. The total hyperfine tensors are calculated using the SCAN functional.

	Diamond			C_3BN		
	A_{xx}	A_{yy}	A_{zz}	A_{xx}	A_{yy}	A_{zz}
C_1	147.959	147.696	231.746	172.525	171.442	263.850
C_2	147.959	147.696	231.747	150.745	150.240	234.171
C_3	147.959	147.696	231.747	135.154	134.460	205.614
N	-2.445	-1.939	-2.445	-1.125	-0.475	-1.204
C_4/B_1	4.041	2.457	4.128	2.398	1.258	3.489
C_5/B_2	-1.846	-1.003	-1.869	-0.888	0.101	-1.039
C_6/B_3	15.589	15.447	21.106	9.016	8.804	13.564
C_7/B_4	17.003	16.908	22.918	5.267	4.997	7.855
C_8/B_5	17.003	16.908	22.918	11.51	11.203	14.88

5.5 Summary

To summarize, we have shown that a negative charged (q = -1) B vacancy defect in a diamond-like compound C3BN forms an NV center analog that shares a number of common properties to the NV center in diamond. Specifically, the band structure computed from the SCAN functional exhibits a wide band gap of 3.75 eV and negligible SOC. The charged defect state is energetically stable in a wide range of Fermi energies. The ground state of this charged vacancy state has a total spin of 1 that can be manipulated via optical approaches to form a two-level system. These properties make C_3BN a promising semiconductor to host spin qubits made of the NV center analog for quantum information processing. We also showed that the experimental and HSE06 ZPL energies of the NV center in diamond are well reproduced using the SCAN functional. We therefore suggest this functional used for discovering other candidates of qubit host materials. Furthermore, we computed the ZPL energies of the NV center and its analog and found that the ZPL wavelengths of the NV center are longer and closer to the ideal telecommunication band wavelength, indicating less optical loss if the analog is used in a quantum network with multiple qubits. The computed hyperfine structures of the analog and the NV center are comparable and sufficiently strong to form a quantum register beneficial for quantum error correction. Exemplified by C_3BN, many other A_3XY compounds and their potential of hosting NV center analogs will be explored is our future work.

CHAPTER VII

TOWARDS OBTAINING 2D AND 3D AND 1D PTPN WITH PENTAGONAL PATTERN

6.1 Abstract

We apply an alloying strategy to single-layer PtN_2 and PtP_2, aiming to obtain a single-layer Pt-P-N alloy with a relatively low formation energy with reference to its bulk structure. We perform structure search based on a cluster-expansion method and predict single-layer and bulk PtPN consisting of pentagonal networks. The formation energy of single-layer PtPN is significantly lower in comparison with that of single-layer PtP_2. The predicted bulk structure of PtPN adopts a structure that is similar to the pyrite structure. We also find that single-layer pentagonal PtPN, unlike PtN_2 and PtP_2, exhibits a sizable, direct PBE band gap of 0.84 eV. Furthermore, the band gap of single-layer pentagonal PtPN calculated with the hybrid density functional theory is 1.60 eV, which is within visible light spectrum and promising for optoelectronics applications. In addition to predicting PtPN in the 2D and 3D forms, we study the flexural rigidity and electronic structure of PtPN in the nanotube form. We find that single-layer PtPN has similar flexural rigidity to that of single-layer carbon and boron nitride nanosheets and that the band gaps of PtPN nanotubes depend on their radii. Our work shed light on obtaining an isolated 2D planar, pentagonal PtPN nanosheet from its 3D counterpart and on obtaining 1D nanotubes with tunable bandgaps.

6.2 Introduction

Two-dimensional (2D) materials such as single-layer graphene and boron nitride hold great promise for a wide range of applications such as electronic devices [399,400], optoelectronic systems [401-403], and energy-related applications [404-406]. Hexagons dominate the building blocks of many 2D materials, which have issues such as the absence of anisotropy, a desirable feature for certain applications like photodetectors [407]. To introduce anisotropy, one may resort to 2D materials that adopt other shapes—in particular, pentagons—as their building blocks.

Because only 15 types of pentagons can tessellate an infinite plane and pentagons possess intrinsic anisotropy [408], 2D materials consisting of a pattern of pentagons represent an important addition to the large family of 2D materials whose structures are dominated by patterns of other shapes especially hexagons. As two most promising examples, single-layer PtN_2 and PtP_2 [409-412] have been predicted to exhibit a unique planar, pentagonal structure and attractive electronic structures such as direct band gaps calculated at the level of hybrid density functional theory—note that the band gaps at the level of Perdew-Burke-Ernzerhof (PBE) functional theory are negligibly small [410,413]. But the stability of the bulk counterparts of these two single-layer pentagonal materials and their formation energies are likely to prohibit successful synthesis or exfoliation. In particular, bulk PtN_2 with the pyrite structure is stable only at high pressures [414]. As a result, the formation energy of single-layer PtN_2 is unphysically negative (i.e., energy is gained from reducing bulk to single-layer PtN_2) if using the pyrite structure as the reference.

On the other hand, although bulk PtP_2 crystallizes as the pyrite structure at ambient conditions [415], the theoretical formation energy of single-layer PtP_2 could be too high (positive) to exist as an isolated nanosheet.

In this work, we apply density functional theory (DFT) calculations and a cluster expansion method to search for stable single-layer (2D) and bulk (3D) Pt-P-N alloys based on single-layer PtN_2 and PtP_2 by taking the advantage of the low formation energy of single-layer PtN_2 and stable bulk counterpart of single-layer PtP_2. In addition to designing 2D and 3D Pt-P-N alloys, we also examine the feasibility of obtaining 1D Pt-P-N nanotubes from bending 2D Pt-P-N nanosheets, with the goal of achieving tunable electronic structures.

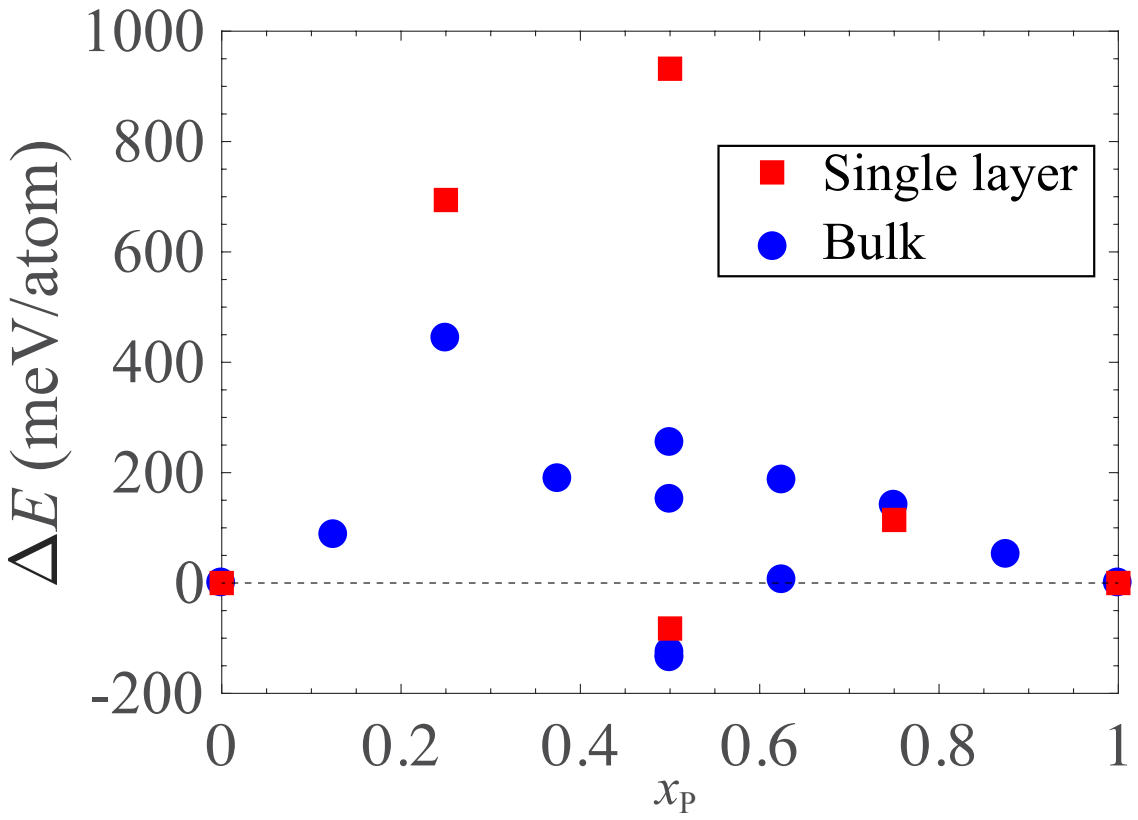

Figure 6.1. Energy difference ΔE as a function of the concentration of P x_P in single-layer and bulk PtPN with chemical formulas $Pt_2N_{4(1-x)}P_{4x}$ and $Pt_4N_{8(1-x)}P_{8x}$, respectively.

6.3 Simulation Methods

We perform the DFT calculations with the Vienna Ab-initio Simulation Package (VASP, version 5.4.4) [283,366]. We use the PBE functional for describing the exchange-correlation interactions [79]. We also use the standard Pt, P, and N potential datasets based on the PBE functional along with the projector-augmented wave (PAW) method [80,81]. Among the potentials, the $5d^9$ and $6s$ electrons of Pt atoms, the $3s^2$ and $3p^3$ electrons of P atoms, and the $2s^2$ and $2p^3$ electrons of N atoms are treated as valence electrons. We adopt the plane waves with the cut-off kinetic energy of 550 eV to approximate the electron wave

functions. We use Γ-centered 12 × 12 × 12, 12 × 12 × 1, and 9 × 1× 1 Monkhorst-Pack [82] *k*-point grids to sample the *k* points in the reciprocal space for 3D, 2D, and 1D PtPN, respectively. A vacuum spacing of 18.0 Å is applied to the surface slabs simulating isolated 2D and 1D PtPN. For 3D, 2D, and 1D PtPN, we optimize the atomic positions completely. Furthermore, for 3D PtPN, we relax all the lattice parameters; for 2D PtPN, we optimize the in-plane lattice constants; for 1D PtPN, we optimize the cell length along the axial direction. The force criterion for all of the geometry-optimization calculations is set to 0.01 eV/Å.

6.4 Results and Discussion

6.4.1 Structural and electronic properties of 2D single-layer PtPN

We first use the Alloy Theoretic Automated Toolkit (ATAT) to generate inequivalent structures of single-layer $Pt_2N_{4(1-x)}P_{4x}$ with five different concentrations x of P (x = 0, 0.25, 0.5, 0.75, and 1) and to automate the geometry optimizations and energy calculations [284]. The chemical formula written in this form is because each unit cell of single-layer PtN_2 and PtP_2 consists of two Pt atoms and four N/Pt atoms (each Pt atom is four-fold coordinated by N/P atoms; each N/P atom is three-fold coordinated by the same atoms). When x = 0 and 1, the systems correspond to single-layer PtN_2 and PtP_2, respectively. For x = 0.25, one P atom can replace any of the four N atoms in a unit cell, but all of the four structures are equivalent due to the four-fold rotational symmetry in single-layer PtN_2 and PtP_2. Therefore, only one of these four structures are optimized, and its energy is calculated.

For x = 0.5, there are two different structures with and without a center of inversion symmetry, respectively. Similarly, for x = 0.75, there is only one inequivalent structure. We compute the energy change ΔE of the following 'reaction':

$$(1-x)\mathrm{Pt_2N_4} + x\mathrm{Pt_2P_4} \rightarrow \mathrm{Pt_2N_{4(1-x)}P_{4x}} \quad (6.1)$$

By this definition ΔE = 0, when x = 0 or 1. Figure 6.1 shows the ΔE results for the six single-layer $Pt_2N_{4(1-x)}P_{4x}$ structures optimized from VASP calculations. We find that the structure with x = 0.5 is the most stable, corresponding to the chemical formula PtPN. The energy difference between single-layer PtPN and PtN_2 and PtP_2, i.e., $\Delta E = E_{PtPN}-(E_{PtN2} + E_{PtP2})/2$ is determined as ΔE = -82 meV/atom. Figure 6.2 shows the top and side views of a 3 × 3 × 1 supercell of this structure. Similar to single-layer PtN_2 and PtP_2, single-layer pentagonal PtPN exhibits a completely planar structure and the optimized in-plane lattice constants a and b are 5.30 and 5.29 Å, respectively.

The optimized structure of single-layer PtPN exhibits no four-fold rotational symmetry, so the two in-plane lattice constants are not identical. As a result, instead of observing a pattern of same pentagons as in single-layer PtN_2 and PtP_2—these pentagons below to the same type and the tessellation pattern from this type of pentagons is called the Cairo tessellation, there are two different types of pentagons in single-layer PtPN. Table 6.1 lists the side lengths (bond lengths) and angles (bond angles) forming the two distinct pentagons illustrated in Figure 6.2(a). Referring to the definitions for the 15 types of pentagons that can monohedrally tile a plane [416], neither of the two types of pentagons

in single-layer PtPN belongs to any of the 15 types. Therefore, the geometry of PtPN shows an example that a plane can still be tiled gaplessly by a combination of different types of pentagons from the 15 ones, retaining the anisotropy for a 2D material.

We next examine the dynamical stability of the predicted structure of single-layer PtPN. Figure 6.3 shows the computed phonon spectrum of single-layer PtPN. The real phonon frequencies confirm the dynamical stability of the completely planar structure of single-layer PtPN.

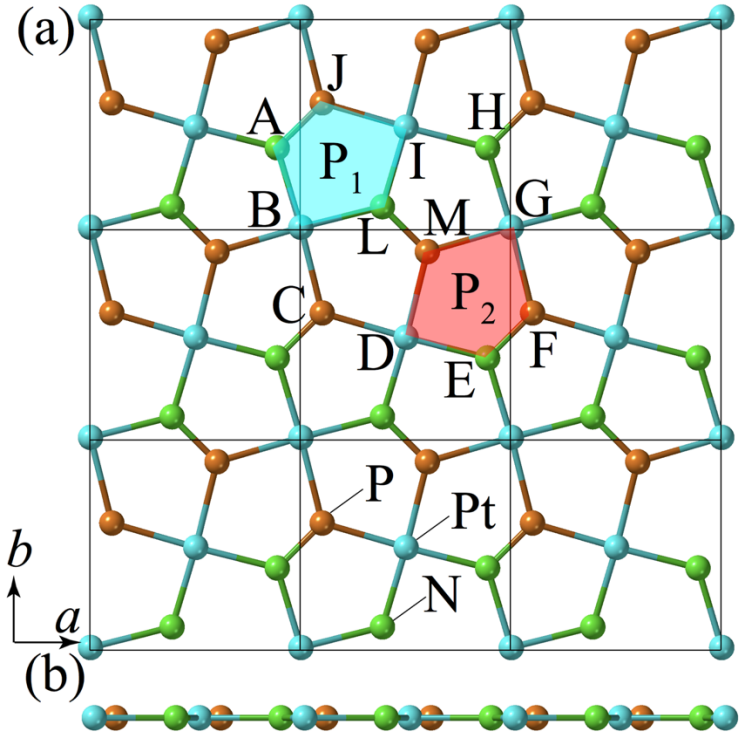

Figure 6.2. (a) Top and (b) side views of a 3 × 3 × 1 supercell of single-layer PtPN. Two distinct pentagons denoted as P_1 and P_2 are enclosed in the cyan and red shaded areas.

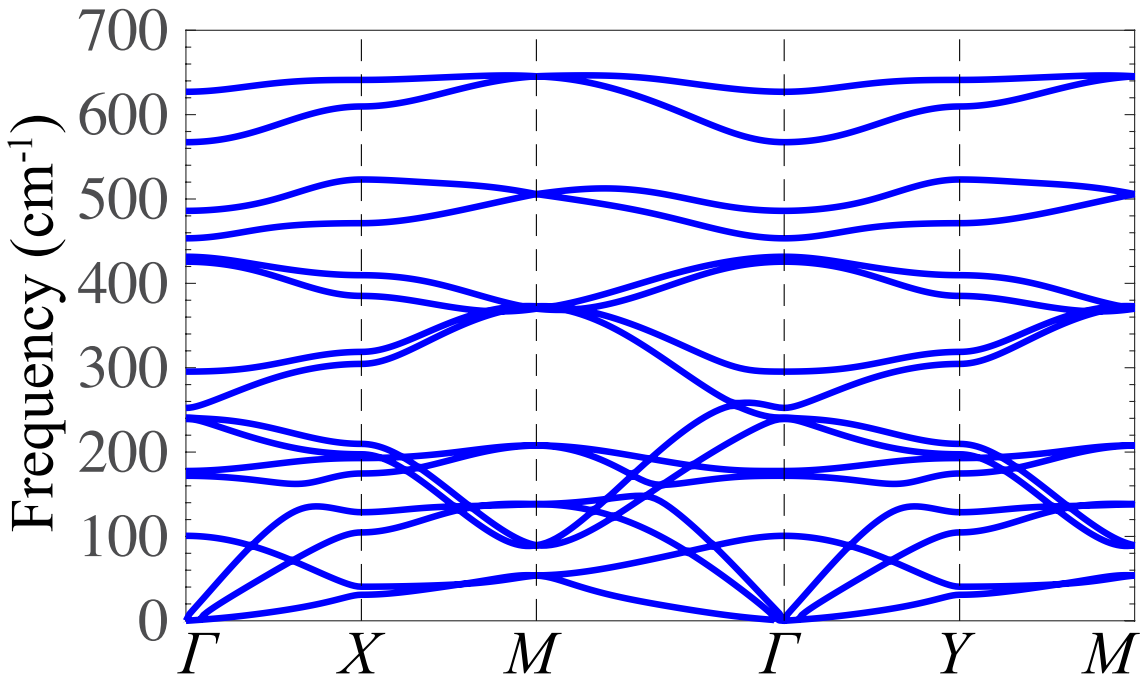

Figure 6.3. Predicted phonon spectrum of single-layer PtPN.

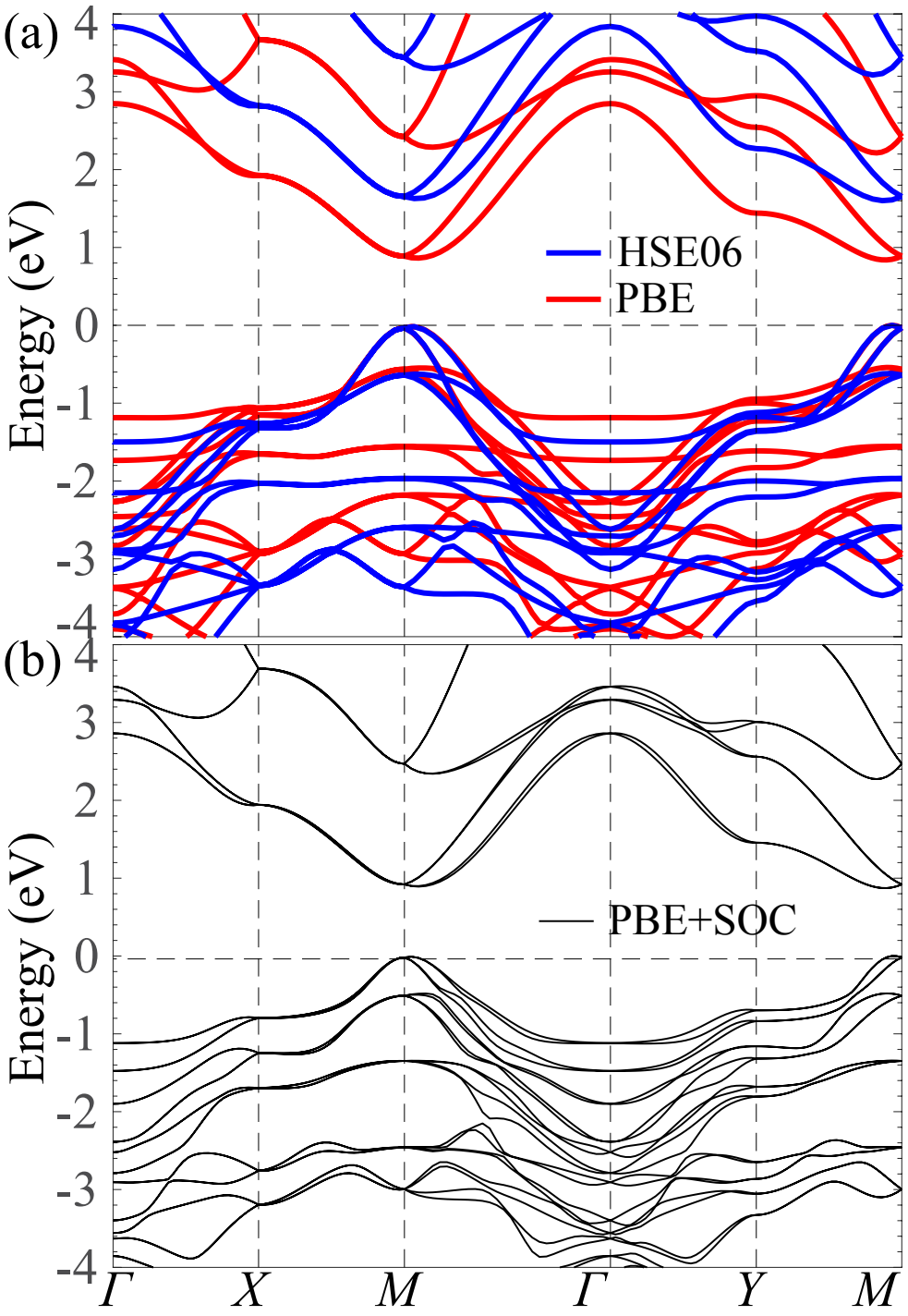

Figure 6.4. Band structures of single-layer PtPN calculated (a) with the PBE and HSE06 functionals and (b) with the PBE functional considering spin-orbit coupling (SOC).

Table 6.1. Bond lengths (in Å) and angles (in degrees) of the two distinct pentagons P_1 and P_2 embedded in the atomic structure of single-layer pentagonal PtPN (see Figure 6.2(a)).

Pentagon	AB	BL	LI	IJ	JA
P_1	2.09	2.12	2.09	2.20	1.60
	ED	DM	MG	GF	FE
P_2	2.12	2.22	2.20	2.22	1.60
Pentagon	∠ABL	∠BLI	∠LIJ	∠IJA	∠JAB
P_1	92.47	120.80	89.54	118.88	118.32
	∠EDM	∠DMG	∠MGF	∠GFE	∠FED
P_2	90.21	120.13	87.78	121.00	120.88

Figure 6.4(a) shows the band structures of single-layer PtPN calculated with the PBE and Heyd-Scuderia-Ernzerhof (HSE06) [93] functionals. Unlike single-layer PtN_2 and PtP_2, where the PBE band gaps are nearly zero [409-412], the PBE band gap of single-layer PtPN has already shown a direct band gap of 0.84 eV. The conduction band minimum (CBM) and valence band maximum (VBM) both locate at a *k* point near the M point. Using the HSE06 hybrid density functional theory corrects the band gap to 1.60 eV, much larger than the HSE06 band gaps of single-layer pentagonal PtN_2 (1.11 eV) [413] and PtP_2 (0.52 eV) [410]. The HSE06 band gap indicates that single-layer PtPN is promising for optoelectronics applications that can utilize the direct band gap within visible light

spectrum. Considering spin-orbit coupling (SOC) leads to the band structure shown in Figure 6.4(b). We observe that SOC splits the bands at some *k* points, but the bands near the CBM and VBM are almost unaffected. Comparing with single-layer PtN_2 and PtP_2, the enhanced band gaps in single-layer PtPN may be correlated with the bonding characteristics, which can be revealed from the electron localization function (ELF) shown in Figure 6.5(a). For comparison, Figure 6.5 (b) shows the ELF for single-layer PtN_2, which is consistent with the ELF in Ref. [412]. Different from single-layer PtN_2 and PtP_2 showing both ionic and covalent bonding characteristics [409-412], the bonding type in single-layer PtPN is dominantly ionic. The existence of a covalent bond (e.g., the N-N bond with shared electrons) reduces the number of electrons that can be transferred between dissimilar atoms (e.g., Pt and N atoms in single-layer PtN_2), leading to the weakened ionic Pt-N bond in PtN_2 in comparison with the same bond in PtPN. Ionic bond (e.g., in BN) is often associated with large band gaps due to the large charge transfer between cations and anions.

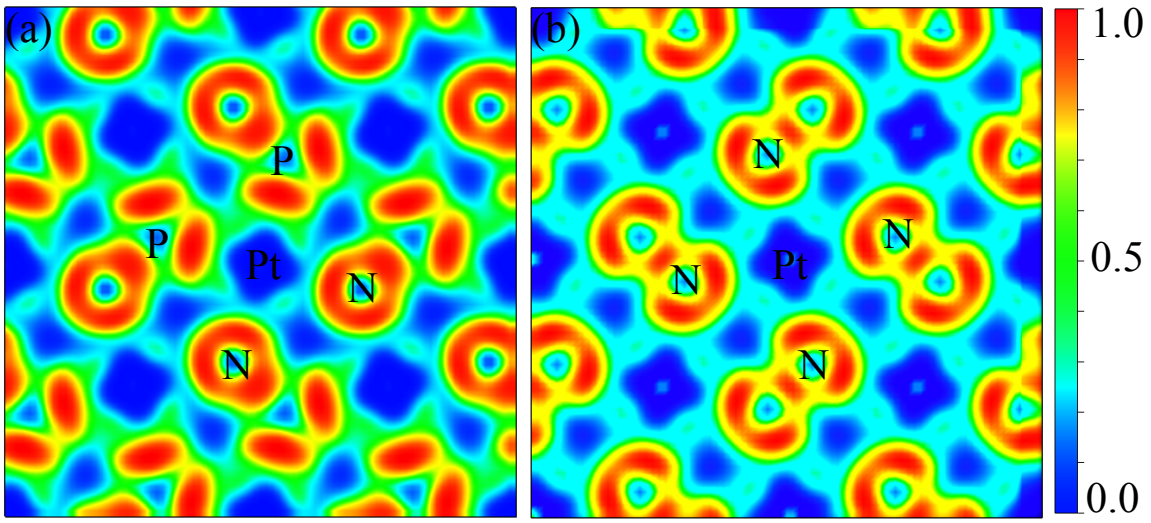

Figure 6.5. Electron localization function of single-layer (a) PtPN and (b) PtN_2.

6.4.2 3D Bulk counterpart of PtPN

Having predicted the stable structure of single-layer PtPN and its attractive direct band gap, we aim to predict the bulk counterpart from which single-layer PtPN could be exfoliated. The existence of a bulk counterpart appears to be a necessary condition for all the 2D materials that have been successfully synthesized or exfoliated. We apply ATAT again to enumerate all the possible bulk structures at different concentrations of P for bulk $Pt_4N_{8(1-x)}P_{8x}$ in a 12-atom unit cell. We compute the ΔE for the following 'reaction':

$$(1-x)\mathrm{Pt_4N_8} + x\mathrm{Pt_4P_8} \rightarrow \mathrm{Pt_4N_{4(1-x)}P_{4x}} \quad (6.2)$$

Figure 6.1 display all the ΔE results. Similar to the single-layer cases, the most stable bulk compound occurs at x = 0.5, and the structure is illustrated in Figure 6.6. This bulk structure is nearly a cubic structure with space group $Pca2_1$ and the lattice constants are 5.301, 5.301, and 5.305 Å, respectively. Moreover, the bulk structure resembles the pyrite

structure adopted by bulk PtP_2 [415]. Namely, viewing along the *a*/*b*/*c* axis, the bulk structure can be regarded stacked PtPN single layers with a buckled structure. In contrast to PtP_2, the stable bulk structure of PtN_2 remains unclear. If assuming bulk PtN_2 also adopts the pyrite structure, we encounter an incorrect conclusion that single-layer PtN_2 is more stable than bulk PtN_2 with the pyrite structure [413]. We recently proposed a new structure of bulk PtN_2 with layered structure. We recently proposed a new structure of bulk PtN_2 with layered structure. We also compute the energy of bulk PtPN with a similar layered structure, but it is higher than that of bulk PtPN with the pyrite-type structure by 180 meV/atom, confirming that the latter structure is the most stable one.

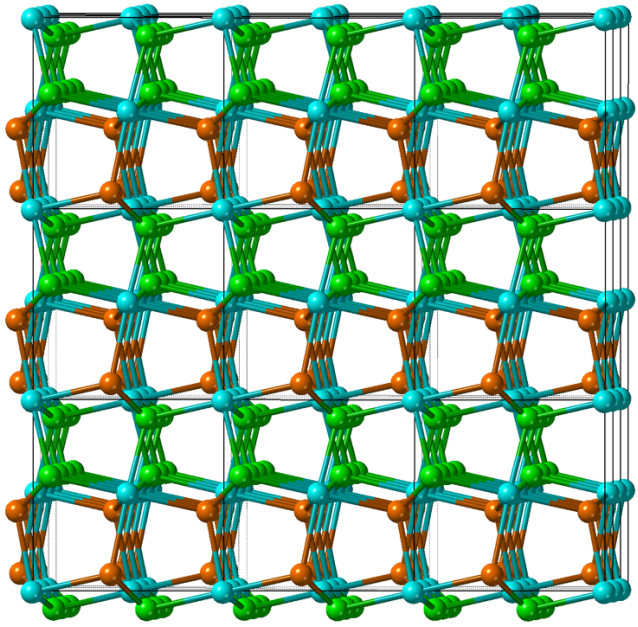

Figure 6.6. A 3 × 3 × 3 supercell of the predicted bulk structure of PtPN.

With the predicted stable structure of bulk PtPN, we calculate the formation energy of

single-layer PtPN, namely the energy difference between single-layer PtPN and the stable bulk structure. We find that the formation energy is 174 meV/atom, which is much smaller than that (410 meV/atom calculated with the PBE functional) [410] of single-layer pentagonal PtP_2. The formation energy of a 2D material at this scale often implies the 2D material could be exfoliated if the bulk counterpart exists or synthesized if there is no bulk counterpart [417]. The small theoretical formation energy of single-layer PtPN suggests a possible route to obtain this single-layer material, i.e., alloying the stable bulk PtP_2 compound by N atoms to obtain the bulk structure of PtPN and then applying the mechanical exfoliation method to the ternary bulk compound to acquire single-layer sheets of PtPN. Alternatively, it is also worth attempting the molecular beam epitaxy method [418] to obtain the single-layer sheets.

Figure 6.7 shows the PBE band structure of bulk PtPN with the pyrite-type structure. As can be seen, it is semiconducting with an indirect band gap of 1.21 eV. Bulk PtN_2 and PtP_2 with the pyrite structure are also found to have indirect PBE band gaps of 1.35 [413] and 1.06 eV [410], respectively. It seems to be expected that the band gap of bulk PtPN lies between those of bulk PtN_2 and PtP_2. This trend also holds as the HSE06 band gaps of bulk PtN_2, PtPN, and PtP_2 are 2.22 [413], 1.76, and 1.59 eV [410], respectively. For the three materials, one common feature is the decrease in their band gaps due to the dimension reduction—the PBE band gaps of single-layer PtN_2 and PtP_2 are so small that they should probably be regarded as metallic [413]. The PBE functional therefore not only

underestimates the band gap of single-layer PtPN, but also performs poorly in determining the electronic structures (metallic or semiconducting) of single-layer PtN_2 and PtP_2 possibly due to their four-fold rotational symmetry, leading to the degenerate energy levels at the M point and at the Fermi level. By contrast, all the single-layer forms of these three systems have direct band gaps at the HSE06 hybrid density functional level of theory and the HSE06 band gap of single-layer PtPN no longer lies between those of single-layer PtN_2 and PtP_2.

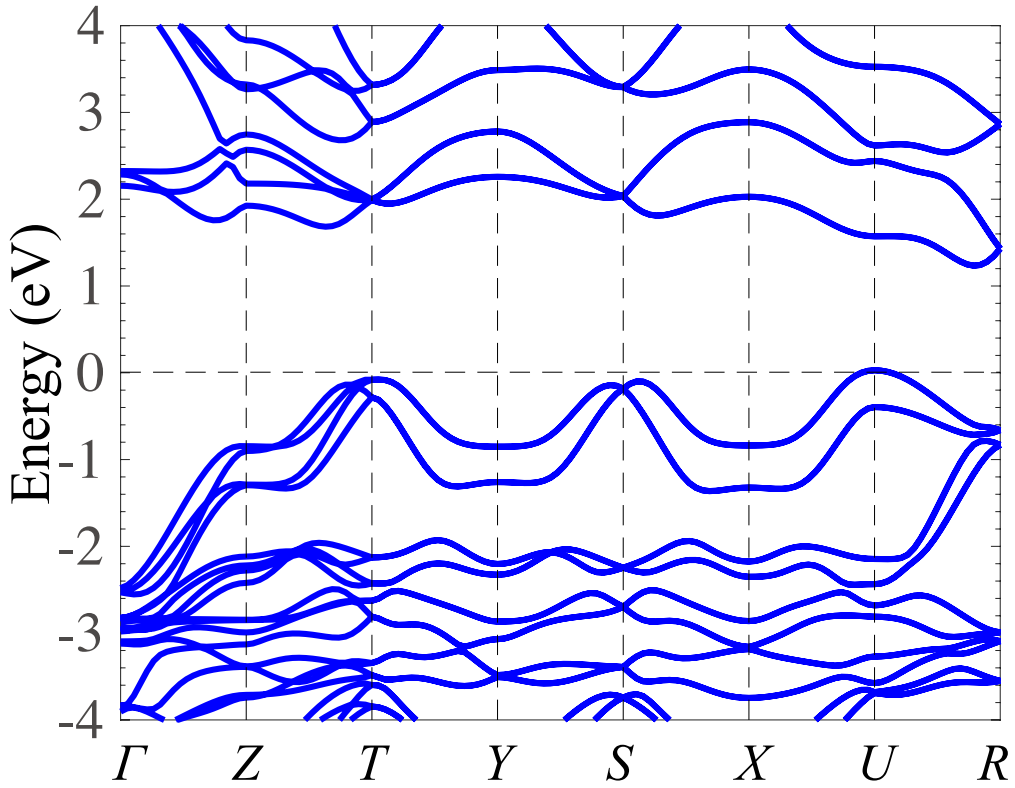

Figure 6.7. Band structure of bulk PtPN calculated with the PBE functional. The fractional coordinates of the high-symmetry k-points are Γ (0, 0, 0), Z (0, 0, 1/2), T (0, 1/2, 1/2), Y (0, 1/2, 0), S (1/2, 1/2, 0), X (1/2, 0, 0), U (1/2, 0, 1/2), R (1/2, 1/2, 1/2).

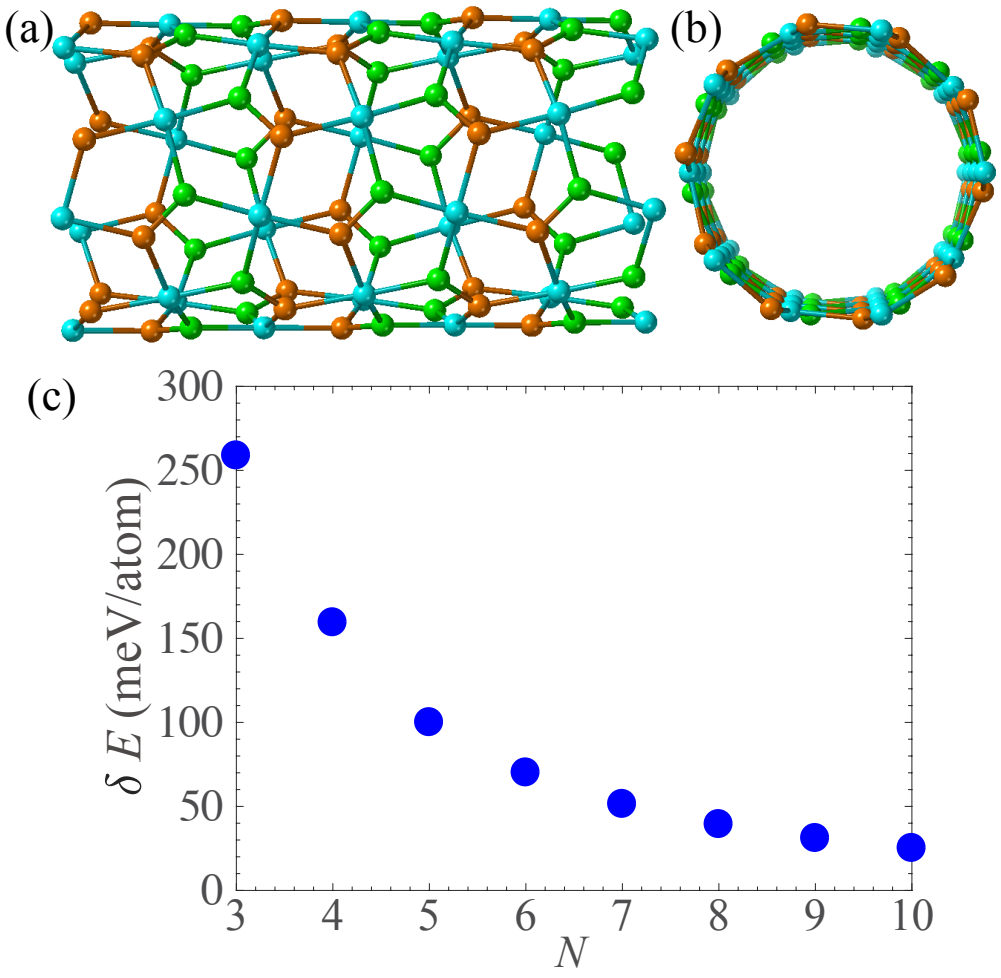

Figure 6.8. (a) Side and (b) top views of a PtPN nanotube. (c) Energy difference of PtPN nanotubes with reference to single-layer PtPN as a function of N, which determines the number of unit cells of single-layer PtPN that form a nanotube.

6.4.3 Tunable band gap in 1D PtPN nanotube

If 3D and 2D PtPN can be obtained, one naturally continues to explore the structures and properties of 1D PtPN, i.e., PtPN nanotubes. We create the simulation models of PtPN nanotubes by bending a $N \times 1 \times 1$ (N ranges from 3 to 10) supercell of single-layer PtPN

about the *b* axis into a tube (see Figure 6.8(a) and (b)). The integer *N* therefore determines the radius *R* of a PtPN nanotube. Because the unit cell of single-layer PtPN is nearly in a square shape, bending about the *a* axis results in nearly the same PtPN nanotubes. We first assess the energy change δE from 2D to 1D PtPN as a function of *N*. δE stands for the average energy change between a flat atomic layer and a nanotube due to the change in curvature, which represents the energy required per atom to bend the flat PtPN nanosheet into the PtPN nanotubes of different radii [419]. Figure 6.8(c) shows that δE decreases as *N* increases and the decrease is more significant when the *N* values are small. As *N* is close to infinity, the nanotubes are similar to single-layer sheets and δE therefore approaches to zero.

To quantify the feasibility of obtaining PtPN nanotubes from single-layer PtPN sheets, we convert *N* to *R* and adopt the following model describing the relationship between δE and R^{-2} [420,421]:

$$\delta E = \frac{D}{2} R^{-2} \tag{6.3}$$

where *D* is called the flexural rigidity also known as the bending stiffness of nanotubes. *D* is a metric of the requirement of a force couple to bend the nanosheet per unit curvature [422]. The flexural rigidity of single-layer PtPN nanosheet arises from the combined effects of the resistance from both in-plane bond angle changes and out-of-plane electron clouds overlapping from Pt, P, and N atoms [423]. Figure 6.9 shows the variation of δE with R^{-2} for PtPN nanotubes. In our recent work, we calculated δE for armchair and zigzag C and

BN nanotubes obtained from bending their nanosheets [413]. We therefore plot the same variations for C and BN nanotubes shown in Figure 6.9. By linear fitting the δE and R^{-2} data to Eq.6.3, we compute and list D for the different systems in Table 6.2. The D results of both C and BN nanotubes are consistent with previous work [420]. We also observe that the D values for PtPN, C, BN nanotubes are comparable and the flexural rigidity of the PtPN nanotubes lies between those of C and BN nanotubes, which have both been available in experiment [424], indicating that it is also feasible to obtain PtPN nanotubes.

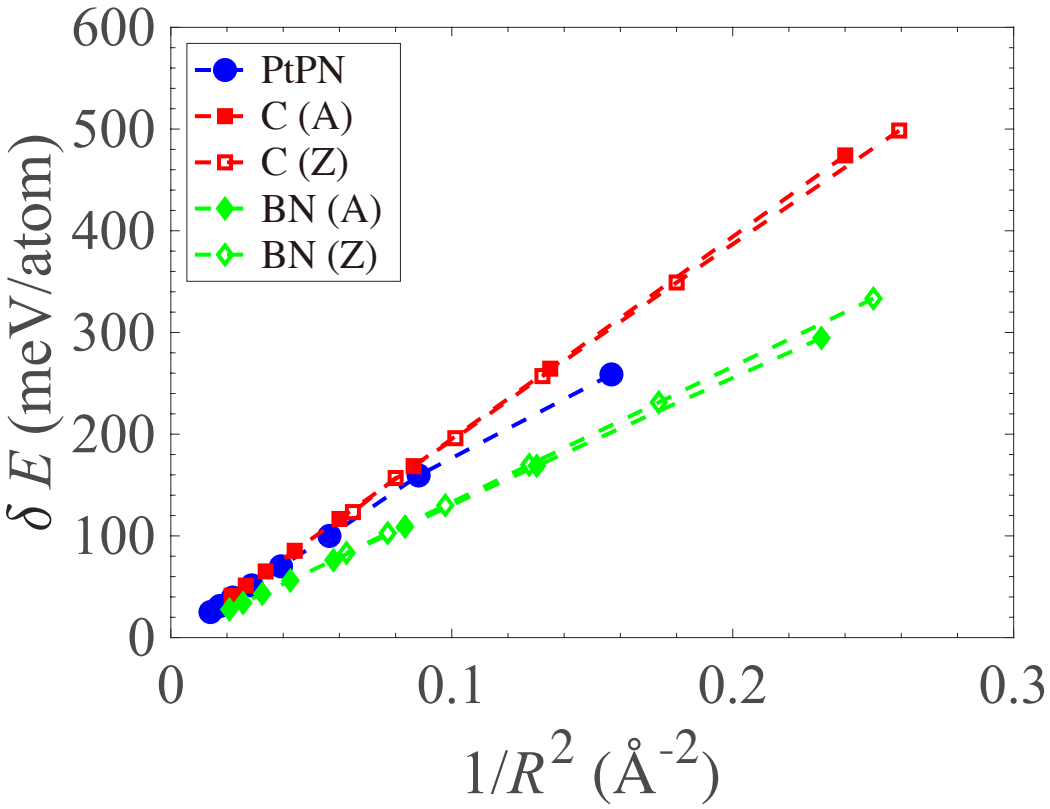

Figure 6.9. Variation of energy difference δE of PtPN nanotubes with reference to their corresponding 2D sheets with 1/ R^{-2}, where R denotes the radii of the nanotubes. A and Z in the brackets stand for armchair and zigzag, respectively.

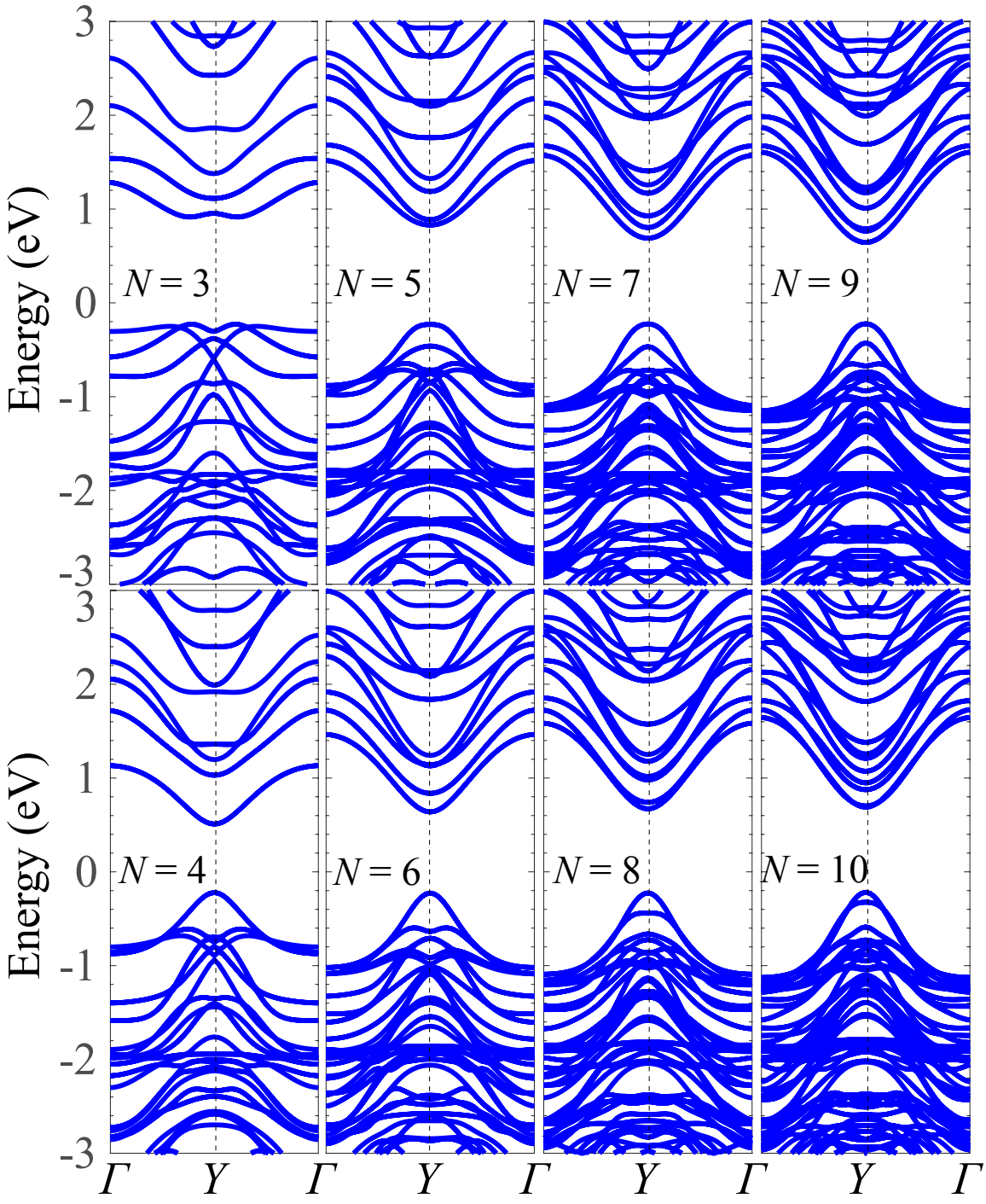

Figure 6.10. PBE band structures for PtPN nanotubes formed from $N \times 1 \times 1$ supercells of single-layer PtPN.

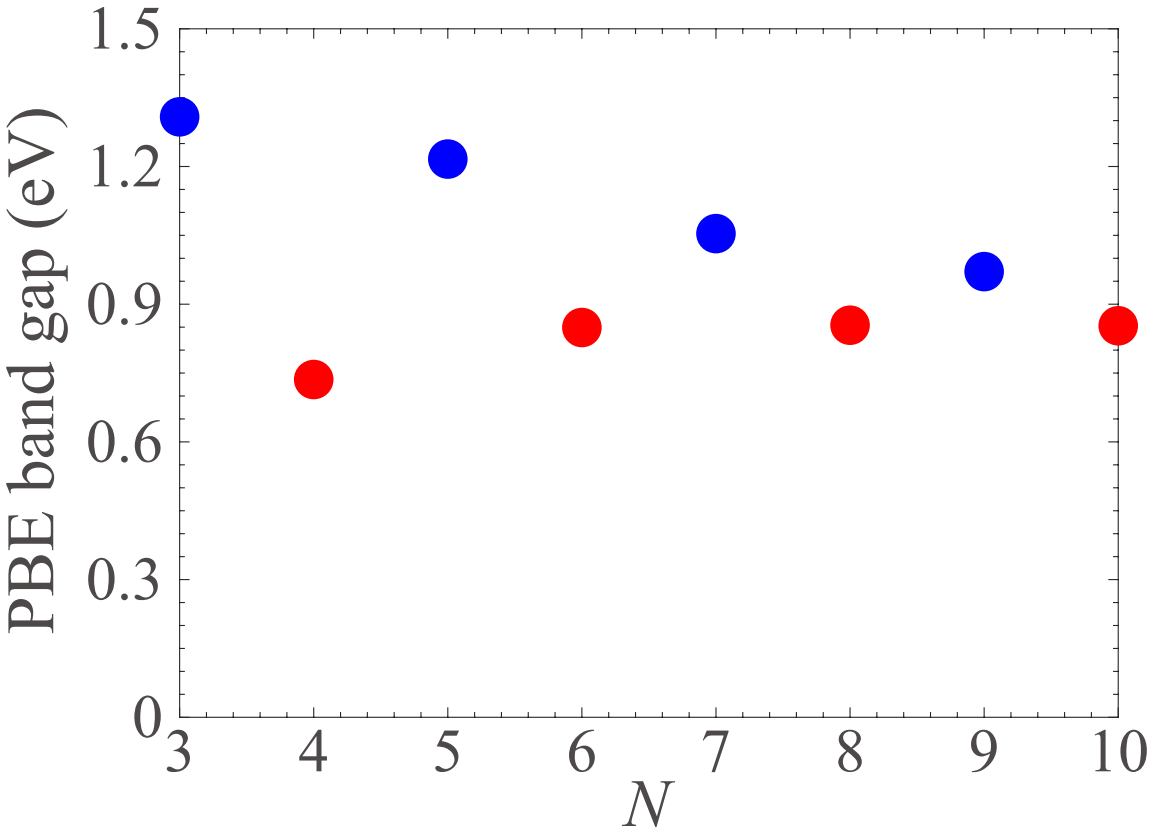

Figure 6.11. Dependence of PBE band gaps of PtPN nanotubes on N, which determines the number of unit cells of single-layer PtPN that form a nanotube.

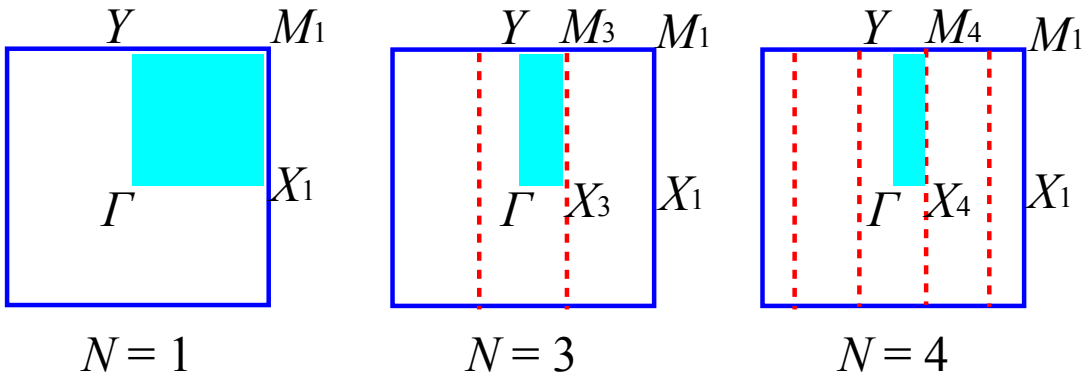

Figure 6.12. A quarter of the first Brillouin zones (represented by the cyan shaded areas) of $N \times 1 \times 1$ ($N = 1$, 3, and 4) supercells of single-layer PtPN. The red dashed lines divide

the first Brillouin zone (enclosed by the solid blue lines) of a unit cell of single-layer PtPN into N equal portions.

Table 6.2. Predicted flexural rigidity D (in eV·Å^2/atom) of C, BN, and PtPN nanotubes. A and Z in the brackets represent armchair and zigzag, respectively.

C (A)	C (Z)	BN (A)	BN (Z)	PtPN
3.96	3.85	2.54	2.67	3.31

Finally, we calculate the PBE band structures of the eight PtPN nanotubes shown in Figure 6.10, revealing that all of these nanotubes are direct-gap semiconductors. The variation of the band gaps of the PtPN nanotubes with N is shown in Figure 6.11. We observe that as N increases, the band gaps of PtPN nanotubes with odd and even N values decrease and increase, respectively, and appear to converge to a constant (~0.9 eV, close to the PBE band gap, 0.84 eV, of single-layer PtPN) if N is beyond 10. A similar dependence of band gaps on N is also found in NiP_2 nanotubes [425]. Furthermore, the band gaps of the PtPN nanotubes with odd N are wider than the nanotubes with even N. The relationship between the band gaps and N shows that controlling the radii of PtPN nanotubes can tune their band gaps.

To understand the larger band gaps of PtPN nanotubes when N is odd, Figure 6.12 shows the high-symmetry k points Γ, X_N, M_N, and Y in the first Brillouin zones of single-layer PtPN represented by $N \times 1 \times 1$ (N = 1, 3, and 4) supercells. For N = 1, the X_1 and M_1

points are the same as the X and M points, respectively, as denoted in Figure 6.4. The band gap at the M point is smaller than that at the X point calculated with either the PBE or HSE06 functional. When N is larger and odd, e.g., $N = 3$, the first Brillouin zone shrinks by three times, and the wave vectors and their corresponding energy levels along the X_1-M_1 direction are zone-folded to the X_3-M_3 direction, different from the Γ-Y direction that is common for any $N \times 1 \times 1$ supercell. By contrast, if N is even, e.g., $N = 4$, the energy levels for the wave vectors along the X_1-M_1 direction will overlap with the energy levels of the wave vectors along the Γ-Y direction. As a result, we can observe the band gap (originally at the M point) along the Γ-Y direction. For PtPN nanotubes, only the wave vectors along the Γ-Y direction are allowed, so the even and odd N lead to the occurrence and absence of the overlap along the Γ-Y direction, respectively. The band gaps of PtPN nanotubes with odd N are therefore wider than those of PtPN nanotubes with even N.

6.5 Summary

In summary, we predict a single-layer alloy PtPN with DFT calculations. This novel single-layer material consists of a pentagonal pattern and is completely planar and dynamically stable. We also find that single-layer PtPN exhibits direct band gaps of 0.84 and 1.60 eV calculated with the PBE and HSE06 functionals, respectively. Given the generally more accurate band gaps described by a hybrid density functional, the HSE06 band gap ensures a variety of promising optoelectronics applications of single-layer PtPN. We suggest that single-layer PtPN can be obtained from exfoliating bulk PtPN with a

relatively low energy and the bulk pyrite-type structure can be acquired from alloying bulk PtP_2 with N atoms. We finally show that bending single-layer PtPN into the nanotube form result in nanotubes that exhibit tunable band gaps dependent on the radii of the nanotubes.

CHAPTER VIII

DIMENSION ENGINEERING OF SINGLE-LAYER PTN_2 WITH THE CAIRO TESSELLATION

7.1 Abstract

Single-layer PtN_2 exhibits an intriguing structure consisting of a tessellation pattern called the Cairo tessellation of type 2 pentagons, which belong to one of the existing 15 types of convex pentagons discovered so far that can monohedrally tile a plane. Single-layer PtN_2 has also been predicted to show semiconducting behavior with direct band gaps. Full exploration of the structure-property relationship awaits the successful exfoliation or synthesis of this novel single-layer material, which depends on the structure of its bulk counterpart with the same stoichiometry to some extent. Bulk PtN_2 with the pyrite structure is commonly regarded as the most stable structure in the literature. But comparing the energies of single-layer PtN_2 and bulk PtN_2 leads to a dilemma that a single-layer material is more stable than its bulk counterpart. To solve this dilemma, we propose stacking single-layer PtN_2 sheets infinitely to form a new bulk structure of PtN_2. The resulting tetrahedral layered structure is energetically more stable than the pyrite structure and single-layer PtN_2. We also find that the predicted bulk structure is metallic, in contrast to the semiconducting pyrite structure. In addition to predicting the 3D structure, we explore the possibility of rolling single-layer PtN_2 sheets into nanotubes. The required energies are comparable to those needed to form carbon or boron nitride nanotubes from their single-layer sheets,

implying the feasibility of obtaining PtN_2 nanotubes. We finally study the electronic structures of PtN_2 nanotubes and find that the band gaps of PtN_2 nanotubes are tunable by changing the number of unit cells N of single-layer PtN_2 used to construct the nanotubes. Our work shows that dimension engineering of PtN_2 not only leads to a more stable 3D structure but also 1D materials with novel properties.

7.2 Introduction

A number of two-dimensional (2D) materials have been predicted and recorded in various databases such as the computational 2D materials database [317] and Materialsweb [426]. But many of these materials, in spite of their exotic properties, exhibit no known bulk counterparts especially those with the same stoichiometry, making it challenging to obtain these 2D materials. Being such an example, single-layer platinum nitride PtN_2 has recently been predicted in several theoretical studies [409,411,412]. The reason for the uniqueness of this single-layer material is twofold: First, the structure as illustrated in Figure 7.1(a) is completely planar with a tessellation of type 2 pentagons that are able to tessellate a plane; This tessellation is called the Cairo tessellation, as it appears in the streets of Cairo [427]. Second, it is a semiconductor with predicted high carrier mobility and Young's modulus [409]. The peculiar structure and properties of single-layer PtN_2 call for its synthesis, which largely rely on the existence of stable structure of bulk PtN_2.

Even without in the above context of single-layer PtN_2, bulk PtN_2 on its own has attracted considerable attention as an example in the family of transition-metal nitrides,

which generally possess notable electrical, mechanical, and thermal properties [428-430].

The pyrite structure of bulk PtN_2 is commonly regarded as the most stable [414,429,431,432]. Figure 7.1(b) illustrates the pyrite structure, consisting of Pt atoms occupying the lattice sites of a face-centered cubic (FCC) lattice and each Pt atom is six-fold coordinated with N atoms to form corner-sharing Pt-N octahedra. Two other possible structures including the fluorite (as shown in Figure 7.1(c)) and marcasite (as shown in Figure 7.1(d)) structures have also been studied [431,433,434]. In the fluorite structure, Pt atoms are also located at the FCC lattice sites, but each Pt atom has eight nearest neighboring N atoms. In the marcasite structure, the Pt and N atoms also form corner-sharing Pt-N octahedra, but the Pt atoms occupy the sites of a body-centered tetragonal lattice.

In addition to 2D materials, 1D nanotubes have sparked wide interest since the discovery of carbon nanotubes (CNTs) [435,436]. Their mechanical, electrical, and optical properties can be tuned by modifying the diameters and chirality [437], making CNTs promising for a wealth of applications [438], such as field emission electron source [436] and light-emitting diodes [439]. Successful fabrication of CNTs indicates the feasibility of obtaining non-carbon nanotubes based on other single-layer materials. Indeed, extensive experimental and theoretical research has been extended to study boron nitride BN, carbonitrides $B_xC_yN_z$, and transition-metal dichalcogenides MX_2 (M and X represent transition-metal and chalcogen elements, respectively) nanotubes [440-442].

Although many 2D materials and their structures have been predicted based on the bulk counterparts of these 2D materials with the same stoichiometry, we revert this process in this work by first showing a counter-intuitive result that single-layer PtN_2 is more energetically stable than bulk PtN_2 with the pyrite structure. We then study the interactions between two layers of PtN_2 and suggest a layered structure with on-top stacking of single-layer PtN_2 sheets as the more stable bulk structure. Furthermore, due to the above-mentioned excellent properties of nanotubes, we explore the structure-property relationships of PtN_2 nanotubes.

7.3 Simulation Methods

All the DFT calculations are performed using the Vienna Ab initio Simulation Package (VASP, version 5.4.4) [283,366]. We apply the Perdew-Burke-Ernzerhof (PBE) functional to approximate the exchange-correlation interactions [79]. We use Grimme's DFT-D3 method to describe the van der Waals (vdW) interactions in bilayer PtN_2 and our proposed layered structure of bulk PtN_2 [443]. We also use the optB88-vdW functional to compare against the accuracy of some of the DFT-D3 results [444-446]. We use the standard potential datasets created with the PBE functional for Pt and N generated according to the projector augmented wave method [80,81]. These datasets treat the $5d^9$ and $6s$ electrons of Pt atoms and the $2s^2$ and $2p^3$ electrons of N atoms as valence electrons. Plane waves with their cut-off kinetic energies below 550 eV are used to approximate the electron wave functions. We use a Γ-centered 12 × 12 × 1 Monkhorst-Pack [82] *k*-point grid for single-

layer and bilayer PtN_2, and a 12 × 12 × 12 grid for bulk PtN_2 with the pyrite, fluorite, marcasite, and AB-stacked structures, and a 12 × 12 × 15 grid for bulk PtN_2 with the tetragonal AA-stacked layered structure, and a 9 × 1 × 1 grid for PtN_2, carbon, and boron nitride nanotubes, to sample the *k* points in the reciprocal space. A sufficiently large vacuum spacing (>18.0 Å) is applied to the slabs of single-layer and bilayer PtN_2 and nanotubes to avoid the image interactions due to the periodic boundary conditions. The lattice constants and atomic coordinates of bulk PtN_2 with different structures are completely optimized. For single-layer and bilayer PtN_2, we optimize the in-plane lattice constant and the atomic positions. For the PtN_2 nanotubes, we relax only the lattice constant along the tube direction and the atomic positions. The force threshold value for all of these geometry optimizations is the same, i.e., 0.01 eV/ Å.

7.4 Results and Discussion

7.4.1 Structural and electronic properties of 2D single-layer PtN_2

We first benchmark our calculations on single-layer PtN_2 with previous theoretical studies. Our calculated in-plane lattice constant (4.81 Å) is consistent with the reported results (4.80 [409], 4.81 [411], and 4.83 [412] Å). For the electronic structure, Figure 7.2(a) shows the density of states (DOS) of single-layer PtN_2 calculated with the PBE and HSE06 functionals. The PBE functional seriously underestimates the band gap of single-layer PtN_2. The PBE DOS curve shows that this functional actually leads to a conclusion that single-layer PtN_2 is metallic, agreeing with the rather small bandgaps (0.075 and 0.07 eV) reported

in Refs. [412] and [411], respectively. Our HSE06 DOS shows a corrected band gap of single-layer PtN_2 as 1.11 eV, which is the same as the band gaps reported in Refs. [409] and [411]. Note that the work of Yang *et al* also considers spin-orbit coupling (SOC) and the PBE+SOC and HSE06+SOC band gaps (0.33 and 1.17 eV) are slightly larger than the PBE and HSE06 band gaps [409].

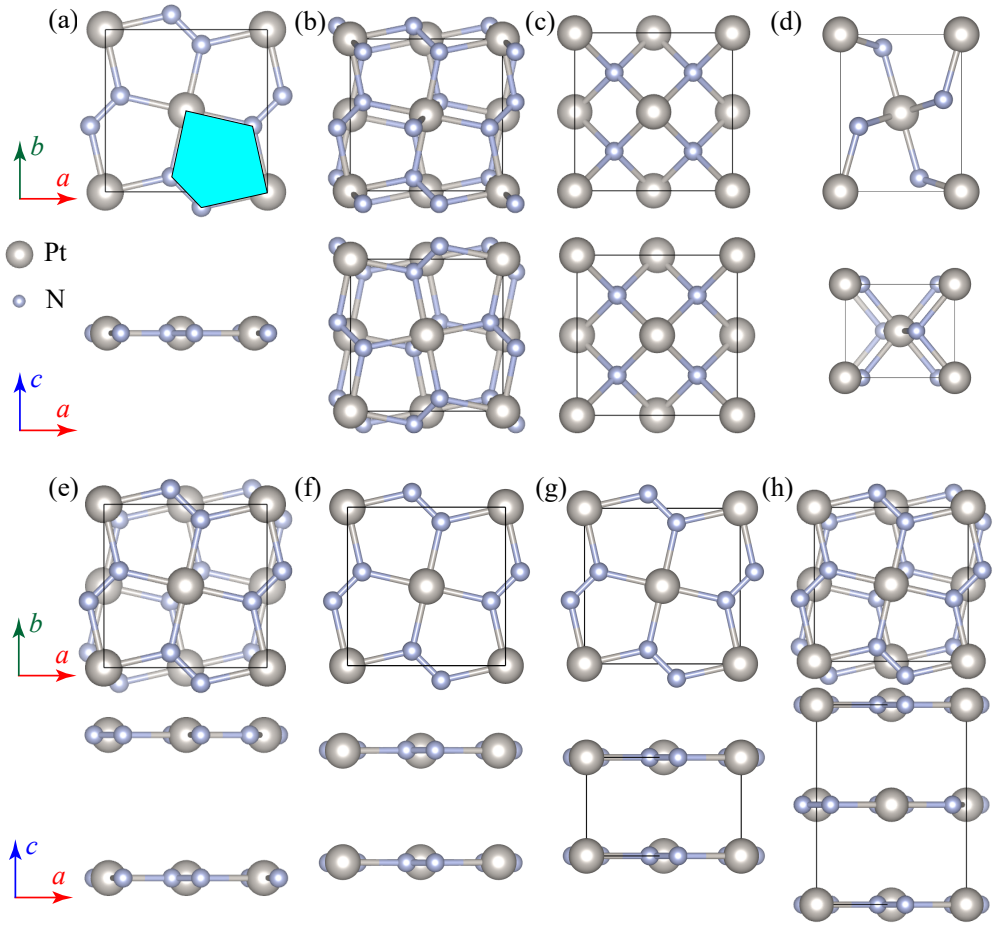

Figure 7.1. Top and side views of the unit cells of (a) single-layer PtN_2 and bulk PtN_2 with the (b) pyrite, (c) fluorite, and (d) marcasite structures, and of (e) AB-stacked and (f) AA-stacked bilayer PtN_2, and of bulk PtN_2 with (g) AA-stacked and (h) AB-stacked tetragonal layered structures. A type 2 pentagon is enclosed by the cyan shaded area sketched in (a).

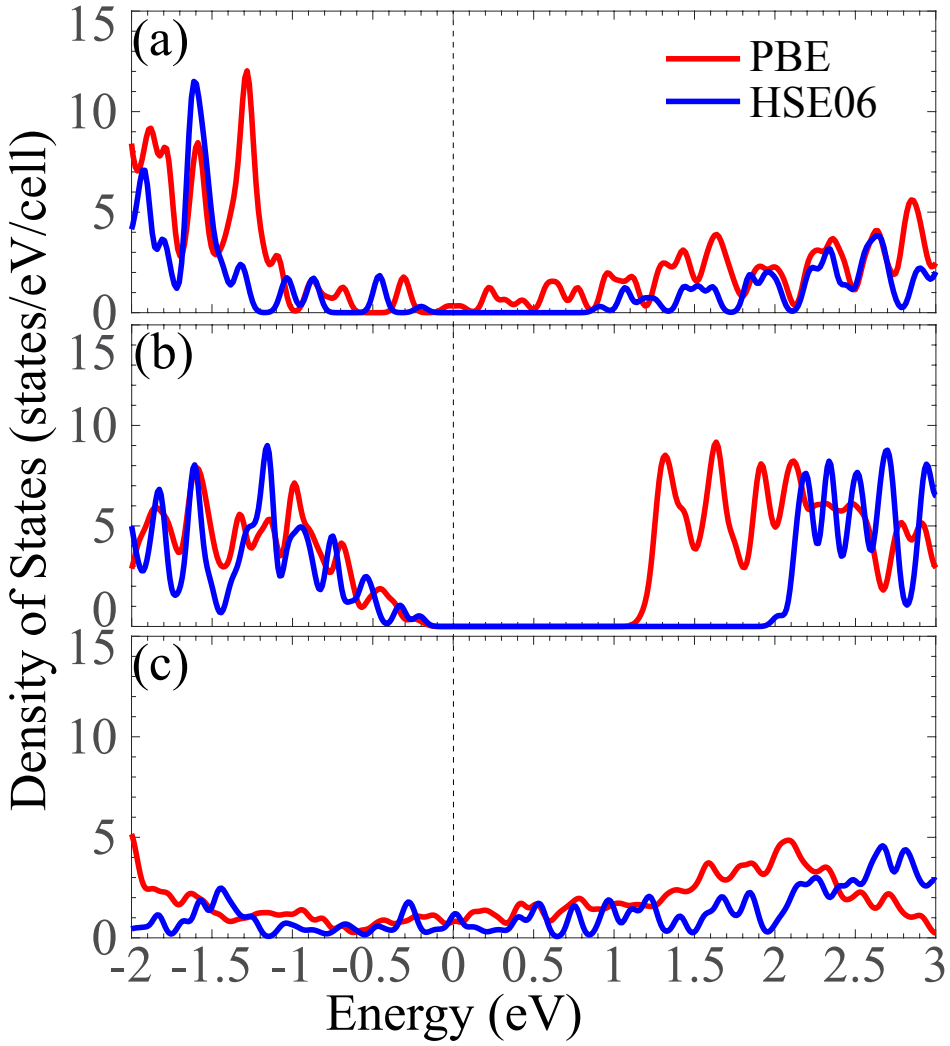

Figure 7.2. Density of states of (a) single-layer PtN_2, (b) bulk PtN_2 with the pyrite structure, and (c) bulk PtN_2 with the tetragonal layered structure calculated with the PBE and HSE06 functionals.

We next calculate the energy difference between single-layer PtN_2 and bulk PtN_2 with the pyrite, fluorite, and marcasite structures. This energy difference (i.e., E_{2D}-E_{3D}, the formation energy of 2D materials) is a metric of the energy cost to exfoliate a single-layer nanosheet from its 3D counterpart and also an indicator of the feasibility of chemical

synthesis [417]. We find the formation energies with reference to the three bulk structures are all negative: -168, -1076, and -207 meV/atom. The more negative formation energy implies the less stable of the bulk structure used for comparison. These energy differences therefore show that the pyrite structure is the most stable in comparison with the fluoride and marcasite structures, consistent with previous theoretical studies [414,431,447]. We conclude that single-layer PtN_2 is more stable than the pyrite structure. More important, the negative formation energies show that all the three bulk structures used for references are not the ground state of bulk PtN_2. In parallel with this observation, we also perform the same calculations on single-layer graphene and compare its energy to the face-centered-cubic diamond structure. We obtain a negative formation energy of -128 meV/atom using the PBE functional, which is expected as the bulk ground state is graphite.

Table 7.1. Relative energy (in meV/atom) of single-layer (SL) PtN_2, bulk PtN_2 with the pyrite (B-p), fluorite (B-f), and marcasite (B-m) structures, AB and AA-stacked bilayer (AB-bl, and AA-bl) PtN_2, and AB-stacked bulk PtN_2 (b-PtN_2). The energy of the tetragonal AA-stacked layered structure is set to zero. All the relative energies are calculated using both the PBE and DFT-D3 methods.

Method	SL	B-p	B-f	B-m	AB-bl	AA-bl	b-PtN_2
PBE	34	202	1110	241	33	25	97
DFT-D3	199	139	1067	184	156	130	156

7.4.2 3D Bulk counterpart of PtN_2

To search for the more stable bulk structure, we begin with studying the energy change by stacking two sheets of single-layer PtN_2 to form bilayer PtN_2. We account for two types of stacking for bilayer PtN_2. One is called the AB stacking (see Figure 7.1(e)), where the Pt atoms in one layer of bilayer PtN_2 are located above/below the center of a pair of N atoms in another layer. The other one is the AA stacking (see Figure 7.1(f)), where the second layer is located on top of the first layer. We find that AB-stacked bilayer PtN_2 is energetically less stable than the AA-stacked structure by 8 meV/atom, so we focus on the AA-stacked bilayer PtN_2 and compute the binding energy E_b between the two layers defined as $E_b = E_{bilayer} - 2E_{single\text{-}layer}$. Figure 7.3 displays the E_b of AA-stacked bilayer PtN_2 as a function of the interlayer distance. As can be seen, without using the DFT-D3 method to describe the vdW interactions, the E_b values resulting from the interactions between the two PtN_2 layers are negligibly small with the maximum binding energy of -9 meV/atom. Taking into account the vdW interactions, the binding energy is corrected to -69 meV/atom (we obtain the same binding energy using the optB88-vdW functional), which is similar to the binding energy (-31.1 meV/atom) of AA-stacked bilayer graphene calculated using the DFT-D method [448], showing the weak interactions between single-layer PtN_2 sheets.

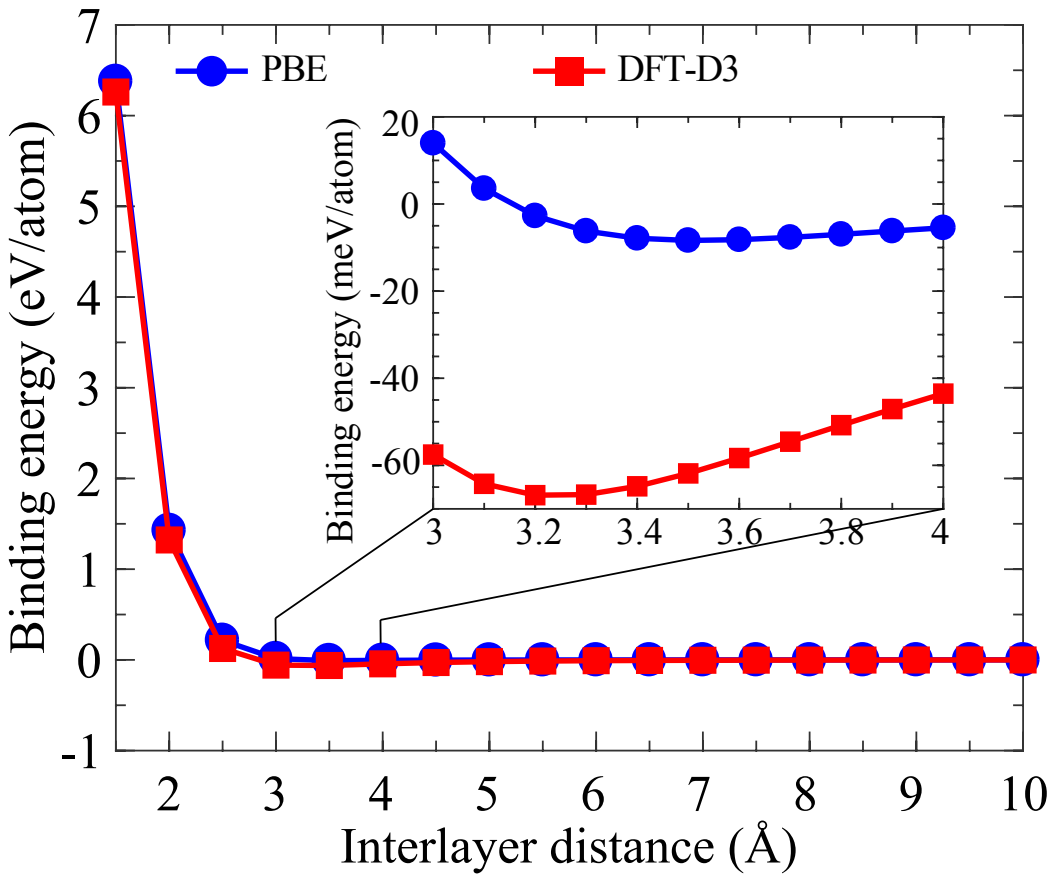

Figure 7.3. Binding energy of AA-stacked bilayer PtN_2 as a function of the interlayer distance computed using the PBE and DFT-D3 methods. The inset is an enlarged view of the two binding energy curves where interlayer distance ranges from 3 to 4 Å

Because bilayer AA-stacked PtN_2 is more stable than single-layer PtN_2, we expect to stack an infinite number of single-layer PtN_2 sheets in the AA-stacking manner to result in a more stable structure of bulk PtN_2 as illustrated in Figure 7.1(g). A symmetry analysis of this infinitely AA-stacked layered structure shows that the bulk structure is tetragonal with the space group P4/mbm (No.127). We henceforth refer to this new bulk structure as the tetragonal layered (TL) structure. For the completeness of comparison, we also compute the energy of the bulk structure with AB-stacked layers (see Figure 7.1(h)). We find that

the TL structure is the most stable among the eight structures displayed in Figure 7.1. Table 7.1 lists all the relative energies of the eight structures using the energy of the TL structure as the reference. The lattice constants of these two bulk structures are reported in Table 7.2. With the new bulk structure, the formation energies of single-layer PtN_2 become physically positive, which are 34 and 199 meV/atom calculated with the PBE and DFT-D3 methods, respectively. These small formation energies manifest the weak interactions between layers and also indicate a feasible approach to obtain single-layer may be the mechanical exfoliation method as used to obtain single-layer graphene [335].

Since we have identified the more energetically stable structure of bulk PtN_2, we now examine the mechanical stability of bulk PtN_2 with the TL structure. We also calculate the same properties of bulk PtN_2 with the pyrite structure for comparison, as the pyrite structure is the most stable among the previously reported bulk structures. Table 7.2 summarizes the predicted independent elastic stiffness constants for cubic and tetragonal PtN_2 using a symmetry-general approach [449]. According to Born's criteria of mechanical stability, the following conditions [450]:

$$C_{11} - C_{12} > 0, C_{11} + 2C_{12} > 0, C_{44} > 0, \tag{7.1}$$

and

$$C_{11} > |C_{12}|, 2C_{13}^2 < C_{11}(C_{11} + C_{11}), C_{44} > 0, C_{66} > 0 \tag{7.2}$$

need to be satisfied for cubic and tetragonal PtN_2, respectively. The computed elastic constants show that both the pyrite and TL structures of bulk PtN_2 are mechanically stable.

Table 7.2. Lattice constants (in Å) and elastic stiffness constants and hardness (in GPa) of bulk PtN_2 with the pyrite and tetragonal layered (TL) structures. Theoretical results using different methods are cited for comparison. For the pyrite structure, $C_{13} = C_{12}$, $C_{33} = C_{11}$, and $C_{66} = C_{44}$ due to the cubic symmetry.

	Method	a	b	c	B_{VRH}	G_{VRH}	H
Pyrite	PBE	4.85	4.85	4.85	290	187	22.5
	DFT-D3	4.82	4.82	4.82	311	195	22.3
	LDA[a]	4.81	4.81	4.81	351	218	23.7
	PW91[b]	4.88	4.88	4.88	267	181	23.7
	LAPW[c]	4.77	4.77	4.77	353	215	22.9
	LAPW[d]	4.86	4.86	4.86	275	184	23.5
SL	PBE	4.83	4.83	3.07	125	74	10.5
	DFT-D3	4.81	4.81	2.90	159	87	10.4
	Method	C_{11}	C_{22}	C_{13}	C_{33}	C_{44}	C_{66}
Pyrite	PBE	695	87	-	-	133	-
	DFT-D3	746	93	-	-	136	-
	LDA[a]	828	113	-	-	155	
	PW91[b]	662	69	-	-	129	-
	LAPW[c]	824	117	-	-	152	-
	LAPW[d]	668	78	-	-	133	-

SL	PBE	709	120	18	55	14	135
	DFT-D3	782	134	17	110	18	143

[a]Ref. [451]; NC: norm-conserving pseudopotentials
[b]Ref. [452];
[c]Ref. [431]; PBE-LAPW: linearized augmented plane waves
[d]Ref. [431]; LDA-LAPW: linearized augmented plane waves

Hardness is an important property of platinum nitrides for their engineering applications [453]. We therefore calculate the Vicker hardness H_V of bulk PtN_2 with the pyrite and TL structures using the following empirical equation [454]:

$$H_V = 2(G_{VRH}^3/B_{VRH}^3)^{0.585} - 3 \tag{7.3}$$

where the bulk and shear moduli (B_{VRH} and G_{VRH}) are calculated using the Voigt-Reuss-Hill (VRH) approximation [455,456]:

$$B_{VRH} = \frac{B_V + B_V}{2} \tag{7.4}$$

and

$$G_{VRH} = \frac{G_V + G_V}{2} \tag{7.5}$$

B_V and G_V are the upper bounds of bulk and shear moduli written as,

$$B_V = \frac{2C_{11} + 2C_{12} + C_{33} + 4C_{13}}{9} \tag{7.6}$$

and

$$G_V = \frac{2C_{11} - C_{12} + C_{33} - 2C_{13} + 6C_{44} + 3C_{66}}{15} \tag{7.7}$$

respectively. B_R and G_R are the lower bounds of bulk and shear moduli, i.e.,

$$B_R = \frac{1}{2S_{11}+2S_{12}+S_{33}+4S_{13}} \quad (7.8)$$

and

$$G_R = \frac{1}{8S_{11}-24+4S_{33}-8S_{13}+6S_{44}+3S_{66}} \quad (7.9)$$

where S_{ij} (i, j = 1-6) are the elastic compliant constants and matrix S is equal to the inverse of matrix C. Table 8.2 lists the predicted B_{VRH} and G_{VRH}, and H_V obtained from using the PBE and DFE-D3 methods. Our calculated elastic constants agree well with those reported Refs. [409] and [431] computed using the PW91 and PBE functionals with the general gradient approximation [79]. The local-density approximations (LDA) [76,457] are also used in Refs. [451] and [431], but this method seems to lead to larger elastic constants. However, the resulting hardness (22.5 GPa) in this work is similar to those in all the references, in spite of the methods used. Although several elastic stiffness constants of the TL structure (e.g., C_{33} are significantly affected by the consideration of the vdW interactions, Table 7.2 also shows that our hardness values from the PBE and DFT-D3 methods are similar. The much smaller Vicker hardness of the TL structure suggests that it is much softer than the pyrite structure. This softness appears to be a common feature for layered materials such as graphite in contrast to superhard diamond [458].

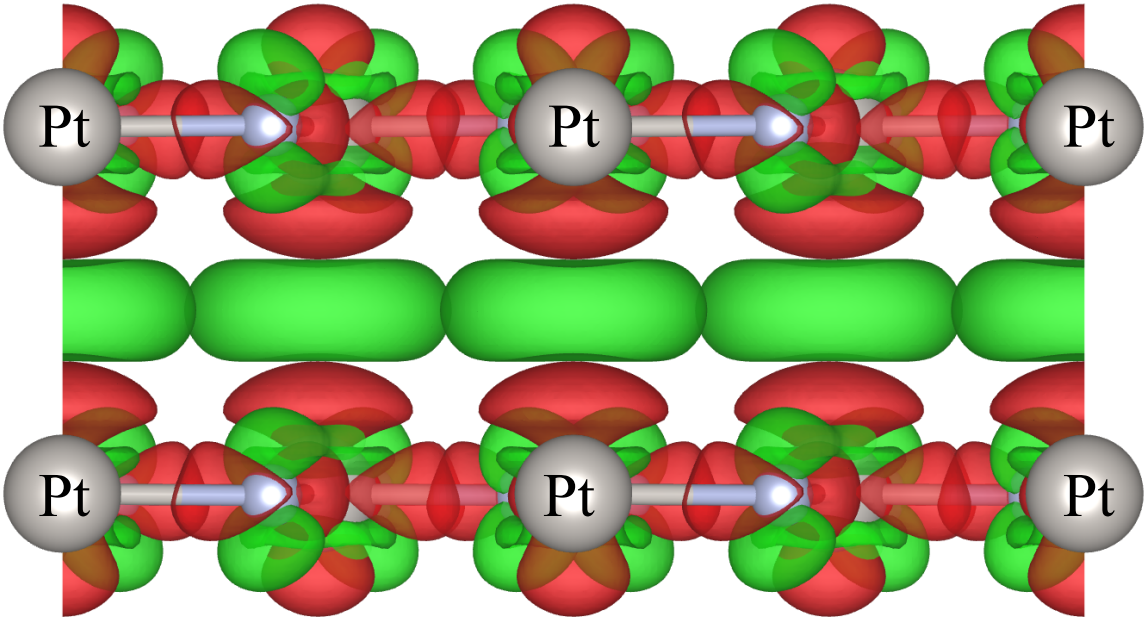

Figure 7.4. Charge density difference between AA-stacked bilayer PtN_2 and two isolated sheets of single-layer PtN_2. Green and red isosurfaces represent charge accumulation and depletion, respectively. The isosurface value is 2×10^{-4} e/a_0^3 (a_0: Bohr radius).

We now compare the electronic structures of bulk PtN_2 with the pyrite and TL structures. Figure 7.2(b) shows the density of states of bulk PtN_2 with the pyrite and TL structures calculated with the PBE and HSE06 functionals. For the former structure, both the PBE and HSE06 functionals predict that it is semiconducting, and the band gaps are 1.35 and 2.22 eV, respectively. Our calculated PBE band gap is consistent with the previously reported band gap of 1.30 eV [429]. For the TL structure, the PBE and HSE06 functionals consistently show that the structure is metallic. To gain a qualitative understanding of the semiconductor-to-metal transition as the number of single-layer sheets increases, we calculate the charge density difference between AA-stacked bilayer PtN_2 and two isolated single-layer PtN_2 sheets. Figure 7.4 shows that the electrons of Pt

atoms in both layers are transferred to the region between two Pt atoms, when the two layers interact to form bilayer PtN_2. These electrons between the layers form Pt-Pt metallic bonds, leading to the metallic behavior of bilayer as well as bulk PtN_2. In other words, the interlayer interactions in bilayer PtN_2 or bulk PtN_2 with the TL structure consist of mixed vdW and metallic bonding types. Note that the bond strength of these metallic bonds is small as reflected by the small isosurface value. We also expect the metallic bonding is significantly smaller than the vdW interactions, as including the vdW interactions drastically changes the energy difference between single-layer and bilayer PtN_2 (see Table 8.1). Extracting a sheet of single-layer PtN_2 from bilayer and bulk PtN_2 prohibits the delocalization of the electrons. As a result, the electrons are localized around Pt atoms in the region enclosed by the red isosurface as shown in Figure 7.4 causing single-layer PtN_2 to be semiconducting.

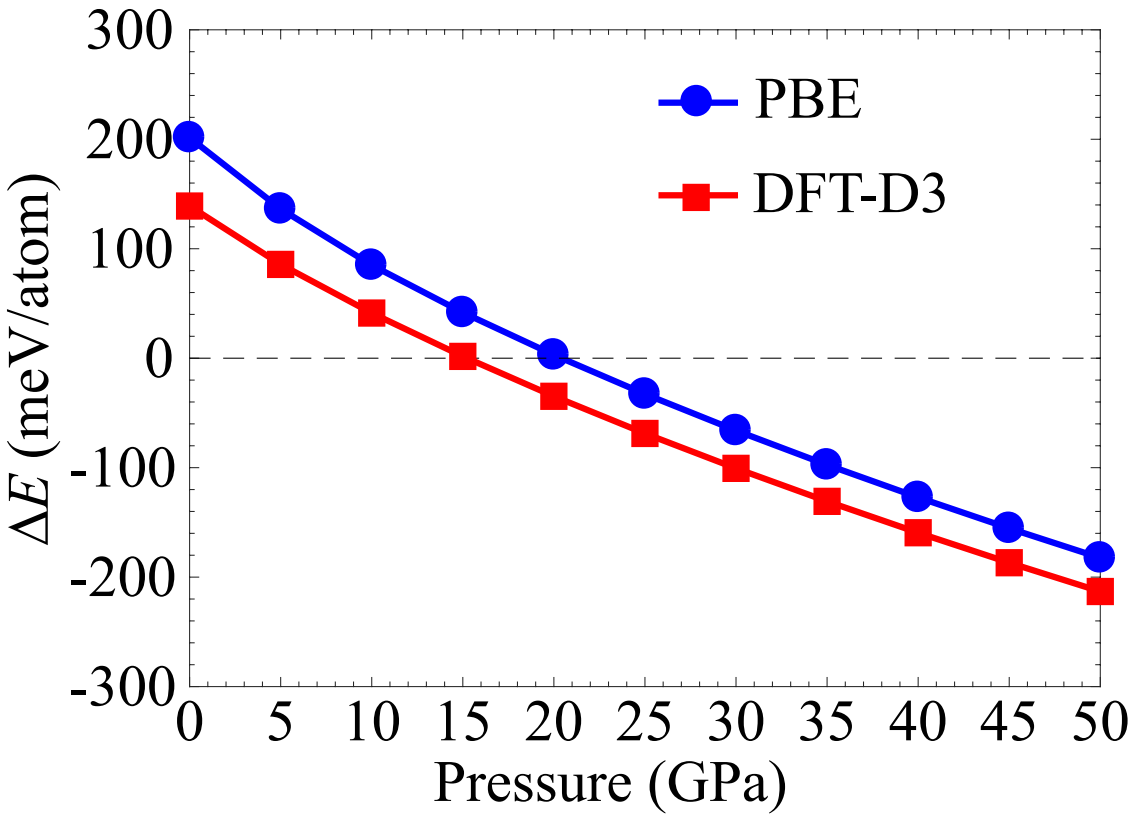

Figure 7.5. Pressure-dependent energy difference ΔE ($\Delta E = E_{\text{pyrite}}$-$E_{\text{TL}}$) between bulk PtN_2 with the pyrite and tetragonal layered (TL) structures.

Experiments on bulk PtN_2 with the pyrite structure indicate the importance of stabilizing this bulk phase by external pressure[459,460]. We therefore compare the stability of bulk PtN_2 with the pyrite and TL structures at different pressures by computing their energy difference ΔE ($\Delta E = E_{\text{pyrite}} - E_{\text{vdW}}$). Figure 7.5 shows ΔE as a function of pressure calculated with the PBE and DFT-D3 methods. The two curves reveal the same trend: ΔE changes almost linearly from positive to negative as pressure increases, showing that the TL structure is more stable below a critical pressure, above which the pyrite structure is more stable. This trend may be caused by the exponentially increased energy

as the interlayer distance in the TL structure decreases due to the pressure (see Figure 7.3). We also find that the critical pressures resulted from the PBE and DFT-D3 methods are similar. For the PBE method, the transition pressure is around 20 GPa; For the latter method, the pressure is about 15 GPa.

7.4.3 Tunable band gap in 1D PtN_2 nanotube

Having studied the case of increasing the dimension of PtN_2 from 2D to 3D, we set to reduce the dimension to 1D to obtain PtN_2 nanotubes. Many 2D materials such as single-layer graphene and boron nitride have their corresponding forms of nanotubes and exhibit novel properties [461,462]. We create simulation models of PtN_2 nanotubes by wrapping $N \times 1 \times 1$ ($3 \leq N \leq 10$) supercells of single-layer PtN_2 about the *a* axis as shown in Figure 7.1(a). Due to the square symmetry of single-layer PtN_2, wrapping the supercells about the *b* axis leads to the same nanotubes. The integer N therefore controls the diameters of the nanotubes. Figure 7.6(a) and (b) illustrates the side and top views of a model of PtN_2 nanotube. Notice that the side view actually demonstrates a curved Cairo tessellation pattern of type 2 pentagons.

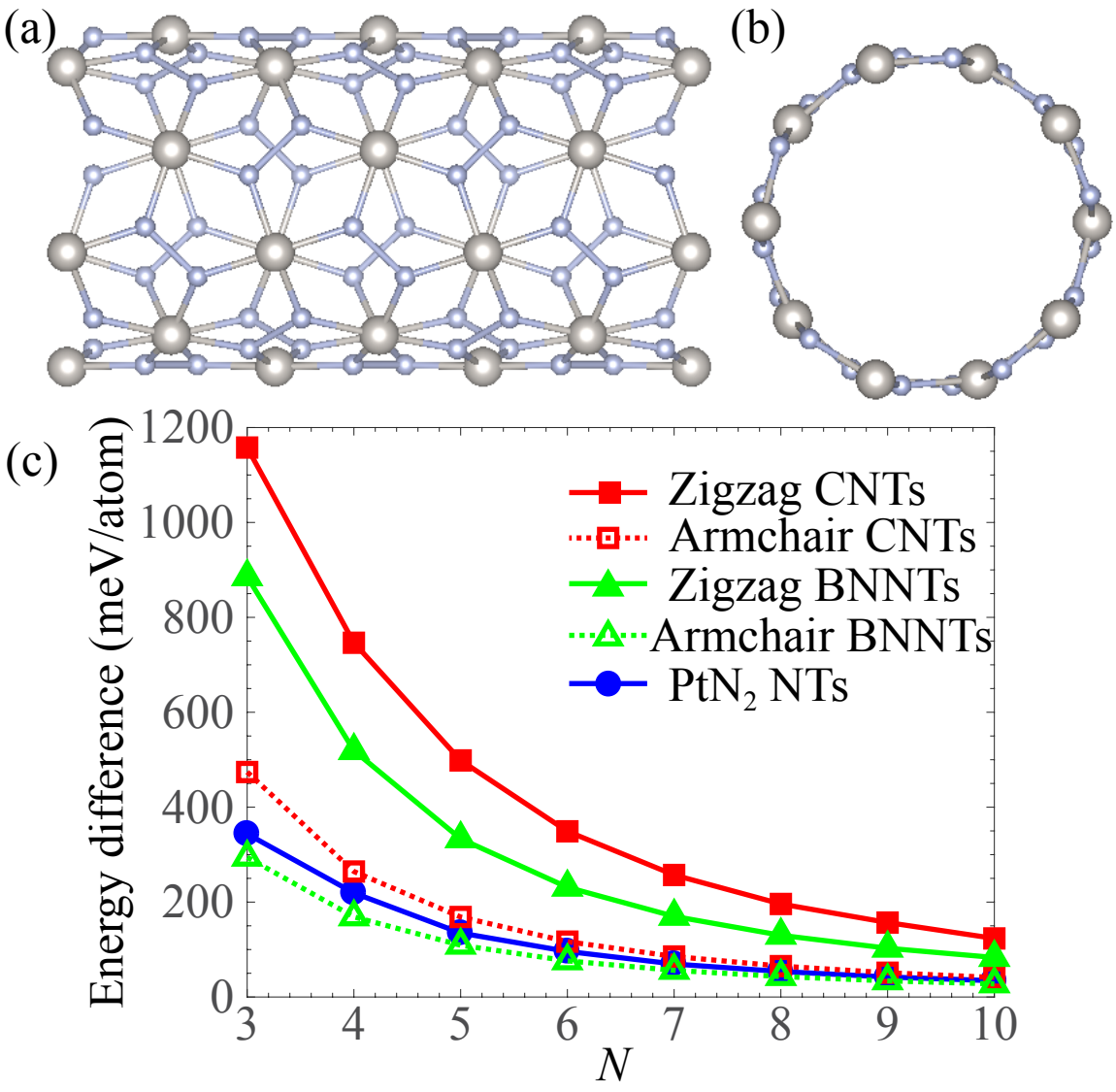

Figure 7.6. (a) Side and (b) top views of a PtN_2 nanotube model formed by wrapping a 5 × 3 × 1 supercell of single-layer PtN_2 about the a/b axis denoted in Figure 7.1(c) *N*-dependent energy difference between PtN_2 nanotubes (NTs) and single- layer PtN_2. The energy differences for zigzag and armchair carbon nanotubes (CNTs) and boron nitride nanotubes (BNNTs) are also shown for comparison.

We compute the energy cost to obtain these nanotubes using the energy of single-layer PtN_2 as a reference. We additionally calculate the energy costs of wrapping single-layer

graphene and boron nitride into zigzag (N, 0) and armchair (N, N) nanotubes for comparison. As can be seen from Figure 7.6(c), the energy costs of all the nanotubes decrease with the increasing sizes of the nanotubes. This trend is expected as N increases towards infinity, the diameters increase along with the decreasing curvatures of the nanotubes until they are close to zero, corresponding to the curvature of single-layer planar PtN_2. We observe that the energy costs of PtN_2 nanotubes are much smaller than those of zigzag carbon and BN nanotubes with the same N values. The energy costs of CNTs and BNNTs are significantly dependent on the chirality, i.e., the energy costs of armchair CNTs and BNNTs are drastically smaller and comparable to those of armchair nanotubes. Zigzag and armchair CNTs and BNNTs have been successfully synthesized [424], indicating that it is also possible to synthesize PtN_2 nanotubes. From the geometry perspective, if successfully synthesized, PtN_2 nanotubes will be the first nanotubes with a curved Cairo tessellation of type 2 pentagons.

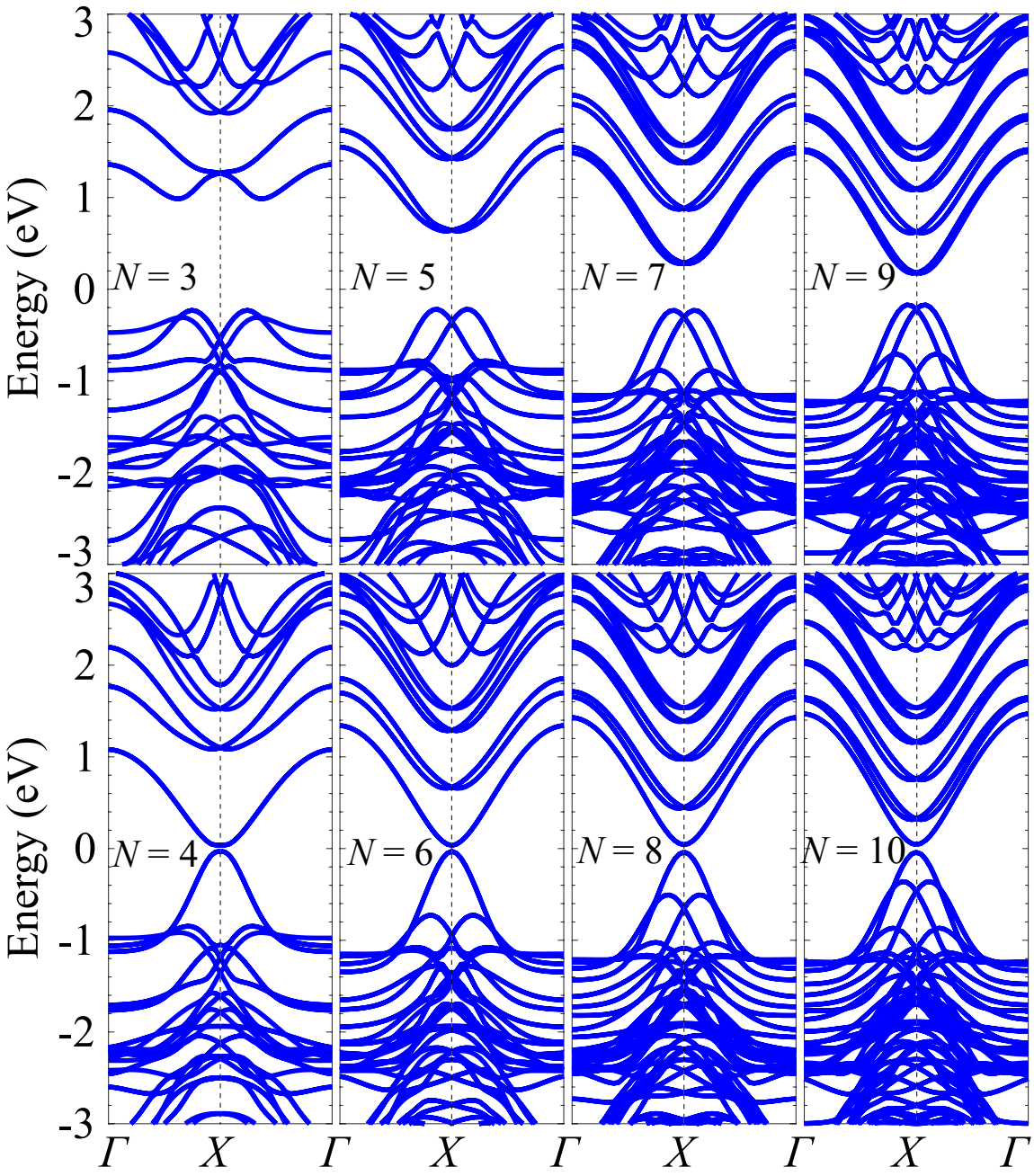

Figure 7.7. Band structures of PtN_2 nanotubes with N ranging from 3 to 10 calculated at the DFT-PBE level of theory.

Finally, we calculate the electronic structures of PtN_2 nanotubes. Figure 7.7 shows the PBE band structures of PtN_2 nanotubes with the eight *N* values. We notice that these band

structures strongly depend on the N values, similar to the dependence of the electronic structures of CNTs on their chiral indices [463]. The PtN_2 nanotubes with odd N values are semiconducting with indirect PBE bandgaps of are 1.24, 0.87, 0.54, and 0.40 eV, for N = 3, 5, 7, and 9, respectively. By contrast, the PtN_2 nanotubes with even N (4, 6, 8, and 10) are quasi-metallic with nearly the same tiny PBE direct band gaps of 0.07, 0.06, 0.08, and 0.08 eV, respectively. These different electronic structures of the PtN_2 nanotubes with N being odd and even may be because of their different symmetries. Due to the intense computational cost, we are able to calculate the HSE06 electronic structures for only two PtN_2 nanotubes (N = 3 and 4). We find that the HSE06 bandgaps of the PtN_2 with N = 3 and 4 are 1.96 and 0.77 eV, respectively. Note that the PBE functional once again is inaccurate to describe the bandgaps of PtN_2 nanotubes. This deficiency is worse for the nanotubes with even N values. Assuming the trend of the PBE band gaps of PtN_2 nanotubes holds for the HSE06 bandgaps, namely, the bandgaps of PtN_2 nanotubes will decrease with increasing (odd) N values and the range of tunable bandgaps is between 1.11 eV for single-layer PtN_2 and 1.96 eV for the (N = 3) PtN_2 nanotube. In contrast to narrow-gap CNTs and large-gap BNNTs [464,465], the wide range of tunable bandgaps are within the visible light spectrum, making PtN_2nanotubes promising 1D materials for optoelectronics applications.

7.5 Summary

In summary, by increasing the dimension of single-layer PtN_2, we have predicted a more stable structure of bulk PtN_2 with tetragonal AA-stacked layered structure using DFT

calculations. This structure is energetically more favorable than the pyrite structure or single-layer PtN_2, therefore resulting in a physically negative formation energy of the single-layer PtN_2, which is otherwise positive if using the energy of the pyrite structure as the reference. Owing to the layered structure, our predicted bulk structure provides a promising source for mechanically exfoliate single-layer semiconducting PtN_2, consisting of a pattern of type 2 pentagons. We also find that applying external pressure can lead to the phase transition between the pyrite and tetragonal layered structures of PtN_2 and the transition pressures are about 20 and 15 GPa determined by the PBE and DFT-D3 methods, respectively. On the other hand, by reducing the dimension, we have predicted PtN_2 nanotubes with tunable band gaps (by varying their sizes) within the visible light spectrum. Furthermore, wrapping single-layer PtN_2 into nanotubes costs a comparable or smaller amount of energy in comparison to wrapping single-layer graphene and boron nitride into CNTs and BNNTs, respectively. The predicted PtN_2 nanotubes may find applications in optoelectronics devices.

CHAPTER IX

OUTLOOK

We have discussed the endeavors in the design and discovery of compositionally complex semiconductors. The works in this thesis enable the efficient searching for compositionally complex semiconductors with potential applications from electronic devices to quantum bits. Besides, taking the advantage multiscale simulation techniques such as density functional theory (DFT) and classic molecular dynamics (MD), research on understanding the properties of these semiconductors can reach a more comprehensive level. We note that there are still more challenges and opportunities that described below.

For example, in Chapter 3, we used the classical Stillinger–Weber potential in MD simulation to predict the thermal conductivity. However, these work is limited by the accuracy of the potential utilized in the MD calculations. To achieve higher accuracy, state-of-the-art machine learning algorithms such as spectral neighbor analysis approach can be employed to parameterize the interaction potentials.

In Chapter 3 and 4, we showed that various structural and electronic properties such as lattice parameter, band gap, band alignment, and effective carrier mass are strongly dependent on the relative content of each component. However, by utilizing the VCA models, special quasi-random models, or the random alloy models, these properties are limited in the multinary systems yet cannot be extended into other systems of more major components. Various approaches based on machine learning models such as random forest,

kernel rigid regressions, and artificial neural network are proposed to utilize the results from ternary, quaternary systems to predict the properties of alloys with more major constituent.

The tunable properties of compositionally complex semiconductors exhibit versatility in various applications, drawing attention from both computational design and experimental synthesis. The improvement of computational simulation in compositionally complex semiconductors for high efficiency and high accuracy is always in need for not only contributing to the theoretically understanding of materials properties, but also providing guidance for experimental studies.

BIBLIOGRAPHY

[1] A. Nardelli, E. Deuschle, L. D. de Azevedo, J. L. N. Pessoa, and E. Ghisi, Assessment of Light Emitting Diodes technology for general lighting: A critical review, Renewable and Sustainable Energy Reviews **75**, 368 (2017).

[2] Y. Cao and K. E. Uhrich, Biodegradable and biocompatible polymers for electronic applications: A review, Journal of Bioactive and Compatible Polymers **34**, 3 (2019).

[3] Y. Shirasaki, G. J. Supran, M. G. Bawendi, and V. Bulović, Emergence of colloidal quantum-dot light-emitting technologies, Nature Photonics **7**, 13 (2013).

[4] Y. Shang and Z. Ning, Colloidal quantum-dots surface and device structure engineering for high-performance light-emitting diodes, National Science Review **4**, 170 (2017).

[5] L. Landrum and M. M. Holland, Extremes become routine in an emerging new Arctic, Nature Climate Change (2020).

[6] M. Meinshausen *et al.*, The RCP greenhouse gas concentrations and their extensions from 1765 to 2300, Climatic change **109**, 213 (2011).

[7] S. Susarla *et al.*, Quaternary 2D transition metal dichalcogenides (TMDs) with tunable bandgap, Advanced Materials **29**, 1702457 (2017).

[8] V. Kochat *et al.*, Re doping in 2D transition metal dichalcogenides as a new route to tailor structural phases and induced magnetism, Advanced Materials **29**, 1703754 (2017).

[9] W. Ma, J. M. Luther, H. Zheng, Y. Wu, and A. P. Alivisatos, Photovoltaic devices employing ternary pbs x se1-x nanocrystals, Nano letters **9**, 1699 (2009).

[10] Q. Guo, G. M. Ford, H. W. Hillhouse, and R. Agrawal, Sulfide nanocrystal inks for dense Cu (In1− x Gax)(S1− y Se y) 2 absorber films and their photovoltaic performance, Nano letters **9**, 3060 (2009).

[11] J. Xu *et al.*, Arrays of ZnO/Zn_xCd_{1-x} Se Nanocables: Band Gap Engineering and Photovoltaic Applications, Nano letters **11**, 4138 (2011).

[12] A. Glass, D. Von der Linde, D. Auston, and T. Negran, Excited state polarization, bulk photovoltaic effect and the photorefractive effect in electrically polarized media, Journal of Electronic Materials **4**, 915 (1975).

[13] G. J. Snyder and A. H. Snyder, Figure of merit ZT of a thermoelectric device defined from materials properties, Energy & Environmental Science **10**, 2280 (2017).

[14] T. Power, Generation: Efficiency and Compatibility, Thermoelectrics handbook: macro to nano (2005).

[15] M. Zhou, Z. M. Gibbs, H. Wang, Y. Han, C. Xin, L. Li, and G. J. Snyder, Optimization of thermoelectric efficiency in SnTe: the case for the light band, Physical Chemistry Chemical Physics **16**, 20741 (2014).

[16] T. D. Ladd, F. Jelezko, R. Laflamme, Y. Nakamura, C. Monroe, and J. L. O'Brien, Quantum computers, Nature **464**, 45 (2010).

[17] B. Hensen *et al.*, Loophole-free Bell inequality violation using electron spins separated by 1.3 kilometres, Nature **526**, 682 (2015).

[18] B. Cantor, Multicomponent and high entropy alloys, Entropy **16**, 4749 (2014).

[19] K.-H. Huang and J. Yeh, A study on the multicomponent alloy systems containing equal-mole elements, Hsinchu: National Tsing Hua University, 1 (1996).

[20] D. Miracle, High entropy alloys as a bold step forward in alloy development, Nature communications **10**, 1 (2019).

[21] Y. Zhang, T. T. Zuo, Z. Tang, M. C. Gao, K. A. Dahmen, P. K. Liaw, and Z. P. Lu, Microstructures and properties of high-entropy alloys, Progress in Materials Science **61**, 1 (2014).

[22] Z. Li, K. G. Pradeep, Y. Deng, D. Raabe, and C. C. Tasan, Metastable high-entropy dual-phase alloys overcome the strength–ductility trade-off, Nature **534**, 227 (2016).

[23] M.-H. Chuang, M.-H. Tsai, W.-R. Wang, S.-J. Lin, and J.-W. Yeh, Microstructure and wear behavior of AlxCo1. 5CrFeNi1. 5Tiy high-entropy alloys, Acta Materialia **59**, 6308 (2011).

[24] L. Wen, H. Kou, J. Li, H. Chang, X. Xue, and L. Zhou, Effect of aging temperature on microstructure and properties of AlCoCrCuFeNi high-entropy alloy, Intermetallics **17**, 266 (2009).

[25] C.-M. Lin and H.-L. Tsai, Evolution of microstructure, hardness, and corrosion properties of high-entropy Al0. 5CoCrFeNi alloy, Intermetallics **19**, 288 (2011).

[26] T. Fujieda, M. Chen, H. Shiratori, K. Kuwabara, K. Yamanaka, Y. Koizumi, A. Chiba, and S. Watanabe, Mechanical and corrosion properties of CoCrFeNiTi-based high-entropy alloy additive manufactured using selective laser melting, Additive Manufacturing **25**, 412 (2019).

[27] J. W. Yeh, S. K. Chen, S. J. Lin, J. Y. Gan, T. S. Chin, T. T. Shun, C. H. Tsau, and S. Y. Chang, Nanostructured high-entropy alloys with multiple principal elements: novel alloy design concepts and outcomes, Advanced Engineering Materials **6**, 299 (2004).

[28] J. W. Yeh, Y. L. Chen, S. J. Lin, and S. K. Chen, in *Materials Science Forum* (Trans Tech Publ, 2007), pp. 1.

[29] B. Fultz, Vibrational thermodynamics of materials, Progress in Materials Science **55**, 247 (2010).

[30] B. S. Murty, J.-W. Yeh, S. Ranganathan, and P. Bhattacharjee, *High-entropy alloys* (Elsevier, 2019).

[31] Y. Jien-Wei, Recent progress in high entropy alloys, Ann. Chim. Sci. Mat **31**, 633 (2006).

[32] J.-W. Yeh, Alloy design strategies and future trends in high-entropy alloys, Jom **65**, 1759 (2013).

[33] S. Ranganathan, Alloyed pleasures: multimetallic cocktails, Current science **85**, 1404 (2003).

[34] S. Singh, N. Wanderka, K. Kiefer, K. Siemensmeyer, and J. Banhart, Effect of decomposition of the Cr–Fe–Co rich phase of AlCoCrCuFeNi high entropy alloy on magnetic properties, Ultramicroscopy **111**, 619 (2011).

[35] T. Borkar *et al.*, A combinatorial assessment of AlxCrCuFeNi2 (0< x< 1.5) complex concentrated alloys: Microstructure, microhardness, and magnetic properties, Acta Materialia **116**, 63 (2016).

[36] Z. Lu, H. Wang, M. Chen, I. Baker, J. Yeh, C. Liu, and T. Nieh, An assessment on the future development of high-entropy alloys: summary from a recent workshop, Intermetallics **66**, 67 (2015).

[37] O. Senkov, J. Miller, D. Miracle, and C. Woodward, Accelerated exploration of multi-principal element alloys with solid solution phases, Nature communications

6, 1 (2015).

[38] J.-W. Yeh, Physical metallurgy of high-entropy alloys, Jom **67**, 2254 (2015).

[39] L. J. Santodonato, Y. Zhang, M. Feygenson, C. M. Parish, M. C. Gao, R. J. Weber, J. C. Neuefeind, Z. Tang, and P. K. Liaw, Deviation from high-entropy configurations in the atomic distributions of a multi-principal-element alloy, Nature communications **6**, 1 (2015).

[40] K.-Y. Tsai, M.-H. Tsai, and J.-W. Yeh, Sluggish diffusion in Co–Cr–Fe–Mn–Ni high-entropy alloys, Acta Materialia **61**, 4887 (2013).

[41] C.-J. Tong, M.-R. Chen, J.-W. Yeh, S.-J. Lin, S.-K. Chen, T.-T. Shun, and S.-Y. Chang, Mechanical performance of the Al x CoCrCuFeNi high-entropy alloy system with multiprincipal elements, Metallurgical and Materials Transactions A **36**, 1263 (2005).

[42] Y. Zhou, Y. Zhang, Y. Wang, and G. Chen, Solid solution alloys of Al Co Cr Fe Ni Ti x with excellent room-temperature mechanical properties, Applied physics letters **90**, 181904 (2007).

[43] S. Gorsse, M. Nguyen, O. N. Senkov, and D. B. Miracle, Database on the mechanical properties of high entropy alloys and complex concentrated alloys, Data in brief **21**, 2664 (2018).

[44] M. C. Gao, J.-W. Yeh, P. K. Liaw, and Y. Zhang, High-entropy alloys, Cham: Springer International Publishing (2016).

[45] S. Sun, Y. Tian, H. Lin, X. Dong, Y. Wang, Z. Zhang, and Z. Zhang, Enhanced strength and ductility of bulk CoCrFeMnNi high entropy alloy having fully recrystallized ultrafine-grained structure, Materials & Design **133**, 122 (2017).

[46] O. Senkov, S. Senkova, D. Miracle, and C. Woodward, Mechanical properties of low-density, refractory multi-principal element alloys of the Cr–Nb–Ti–V–Zr system, Materials Science and Engineering: A **565**, 51 (2013).

[47] L. Chen, R. Wei, K. Tang, J. Zhang, F. Jiang, L. He, and J. Sun, Heavy carbon alloyed FCC-structured high entropy alloy with excellent combination of strength and ductility, Materials Science and Engineering: A **716**, 150 (2018).

[48] M. A. Hemphill, T. Yuan, G. Wang, J. Yeh, C. Tsai, A. Chuang, and P. Liaw, Fatigue behavior of Al0. 5CoCrCuFeNi high entropy alloys, Acta Materialia **60**, 5723

(2012).

[49] Z. Tang, T. Yuan, C.-W. Tsai, J.-W. Yeh, C. D. Lundin, and P. K. Liaw, Fatigue behavior of a wrought Al0. 5CoCrCuFeNi two-phase high-entropy alloy, Acta Materialia **99**, 247 (2015).

[50] P. Chen *et al.*, Fatigue behavior of high-entropy alloys: A review, Science China Technological Sciences **61**, 168 (2018).

[51] T. Yang *et al.*, Precipitation behavior of Al x CoCrFeNi high entropy alloys under ion irradiation, Scientific reports **6**, 1 (2016).

[52] C. Lu *et al.*, Enhancing radiation tolerance by controlling defect mobility and migration pathways in multicomponent single-phase alloys, Nature communications **7**, 1 (2016).

[53] M. C. Gao, D. B. Miracle, D. Maurice, X. Yan, Y. Zhang, and J. A. Hawk, High-entropy functional materials, Journal of Materials Research **33**, 3138 (2018).

[54] S. Ma and Y. Zhang, Effect of Nb addition on the microstructure and properties of AlCoCrFeNi high-entropy alloy, Materials Science and Engineering: A **532**, 480 (2012).

[55] X. Wang, Y. Zhang, Y. Qiao, and G. Chen, Novel microstructure and properties of multicomponent CoCrCuFeNiTix alloys, Intermetallics **15**, 357 (2007).

[56] S.-M. Na, J.-H. Yoo, P. K. Lambert, and N. J. Jones, Room-temperature ferromagnetic transitions and the temperature dependence of magnetic behaviors in FeCoNiCr-based high-entropy alloys, AIP Advances **8**, 056412 (2018).

[57] L. Hu *et al.*, Entropy Engineering of SnTe: Multi-Principal-Element Alloying Leading to Ultralow Lattice Thermal Conductivity and State-of-the-Art Thermoelectric Performance, Advanced Energy Materials **8**, 1802116 (2018).

[58] S. Zaima, O. Nakatsuka, N. Taoka, M. Kurosawa, W. Takeuchi, and M. Sakashita, Growth and applications of GeSn-related group-IV semiconductor materials, Science and technology of advanced materials **16**, 043502 (2015).

[59] P. Moontragoon, R. Soref, and Z. Ikonic, The direct and indirect bandgaps of unstrained SixGe1− x− ySny and their photonic device applications, Journal of Applied Physics **112**, 073106 (2012).

[60] P. Moontragoon, Z. Ikonić, and P. Harrison, Band structure calculations of Si–Ge–Sn alloys: achieving direct band gap materials, Semiconductor science and technology **22**, 742 (2007).

[61] R. Olesinski and G. Abbaschian, The Ge− Si (germanium-silicon) system, Bulletin of Alloy Phase Diagrams **5**, 180 (1984).

[62] L. Colace and G. Assanto, Germanium on silicon for near-infrared light sensing, IEEE Photonics Journal **1**, 69 (2009).

[63] R. Olesinski and G. Abbaschian, The Si− Sn (silicon− tin) system, Bulletin of Alloy Phase Diagrams **5**, 273 (1984).

[64] R. Olesinski and G. Abbaschian, The Ge− Sn (Germanium− Tin) system, Bulletin of Alloy Phase Diagrams **5**, 265 (1984).

[65] W. Hume-Rothery, The structure of metals and alloys, Indian Journal of Physics **11**, 74 (1969).

[66] D. B. Miracle and O. N. Senkov, A critical review of high entropy alloys and related concepts, Acta Materialia **122**, 448 (2017).

[67] S. Wirths, D. Buca, and S. Mantl, Si–Ge–Sn alloys: From growth to applications, Progress in crystal growth and characterization of materials **62**, 1 (2016).

[68] M. Oehme, D. Buca, K. Kostecki, S. Wirths, B. Holländer, E. Kasper, and J. Schulze, Epitaxial growth of highly compressively strained GeSn alloys up to 12.5% Sn, Journal of crystal growth **384**, 71 (2013).

[69] J. Xie, A. V. Chizmeshya, J. Tolle, V. R. D'Costa, J. Menendez, and J. Kouvetakis, Synthesis, stability range, and fundamental properties of Si− Ge− Sn semiconductors grown directly on Si (100) and Ge (100) platforms, Chemistry of Materials **22**, 3779 (2010).

[70] J. Kouvetakis, M. Bauer, and J. Tolle, (Google Patents, 2009).

[71] G.-E. Chang, S.-W. Chang, and S. L. Chuang, Strain-Balanced ${\rm Ge} _ {z}{\rm Sn} _ {1-z}\hbox {--}{\rm Si} _ {x}{\rm Ge} _ {y}{\rm Sn} _ {1-xy} $ Multiple-Quantum-Well Lasers, IEEE journal of Quantum Electronics **46**, 1813 (2010).

[72] A. Saidov, S. N. Usmonov, U. Asatova, and S. K. Ismailov, Growing and Studying

The Photoelectric and Electrical Properties of Epitaxial Films of Ge1-X Snx Solid Solutions, Acta of Turin Polytechnic University in Tashkent **9**, 93 (2019).

[73] M. Bauer, C. Ritter, P. Crozier, J. Ren, J. Menendez, G. Wolf, and J. Kouvetakis, Synthesis of ternary SiGeSn semiconductors on Si (100) via Sn x Ge 1− x buffer layers, Applied physics letters **83**, 2163 (2003).

[74] G. Sun, R. Soref, and H. Cheng, Design of an electrically pumped SiGeSn/GeSn/SiGeSn double-heterostructure midinfrared laser, Journal of Applied Physics **108**, 033107 (2010).

[75] P. Hohenberg and W. Kohn, Inhomogeneous electron gas, Physical review **136**, B864 (1964).

[76] W. Kohn and L. J. Sham, Self-consistent equations including exchange and correlation effects, Physical review **140**, A1133 (1965).

[77] A. Tamm, A. Aabloo, M. Klintenberg, M. Stocks, and A. Caro, Atomic-scale properties of Ni-based FCC ternary, and quaternary alloys, Acta Materialia **99**, 307 (2015).

[78] J. Ding, Q. Yu, M. Asta, and R. O. Ritchie, Tunable stacking fault energies by tailoring local chemical order in CrCoNi medium-entropy alloys, Proceedings of the National Academy of Sciences **115**, 8919 (2018).

[79] J. P. Perdew, K. Burke, and M. Ernzerhof, Generalized gradient approximation made simple, Physical review letters **77**, 3865 (1996).

[80] P. E. Blöchl, Projector augmented-wave method, Physical review B **50**, 17953 (1994).

[81] G. Kresse and D. Joubert, From ultrasoft pseudopotentials to the projector augmented-wave method, Physical review B **59**, 1758 (1999).

[82] H. J. Monkhorst and J. D. Pack, Special points for Brillouin-zone integrations, Physical review B **13**, 5188 (1976).

[83] A. Zunger, S.-H. Wei, L. Ferreira, and J. E. Bernard, Special quasirandom structures, Physical review letters **65**, 353 (1990).

[84] A. Van de Walle *et al.*, Efficient stochastic generation of special quasirandom structures, Calphad **42**, 13 (2013).

[85] A. Van De Walle, Multicomponent multisublattice alloys, nonconfigurational entropy and other additions to the Alloy Theoretic Automated Toolkit, Calphad **33**, 266 (2009).

[86] C. Kittel, P. McEuen, and P. McEuen, *Introduction to solid state physics* (Wiley New York, 1996), Vol. 8.

[87] G. I. Csonka, J. P. Perdew, A. Ruzsinszky, P. H. Philipsen, S. Lebègue, J. Paier, O. A. Vydrov, and J. G. Ángyán, Assessing the performance of recent density functionals for bulk solids, Physical review B **79**, 155107 (2009).

[88] J. Heyd, J. E. Peralta, G. E. Scuseria, and R. L. Martin, Energy band gaps and lattice parameters evaluated with the Heyd-Scuseria-Ernzerhof screened hybrid functional, The Journal of chemical physics **123**, 174101 (2005).

[89] F. Tran and P. Blaha, Accurate band gaps of semiconductors and insulators with a semilocal exchange-correlation potential, Physical review letters **102**, 226401 (2009).

[90] A. Jain *et al.*, Commentary: The Materials Project: A materials genome approach to accelerating materials innovation, Apl Materials **1**, 011002 (2013).

[91] F. Zhang *et al.*, Local structure and short-range order in a NiCoCr solid solution alloy, Physical review letters **118**, 205501 (2017).

[92] Y. Ma, Q. Wang, C. Li, L. J. Santodonato, M. Feygenson, C. Dong, and P. K. Liaw, Chemical short-range orders and the induced structural transition in high-entropy alloys, Scripta Materialia **144**, 64 (2018).

[93] J. Heyd, G. E. Scuseria, and M. Ernzerhof, Hybrid functionals based on a screened Coulomb potential, The Journal of chemical physics **118**, 8207 (2003).

[94] M. Rowan-Robinson, *Night vision: exploring the infrared universe* (Cambridge University Press, 2013).

[95] A. Krier, *Mid-infrared semiconductor optoelectronics* (Springer, 2007), Vol. 118.

[96] R. W. Waynant, I. K. Ilev, and I. Gannot, Mid–infrared laser applications in medicine and biology, Philosophical Transactions of the Royal Society of London. Series A: Mathematical, Physical and Engineering Sciences **359**, 635 (2001).

[97] V. Singh *et al.*, Mid-infrared materials and devices on a Si platform for optical

sensing, Science and technology of advanced materials **15**, 014603 (2014).

[98] Y. Tong, S. Zhao, K. Jin, H. Bei, J. Ko, Y. Zhang, and F. Zhang, A comparison study of local lattice distortion in Ni80Pd20 binary alloy and FeCoNiCrPd high-entropy alloy, Scripta Materialia **156**, 14 (2018).

[99] Y. Zhang, Y. J. Zhou, J. P. Lin, G. L. Chen, and P. K. Liaw, Solid-solution phase formation rules for multi-component alloys, Advanced Engineering Materials **10**, 534 (2008).

[100] Y.-N. Wu, X.-G. Zhang, and S. T. Pantelides, Fundamental resolution of difficulties in the theory of charged point defects in semiconductors, Physical review letters **119**, 105501 (2017).

[101] C. E. Dreyer, A. Alkauskas, J. L. Lyons, A. Janotti, and C. G. Van de Walle, First-principles calculations of point defects for quantum technologies, Annual Review of Materials Research **48**, 1 (2018).

[102] M. Gajdoš, K. Hummer, G. Kresse, J. Furthmüller, and F. Bechstedt, Linear optical properties in the projector-augmented wave methodology, Physical review B **73**, 045112 (2006).

[103] J. Piochaud, T. Klaver, G. Adjanor, P. Olsson, C. Domain, and C. Becquart, First-principles study of point defects in an fcc Fe-10Ni-20Cr model alloy, Physical review B **89**, 024101 (2014).

[104] W. Chen *et al.*, Vacancy formation enthalpies of high-entropy FeCoCrNi alloy via first-principles calculations and possible implications to its superior radiation tolerance, Journal of Materials Science & Technology **34**, 355 (2018).

[105] N. Fukata, A. Kasuya, and M. Suezawa, Formation energy of vacancy in silicon determined by a new quenching method, Physica B: Condensed Matter **308**, 1125 (2001).

[106] H. Pinto, J. Coutinho, V. Torres, S. Öberg, and P. Briddon, Formation energy and migration barrier of a Ge vacancy from ab initio studies, Materials science in semiconductor processing **9**, 498 (2006).

[107] J. Vanhellemont, P. Śpiewak, and K. Sueoka, (American Institute of Physics, 2007).

[108] K.-P. Huber, *Molecular spectra and molecular structure: IV. Constants of diatomic*

molecules (Springer Science & Business Media, 2013).

[109] A. Ciccioli, G. Gigli, and G. Meloni, The Si? Sn Chemical Bond: An Integrated Thermochemical and Quantum Mechanical Study of the SiSn Diatomic Molecule and Small Si–Sn Clusters, Chemistry–A European Journal **15**, 9543 (2009).

[110] B. d. Darwent, Bond dissociation energies in simple molecules, 1970.

[111] R. W. Schmude Jr and K. A. Gingerich, Thermodynamic investigation of small germanium–tin clusters with a mass spectrometer, The Journal of chemical physics **109**, 3069 (1998).

[112] D. Ricci, G. Bano, G. Pacchioni, and F. Illas, Electronic structure of a neutral oxygen vacancy in SrTiO 3, Physical review B **68**, 224105 (2003).

[113] Y. T. Shah, *Thermal energy: sources, recovery, and applications* (CRC Press, 2018).

[114] L. E. Bell, Cooling, heating, generating power, and recovering waste heat with thermoelectric systems, Science **321**, 1457 (2008).

[115] V. Dusastre, *Materials for sustainable energy: a collection of peer-reviewed research and review articles from Nature Publishing Group* (World Scientific, 2011).

[116] S. Johnsen, J. He, J. Androulakis, V. P. Dravid, I. Todorov, D. Y. Chung, and M. G. Kanatzidis, Nanostructures boost the thermoelectric performance of PbS, Journal of the American Chemical Society **133**, 3460 (2011).

[117] T. Fu *et al.*, Enhanced thermoelectric performance of PbTe bulk materials with figure of merit zT> 2 by multi-functional alloying, Journal of Materiomics **2**, 141 (2016).

[118] S. Brückner, S. Liu, L. Miró, M. Radspieler, L. F. Cabeza, and E. Lävemann, Industrial waste heat recovery technologies: An economic analysis of heat transformation technologies, Applied Energy **151**, 157 (2015).

[119] R. Bertani, Geothermal power generation in the world 2010–2014 update report, Geothermics **60**, 31 (2016).

[120] D.-Y. Chung, T. Hogan, P. Brazis, M. Rocci-Lane, C. Kannewurf, M. Bastea, C. Uher, and M. G. Kanatzidis, CsBi4Te6: A high-performance thermoelectric material for low-temperature applications, Science **287**, 1024 (2000).

[121] D.-Y. Chung, T. P. Hogan, M. Rocci-Lane, P. Brazis, J. R. Ireland, C. R. Kannewurf, M. Bastea, C. Uher, and M. G. Kanatzidis, A new thermoelectric material: CsBi4Te6, Journal of the American Chemical Society **126**, 6414 (2004).

[122] S. Yoshida, T. Ikeuchi, T. Bhattacharjee, Y. Bai, A. Shibata, and N. Tsuji, Effect of elemental combination on friction stress and Hall-Petch relationship in face-centered cubic high/medium entropy alloys, Acta Materialia **171**, 201 (2019).

[123] S. S. Sohn *et al.*, Ultrastrong medium-entropy single-phase alloys designed via severe lattice distortion, Advanced Materials **31**, 1807142 (2019).

[124] S. Wirths *et al.*, SiGeSn growth studies using reduced pressure chemical vapor deposition towards optoelectronic applications, Thin Solid Films **557**, 183 (2014).

[125] D. Wang, L. Liu, W. Huang, and H. L. Zhuang, Semiconducting SiGeSn high-entropy alloy: A density functional theory study, Journal of Applied Physics **126**, 225703 (2019).

[126] W. Huang, P. Martin, and H. L. Zhuang, Machine-learning phase prediction of high-entropy alloys, Acta Materialia **169**, 225 (2019).

[127] N. Islam, W. Huang, and H. L. Zhuang, Machine learning for phase selection in multi-principal element alloys, Computational Materials Science **150**, 230 (2018).

[128] O. Senkov, G. Wilks, D. Miracle, C. Chuang, and P. Liaw, Refractory high-entropy alloys, Intermetallics **18**, 1758 (2010).

[129] A. Chizmeshya and J. Kouvetakis, Practical Strategies for Tuning Optical, Structural and Thermal Properties in Group IV Ternary Semiconductors, ECS Transactions **33**, 717 (2010).

[130] O. N. Senkov, G. Wilks, J. Scott, and D. B. Miracle, Mechanical properties of Nb25Mo25Ta25W25 and V20Nb20Mo20Ta20W20 refractory high entropy alloys, Intermetallics **19**, 698 (2011).

[131] K. Zhang, Z. Fu, J. Zhang, W. Wang, H. Wang, Y. Wang, Q. Zhang, and J. Shi, Microstructure and mechanical properties of CoCrFeNiTiAlx high-entropy alloys, Materials Science and Engineering: A **508**, 214 (2009).

[132] X. Yang, Y. Zhang, and P. Liaw, Microstructure and compressive properties of NbTiVTaAlx high entropy alloys, Procedia Engineering **36**, 292 (2012).

[133] A. Haglund, M. Koehler, D. Catoor, E. P. George, and V. Keppens, Polycrystalline elastic moduli of a high-entropy alloy at cryogenic temperatures, Intermetallics **58**, 62 (2015).

[134] J. Wittig, Pressure-induced superconductivity in cesium and yttrium, Physical review letters **24**, 812 (1970).

[135] S. Vrtnik, P. Koželj, A. Meden, S. Maiti, W. Steurer, M. Feuerbacher, and J. Dolinšek, Superconductivity in thermally annealed Ta-Nb-Hf-Zr-Ti high-entropy alloys, Journal of Alloys and Compounds **695**, 3530 (2017).

[136] P. Koželj, S. Vrtnik, A. Jelen, S. Jazbec, Z. Jagličić, S. Maiti, M. Feuerbacher, W. Steurer, and J. Dolinšek, Discovery of a superconducting high-entropy alloy, Physical review letters **113**, 107001 (2014).

[137] G. A. Slack and D. Rowe, (CRC press Boca Raton, FL, 1995).

[138] S. Shafeie, S. Guo, Q. Hu, H. Fahlquist, P. Erhart, and A. Palmqvist, High-entropy alloys as high-temperature thermoelectric materials, Journal of Applied Physics **118**, 184905 (2015).

[139] Z. Fan, H. Wang, Y. Wu, X. Liu, and Z. Lu, Thermoelectric high-entropy alloys with low lattice thermal conductivity, Rsc Advances **6**, 52164 (2016).

[140] R. Liu *et al.*, Entropy as a gene-like performance indicator promoting thermoelectric materials, Advanced Materials **29**, 1702712 (2017).

[141] Z. Fan, H. Wang, Y. Wu, X. Liu, and Z. Lu, Thermoelectric performance of PbSnTeSe high-entropy alloys, Materials Research Letters **5**, 187 (2017).

[142] G. A. Slack and M. A. Hussain, The maximum possible conversion efficiency of silicon-germanium thermoelectric generators, Journal of Applied Physics **70**, 2694 (1991).

[143] C. Wood, Materials for thermoelectric energy conversion, Reports on progress in physics **51**, 459 (1988).

[144] S. Ghamaty, J. Bass, and N. Elsner, in *Proceedings ICT'03. 22nd International Conference on Thermoelectrics (IEEE Cat. No. 03TH8726)* (IEEE, 2003), pp. 563.

[145] R. Basu *et al.*, Improved thermoelectric performance of hot pressed nanostructured n-type SiGe bulk alloys, Journal of Materials Chemistry A **2**, 6922 (2014).

[146] X. Wang, C. Ratanawadee, and N. Raymoul, A review of the research progress of transformational leadership in nursing management, Journal of Nursing Administration **3**, 19 (2008).

[147] D. Rowe, V. Shukla, and N. Savvides, Phonon scattering at grain boundaries in heavily doped fine-grained silicon–germanium alloys, Nature **290**, 765 (1981).

[148] J. Kouvetakis, J. Menendez, and J. Tolle, in *Solid State Phenomena* (Trans Tech Publ, 2010), pp. 77.

[149] S. Khatami and Z. Aksamija, Lattice thermal conductivity of the binary and ternary group-IV alloys Si-Sn, Ge-Sn, and Si-Ge-Sn, Physical Review Applied **6**, 014015 (2016).

[150] Y. Lee and G. S. Hwang, Molecular dynamics investigation of the thermal conductivity of ternary silicon–germanium–tin alloys, Journal of Physics D: Applied Physics **50**, 494001 (2017).

[151] V. R. D'costa, C. S. Cook, A. Birdwell, C. L. Littler, M. Canonico, S. Zollner, J. Kouvetakis, and J. Menéndez, Optical critical points of thin-film Ge 1− y Sn y alloys: a comparative Ge 1− y Sn y⁄ Ge 1− x Si x study, Physical review B **73**, 125207 (2006).

[152] P. Moontragoon, P. Pengpit, T. Burinprakhon, S. Maensiri, N. Vukmirovic, Z. Ikonic, and P. Harrison, Electronic properties calculation of Ge1− x− ySixSny ternary alloy and nanostructure, Journal of non-crystalline solids **358**, 2096 (2012).

[153] R. A. Soref and C. H. Perry, Predicted band gap of the new semiconductor SiGeSn, Journal of Applied Physics **69**, 539 (1991).

[154] W. Scanlon, Recent advances in the optical and electronic properties of PbS, PbSe, PbTe and their alloys, Journal of Physics and Chemistry of Solids **8**, 423 (1959).

[155] G. Mahan, Figure of merit for thermoelectrics, Journal of Applied Physics **65**, 1578 (1989).

[156] G. Kissinger and S. Pizzini, *Silicon, germanium, and their alloys: growth, defects, impurities, and nanocrystals* (CRC Press, 2014).

[157] J.-H. Fournier-Lupien *et al.*, Strain and composition effects on Raman vibrational modes of silicon-germanium-tin ternary alloys, Applied physics letters **103**, 263103 (2013).

[158] A. Chroneos, C. Jiang, R. W. Grimes, and U. Schwingenschlögl, Special quasirandom structures for binary/ternary group IV random alloys, Chemical Physics Letters **493**, 97 (2010).

[159] D. Wang, L. Liu, M. Chen, and H. Zhuang, Electrical and thermal transport properties of medium-entropy SiyGeySnx alloys, Acta Materialia (2020).

[160] J. P. Perdew, Density functional theory and the band gap problem, International Journal of Quantum Chemistry **28**, 497 (1985).

[161] G. K. Madsen, J. Carrete, and M. J. Verstraete, BoltzTraP2, a program for interpolating band structures and calculating semi-classical transport coefficients, Computer Physics Communications **231**, 140 (2018).

[162] G. K. Madsen and D. J. Singh, BoltzTraP. A code for calculating band-structure dependent quantities, Computer Physics Communications **175**, 67 (2006).

[163] P. Bhattacharya and P. Bhattacharya, *Properties of III-V quantum wells and superlattices* (Iet, 1996), 15.

[164] S. Hao, V. P. Dravid, M. G. Kanatzidis, and C. Wolverton, Research Update: Prediction of high figure of merit plateau in SnS and solid solution of (Pb, Sn) S, Apl Materials **4**, 104505 (2016).

[165] R. D'Souza and S. Mukherjee, First-principles study of the electrical and lattice thermal transport in monolayer and bilayer graphene, Physical review B **95**, 085435 (2017).

[166] S. Plimpton, Fast parallel algorithms for short-range molecular dynamics, Journal of computational physics **117**, 1 (1995).

[167] F. H. Stillinger and T. A. Weber, Computer simulation of local order in condensed phases of silicon, Physical review B **31**, 5262 (1985).

[168] T. Ito, K. Khor, and S. D. Sarma, Empirical potential-based Si-Ge interatomic potential and its application to superlattice stability, Physical review B **40**, 9715 (1989).

[169] L. Pizzagalli, J. Godet, J. Guénolé, S. Brochard, E. Holmstrom, K. Nordlund, and T. Albaret, A new parametrization of the Stillinger–Weber potential for an improved description of defects and plasticity of silicon, Journal of Physics: Condensed Matter **25**, 055801 (2013).

[170] Y. Lee and G. S. Hwang, Force-matching-based parameterization of the Stillinger-Weber potential for thermal conduction in silicon, Physical review B **85**, 125204 (2012).

[171] M. S. Green, Markoff random processes and the statistical mechanics of time-dependent phenomena. II. Irreversible processes in fluids, The Journal of chemical physics **22**, 398 (1954).

[172] R. Kubo, Statistical-mechanical theory of irreversible processes. I. General theory and simple applications to magnetic and conduction problems, Journal of the Physical Society of Japan **12**, 570 (1957).

[173] D. Surblys, H. Matsubara, G. Kikugawa, and T. Ohara, Application of atomic stress to compute heat flux via molecular dynamics for systems with many-body interactions, Physical Review E **99**, 051301 (2019).

[174] P. Rosales-Pelaez, I. Sanchez-Burgos, C. Valeriani, C. Vega, and E. Sanz, Seeding approach to nucleation in the N V T ensemble: The case of bubble cavitation in overstretched Lennard Jones fluids, Physical Review E **101**, 022611 (2020).

[175] A. Togo and I. Tanaka, First principles phonon calculations in materials science, Scripta Materialia **108**, 1 (2015).

[176] A. Togo, L. Chaput, and I. Tanaka, Distributions of phonon lifetimes in Brillouin zones, Physical review B **91**, 094306 (2015).

[177] V. D'Costa, J. Tolle, C. Poweleit, J. Kouvetakis, and J. Menendez, Compositional dependence of Raman frequencies in ternary Ge 1− x− y Si x Sn y alloys, Physical review B **76**, 035211 (2007).

[178] C. Xu, C. L. Senaratne, J. Kouvetakis, and J. Menéndez, Compositional dependence of optical interband transition energies in GeSn and GeSiSn alloys, Solid-State Electronics **110**, 76 (2015).

[179] C. Xu, R. T. Beeler, G. J. Grzybowski, A. V. Chizmeshya, D. J. Smith, J. Menéndez, and J. Kouvetakis, Molecular synthesis of high-performance near-IR photodetectors with independently tunable structural and optical properties based on Si–Ge–Sn, Journal of the American Chemical Society **134**, 20756 (2012).

[180] S. M. Sze and K. K. Ng, *Physics of semiconductor devices* (John wiley & sons, 2006).

[181] S. Sharma, B. Singh, and P. Kumar, in *AIP Conference Proceedings* (AIP Publishing LLC, 2018), p. 140036.

[182] N. Miao and P. Ghosez, Optimization of thermoelectric properties of MgAgSb-based materials: a first-principles investigation, The Journal of Physical Chemistry C **119**, 14017 (2015).

[183] P. Boulet and M.-C. Record, Influence of the modified Becke-Johnson exchange potential on thermoelectric properties: Application to Mg2Si, The Journal of chemical physics **135**, 234702 (2011).

[184] R. Johnson and J. Moser, The rotation number for almost periodic potentials, Communications in Mathematical Physics **84**, 403 (1982).

[185] T. Ikeshoji and B. Hafskjold, Non-equilibrium molecular dynamics calculation of heat conduction in liquid and through liquid-gas interface, Molecular Physics **81**, 251 (1994).

[186] F. Müller-Plathe, A simple nonequilibrium molecular dynamics method for calculating the thermal conductivity, The Journal of chemical physics **106**, 6082 (1997).

[187] A. Skye and P. K. Schelling, Thermal resistivity of Si–Ge alloys by molecular-dynamics simulation, Journal of Applied Physics **103**, 113524 (2008).

[188] Y. He, I. Savić, D. Donadio, and G. Galli, Lattice thermal conductivity of semiconducting bulk materials: atomistic simulations, Physical Chemistry Chemical Physics **14**, 16209 (2012).

[189] A. D. Stuckes, The thermal conductivity of germanium, silicon and indium arsenide from 40° C to 425° C, Philosophical Magazine **5**, 84 (1960).

[190] R. Guo and B. Huang, Approaching the alloy limit of thermal conductivity in single-crystalline Si-based thermoelectric nanocomposites: A molecular dynamics investigation, Scientific reports **5**, 1 (2015).

[191] P. B. Allen, J. L. Feldman, J. Fabian, and F. Wooten, Diffusons, locons and propagons: Character of atomie yibrations in amorphous Si, Philosophical Magazine B **79**, 1715 (1999).

[192] B. Abeles, Lattice thermal conductivity of disordered semiconductor alloys at high temperatures, Physical review **131**, 1906 (1963).

[193] J. Garg, N. Bonini, B. Kozinsky, and N. Marzari, Role of disorder and anharmonicity in the thermal conductivity of silicon-germanium alloys: A first-principles study, Physical review letters **106**, 045901 (2011).

[194] A. Maradudin and A. Fein, Scattering of neutrons by an anharmonic crystal, Physical review **128**, 2589 (1962).

[195] J. Kulda, A. Debernardi, M. Cardona, F. De Geuser, and E. Haller, Self-energy of zone-boundary phonons in germanium: Ab initio calculations versus neutron spin-echo measurements, Physical review B **69**, 045209 (2004).

[196] B. A. Weinstein, Pressure dependent optical phonon anharmonicity in GaP, Solid State Communications **20**, 999 (1976).

[197] F. Vallée, Time-resolved investigation of coherent LO-phonon relaxation in III-V semiconductors, Physical review B **49**, 2460 (1994).

[198] A. Debernardi, Phonon linewidth in III-V semiconductors from density-functional perturbation theory, Physical review B **57**, 12847 (1998).

[199] R. Cowley, Raman scattering from crystals of the diamond structure, Journal de Physique **26**, 659 (1965).

[200] S. Manzeli, D. Ovchinnikov, D. Pasquier, O. V. Yazyev, and A. Kis, 2D transition metal dichalcogenides, Nature Reviews Materials **2**, 17033 (2017).

[201] Z. Lei, X. Liu, H. Wang, Y. Wu, S. Jiang, and Z. Lu, Development of advanced materials via entropy engineering, Scripta Materialia **165**, 164 (2019).

[202] Y. Ding, Y. Wang, J. Ni, L. Shi, S. Shi, and W. Tang, First principles study of structural, vibrational and electronic properties of graphene-like MX2 (M= Mo, Nb, W, Ta; X= S, Se, Te) monolayers, Physica B: Condensed Matter **406**, 2254 (2011).

[203] J. Chang, L. F. Register, and S. K. Banerjee, Ballistic performance comparison of monolayer transition metal dichalcogenide MX2 (M= Mo, W; X= S, Se, Te) metal-oxide-semiconductor field effect transistors, Journal of Applied Physics **115**, 084506 (2014).

[204] M. M. Ugeda *et al.*, Giant bandgap renormalization and excitonic effects in a monolayer transition metal dichalcogenide semiconductor, Nature materials **13**, 1091 (2014).

[205] B. Radisavljevic, A. Radenovic, J. Brivio, V. Giacometti, and A. Kis, Single-layer MoS 2 transistors, Nature nanotechnology **6**, 147 (2011).

[206] B. Ozdemir and V. Barone, Thickness dependence of solar cell efficiency in transition metal dichalcogenides MX2 (M: Mo, W; X: S, Se, Te), Solar Energy Materials and Solar Cells **212**, 110557 (2020).

[207] A. Kumar and P. Ahluwalia, Electronic structure of transition metal dichalcogenides monolayers 1H-MX 2 (M= Mo, W; X= S, Se, Te) from ab-initio theory: new direct band gap semiconductors, The European Physical Journal B **85**, 1 (2012).

[208] Z. Guan, S. Ni, and S. Hu, Tunable electronic and optical properties of monolayer and multilayer Janus MoSSe as a photocatalyst for solar water splitting: a first-principles study, The Journal of Physical Chemistry C **122**, 6209 (2018).

[209] C. Gong *et al.*, 2D nanomaterial arrays for electronics and optoelectronics, Advanced Functional Materials **28**, 1706559 (2018).

[210] Y. Liu, X. Duan, Y. Huang, and X. Duan, Two-dimensional transistors beyond graphene and TMDCs, Chemical Society Reviews **47**, 6388 (2018).

[211] W. S. Yun, S. Han, S. C. Hong, I. G. Kim, and J. Lee, Thickness and strain effects on electronic structures of transition metal dichalcogenides: 2H-M X 2 semiconductors (M= Mo, W; X= S, Se, Te), Physical review B **85**, 033305 (2012).

[212] P. Johari and V. B. Shenoy, Tuning the electronic properties of semiconducting transition metal dichalcogenides by applying mechanical strains, ACS nano **6**, 5449 (2012).

[213] S. Susarla *et al.*, Thermally Induced 2D Alloy-Heterostructure Transformation in Quaternary Alloys, Advanced Materials **30**, 1804218 (2018).

[214] T. Jakubczyk, V. Delmonte, M. Koperski, K. Nogajewski, C. m. Faugeras, W. Langbein, M. Potemski, and J. Kasprzak, Radiatively limited dephasing and exciton dynamics in MoSe2 monolayers revealed with four-wave mixing microscopy, Nano letters **16**, 5333 (2016).

[215] L. Britnell *et al.*, Field-effect tunneling transistor based on vertical graphene heterostructures, Science **335**, 947 (2012).

[216] X. Li *et al.*, 18.5% efficient graphene/GaAs van der Waals heterostructure solar cell,

Nano Energy **16**, 310 (2015).

[217] Y. Tan, X. Liu, Z. He, Y. Liu, M. Zhao, H. Zhang, and F. Chen, Tuning of interlayer coupling in large-area graphene/WSe2 van der Waals heterostructure via ion irradiation: optical evidences and photonic applications, ACS Photonics **4**, 1531 (2017).

[218] K. Wu, H. Ma, Y. Gao, W. Hu, and J. Yang, Highly-efficient heterojunction solar cells based on two-dimensional tellurene and transition metal dichalcogenides, Journal of Materials Chemistry A **7**, 7430 (2019).

[219] X. Duan *et al.*, Lateral epitaxial growth of two-dimensional layered semiconductor heterojunctions, Nature nanotechnology **9**, 1024 (2014).

[220] W. Wei, Y. Dai, and B. Huang, In-plane interfacing effects of two-dimensional transition-metal dichalcogenide heterostructures, Physical Chemistry Chemical Physics **18**, 15632 (2016).

[221] B. Amin, N. Singh, and U. Schwingenschlögl, Heterostructures of transition metal dichalcogenides, Physical review B **92**, 075439 (2015).

[222] C. Mu, W. Wei, J. Li, B. Huang, and Y. Dai, Electronic properties of two-dimensional in-plane heterostructures of WS2/WSe2/MoS2, Materials Research Express **5**, 046307 (2018).

[223] Y. Gong *et al.*, Vertical and in-plane heterostructures from WS 2/MoS 2 monolayers, Nature materials **13**, 1135 (2014).

[224] E. Abbasi and K. Dehghani, Hot tensile properties of CoCrFeMnNi (NbC) compositionally complex alloys, Materials Science and Engineering: A **772**, 138771 (2020).

[225] E. Abbasi and K. Dehghani, Microstructure and mechanical properties of Co19Cr20Fe20Mn21Ni19 and Co19Cr20Fe20Mn21Ni19Nb0. 06C0. 8 high-entropy/compositionally-complex alloys after annealing, Materials Science and Engineering: A **772**, 138812 (2020).

[226] A. M. Manzoni and U. Glatzel, New multiphase compositionally complex alloys driven by the high entropy alloy approach, Materials Characterization **147**, 512 (2019).

[227] T. M. Butler and M. L. Weaver, Oxidation behavior of arc melted AlCoCrFeNi

multi-component high-entropy alloys, Journal of Alloys and Compounds **674**, 229 (2016).

[228] K. Jin and H. Bei, Single-phase concentrated solid-solution alloys: Bridging intrinsic transport properties and irradiation resistance, Frontiers in Materials **5**, 26 (2018).

[229] Y. Zhang, T. Zuo, Y. Cheng, and P. K. Liaw, High-entropy alloys with high saturation magnetization, electrical resistivity, and malleability, Scientific reports **3**, 1455 (2013).

[230] W. Guo, W. Dmowski, J.-Y. Noh, P. Rack, P. K. Liaw, and T. Egami, Local atomic structure of a high-entropy alloy: an X-ray and neutron scattering study, Metallurgical and Materials Transactions A **44**, 1994 (2013).

[231] C.-C. Tung, J.-W. Yeh, T.-t. Shun, S.-K. Chen, Y.-S. Huang, and H.-C. Chen, On the elemental effect of AlCoCrCuFeNi high-entropy alloy system, Materials letters **61**, 1 (2007).

[232] Y. Zhang *et al.*, Influence of chemical disorder on energy dissipation and defect evolution in concentrated solid solution alloys, Nature communications **6**, 1 (2015).

[233] H. S. Oh *et al.*, Engineering atomic-level complexity in high-entropy and complex concentrated alloys, Nature communications **10**, 1 (2019).

[234] T. Zuo *et al.*, Tailoring magnetic behavior of CoFeMnNiX (X= Al, Cr, Ga, and Sn) high entropy alloys by metal doping, Acta Materialia **130**, 10 (2017).

[235] K. Jin, B. C. Sales, G. M. Stocks, G. D. Samolyuk, M. Daene, W. J. Weber, Y. Zhang, and H. Bei, Tailoring the physical properties of Ni-based single-phase equiatomic alloys by modifying the chemical complexity, Scientific reports **6**, 20159 (2016).

[236] H. Watzinger, J. Kukučka, L. Vukušić, F. Gao, T. Wang, F. Schäffler, J.-J. Zhang, and G. Katsaros, A germanium hole spin qubit, Nature communications **9**, 1 (2018).

[237] A. Perrin, M. Sorescu, M.-T. Burton, D. E. Laughlin, and M. McHenry, The role of compositional tuning of the distributed exchange on magnetocaloric properties of high-entropy alloys, Jom **69**, 2125 (2017).

[238] H. Kato, S. Adachi, H. Nakanishi, and K. Ohtsuka, Optical properties of (AlxGa1-x) 0.5 In0. 5P quaternary alloys, Japanese journal of applied physics **33**, 186 (1994).

[239] G. M. Ford, Q. Guo, R. Agrawal, and H. W. Hillhouse, Earth abundant element Cu2Zn (Sn1− x Ge x) S4 nanocrystals for tunable band gap solar cells: 6.8% efficient device fabrication, Chemistry of Materials **23**, 2626 (2011).

[240] J. He, L. Sun, S. Chen, Y. Chen, P. Yang, and J. Chu, Composition dependence of structure and optical properties of Cu2ZnSn (S, Se) 4 solid solutions: an experimental study, Journal of Alloys and Compounds **511**, 129 (2012).

[241] C. Tan, Z. Lai, and H. Zhang, Ultrathin two-dimensional multinary layered metal chalcogenide nanomaterials, Advanced Materials **29**, 1701392 (2017).

[242] H. Cotal, C. Fetzer, J. Boisvert, G. Kinsey, R. King, P. Hebert, H. Yoon, and N. Karam, III–V multijunction solar cells for concentrating photovoltaics, Energy & Environmental Science **2**, 174 (2009).

[243] S. H. Su, Y. T. Hsu, Y. H. Chang, M. H. Chiu, C. L. Hsu, W. T. Hsu, W. H. Chang, J. H. He, and L. J. Li, Band Gap-Tunable Molybdenum Sulfide Selenide Monolayer Alloy, small **10**, 2589 (2014).

[244] P. Zawadzki, A. Zakutayev, and S. Lany, Entropy-driven clustering in tetrahedrally bonded multinary materials, Physical Review Applied **3**, 034007 (2015).

[245] E. Torun, H. Sahin, S. Cahangirov, A. Rubio, and F. Peeters, Anisotropic electronic, mechanical, and optical properties of monolayer WTe2, Journal of Applied Physics **119**, 074307 (2016).

[246] X. Zhang, X. Shi, W. Ye, C. Ma, and C. Wang, Electrochemical deposition of quaternary Cu 2 ZnSnS 4 thin films as potential solar cell material, Applied Physics A **94**, 381 (2009).

[247] R. J. Walters *et al.*, in *2011 37th IEEE Photovoltaic Specialists Conference* (IEEE, 2011), pp. 000122.

[248] F. Özel, A. Sarılmaz, B. Istanbullu, A. Aljabour, M. Kuş, and S. Sönmezoğlu, Penternary chalcogenides nanocrystals as catalytic materials for efficient counter electrodes in dye-synthesized solar cells, Scientific reports **6**, 1 (2016).

[249] F. Ceballos, M. Z. Bellus, H.-Y. Chiu, and H. Zhao, Ultrafast charge separation and indirect exciton formation in a MoS2–MoSe2 van der Waals heterostructure, ACS nano **8**, 12717 (2014).

[250] L. Li, Growth Mode and Characterization of Si/SiC Heterostructure of Large

Lattice-Mismatch, Heterojunctions and Nanostructures, 67 (2018).

[251] A. Bhattacharyya and D. Maurice, On the evolution of stresses due to lattice misfit at a Ni-superalloy and YSZ interface, Surfaces and Interfaces **12**, 86 (2018).

[252] L. Ju, M. Bie, X. Tang, J. Shang, and L. Kou, Janus WSSe Monolayer: Excellent Photocatalyst for Overall Water-splitting, ACS Applied Materials & Interfaces (2020).

[253] Q.-F. Yao, J. Cai, W.-Y. Tong, S.-J. Gong, J.-Q. Wang, X. Wan, C.-G. Duan, and J. Chu, Manipulation of the large Rashba spin splitting in polar two-dimensional transition-metal dichalcogenides, Physical review B **95**, 165401 (2017).

[254] A. P. Tiwari, T. G. Novak, X. Bu, J. C. Ho, and S. Jeon, Layered ternary and quaternary transition metal chalcogenide based catalysts for water splitting, Catalysts **8**, 551 (2018).

[255] Y. Cheng, Z. Zhu, M. Tahir, and U. Schwingenschlögl, Spin-orbit–induced spin splittings in polar transition metal dichalcogenide monolayers, EPL (Europhysics Letters) **102**, 57001 (2013).

[256] Y. Zhang, H. Ye, Z. Yu, Y. Liu, and Y. Li, First-principles study of square phase MX2 and Janus MXY (M= Mo, W; X, Y= S, Se, Te) transition metal dichalcogenide monolayers under biaxial strain, Physica E: Low-dimensional Systems and Nanostructures **110**, 134 (2019).

[257] X. J. Wu, X. Huang, X. Qi, H. Li, B. Li, and H. Zhang, Copper-Based Ternary and Quaternary Semiconductor Nanoplates: Templated Synthesis, Characterization, and Photoelectrochemical Properties, Angewandte Chemie International Edition **53**, 8929 (2014).

[258] M. C. Johnson, C. Wrasman, X. Zhang, M. Manno, C. Leighton, and E. S. Aydil, Self-regulation of Cu/Sn ratio in the synthesis of Cu2ZnSnS4 films, Chemistry of Materials **27**, 2507 (2015).

[259] J. B. Varley, X. He, A. Rockett, and V. Lordi, Stability of Cd1–x Zn x O y S1–y Quaternary Alloys Assessed with First-Principles Calculations, ACS Applied Materials & Interfaces **9**, 5673 (2017).

[260] Y. Liang, J. Li, H. Jin, B. Huang, and Y. Dai, Photoexcitation dynamics in Janus-MoSSe/WSe2 heterobilayers: ab initio time-domain study, The Journal of Physical Chemistry Letters **9**, 2797 (2018).

[261] M. Idrees, H. Din, R. Ali, G. Rehman, T. Hussain, C. Nguyen, I. Ahmad, and B. Amin, Optoelectronic and solar cell applications of Janus monolayers and their van der Waals heterostructures, Physical Chemistry Chemical Physics **21**, 18612 (2019).

[262] B. K. Ridley, *Quantum processes in semiconductors* (Oxford University Press, 2013).

[263] T. Kirchartz and U. Rau, Linking structural properties with functionality in solar cell materials–the effective mass and effective density of states, Sustainable Energy & Fuels **2**, 1550 (2018).

[264] A. P. Tiwari, D. Kim, Y. Kim, O. Prakash, and H. Lee, Highly active and stable layered ternary transition metal chalcogenide for hydrogen evolution reaction, Nano Energy **28**, 366 (2016).

[265] H. L. Zhuang and R. G. Hennig, Computational search for single-layer transition-metal dichalcogenide photocatalysts, The Journal of Physical Chemistry C **117**, 20440 (2013).

[266] B. Schuler *et al.*, Large spin-orbit splitting of deep in-gap defect states of engineered sulfur vacancies in monolayer WS 2, Physical review letters **123**, 076801 (2019).

[267] D. S. Abergel, J. M. Edge, and A. V. Balatsky, The role of spin–orbit coupling in topologically protected interface states in Dirac materials, New Journal of Physics **16**, 065012 (2014).

[268] J. Kang, S. Tongay, J. Li, and J. Wu, Monolayer semiconducting transition metal dichalcogenide alloys: Stability and band bowing, Journal of Applied Physics **113**, 143703 (2013).

[269] S. Mankovsky, K. Chadova, D. Koedderitzsch, J. Minár, H. Ebert, and W. Bensch, Electronic, magnetic, and transport properties of Fe-intercalated 2 H− TaS 2 studied by means of the KKR-CPA method, Physical review B **92**, 144413 (2015).

[270] D. D. Johnson, D. Nicholson, F. Pinski, B. Gyorffy, and G. Stocks, Density-functional theory for random alloys: total energy within the coherent-potential approximation, Physical review letters **56**, 2088 (1986).

[271] J. Faulkner, N. Moghadam, Y. Wang, and G. M. Stocks, Comparison of the electronic states of alloys from the coherent potential approximation and an order-N calculation, Journal of phase equilibria **19**, 538 (1998).

[272] S. Mu, S. Wimmer, S. Mankovsky, H. Ebert, and G. Stocks, Influence of local lattice distortions on electrical transport of refractory high entropy alloys, Scripta Materialia **170**, 189 (2019).

[273] K. Wood and J. Pendry, Layer method for band structure of layer compounds, Physical review letters **31**, 1400 (1973).

[274] F. Tian, A review of solid-solution models of high-entropy alloys based on ab initio calculations, Frontiers in Materials **4**, 36 (2017).

[275] X. Qian, P. Jiang, P. Yu, X. Gu, Z. Liu, and R. Yang, Anisotropic thermal transport in van der Waals layered alloys WSe2 (1-x) Te2 x, Applied physics letters **112**, 241901 (2018).

[276] U.-G. Jong, C.-J. Yu, J.-S. Ri, N.-H. Kim, and G.-C. Ri, Influence of halide composition on the structural, electronic, and optical properties of mixed CH 3 NH 3 Pb (I 1− x Br x) 3 perovskites calculated using the virtual crystal approximation method, Physical review B **94**, 125139 (2016).

[277] L. Bellaiche and D. Vanderbilt, Virtual crystal approximation revisited: Application to dielectric and piezoelectric properties of perovskites, Physical review B **61**, 7877 (2000).

[278] N. J. Ramer and A. M. Rappe, Virtual-crystal approximation that works: locating a compositional phase boundary in Pb (Zr 1− x Ti x) O 3, Physical review B **62**, R743 (2000).

[279] S. A.-B. Nasrallah, S. B. Afia, H. Belmabrouk, and M. Said, Optoelectronic properties of zinc blende ZnSSe and ZnBeTe alloys, The European Physical Journal B-Condensed Matter and Complex Systems **43**, 3 (2005).

[280] C. Tablero, Electronic and optical property analysis of the Cu–Sb–S tetrahedrites for high-efficiency absorption devices, The Journal of Physical Chemistry C **118**, 15122 (2014).

[281] D. J. Wilson, B. Winkler, E. A. Juarez-Arellano, A. Friedrich, K. Knorr, C. J. Pickard, and V. Milman, Virtual crystal approximation study of nitridosilicates and oxonitridoaluminosilicates, Journal of Physics and Chemistry of Solids **69**, 1861 (2008).

[282] G. Hua and D. Li, A first-principles study on the mechanical and thermodynamic properties of (Nb 1− x Ti x) C complex carbides based on virtual crystal

approximation, Rsc Advances **5**, 103686 (2015).

[283] G. Kresse and J. Furthmüller, Efficient iterative schemes for ab initio total-energy calculations using a plane-wave basis set, Physical review B **54**, 11169 (1996).

[284] A. van de Walle, M. Asta, and G. Ceder, The alloy theoretic automated toolkit: A user guide, arXiv preprint cond-mat/0212159 (2002).

[285] D. O. Scanlon and G. W. Watson, Band gap anomalies of the ZnM 2 III O 4 (M III= Co, Rh, Ir) spinels, Physical Chemistry Chemical Physics **13**, 9667 (2011).

[286] F. Tran, P. Blaha, and K. Schwarz, Band gap calculations with Becke–Johnson exchange potential, Journal of Physics: Condensed Matter **19**, 196208 (2007).

[287] H. Li *et al.*, Anomalous Behavior of 2D Janus Excitonic Layers under Extreme Pressures, Advanced Materials **32**, 2002401 (2020).

[288] A. M. Ganose, A. J. Jackson, and D. O. Scanlon, sumo: Command-line tools for plotting and analysis of periodic* ab initio* calculations, Journal of Open Source Software **3**, 717 (2018).

[289] S. P. Ong *et al.*, Python Materials Genomics (pymatgen): A robust, open-source python library for materials analysis, Computational Materials Science **68**, 314 (2013).

[290] L. D. Whalley, J. M. Frost, B. J. Morgan, and A. Walsh, Impact of nonparabolic electronic band structure on the optical and transport properties of photovoltaic materials, Physical review B **99**, 085207 (2019).

[291] D. M. Riffe, Temperature dependence of silicon carrier effective masses with application to femtosecond reflectivity measurements, JOSA B **19**, 1092 (2002).

[292] J. R. Schaibley, H. Yu, G. Clark, P. Rivera, J. S. Ross, K. L. Seyler, W. Yao, and X. Xu, Valleytronics in 2D materials, Nature Reviews Materials **1**, 1 (2016).

[293] K. F. Mak, K. He, J. Shan, and T. F. Heinz, Control of valley polarization in monolayer MoS 2 by optical helicity, Nature nanotechnology **7**, 494 (2012).

[294] J. Yan *et al.*, Stacking-dependent interlayer coupling in trilayer MoS2 with broken inversion symmetry, Nano letters **15**, 8155 (2015).

[295] Y. Liu, Y. Gao, S. Zhang, J. He, J. Yu, and Z. Liu, Valleytronics in transition metal

dichalcogenides materials, Nano Research, 1 (2019).

[296] R. Herberholz, V. Nadenau, U. Rühle, C. Köble, H. Schock, and B. Dimmler, Prospects of wide-gap chalcopyrites for thin film photovoltaic modules, Solar Energy Materials and Solar Cells **49**, 227 (1997).

[297] T. Minemoto, Y. Hashimoto, T. Satoh, T. Negami, H. Takakura, and Y. Hamakawa, Cu (In, Ga) Se 2 solar cells with controlled conduction band offset of window/Cu (In, Ga) Se 2 layers, Journal of Applied Physics **89**, 8327 (2001).

[298] C. Li, Q. Cao, F. Wang, Y. Xiao, Y. Li, J.-J. Delaunay, and H. Zhu, Engineering graphene and TMDs based van der Waals heterostructures for photovoltaic and photoelectrochemical solar energy conversion, Chemical Society Reviews **47**, 4981 (2018).

[299] U. Dasgupta, A. Bera, and A. J. Pal, Band diagram of heterojunction solar cells through scanning tunneling spectroscopy, ACS Energy Letters **2**, 582 (2017).

[300] M. Xie, B. Cai, Z. Meng, Y. Gu, S. Zhang, X. Liu, L. Gong, X. a. Li, and H. Zeng, Two-Dimensional BAs/InTe: A Promising Tandem Solar Cell with High Power Conversion Efficiency, ACS Applied Materials & Interfaces **12**, 6074 (2020).

[301] N. Wang, D. Cao, J. Wang, P. Liang, X. Chen, and H. Shu, Interface effect on electronic and optical properties of antimonene/GaAs van der Waals heterostructures, Journal of Materials Chemistry C **5**, 9687 (2017).

[302] C. Espejo, T. Rangel, A. Romero, X. Gonze, and G.-M. Rignanese, Band structure tunability in MoS 2 under interlayer compression: A DFT and GW study, Physical review B **87**, 245114 (2013).

[303] S. Bhattacharyya and A. K. Singh, Semiconductor-metal transition in semiconducting bilayer sheets of transition-metal dichalcogenides, Physical review B **86**, 075454 (2012).

[304] R. D. Shannon, Revised effective ionic radii and systematic studies of interatomic distances in halides and chalcogenides, Acta crystallographica section A: crystal physics, diffraction, theoretical and general crystallography **32**, 751 (1976).

[305] B. Cordero, V. Gómez, A. E. Platero-Prats, M. Revés, J. Echeverría, E. Cremades, F. Barragán, and S. Alvarez, Covalent radii revisited, Dalton Transactions, 2832 (2008).

[306] C. Gong, H. Zhang, W. Wang, L. Colombo, R. M. Wallace, and K. Cho, Band alignment of two-dimensional transition metal dichalcogenides: Application in tunnel field effect transistors, Applied physics letters **103**, 053513 (2013).

[307] M. Kan, H. G. Nam, Y. H. Lee, and Q. Sun, Phase stability and Raman vibration of the molybdenum ditelluride (MoTe 2) monolayer, Physical Chemistry Chemical Physics **17**, 14866 (2015).

[308] H. Huang, X. Fan, D. J. Singh, H. Chen, Q. Jiang, and W. Zheng, Controlling phase transition for single-layer MTe 2 (M= Mo and W): modulation of the potential barrier under strain, Physical Chemistry Chemical Physics **18**, 4086 (2016).

[309] C. Zhang *et al.*, Systematic study of electronic structure and band alignment of monolayer transition metal dichalcogenides in Van der Waals heterostructures, 2D Materials **4**, 015026 (2016).

[310] Z. Jin, X. Li, J. T. Mullen, and K. W. Kim, Intrinsic transport properties of electrons and holes in monolayer transition-metal dichalcogenides, Physical review B **90**, 045422 (2014).

[311] D. Rhodes, S. Das, Q. Zhang, B. Zeng, N. Pradhan, N. Kikugawa, E. Manousakis, and L. Balicas, Role of spin-orbit coupling and evolution of the electronic structure of WTe 2 under an external magnetic field, Physical review B **92**, 125152 (2015).

[312] J. Kang, S. Tongay, J. Zhou, J. Li, and J. Wu, Band offsets and heterostructures of two-dimensional semiconductors, Applied physics letters **102**, 012111 (2013).

[313] Y. Liang, S. Huang, R. Soklaski, and L. Yang, Quasiparticle band-edge energy and band offsets of monolayer of molybdenum and tungsten chalcogenides, Applied physics letters **103**, 042106 (2013).

[314] P. M. GEHRING, Neutron diffuse scattering in lead-based relaxor ferroelectrics and its relationship to the ultra-high piezoelectricity, Journal of Advanced Dielectrics **2**, 1241005 (2012).

[315] K. Leung, E. Cockayne, and A. Wright, Effective Hamiltonian study of PbZr 0.95 Ti 0.05 O 3, Physical review B **65**, 214111 (2002).

[316] A. Poursaleh and A. Andalib, An all optical majority gate using nonlinear photonic crystal based ring resonators, Optica Applicata **49** (2019).

[317] S. Haastrup *et al.*, The Computational 2D Materials Database: high-throughput

modeling and discovery of atomically thin crystals, 2D Materials **5**, 042002 (2018).

[318] T. Dargam, R. Capaz, and B. Koiller, Critical analysis of the virtual crystal approximation, Brazilian J. Phys **27**, 299 (1997).

[319] C. Chen, E. Wang, Y. Gu, D. Bylander, and L. Kleinman, Unexpected band-gap collapse in quaternary alloys at the group-III-nitride/GaAs interface: GaAlAsN, Physical review B **57**, 3753 (1998).

[320] L. Vegard, Die konstitution der mischkristalle und die raumfüllung der atome, Zeitschrift für Physik **5**, 17 (1921).

[321] Y. Luo, K. Ren, S. Wang, J.-P. Chou, J. Yu, Z. Sun, and M. Sun, First-principles study on transition-metal dichalcogenide/BSe van der Waals heterostructures: A promising water-splitting photocatalyst, The Journal of Physical Chemistry C **123**, 22742 (2019).

[322] Q. H. Wang, K. Kalantar-Zadeh, A. Kis, J. N. Coleman, and M. S. Strano, Electronics and optoelectronics of two-dimensional transition metal dichalcogenides, Nature nanotechnology **7**, 699 (2012).

[323] M. G. Ju, J. Dai, L. Ma, and X. C. Zeng, Perovskite chalcogenides with optimal bandgap and desired optical absorption for photovoltaic devices, Advanced Energy Materials **7**, 1700216 (2017).

[324] H. I. Eya, E. Ntsoenzok, and N. Y. Dzade, First–Principles Investigation of the Structural, Elastic, Electronic, and Optical Properties of α–and β–SrZrS3: Implications for Photovoltaic Applications, Materials **13**, 978 (2020).

[325] T. Mueller, TMD-Based Photodetectors, Light Emitters and Photovoltaics, 2D Materials for Nanoelectronics **17**, 13 (2016).

[326] D. Huertas-Hernando, F. Guinea, and A. Brataas, Spin-orbit coupling in curved graphene, fullerenes, nanotubes, and nanotube caps, Physical review B **74**, 155426 (2006).

[327] S. Bhatti, R. Sbiaa, A. Hirohata, H. Ohno, S. Fukami, and S. Piramanayagam, Spintronics based random access memory: a review, Materials Today **20**, 530 (2017).

[328] T. Heine, Transition metal chalcogenides: ultrathin inorganic materials with tunable electronic properties, Accounts of chemical research **48**, 65 (2015).

[329] C. Sergio *et al.*, Tuning Ising superconductivity with layer and spin–orbit coupling in two-dimensional transition-metal dichalcogenides, Nature communications **9**, 1 (2018).

[330] N. Zibouche, A. Kuc, J. Musfeldt, and T. Heine, Transition-metal dichalcogenides for spintronic applications, Annalen der Physik **526**, 395 (2014).

[331] J. C. Koziar and D. O. Cowan, Photochemical heavy-atom effects, Accounts of chemical research **11**, 334 (1978).

[332] M.-H. Chiu *et al.*, Determination of band alignment in the single-layer MoS 2/WSe 2 heterojunction, Nature communications **6**, 1 (2015).

[333] M. H. Chiu, W. H. Tseng, H. L. Tang, Y. H. Chang, C. H. Chen, W. T. Hsu, W. H. Chang, C. I. Wu, and L. J. Li, Band alignment of 2D transition metal dichalcogenide heterojunctions, Advanced Functional Materials **27**, 1603756 (2017).

[334] Y. Lv, Q. Tong, Y. Liu, L. Li, S. Chang, W. Zhu, C. Jiang, and L. Liao, Band-offset degradation in van der Waals heterojunctions, Physical Review Applied **12**, 044064 (2019).

[335] K. S. Novoselov, A. K. Geim, S. V. Morozov, D. Jiang, Y. Zhang, S. V. Dubonos, I. V. Grigorieva, and A. A. Firsov, Electric field effect in atomically thin carbon films, Science **306**, 666 (2004).

[336] H. Wang, T. Kubo, J. Nakazaki, T. Kinoshita, and H. Segawa, PbS-quantum-dot-based heterojunction solar cells utilizing ZnO nanowires for high external quantum efficiency in the near-infrared region, The Journal of Physical Chemistry Letters **4**, 2455 (2013).

[337] G. Bai, Z. Yang, H. Lin, W. Jie, and J. Hao, Lanthanide Yb/Er co-doped semiconductor layered WSe 2 nanosheets with near-infrared luminescence at telecommunication wavelengths, Nanoscale **10**, 9261 (2018).

[338] H.-P. Komsa and A. V. Krasheninnikov, Two-dimensional transition metal dichalcogenide alloys: stability and electronic properties, The Journal of Physical Chemistry Letters **3**, 3652 (2012).

[339] J. A. Hachtel, S. Susarla, V. Kochat, C. Tiwary, P. Ajayan, and J. C. Idrobo, Directly Identifying Phase Segregation in 2D Quaternary Alloys, Microscopy and Microanalysis **23**, 1438 (2017).

[340] Z. M. Wang, *MoS2: materials, physics, and devices* (Springer Science & Business Media, 2013), Vol. 21.

[341] D. Rai, T. V. Vu, A. Laref, M. A. Hossain, E. Haque, S. Ahmad, R. Khenata, and R. Thapa, Electronic properties and low lattice thermal conductivity (κ l) of monolayer (ML) MoS 2: FP-LAPW incorporated with spin–orbit coupling (SOC), Rsc Advances **10**, 18830 (2020).

[342] G. Ding, Y. Hu, D. Li, and X. Wang, A comparative study of thermoelectric properties between bulk and monolayer SnSe, Results in Physics **15**, 102631 (2019).

[343] S. Kumar and U. Schwingenschlögl, Thermoelectric performance of functionalized Sc 2 C MXenes, Physical review B **94**, 035405 (2016).

[344] S. N. Sadeghi, M. Zebarjadi, and K. Esfarjani, Non-linear enhancement of thermoelectric performance of a TiSe 2 monolayer due to tensile strain, from first-principles calculations, Journal of Materials Chemistry C **7**, 7308 (2019).

[345] X. Zhao, C. Yao, T. Liu, J. C. Hamill Jr, G. O. Ngongang Ndjawa, G. Cheng, N. Yao, H. Meng, and Y. L. Loo, Extending the Photovoltaic Response of Perovskite Solar Cells into the Near-Infrared with a Narrow-Bandgap Organic Semiconductor, Advanced Materials **31**, 1904494 (2019).

[346] N. T. Hung, A. R. Nugraha, E. H. Hasdeo, M. S. Dresselhaus, and R. Saito, Diameter dependence of thermoelectric power of semiconducting carbon nanotubes, Physical review B **92**, 165426 (2015).

[347] F. A. Rasmussen and K. S. Thygesen, Computational 2D materials database: electronic structure of transition-metal dichalcogenides and oxides, The Journal of Physical Chemistry C **119**, 13169 (2015).

[348] B. Darquié, M. P. Jones, J. Dingjan, J. Beugnon, S. Bergamini, Y. Sortais, G. Messin, A. Browaeys, and P. Grangier, Controlled single-photon emission from a single trapped two-level atom, Science **309**, 454 (2005).

[349] H. O. Everitt, *Experimental aspects of quantum computing* (Springer, 2005), Vol. 61.

[350] G. Fuchs, V. Dobrovitski, R. Hanson, A. Batra, C. Weis, T. Schenkel, and D. Awschalom, Excited-state spectroscopy using single spin manipulation in diamond, Physical review letters **101**, 117601 (2008).

[351] L. Gordon, J. R. Weber, J. B. Varley, A. Janotti, D. D. Awschalom, and C. G. Van de Walle, Quantum computing with defects, MRS bulletin **38**, 802 (2013).

[352] A. D. Greentree, B. A. Fairchild, F. M. Hossain, and S. Prawer, Diamond integrated quantum photonics, Materials Today **11**, 22 (2008).

[353] G. Balasubramanian *et al.*, Ultralong spin coherence time in isotopically engineered diamond, Nature materials **8**, 383 (2009).

[354] L. Childress and R. Hanson, Diamond NV centers for quantum computing and quantum networks, MRS bulletin **38**, 134 (2013).

[355] F. Dolde *et al.*, Room-temperature entanglement between single defect spins in diamond, Nature Physics **9**, 139 (2013).

[356] T. Chakraborty, F. Lehmann, J. Zhang, S. Borgsdorf, N. Wöhrl, R. Remfort, V. Buck, U. Köhler, and D. Suter, CVD growth of ultrapure diamond, generation of NV centers by ion implantation, and their spectroscopic characterization for quantum technological applications, Physical Review Materials **3**, 065205 (2019).

[357] J. Weber, W. Koehl, J. Varley, A. Janotti, B. Buckley, C. Van de Walle, and D. D. Awschalom, Quantum computing with defects, Proceedings of the National Academy of Sciences **107**, 8513 (2010).

[358] W. F. Koehl, B. B. Buckley, F. J. Heremans, G. Calusine, and D. D. Awschalom, Room temperature coherent control of defect spin qubits in silicon carbide, Nature **479**, 84 (2011).

[359] X. Wang, M. Zhao, Z. Wang, X. He, Y. Xi, and S. Yan, Spin-polarization of VGaON center in GaN and its application in spin qubit, Applied physics letters **100**, 192401 (2012).

[360] E. Togan *et al.*, Quantum entanglement between an optical photon and a solid-state spin qubit, Nature **466**, 730 (2010).

[361] J.-H. Yang, Y. Zhai, H. Liu, H. Xiang, X. Gong, and S.-H. Wei, Si3AlP: A new promising material for solar cell absorber, Journal of the American Chemical Society **134**, 12653 (2012).

[362] T. Watkins, A. V. Chizmeshya, L. Jiang, D. J. Smith, R. T. Beeler, G. Grzybowski, C. D. Poweleit, J. Menéndez, and J. Kouvetakis, Nanosynthesis routes to new tetrahedral crystalline solids: Silicon-like Si3AlP, Journal of the American

Chemical Society **133**, 16212 (2011).

[363] F. Langenhorst and V. L. Solozhenko, ATEM-EELS study of new diamond-like phases in the B–C–N system, Physical Chemistry Chemical Physics **4**, 5183 (2002).

[364] P. E. Sims, *Synthesis of Hybrid (III-V) y (IV) 5-2y Semiconductors: A New Approach to Extending the Optoelectronic Capabilities of Si and Ge Technologies* (Arizona State University, 2017).

[365] S. Li and L. Shi, Two novel superhard structures: Monoclinic BC3N, Physica B: Condensed Matter **584**, 412061 (2020).

[366] G. Kresse and J. Furthmüller, Efficiency of ab-initio total energy calculations for metals and semiconductors using a plane-wave basis set, Computational Materials Science **6**, 15 (1996).

[367] J. Sun, A. Ruzsinszky, and J. P. Perdew, Strongly constrained and appropriately normed semilocal density functional, Physical review letters **115**, 036402 (2015).

[368] Z.-h. Yang, H. Peng, J. Sun, and J. P. Perdew, More realistic band gaps from meta-generalized gradient approximations: Only in a generalized Kohn-Sham scheme, Physical review B **93**, 205205 (2016).

[369] S. Steiner, S. Khmelevskyi, M. Marsmann, and G. Kresse, Calculation of the magnetic anisotropy with projected-augmented-wave methodology and the case study of disordered Fe 1− x Co x alloys, Physical review B **93**, 224425 (2016).

[370] S. Nadj-Perge, S. Frolov, E. Bakkers, and L. P. Kouwenhoven, Spin–orbit qubit in a semiconductor nanowire, Nature **468**, 1084 (2010).

[371] Y. Hinuma, G. Pizzi, Y. Kumagai, F. Oba, and I. Tanaka, Band structure diagram paths based on crystallography, Computational Materials Science **128**, 140 (2017).

[372] O. Madelung, *Semiconductors: data handbook* (Springer Science & Business Media, 2012).

[373] M. S. Hybertsen and S. G. Louie, First-principles theory of quasiparticles: calculation of band gaps in semiconductors and insulators, Physical review letters **55**, 1418 (1985).

[374] D. Broberg, B. Medasani, N. E. Zimmermann, G. Yu, A. Canning, M. Haranczyk, M. Asta, and G. Hautier, PyCDT: A Python toolkit for modeling point defects in

semiconductors and insulators, Computer Physics Communications **226**, 165 (2018).

[375] C. Freysoldt, B. Grabowski, T. Hickel, J. Neugebauer, G. Kresse, A. Janotti, and C. G. Van de Walle, First-principles calculations for point defects in solids, Reviews of modern physics **86**, 253 (2014).

[376] C. Freysoldt, J. Neugebauer, and C. G. Van de Walle, Fully ab initio finite-size corrections for charged-defect supercell calculations, Physical review letters **102**, 016402 (2009).

[377] S. Bhagavantam and D. N. Rao, Dielectric constant of diamond, Nature **161**, 729 (1948).

[378] P. Deák, B. Aradi, M. Kaviani, T. Frauenheim, and A. Gali, Formation of NV centers in diamond: A theoretical study based on calculated transitions and migration of nitrogen and vacancy related defects, Physical review B **89**, 075203 (2014).

[379] Á. Gali, Ab initio theory of the nitrogen-vacancy center in diamond, Nanophotonics **8**, 1907 (2019).

[380] B. Deng, R. Zhang, and X. Shi, New insight into the spin-conserving excitation of the negatively charged nitrogen-vacancy center in diamond, Scientific reports **4**, 5144 (2014).

[381] A. Gali, E. Janzén, P. Deák, G. Kresse, and E. Kaxiras, Theory of spin-conserving excitation of the N− V− center in diamond, Physical review letters **103**, 186404 (2009).

[382] J. Wrachtrup and F. Jelezko, Processing quantum information in diamond, Journal of Physics: Condensed Matter **18**, S807 (2006).

[383] D. Toyli, D. Christle, A. Alkauskas, B. Buckley, C. Van de Walle, and D. Awschalom, Measurement and control of single nitrogen-vacancy center spins above 600 K, Physical Review X **2**, 031001 (2012).

[384] J. Franck and E. Dymond, Elementary processes of photochemical reactions, Transactions of the Faraday Society **21**, 536 (1926).

[385] E. U. Condon, Nuclear motions associated with electron transitions in diatomic molecules, Physical review **32**, 858 (1928).

[386] P. Dederichs, S. Blügel, R. Zeller, and H. Akai, Ground states of constrained systems: Application to cerium impurities, Physical review letters **53**, 2512 (1984).

[387] G. Davies and M. Hamer, Optical studies of the 1.945 eV vibronic band in diamond, Proceedings of the Royal Society of London. A. Mathematical and Physical Sciences **348**, 285 (1976).

[388] N. Son *et al.*, Divacancy in 4H-SiC, Physical review letters **96**, 055501 (2006).

[389] C. Nebel, I. Aharonovich, N. Mizuochi, and M. Hatano, *Diamond for Quantum Applications Part 1* (Academic Press, 2020).

[390] J. R. Petta, A. C. Johnson, J. M. Taylor, E. A. Laird, A. Yacoby, M. D. Lukin, C. M. Marcus, M. P. Hanson, and A. C. Gossard, Coherent manipulation of coupled electron spins in semiconductor quantum dots, Science **309**, 2180 (2005).

[391] J. Loubser and J. van Wyk, Electron spin resonance in the study of diamond, Reports on progress in physics **41**, 1201 (1978).

[392] G. Waldherr *et al.*, Quantum error correction in a solid-state hybrid spin register, Nature **506**, 204 (2014).

[393] N. Kalb *et al.*, Entanglement distillation between solid-state quantum network nodes, Science **356**, 928 (2017).

[394] P. Neumann *et al.*, Multipartite entanglement among single spins in diamond, Science **320**, 1326 (2008).

[395] T. H. Taminiau, J. Cramer, T. van der Sar, V. V. Dobrovitski, and R. Hanson, Universal control and error correction in multi-qubit spin registers in diamond, Nature nanotechnology **9**, 171 (2014).

[396] P. E. Blöchl, First-principles calculations of defects in oxygen-deficient silica exposed to hydrogen, Physical review B **62**, 6158 (2000).

[397] R. C. Weast, M. Astle, and W. Beyer, Handbook of Chemistry and Physics, 1983-1984, F34 and F36 ‘Surface tension of various liquids (1983).

[398] C. Zuo, P. Prasad, P. Busse, L. Tang, and R. Zamenhof, Proton nuclear magnetic resonance measurement of p-boronophenylalanine (BPA): A therapeutic agent for boron neutron capture therapy, Medical physics **26**, 1230 (1999).

[399] D. B. Farmer, Y.-M. Lin, and P. Avouris, Graphene field-effect transistors with self-aligned gates, Applied physics letters **97**, 013103 (2010).

[400] G. Eda, G. Fanchini, and M. Chhowalla, Large-area ultrathin films of reduced graphene oxide as a transparent and flexible electronic material, Nature nanotechnology **3**, 270 (2008).

[401] J. Wu, H. A. Becerril, Z. Bao, Z. Liu, Y. Chen, and P. Peumans, Organic solar cells with solution-processed graphene transparent electrodes, Applied physics letters **92**, 237 (2008).

[402] J. J. Dean and H. M. van Driel, Second harmonic generation from graphene and graphitic films, Applied physics letters **95**, 261910 (2009).

[403] F. Xia, T. Mueller, Y.-m. Lin, A. Valdes-Garcia, and P. Avouris, Ultrafast graphene photodetector, Nature nanotechnology **4**, 839 (2009).

[404] H. Wang *et al.*, Interconnected carbon nanosheets derived from hemp for ultrafast supercapacitors with high energy, ACS nano **7**, 5131 (2013).

[405] Q. Liu, C. Chen, M. Du, Y. Wu, C. Ren, K. Ding, M. Song, and C. Huang, Porous hexagonal boron nitride sheets: effect of hydroxyl and secondary amino groups on photocatalytic hydrogen evolution, ACS Applied Nano Materials **1**, 4566 (2018).

[406] R. Raccichini, A. Varzi, S. Passerini, and B. Scrosati, The role of graphene for electrochemical energy storage, Nature materials **14**, 271 (2015).

[407] L. Li *et al.*, Highly in-plane anisotropic 2D GeAs2 for polarization-sensitive photodetection, Advanced Materials **30**, 1804541 (2018).

[408] M. Rao, Exhaustive search of convex pentagons which tile the plane, arXiv preprint arXiv:1708.00274 (2017).

[409] Z. Liu, H. Wang, J. Sun, R. Sun, Z. Wang, and J. Yang, Penta-Pt 2 N 4: an ideal two-dimensional material for nanoelectronics, Nanoscale **10**, 16169 (2018).

[410] L. Liu and H. L. Zhuang, PtP 2: An example of exploring the hidden Cairo tessellation in the pyrite structure for discovering novel two-dimensional materials, Physical Review Materials **2**, 114003 (2018).

[411] J.-H. Yuan, Y.-Q. Song, Q. Chen, K.-H. Xue, and X.-S. Miao, Single-layer planar penta-X2N4 (X= Ni, Pd and Pt) as direct-bandgap semiconductors from first

principle calculations, Applied Surface Science **469**, 456 (2019).

[412] K. Zhao, X. Li, S. Wang, and Q. Wang, 2D planar penta-MN 2 (M= Pd, Pt) sheets identified through structure search, Physical Chemistry Chemical Physics **21**, 246 (2019).

[413] L. Liu, D. Wang, S. Lakamsani, W. Huang, C. Price, and H. L. Zhuang, Dimension engineering of single-layer PtN 2 with the Cairo tessellation, Journal of Applied Physics **125**, 204302 (2019).

[414] J. C. Crowhurst, A. F. Goncharov, B. Sadigh, C. L. Evans, P. G. Morrall, J. L. Ferreira, and A. Nelson, Synthesis and characterization of the nitrides of platinum and iridium, Science **311**, 1275 (2006).

[415] L. Thomassen, Über kristallstrukturen einiger binärer verbindungen der platinmetalle II, Zeitschrift für Physikalische Chemie **4**, 277 (1929).

[416] C. Mann, J. McLoud-Mann, and D. Von Derau, Convex pentagons that admit i-block transitive tilings, Geometriae Dedicata **194**, 141 (2018).

[417] A. K. Singh, K. Mathew, H. L. Zhuang, and R. G. Hennig, Computational screening of 2D materials for photocatalysis, The Journal of Physical Chemistry Letters **6**, 1087 (2015).

[418] D. Fu *et al.*, Molecular beam epitaxy of highly crystalline monolayer molybdenum disulfide on hexagonal boron nitride, Journal of the American Chemical Society **139**, 9392 (2017).

[419] R. Cherian and P. Mahadevan, Elastic properties of carbon nanotubes: an atomistic approach, Journal of nanoscience and nanotechnology **7**, 1779 (2007).

[420] L. D. Landau and E. M. Lifshitz, *Course of theoretical physics* (Elsevier, 2013).

[421] K. N. Kudin, G. E. Scuseria, and B. I. Yakobson, C 2 F, BN, and C nanoshell elasticity from ab initio computations, Physical review B **64**, 235406 (2001).

[422] C. Ru, Effective bending stiffness of carbon nanotubes, Physical review B **62**, 9973 (2000).

[423] A. Pantano, D. M. Parks, and M. C. Boyce, Mechanics of deformation of single- and multi-wall carbon nanotubes, Journal of the Mechanics and Physics of Solids **52**, 789 (2004).

[424] D. Janas, Towards monochiral carbon nanotubes: a review of progress in the sorting of single-walled carbon nanotubes, Materials Chemistry Frontiers **2**, 36 (2018).

[425] S. Qian *et al.*, Penta-MX 2 (M= Ni, Pd and Pt; X= P and As) monolayers: direct band-gap semiconductors with high carrier mobility, Journal of Materials Chemistry C **7**, 3569 (2019).

[426] M. Ashton, J. Paul, S. B. Sinnott, and R. G. Hennig, Topology-scaling identification of layered solids and stable exfoliated 2D materials, Physical review letters **118**, 106101 (2017).

[427] D. Wells, *The Penguin dictionary of curious and interesting geometry* (Penguin Mass Market, 1991), Vol. 1.

[428] S. Yamanaka, K.-i. Hotehama, and H. Kawaji, Superconductivity at 25.5 K in electron-doped layered hafnium nitride, Nature **392**, 580 (1998).

[429] A. F. Young, J. A. Montoya, C. Sanloup, M. Lazzeri, E. Gregoryanz, and S. Scandolo, Interstitial dinitrogen makes PtN 2 an insulating hard solid, Physical review B **73**, 153102 (2006).

[430] H. Fu, W. F. Liu, F. Peng, and T. Gao, Theoretical investigations of structural, elastic and thermodynamic properties for PtN2 under high pressure, Physica B: Condensed Matter **404**, 41 (2009).

[431] R. Yu, Q. Zhan, and X.-F. Zhang, Elastic stability and electronic structure of pyrite type PtN 2: A hard semiconductor, Applied physics letters **88**, 051913 (2006).

[432] H. Gou, L. Hou, J. Zhang, G. Sun, L. Gao, and F. Gao, Theoretical hardness of Pt N 2 with pyrite structure, Applied physics letters **89**, 141910 (2006).

[433] R. Yu and X.-F. Zhang, Platinum nitride with fluorite structure, Applied physics letters **86**, 121913 (2005).

[434] Z. Chen *et al.*, Crystal structure and physical properties of OsN 2 and PtN 2 in the marcasite phase, Physical review B **75**, 054103 (2007).

[435] P. Ajayan, T. Ebbesen, T. Ichihashi, S. Iijima, K. Tanigaki, and H. Hiura, Opening carbon nanotubes with oxygen and implications for filling, Nature **362**, 522 (1993).

[436] W. A. De Heer, A. Chatelain, and D. Ugarte, A carbon nanotube field-emission electron source, Science **270**, 1179 (1995).

[437] N. Hamada, S.-i. Sawada, and A. Oshiyama, New one-dimensional conductors: Graphitic microtubules, Physical review letters **68**, 1579 (1992).

[438] K. Koziol, J. Vilatela, A. Moisala, M. Motta, P. Cunniff, M. Sennett, and A. Windle, High-performance carbon nanotube fiber, Science **318**, 1892 (2007).

[439] J. Chen, V. Perebeinos, M. Freitag, J. Tsang, Q. Fu, J. Liu, and P. Avouris, Bright infrared emission from electrically induced excitons in carbon nanotubes, Science **310**, 1171 (2005).

[440] A. Zettl, Non-carbon nanotubes, Advanced Materials **8**, 443 (1996).

[441] V. V. Pokropivny, Non-Carbon Nanotubes (Review). Part 1. Synthesis Methods, Powder Metallurgy and Metal Ceramics **40**, 485 (2001).

[442] A. L. Ivanovskii, Non-carbon nanotubes: synthesis and simulation, Russian chemical reviews **71**, 175 (2002).

[443] S. Grimme, J. Antony, S. Ehrlich, and H. Krieg, A consistent and accurate ab initio parametrization of density functional dispersion correction (DFT-D) for the 94 elements H-Pu, The Journal of chemical physics **132**, 154104 (2010).

[444] M. Dion, H. Rydberg, E. Schröder, D. C. Langreth, and B. I. Lundqvist, Van der Waals density functional for general geometries, Physical review letters **92**, 246401 (2004).

[445] G. Román-Pérez and J. M. Soler, Efficient implementation of a van der Waals density functional: application to double-wall carbon nanotubes, Physical review letters **103**, 096102 (2009).

[446] J. Klimeš, D. R. Bowler, and A. Michaelides, Van der Waals density functionals applied to solids, Physical review B **83**, 195131 (2011).

[447] W. Chen, J. Tse, and J. Jiang, An ab initio study of 5d noble metal nitrides: OsN2, IrN2, PtN2 and AuN2, Solid State Communications **150**, 181 (2010).

[448] E. Mostaani, N. Drummond, and V. Fal'Ko, Quantum Monte Carlo calculation of the binding energy of bilayer graphene, Physical review letters **115**, 115501 (2015).

[449] Y. Le Page and P. Saxe, Symmetry-general least-squares extraction of elastic data for strained materials from ab initio calculations of stress, Physical review B **65**, 104104 (2002).

[450] F. Mouhat and F.-X. Coudert, Necessary and sufficient elastic stability conditions in various crystal systems, Physical review B **90**, 224104 (2014).

[451] J. Camacho-García, J. Moreno-Hernández, M. L. Ruiz-Peralta, A. Bautista-Hernandez, and A. Escobedo-Morales, Ab initio calculations of hardness, elastic, thermodynamic and electronic properties of metal nitrides (XN2; X= Pd, Pt) under high-pressure, Materials Research Express **6**, 045904 (2019).

[452] Z. Liu, D. Gall, and S. Khare, Electronic and bonding analysis of hardness in pyrite-type transition-metal pernitrides, Physical review B **90**, 134102 (2014).

[453] X.-J. Chen *et al.*, Hard superconducting nitrides, Proceedings of the National Academy of Sciences **102**, 3198 (2005).

[454] X.-Q. Chen, H. Niu, D. Li, and Y. Li, Modeling hardness of polycrystalline materials and bulk metallic glasses, Intermetallics **19**, 1275 (2011).

[455] W. Voigt, *Lehrbuch der kristallphysik* (Teubner Leipzig, 1928), Vol. 962.

[456] R. Hill, The elastic behaviour of a crystalline aggregate, Proceedings of the Physical Society. Section A **65**, 349 (1952).

[457] D. M. Ceperley and B. J. Alder, Ground state of the electron gas by a stochastic method, Physical review letters **45**, 566 (1980).

[458] G. L. Hornyak, J. Dutta, H. F. Tibbals, and A. Rao, *Introduction to nanoscience* (CRC press, 2008).

[459] E. Gregoryanz, C. Sanloup, M. Somayazulu, J. Badro, G. Fiquet, H.-K. Mao, and R. J. Hemley, Synthesis and characterization of a binary noble metal nitride, Nature materials **3**, 294 (2004).

[460] A. L. Ivanovskii, Platinum group metal nitrides and carbides: synthesis, properties and simulation, Russian chemical reviews **78**, 303 (2009).

[461] C. Zhi, Y. Bando, C. Tang, and D. Golberg, Boron nitride nanotubes, Materials Science and Engineering: R: Reports **70**, 92 (2010).

[462] X. Chen, C. M. Dmuchowski, C. Park, C. C. Fay, and C. Ke, Quantitative characterization of structural and mechanical properties of boron nitride nanotubes in high temperature environments, Scientific reports **7**, 1 (2017).

[463] G. Dresselhaus, M. S. Dresselhaus, and R. Saito, *Physical properties of carbon nanotubes* (World scientific, 1998).

[464] X. Blase, A. Rubio, S. Louie, and M. Cohen, Stability and band gap constancy of boron nitride nanotubes, EPL (Europhysics Letters) **28**, 335 (1994).

[465] Y. Matsuda, J. Tahir-Kheli, and W. A. Goddard III, Definitive band gaps for single-wall carbon nanotubes, The Journal of Physical Chemistry Letters **1**, 2946 (2010).

APPENDIX A

APPENDIX OF CHAPTER III

THE DATASET FOR THE 11 SI-GE-SN MEAS

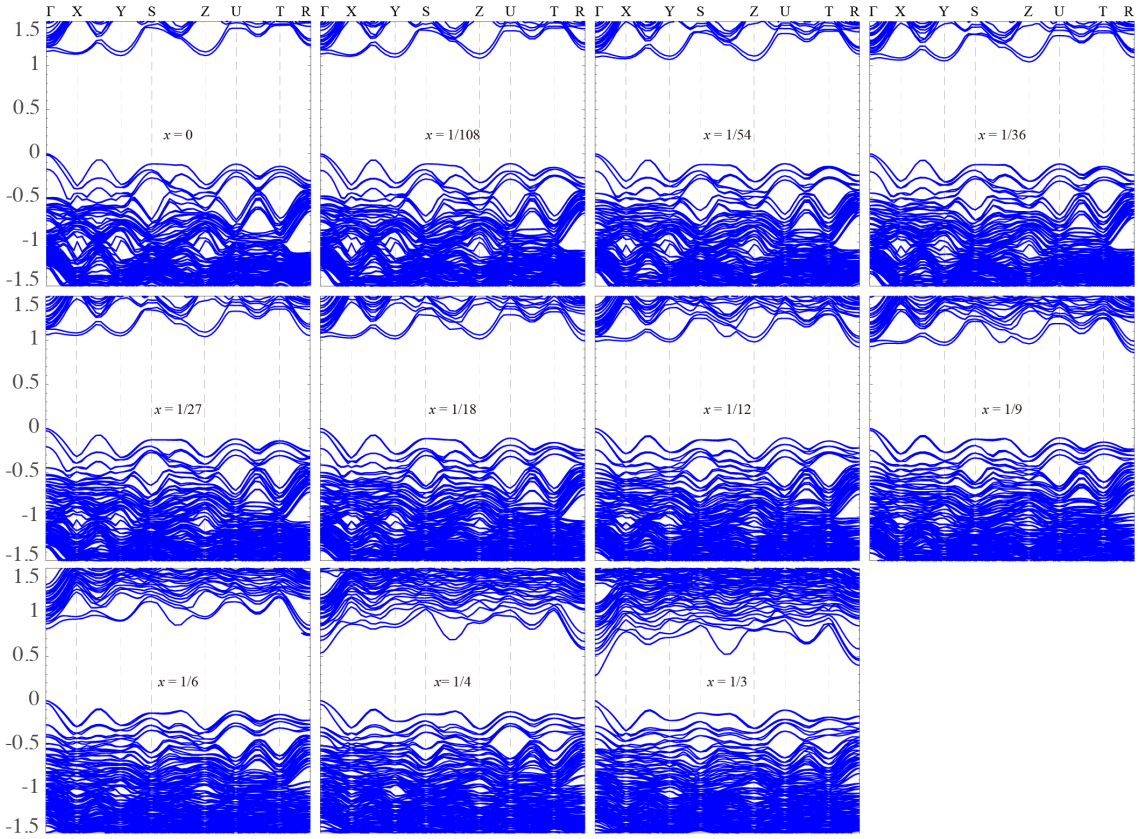

Figure A1. Band structures of $Si_yGe_ySn_x$ MEAs with $x = 0$, $x = 1/108$, $x = 1/54$, $x = 1/36$, $x = 1/27$, $x = 1/18$, $x = 1/12$, $x = 1/9$, $x = 1/6$, $x = 1/4$, and $x = 1/3$. The band structures are obtained from the modified Becke-Johnson exchange potential using the optimized structures from DFT calculations with the PBE functional. Spin-orbit coupling is taken into account and the valence band maxima are set to zero. The coordinates of X, Y, S, Z, U, T, and R are (1/2,0,0), (0,1/2,0), (1/2,1/2,0), (0,0,1/2), (1/2,0,1/2), (1/2,1/2,0), and (1/2,1/2,1/2) respectively.

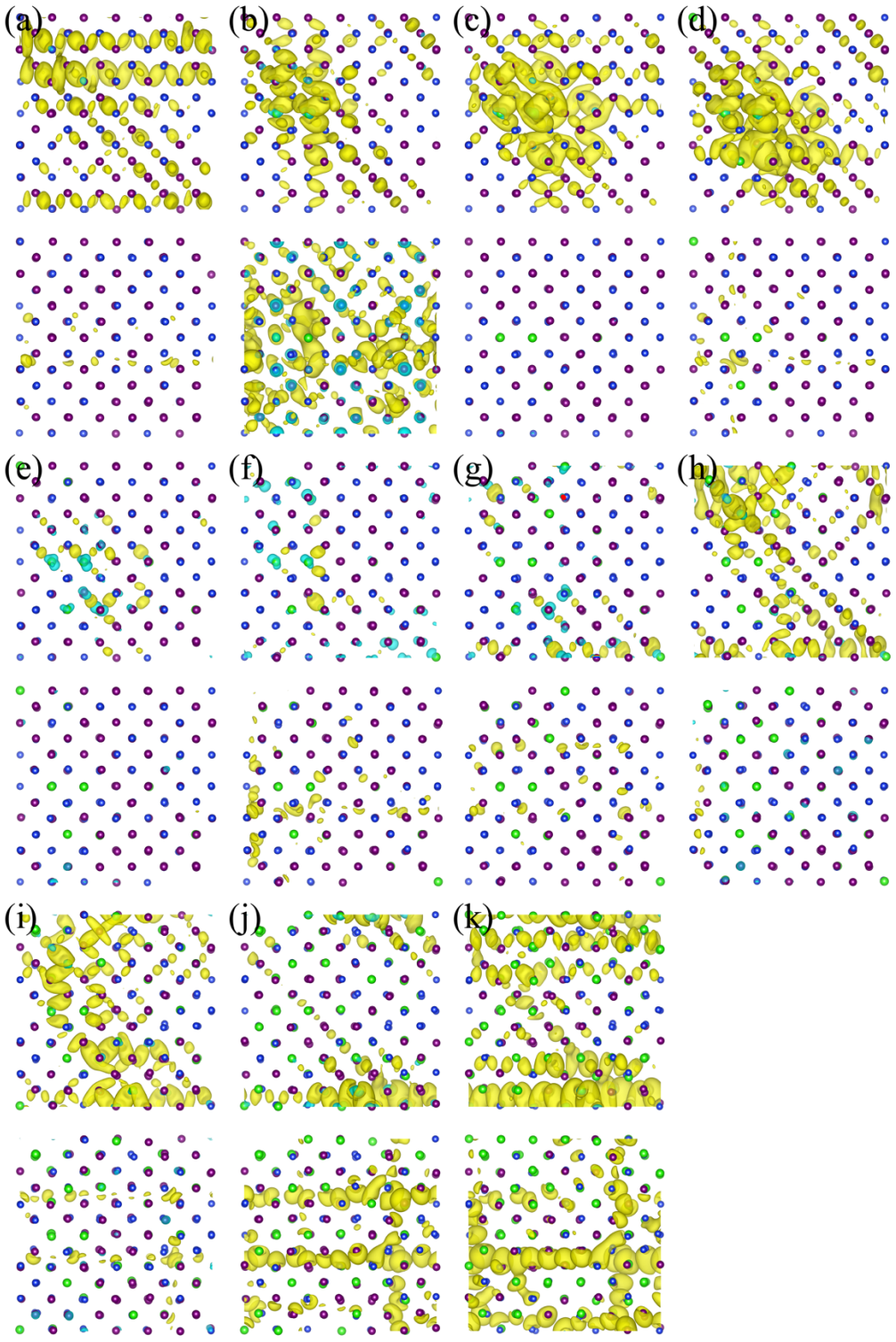

Figure A2. Charge density of the valence (top) and conduction (bottom) bands of

$Si_yGe_ySn_x$ MEAs with (a) $x = 0$, (b) $x = 1/108$, (c) $x = 1/54$, (d) $x = 1/36$, (e) $x = 1/27$, (f) $x = 1/18$, (g) $x = 1/12$, (h) $x = 1/9$, (i) $x = 1/6$, (j) $x = 1/4$, and (k) $x = 1/3$. The isosurface value of $Si_yGe_ySn_x$ MEAs is 1.0×10^{-4} e/Bohr^3.

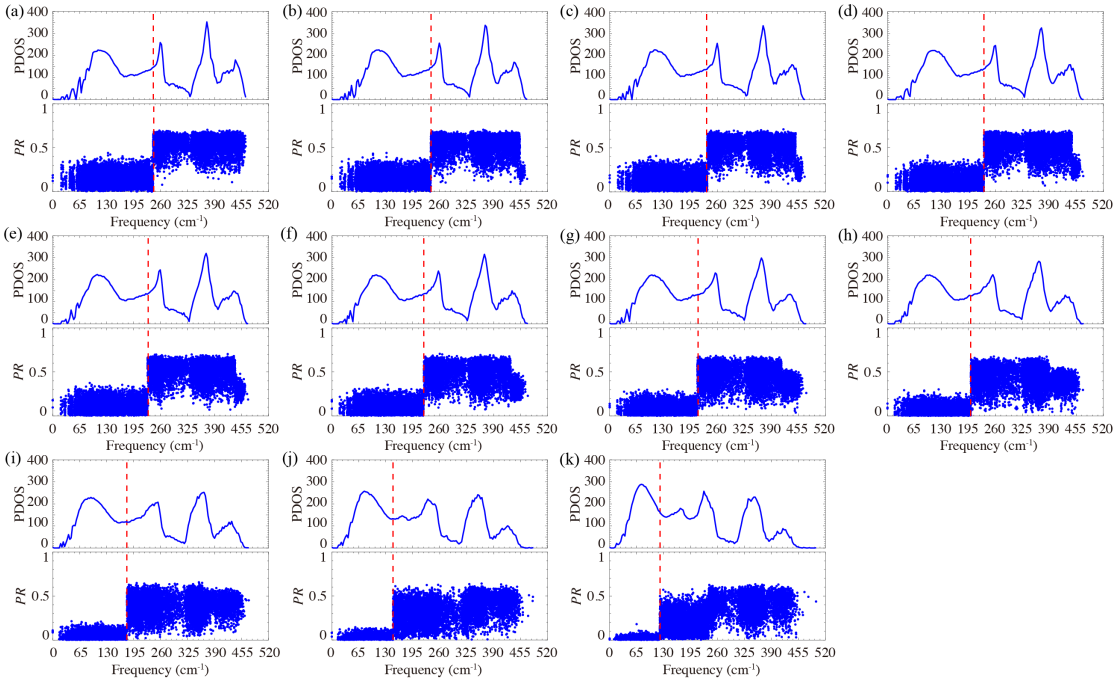

Figure A3. Phonon density of states (PDOS) and partition ratio (*PR*) of $Si_yGe_ySn_x$ MEAs with (a) $x = 0$, (b) $x = 1/108$, (c) $x = 1/54$, (d) $x = 1/36$, (e) $x = 1/27$, (f) $x = 1/18$, (g) $x = 1/12$, (h) $x = 1/9$, (i) $x = 1/6$, (j) $x = 1/4$, and (k) $x = 1/3$.

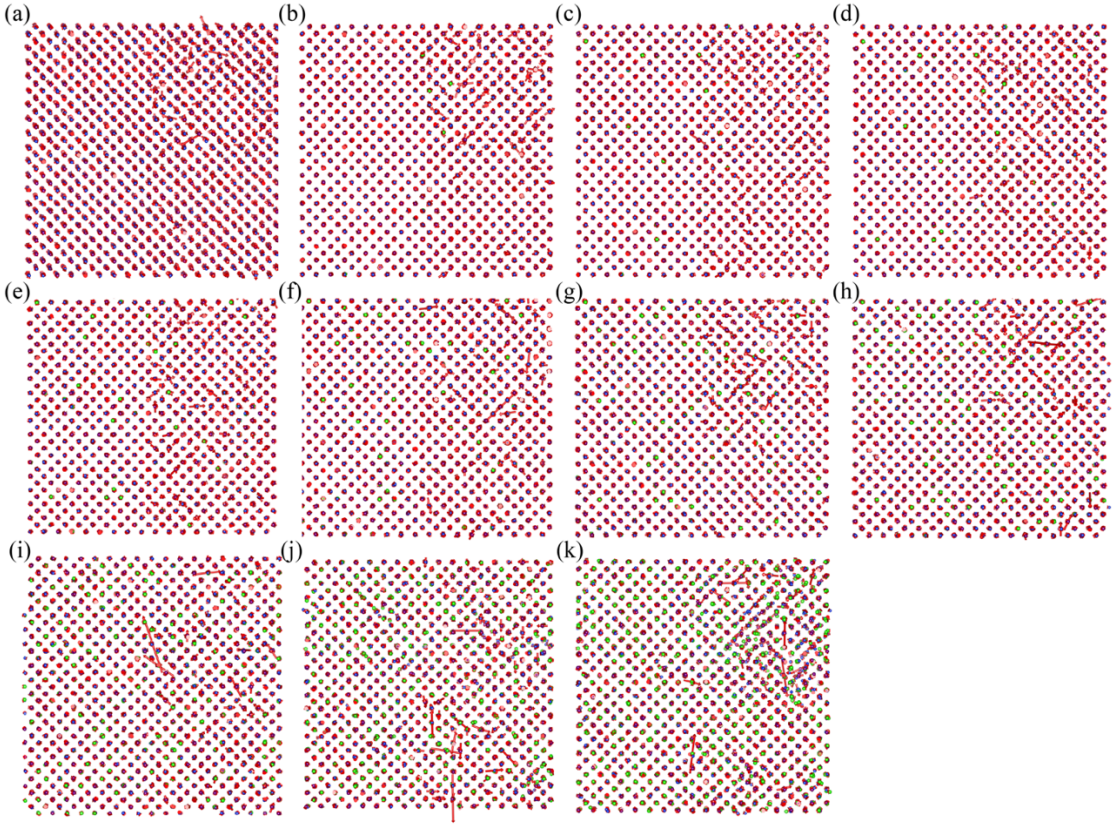

Figure A4. Phonon eigenvectors that correspond to the same low partition ratio, 0.022, of $Si_yGe_ySn_x$ MEAs with (a) $x = 0$, (b) $x = 1/108$, (c) $x = 1/54$, (d) $x = 1/36$, (e) $x = 1/27$, (f) $x = 1/18$, (g) $x = 1/12$, (h) $x = 1/9$, (i) $x = 1/6$, (j) $x = 1/4$, and (k) $x = 1/3$. To aid the visualization of the normal modes, we scale the computed eigenvectors by a factor of 20.